

Project Report
EO-1-9

EO-1 Advanced Land Imager Technology Validation Report

J.A. Mendenhall
C.F. Bruce
C.J. Digenis
D.R. Hearn
D.E. Lencioni

4 June 2002

Lincoln Laboratory

MASSACHUSETTS INSTITUTE OF TECHNOLOGY

LEXINGTON, MASSACHUSETTS



Prepared for the National Aeronautics and Space Administration
under Air Force Contract F19628-00-C-0002.

Approved for public release; distribution is unlimited.

20020801 183


This report is based on studies performed at Lincoln Laboratory, a center for research operated by Massachusetts Institute of Technology. This work was sponsored by NASA/Goddard Space Flight Center under Air Force Contract F19628-00-C-0002. Opinions, interpretations, conclusions, and recommendations are those of the authors and are not necessarily endorsed by the United States Air Force.

This report may be reproduced to satisfy needs of U.S. Government agencies.

The ESC Public Affairs Office has reviewed this report, and it is releasable to the National Technical Information Service, where it will be available to the general public, including foreign nationals.

This technical report has been reviewed and is approved for publication.

FOR THE COMMANDER


Gary Tutungian
Administrative Contracting Officer
Plans and Programs Directorate
Contracted Support Management

Non-Lincoln Recipients

PLEASE DO NOT RETURN

Permission has been granted by the Contracting Officer to destroy this document, when it is no longer required by the using agency, according to applicable security regulations.

Massachusetts Institute of Technology
Lincoln Laboratory

**EO-1 Advanced Land Imager
Technology Validation Report**

*J.A. Mendenhall
C.F. Bruce
C.J. Digenis
D.R. Hearn
D.E. Lencioni
Group 99*

Project Report EO-1-9

4 June 2002

Approved for public release; distribution is unlimited.

TABLE OF CONTENTS

	Page
1. INTRODUCTION	1
2. ADVANCED LAND IMAGER DESCRIPTION	3
2.1 Telescope	3
2.2 Focal Plane	4
2.3 Internal Reference Source	8
2.4 Mechanisms	10
2.5 High Output Paraffin Actuators	11
3. TECHNOLOGY VALIDATION	13
3.1 Ground Test Verification	13
3.1.1 Functional Verification	13
3.1.2 Spatial Calibration	48
3.1.3 Spectral Calibration	82
3.1.4 Radiometric Calibration	98
3.2 On-Orbit Test Validation	111
3.2.1 Spatial Validation	111
3.2.2 Radiometric Validation	119
3.3 On-Orbit Usage Experience	167
3.3.1 Electrical and Mechanical Operations	167
3.3.2 Detector Trending	167
3.3.3 Focal Plane Contamination	214
4. LESSONS LEARNED	217
4.1 Introduction	217
4.2 Programmatic Issues	217
4.2.1 Instrument Additions	217
4.2.2 Spacecraft Interface Change	217
4.2.3 Engineering Development Units	217
4.2.4 Contingency Reserve	218
4.3 Technical Issues	218
4.3.1 Focal Plane Contamination	218
4.3.2 Leaky Detectors	219
4.3.3 Vacuum Chamber Window Effects	219
4.3.4 Instrument Alignment on the Spacecraft	219
4.3.5 Instrument Pointing	219
4.3.6 Internal Reference Lamps	220
4.3.7 Subsystem Early Consideration	220
4.3.8 Processing of Flight Data	220
4.3.9 Schedule	220
4.4 More Lessons Learned	220
4.5 Summary	221

TABLE OF CONTENTS
(continued)

	Page
5. TECHNOLOGY INFUSION	223
5.1 Introduction	223
5.2 Technology for Infusion	224
5.3 Technology Infusion Process	227
5.4 Summary	228
6. CONTACT INFORMATION	229
7. SUMMARY/CONCLUSIONS	231
8. TECHNICAL REFERENCES	233
9. PUBLICATIONS	235

LIST OF ILLUSTRATIONS

Figure	Page
1-1 Photograph of the Earth Observing-1 Advanced Land Imager	1
2-1 ALI instrument configuration	3
2-2 A conceptual sketch of the ALI telescope and Focal Plane Assembly	4
2-3 Photograph of the silicon carbide mirrors supported by the Invar metering truss	4
2-4 ALI Focal Plane Assembly	5
2-5 Photograph of the ALI Focal Plane Assembly	6
2-6 Photograph of populated Sensor Chip Assembly	6
2-7 ALI spectral response functions for the visible and near infrared bands	7
2-8 ALI spectral response functions for the short wave infrared bands	8
2-9 EO-1 ALI internal reference source	9
2-10 Photograph of internal reference source	9
2-11 Mechanisms used in ALI	10
2-12 Photograph of the ALI Aperture Cover Assembly	10
2-13 Photograph of the Spectralon diffuser plate and motor	11
2-14 Location of aperture cover HOPAs	12
3-1 ALI being placed into thermal-vacuum test chamber	15
3-2 ALI thermal vacuum testing temperature ranges	15
3-3 Band 1p, 1, 2, 3, 4 dark current values at 220 K	17
3-4 Band 4p, 5p, 5, 7 and pan band dark current values at 220 K	18
3-5 Band 1p, 1, 2, 3, 4 noise values at 220 K	21
3-6 Band 4p, 5p, 5, 7 and pan band noise values at 220 K	22
3-7 Band 1p, 1, 2, 3, 4 dark current repeatability at 220 K	25
3-8 Band 4p, 5p, 5, 7 and pan band dark current repeatability at 220 K	26
3-9 Band 1p, 1, 2, 3, 4 noise repeatability at 220 K	27
3-10 Band 4p, 5p, 5, 7 and pan band noise repeatability at 220 K	28
3-11 Band 2 image of Lincoln Laboratory before the effects of the leaky detector (1149) are corrected	34
3-12 Band 3 image of Lincoln Laboratory before the effects of the leaky detector (864) are corrected	35
3-13 Photograph of ALI filter assembly	37
3-14 Photograph of detector rows for Bands 1-4p	37
3-15 Example of geometric correction performed on images before the leaky detector correction is implemented	38
3-16 Effects of leaky detector corruption of frame 1050 of the Band 2 image of Lincoln Laboratory	39
3-17 Frame 1050 difference array as a function of standard detector radiance	40
3-18 Frame 1050 difference array as a function of standard detector radiance. Overlaid is the linear fit leakage function.	40
3-19 Frame 1050 with leaky detector correction applied	41
3-20 Band 2 image of Lincoln Laboratory before and after leaky detector correction applied	42
3-21 Band 3 image of Lincoln Laboratory before and after leaky detector correction applied	42
3-22 Illumination of the ALI focal plane using the internal reference lamp assembly	44
3-23 Image of a portion of the top surface of the focal plane filters when contaminated and after a bake out	45

LIST OF ILLUSTRATIONS (continued)

Figure		Page
3-24	History of focal plane contamination for two periods during instrument characterization at Lincoln Laboratory	46
3-25	Top view of Imaging Collimator	47
3-26	Edge-spread functions f SCA2, Band 4 pixels scanned in the cross-track direction	51
3-27	Average line-spread function derived from the data shown in Figure 3-26	51
3-28	Normalized transfer functions derived from the data shown in Figure 3-26	52
3-29	Average normalized transfer function derived from the data shown in Figure 3-26	52
3-30	ALI focus figure of merit vs axial displacement of the knife-edge from the collimator focus	54
3-31	Surface plot of the wavefront error near the middle of the MS/Pan array	55
3-32	Optical point-spread function of the Pan band, computed from the full wavefront error, including the focus term	55
3-33	Optical transfer function of the Pan band, computed from the wavefront error, including the focus term	56
3-34	Measure and modeled Average MFTs for the Pan band, and measured MTFs for the individual SCAs	56
3-35	System MTF of the Panchromatic band near the center of the detector array	57
3-36	System PSF of the Panchromatic band near the center of the detector array	57
3-37	System MTF of band 1' near the center of the detector array	58
3-38	System MTF of band 4' near the center of the detector array	58
3-39	System MTF of band 7 near the center of the detector array	59
3-40	System PSF of band 1' near the center of the detector array	59
3-41	System PSF of band 4' near the center of the detector array	60
3-42	System PSF of band 7 near the center of the detector array	60
3-43	ALI telescope optical sitortion, from SSG measurement data	62
3-44	Residual ALI optical distortion after subtracting a cubic polynomial fit from measurement data	62
3-45	Measured detector signals and modeled signals for the Pan Band, 59.47° Ronchi orientation	65
3-46	Vector plot of the MS/Pan end of the focal plane	66
3-47	Plan view of clean room setup to measure alignment of the ALI reference cube	67
3-48	True-color image of Sutton, AK and the Matanooska River Valley	72
3-49	Selected portion of the panchromatic image of Sutton, AK	73
3-50	Panchromatic image Washington, D.C.	74
3-51	True-color image of Cape Canaveral	75
3-52	False-color image of Cape Canaveral	76
3-53	True-color image of Yuma, Arizona and the Colorado River	77
3-54	True-color image Oahu, Hawaii	78
3-55	Panchromatic image of Boston	79
3-56	Multispectral images of Lake Frome, South Australia	80
3-57	Multispectral images of Antarctica, near McMurdo Sound	81
3-58	Focal plane array Sensor Chip Assembly cross-section	83
3-59	Collimator used during spectral calibration of the EO-1 Advanced Land Imager	84
3-60	Spectral response of band 1p	87
3-61	Spectral response of band 1	88
3-62	Spectral response of band 2	89
3-63	Spectral response of band 3	90
3-64	Spectral response of band 4	91
3-65	Spectral response of band 4p	92

LIST OF ILLUSTRATIONS (continued)

Figure	Page
3-66 Spectral response of band 5p	93
3-67 Spectral response of band 5	94
3-68 Spectral response of band 7	95
3-69 Spectral response of the panchromatic band	96
3-70 Normalized visible and near infrared spectral response functions based on subsystem level measurements	97
3-71 Normalized short wave infrared spectral response functions based on subsystem level measurements	97
3-72 Integrating sphere and spectroradiometer used during radiometric calibration of the Advanced Land Imager	99
3-73 Radiometric transfer standard system built at Lincoln Laboratory	100
3-74 Example of linear fit to Band 3 detector 100 data	103
3-75 Radiometric calibration coefficients for Band 1p	104
3-76 Radiometric calibration coefficients for Band 1	104
3-77 Radiometric calibration coefficients for Band 2	105
3-78 Radiometric calibration coefficients for Band 3	105
3-79 Radiometric calibration coefficients for Band 4	106
3-80 Radiometric calibration coefficients for Band 4p	106
3-81 Radiometric calibration coefficients for Band 5p	107
3-82 Radiometric calibration coefficients for Band 5	107
3-83 Radiometric calibration coefficients for Band 7	108
3-84 Radiometric calibration coefficients for Panchromatic Band	108
3-85 EO-1ALI internal reference source	109
3-86 Photograph of internal reference source	109
3-87 Band 4 image of Lincoln Laboratory	110
3-88 Portion of the panchromatic image of New York City, scanned on March 20, 2001	112
3-89 Panchromatic radiances of the region of interest shown in Figure 3-88, projected to the axis perpendicular to the Bronx Whitestone Bridge	113
3-90 Radiance profile of the Bronx Whitestone Bridge	114
3-91 Panchromatic image of the first quarter moon from a lunar calibration scan of Feb 2, 2201	115
3-92 Scaled panchromatic radiance of the lunar limb as a function of distance perpendicular to the limb in the focal plane space	116
3-93 Panchromatic image of the star Vega	117
3-94 Panchromatic radiance profiles of Vega in the in-scan and cross-scan directions	117
3-95 False-color multispectral image of part of the South Island of New Zealand	118
3-96 Panchromatic image of Las Vegas at night	120
3-97 Celestial observations performed by the ALI	121
3-98 Band 4, 3, 2 image of Hawaii, HI	122
3-99 Band 4, 3, 2 image of East Antarctica	122
3-100 Earth limb scan history for detector 100, Band 3	126
3-101 Stray light model and flight data for Band 3	128
3-102 Effects of stray light for bands 1, 2, 3	128
3-103 Stray light impact example for West Coast, Africa scene	130
3-104 Raster scan for a typical ALI Lunar calibration	131

LIST OF ILLUSTRATIONS (continued)

Figure	Page
3-105 Direction of a typical Lunar calibration scan on the SCA module	131
3-106 Images of the moon from a typical Lunar calibration	132
3-107 Stretched images from a typical Lunar calibration	133
3-108 Ghosting effects observed in Mount Etna lava flows	134
3-109 Cross section of ALI SCA	135
3-110 Generation of Lunar ghosts by scattering off the VNIR/SWIR filter boundary	137
3-111 Generation of lava flow ghosts by scattering off the VNIR/SWIR filter boundary	138
3-112 Illustration of the solar calibration mode and laboratory test data from a solar simulator	141
3-113 Measured detector responses from the ten ALI bands during a solar calibration	142
3-114 BRDF of diffuser in front of the ALI secondary mirror used in the solar calibration model	143
3-115 Results of solar calibration of the ALI from 2/9/01	143
3-116 Overlay of ground truth results obtained by the Univ. of Arizona and solar calibration data	145
3-117 Image of the Moon taken by the ALI on 2/7/01	147
3-118 Results from solar, ground truth, and lunar absolute radiometric calibrations	147
3-119 EO-1 ALI internal reference source	148
3-120 Photograph of internal reference source	149
3-121 Results of solar, lunar, ground truth, and intersatellite radiometric calibrations	149
3-122 Radiometric calibration measurement periods during the first year on orbit	152
3-123 Effects of contamination on Band 3 data	152
3-124 Solar calibration correction factors	154
3-125 Instrument response stability for Band 3 based on solar calibration data	155
3-126 Change in instrument response for Band 3 derived from solar calibration data	155
3-127 Instrument response stability for Band 3 based on ground truth measurements	156
3-128 Instrument response stability for Band 3 based on lunar calibration measurements	157
3-129 Instrument response stability based on internal reference lamp data	158
3-130 Change in instrument response for Band 3 derived from internal reference lamp data	158
3-131 Trending of ALI radiometric calibration data for Band 2	159
3-132 Trending of ALI radiometric calibration data for Band 3	159
3-133 Radiometric stability of detectors for Band 2 as determined by internal lamp calibration data collected during the first year on orbit	160
3-134 Radiometric stability of detectors for Band 3 as determined by internal lamp calibration data collected during the first year on orbit	161
3-135 Band 3 radiometric error model and flight data	163
3-136 Results of ALI absolute radiometric calibration after the corrections to pre-flight calibration coefficients are applied	164
3-137 Noise trending for Band 1p	170
3-138 Noise trending for Band 1	171
3-139 Noise trending for Band 2	171
3-140 Noise trending for Band 3	172
3-141 Noise trending for Band 4	172
3-142 Noise trending for Band 4p	173
3-143 Noise trending for Band 5p	173
3-144 Noise trending for Band 5	174
3-145 Noise trending for Band 7	174
3-146 Noise trending for the Panchromatic Band	175

LIST OF ILLUSTRATIONS (continued)

Figure	Page
3-147 Dark current trending for Band 1p odd detectors	178
3-148 Dark current trending for Band 1p even detectors	179
3-149 Dark current trending for Band 1 odd detectors	180
3-150 Dark current trending for Band 1 even detectors	181
3-151 Dark current trending for Band 2 odd detectors	182
3-152 Dark current trending for Band 2 even detectors	183
3-153 Dark current trending for Band 3 odd detectors	184
3-154 Dark current trending for Band 3 even detectors	185
3-155 Dark current trending for Band 4 odd detectors	186
3-156 Dark current trending for Band 4 even detectors	187
3-157 Dark current trending for Band 4p odd detectors	188
3-158 Dark current trending for Band 4p even detectors	189
3-159 Dark current trending for Band 5p odd detectors	190
3-160 Dark current trending for Band 5p even detectors	191
3-161 Dark current trending for Band 5 odd detectors	192
3-162 Dark current trending for Band 5 even detectors	193
3-163 Dark current trending for Band 7 odd detectors	194
3-164 Dark current trending for Band 7 even detectors	195
3-165 Dark current trending for Panchromatic Band tri-read #1 odd detectors	196
3-166 Dark current trending for Panchromatic Band tri-read #2 odd detectors	197
3-167 Dark current trending for Panchromatic Band tri-read #3 odd detectors	198
3-168 Dark current trending for Panchromatic Band tri-read #1 even detectors	199
3-169 Dark current trending for Panchromatic Band tri-read #2 even detectors	200
3-170 Dark current trending for Panchromatic Band tri-read #3 even detectors	201
3-171 Dark current drift for Band 1p	205
3-172 Dark current drift for Band 1	206
3-173 Dark current drift for Band 2	206
3-174 Dark current drift for Band 3	207
3-175 Dark current drift for Band 4	207
3-176 Dark current drift for Band 4p	208
3-177 Dark current drift for Band 5p	208
3-178 Dark current drift for Band 5	209
3-179 Dark current drift for Band 7	209
3-180 Dark current drift for Panchromatic Band tri-read #1	210
3-181 Dark current drift for Panchromatic Band tri-read #2	210
3-182 Dark current drift for Panchromatic Band tri-read #3	211
3-183 Dark current non-linear drift distribution for Band 5p	211
3-184 Dark current non-linear drift distribution for Band 5	212
3-185 Dark current non-linear drift distribution for Band 7	212
3-186 Pan Band on-orbit contamination history	214
3-187 Pan Band on-orbit contamination history	214
3-188 Pan Band on-orbit contamination history	215
3-189 Pan Band on-orbit contamination history	215
5-1 Advanced Land Imager instrument	223
5-2 Technology infusion path	224

LIST OF ILLUSTRATIONS (continued)

Figure		Page
5-3	Wide field of view, silicon carbide optics	224
5-4	Focal plane array	225
5-5	Focal plane electronics board and chassis	226
5-6	Mechanisms, pallet, and telescope flexures	226
5-7	Advanced Land Imager control electronics boards	227
5-8	Technology infusion path	227

LIST OF TABLES

Table	Page
2-1 ALI spectral coverage and ground sample distances	7
3-1 Thermal and mechanical tests during development	14
3-2 Inoperable detectors with marked dark current	19
3-3 Detectors with marked dark current	19
3-4 Detectors with marked random or white noise	23
3-5 Detectors with noise repeatability $> \pm 0.5$ DN	29
3-6 Inoperable detectors	30
3-7 Detectors with marked dark current	31
3-8 Detectors with marked noise	31
3-9 Detectors with anomalous gain values	32
3-10 Detectors with marked cross talk	32
3-11 Master anomalous detector list	33
3-12 Direction vectors in the cube frame	68
3-13 Direction vectors in the telescope frame	69
3-14 Spectral and spatial definitions for the ten EO-1 ALI bands	82
3-15 Materials used for focal plane filter construction	83
3-16 Radiometric calibration error budget	101
3-17 ALI sensitivity	121
3-18 Response of ALI to high albedo scenes	123
3-19 Signal to noise ratio for varying radiances	123
3-20 Stray light parameters	125
3-21 Radiance error derived from the stray light model and flight data	129
3-22 Ghost generation model predictions	139
3-23 Dates of EO-1 ALI on-orbit radiometric calibrations during the first year on orbit	151
3-24 Radiometric corrections used to remove contamination effects	153
3-25 Radiometric stability trending for the first year on-orbit	160
3-26 Radiometric correction factors used to update preflight calibration coefficients	164
3-27 Data collection event dates	169
3-28 Noise trending statistics	176
3-29 Dark current trending statistics	202
3-30 Detectors with non-linear drifting > 1.5 digital numbers over a 40-min period	213

1. INTRODUCTION

The primary instrument on the first Earth Observing satellite (EO-1) under the New Millennium Program (NMP) is the Advanced Land Imager (ALI) multispectral instrument [1] (Figure 1-1). Overall direction of the EO-1 mission and acquisition of the spacecraft is being carried out by the Goddard Space Flight Center (GSFC) of NASA. MIT Lincoln Laboratory developed the Advanced Land Imager with NMP instrument team members Raytheon Systems Santa Barbara Remote Sensing (focal plane) and SSG Inc. (optical system). This instrument includes an optical system, a focal plane system, a calibration system, and the structural, thermal, and electrical components required to form an integrated unit. Lincoln Laboratory was responsible for the design, fabrication, test and development of the instrument, the software and databases for calibration, and is responsible for on-orbit performance assessment.

This document provides a detailed overview of the instrument, preflight calibration techniques and results, and pre-flight environmental testing. In-flight calibration techniques and results are also reviewed and lessons learned related to the transfer of ALI technology to the Landsat Data Continuity Mission (LDCM) are provided.

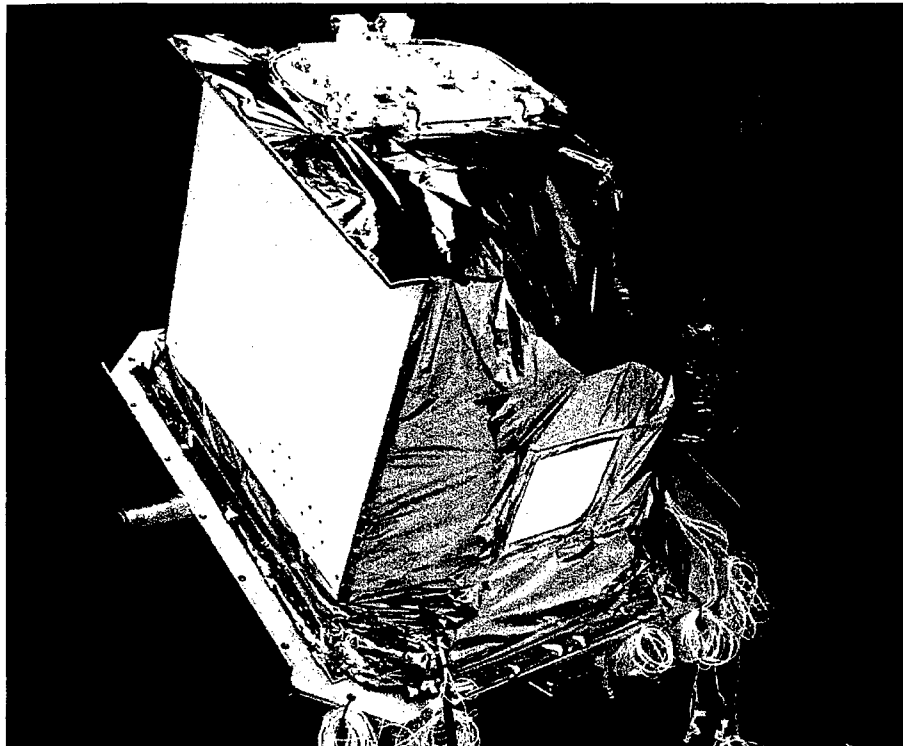


Figure 1-1. Photograph of the Earth Observing-1 Advanced Land Imager.

2. ADVANCED LAND IMAGER INSTRUMENT DESCRIPTION

The overall envelope and configuration of the Advanced Land Imager is depicted in Figure 2-1. The instrument is approximately 0.9m (X) \times 0.9m (Y) \times 0.7m (Z) and sits on an aluminum pallet that attaches to the spacecraft. The instrument has a velocity vector in the +X direction with the base pallet mounted on the nadir deck of the spacecraft so that earth is in the +Z direction. The focal plane and focal plane electronics each have radiators to help regulate the thermal environment of these components. The telescope is under multi-layer insulation (MLI), is surrounded by a thin (~1mm) aluminum housing, and supports an aperture cover. The ALI Control Electronics and the Focal Plane Electronics (FPE) packages are supported on the pallet outside the telescope housing.

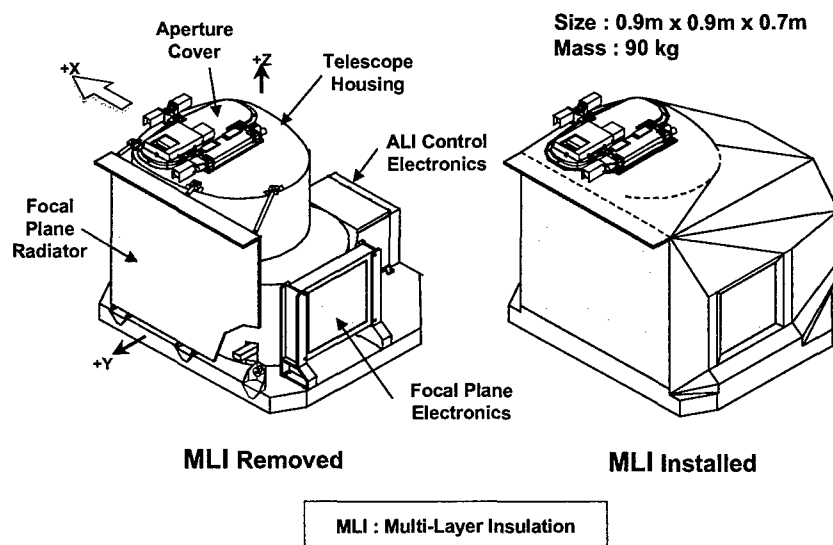


Figure 2-1. ALI instrument configuration showing the main thermal, mechanical, and electronic components.

2.1 TELESCOPE

A conceptual sketch of the interior of the ALI illustrating the major design features is shown in Figure 2-2. The telescope is a $f/7.5$ reflective triplet design with a 12.5 cm unobscured entrance pupil and a FOV of 15° cross-track by 1.256° in-track. It employs reflecting optics throughout, to cover the fullest possible spectral range. The design uses four mirrors: the primary is an off-axis asphere, the secondary is an ellipsoid, the tertiary is a concave sphere, and the fourth is a flat folding mirror. The optical design features a flat focal plane and telecentric performance, which greatly simplifies the placement of the filter and detector array assemblies. The focal plane consists of five modules, only one of which is populated with detectors for the technology demonstration. When the focal plane is fully populated, the detector arrays will cover an entire 185 km swath on the ground, equivalent to Landsat, in a 'push-broom' mode.

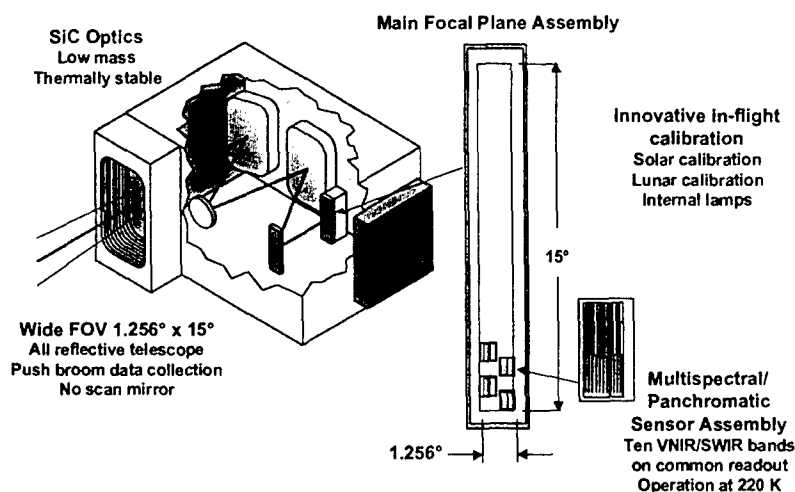
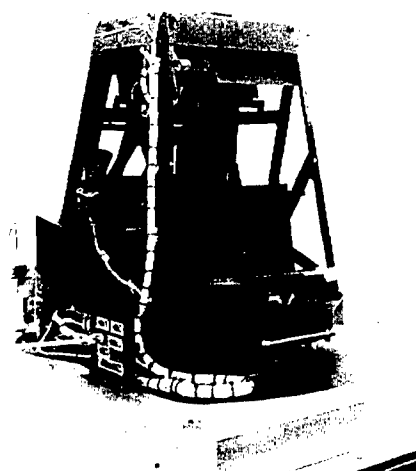


Figure 2-2. A conceptual sketch of the ALI telescope and Focal Plane Assembly.

The telescope design incorporates silicon carbide mirrors and an Invar truss structure with appropriate mounting and attachment fittings. Silicon carbide has many favorable properties for space optical systems. It possesses a high stiffness to weight ratio and a low coefficient of thermal expansion. Although it has been used for space optical elements previously, it has not been used for such large mirrors. A photograph of the silicon carbide mirrors that are held in place by the Invar metering truss is shown in Figure 2-3.



Telescope features

- 12.5 cm entrance pupil
- 15° x 1.26° field-of-view
- Telecentric, $f/7.5$ design
- Unobscured, reflective optics
- Silicon carbide mirrors
- Wavefront error = 0.11λ RMS @ 633 nm

Figure 2-3. Photograph of the silicon carbide mirrors supported by the Invar metering truss.

2.2 FOCAL PLANE

Although the optical system supports a 15° wide FOV, only 3° was populated with detector arrays, as illustrated in Figures 2-4, 2-5, 2-6. The multispectral panchromatic (MS/Pan) array has 10 spectral bands in the visible, near infrared (VNIR), and short wave infrared (SWIR) (Figures 2-7 and 2-8). The pan detectors subtend 10 m square pixels on the ground and are sampled every 10 m as the

earth image moves across the array. The MS detectors subtend 30 m and are sampled every 30 m. The wavelength coverage and ground sampling distance (GSD) are summarized in Table 2-1. Six of the nine multispectral bands are the same with those of the Enhanced Thematic Mapper (ETM+) on Landsat 7 [2] for direct comparison. The additional bands, indicated with primes, were chosen for other science objectives.

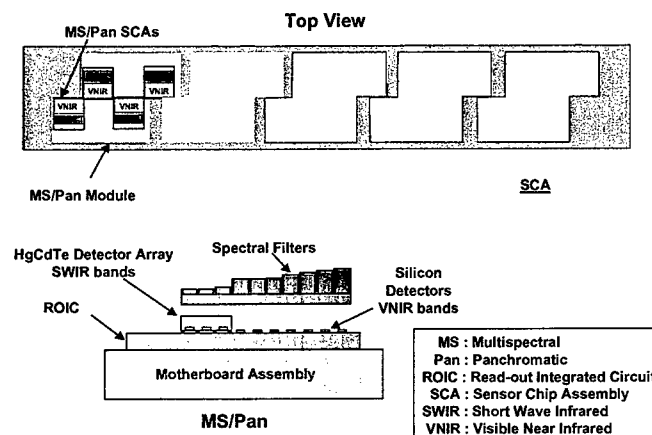


Figure 2-4. ALI Focal Plane Assembly.

Four sensor chip assemblies (SCAs) populate the 3° cross-track segment of the focal plane to form the focal plane array or FPA. Each MS band on each SCA contains 320 detectors in the cross-track direction, while each pan band contains 960 detectors. The total cross-track coverage from the single MS/Pan module is 37 km.

The MS/Pan arrays use silicon-diode VNIR detectors fabricated on the silicon substrate of the Readout Integrated Circuit (ROIC). The SWIR detectors are mercury-cadmium-telluride (HgCdTe) photo-diodes that are indium bump-bonded onto the ROIC that services the VNIR detectors. These SWIR detectors promise high performance over the 0.9 to 2.5 μm wavelength region at temperatures that can be reached by passive or thermoelectric cooling. The nominal focal plane temperature is 220 K and is maintained by the use of a radiator and heater controls.

Application of detectors of different materials to a single readout integrated circuit (ROIC) enables a large number of arrays covering a broad spectral range to be placed closely together. This technology is extremely effective when combined with the wide cross-track FOV optical design being used on the ALI.

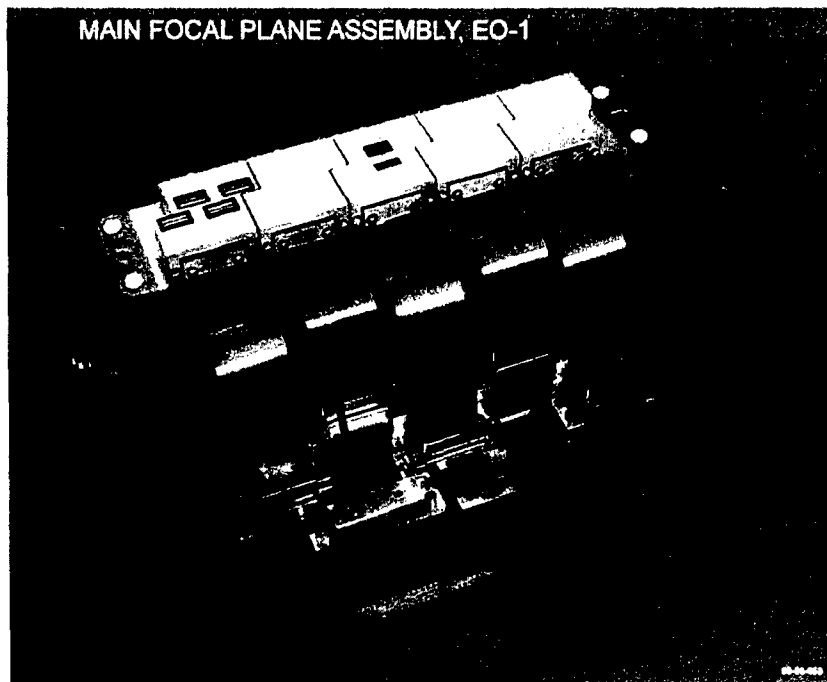


Figure 2-5. Photograph of ALI Focal Plane Assembly.

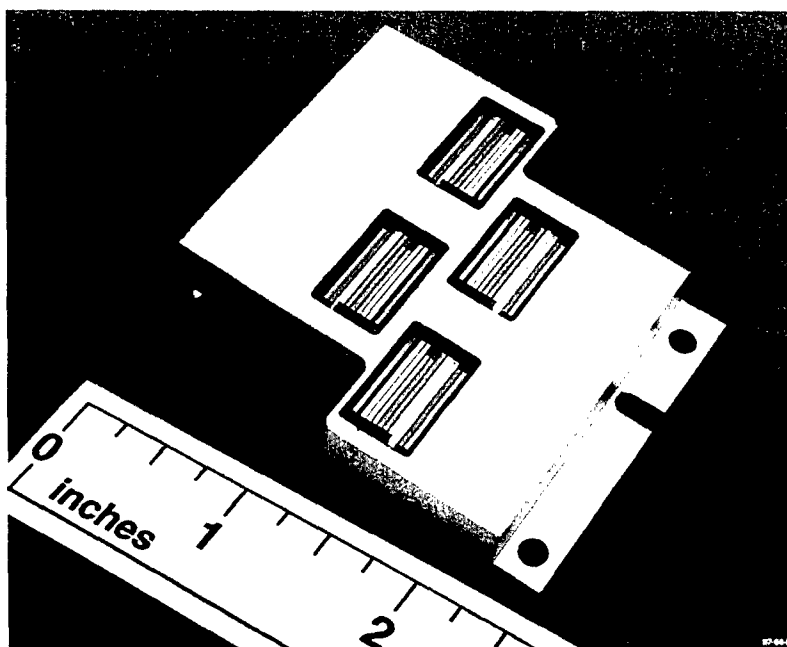


Figure 2-6. Photograph of populated Sensor Chip Assembly.

Table 2-1
ALI spectral coverage and ground sample distances

Band	Wavelength (μm)	GSD (m)
Pan	0.480-0.690	10
MS-1'	0.433-0.453	30
MS-1	0.450-0.515	30
MS-2	0.525-0.605	30
MS-3	0.630-0.690	30
MS-4	0.775-0.805	30
MS-4'	0.845-0.890	30
MS-5'	1.200-1.300	30
MS-5	1.550-1.750	30
MS-7	2.080-2.350	30

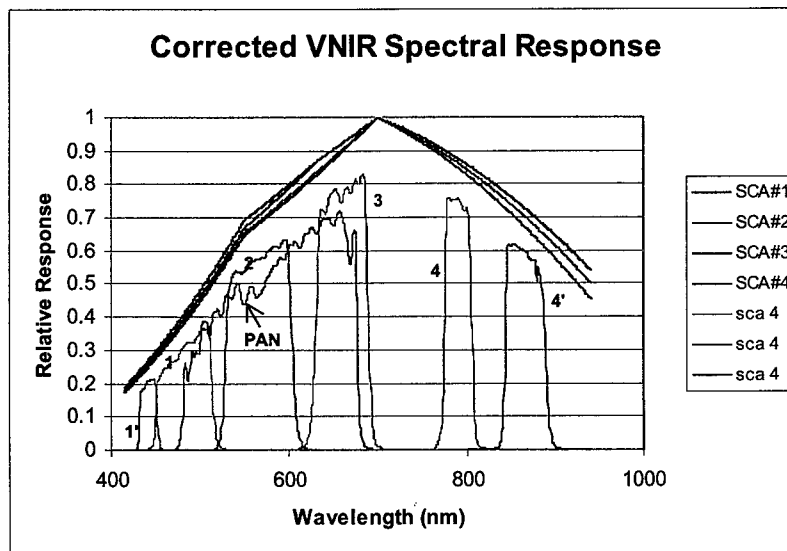


Figure 2-7. ALI spectral response functions for the visible and near infrared bands obtained from component level measurements. The smoothly varying curves at the top represent the responsivities of the silicon detectors for each SCA. The final responses for each band, considering mirror reflectivities, filter transmissions, and detector responsivities are shown in the lower curves.

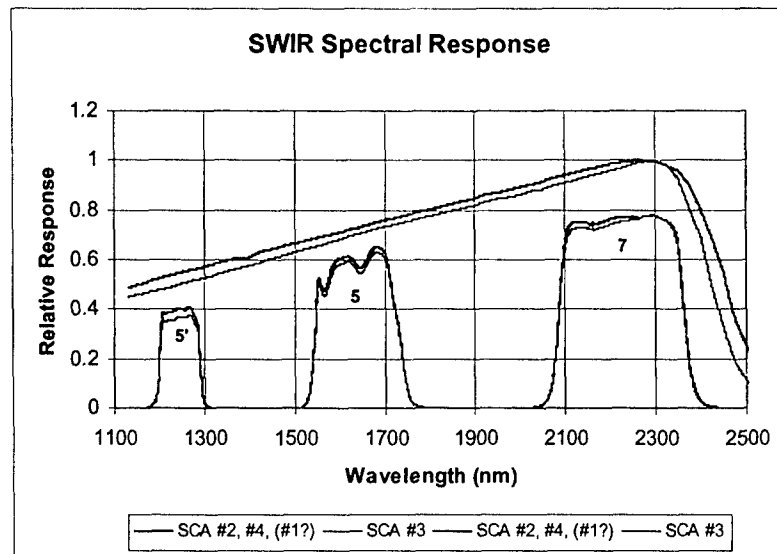


Figure 2-8. ALI spectral response functions for the short wave infrared bands obtained from component level measurements. The smoothly varying curves at the top represent the responsivities of the HgCdTe detectors for each SCA. The final responses for each band, considering mirror reflectivities, filter transmissions, and detector responsivities are shown in the lower curves.

The focal plane electronics (FPE) provides the necessary bias and clock voltages to operate and control the FPA. Both the array frame rate and the detector integration times can be set by commands to the FPE. The nominal frame rate is 226 frames/sec. The nominal integration time for the MS detectors is 4.05 msec while 1.35 msec for the Pan. The frame rate can be adjusted in 312.5 nsec increments to synchronize frame rate with ground scan velocity variations due to altitude and velocity variations during orbit.

The FPE samples the output of each detector with a 12-bit converter. The samples are then multiplexed into a 32-bit parallel word (two detector samples plus an 8 bit header) RS-422 output channel that streams the data at a 102.4 Mbit/sec rate to a 44 Gbit capacity, Wideband Advanced Recorder-Processor (WARP) onboard the spacecraft.

2.3 INTERNAL REFERENCE SOURCE

Daily in-flight radiometric checks of the Advanced Land Imager are conducted by observing the on-board internal reference source (Figures 2-9, 2-10). This source consists of three Welch Allyn 997418-7 (modified) gas-filled lamps mounted on a small, 0.8-inch diameter integrating sphere. Light emerging from the exit slit of the sphere passes through a BK 7 lens and infrared filter, is reflected off the ALI flat mirror, and floods the focal plane. This source provides radiometric stability monitoring of the instrument. Extensive stability and lifetime testing of the internal reference source for spaceflight operation was conducted at Lincoln Laboratory.

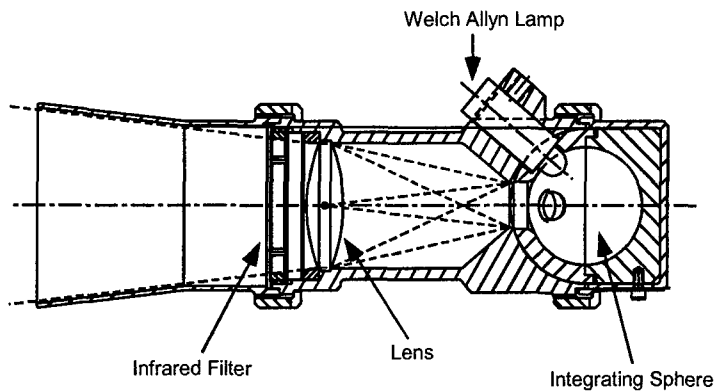


Figure 2-9. EO-1 ALI internal reference source.

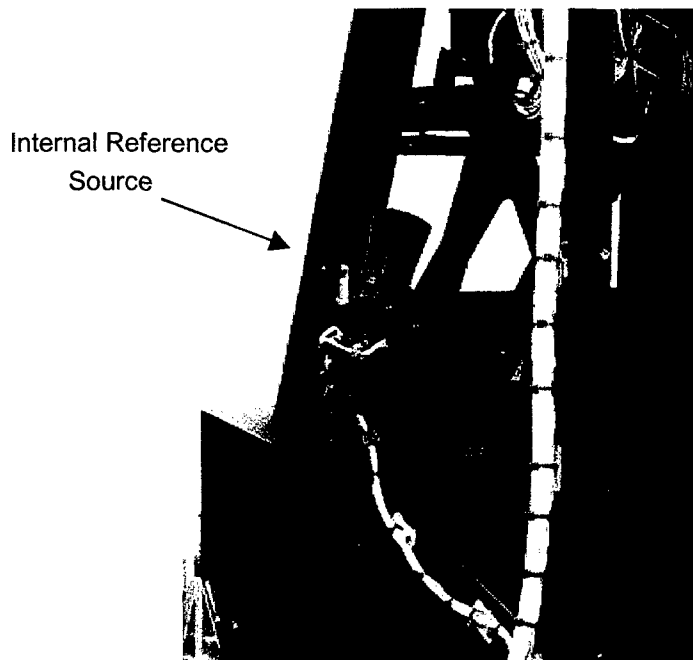


Figure 2-10. Photograph of internal reference source.

Following each observation, after the aperture cover has been closed, the three internal calibration lamps are powered by the ALI Control Electronics. After an eight-second stabilization period the lamps are sequentially powered down in a staircase fashion, with two-second exposures between each step. In this manner, the focal plane will receive a three point radiometric calibration after each observation.

2.4 MECHANISMS

Figures 2-11 and 2-12 illustrate the three motor-driven mechanisms employed by the ALI. The aperture cover opens for a data collection event and closes after data collection. The cover is driven by a two-phase stepper motor. There are four LEDs mounted near the cover for discrete status monitoring (open, closed, launch latch released, fail safe released). There is also an aperture cover throwback spring that is enabled by firing a High Output Paraffin Actuator (HOPA). The throwback spring would be used in case of motor failure; however, shutting the aperture cover would not be possible after invoking this option.

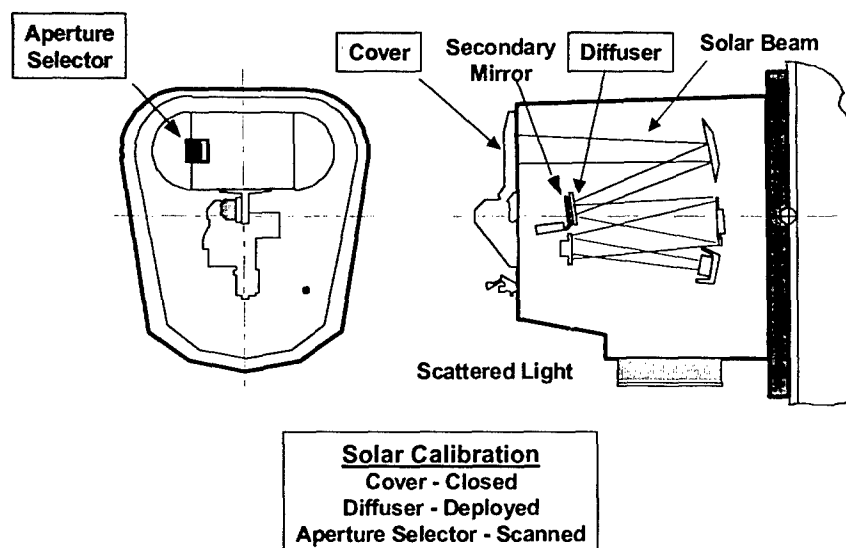


Figure 2-11. Mechanisms used in ALI

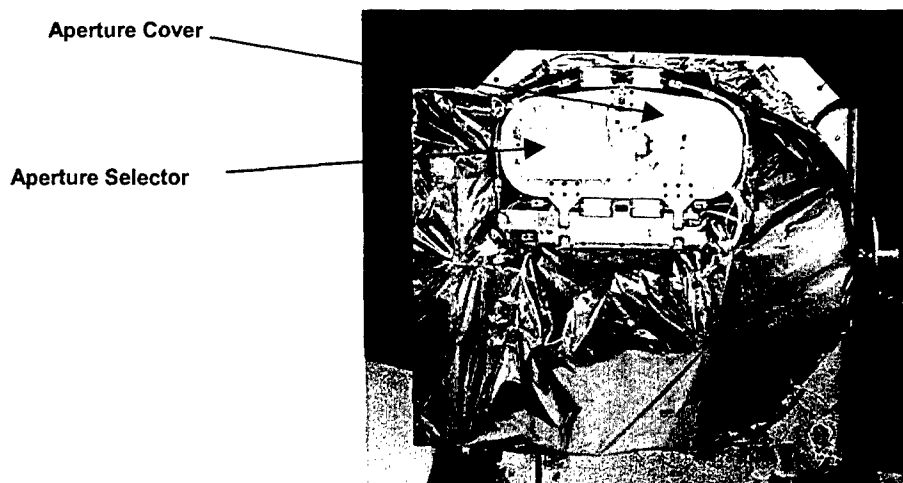


Figure 2-12. Photograph of the ALI Aperture Cover Assembly.

For solar calibration, the aperture cover is closed and a Spectralon diffuser plate is swung over the secondary mirror by a second stepper motor (Figure 2-13). Four LEDs are mounted near the diffuser assembly for discrete status monitoring (deployed, stowed, launch latch released, fail safe released). Fully deployed, the diffuser panel will reflectively scatter any sunlight that would otherwise impinge on the secondary. Once the diffuser is in place, an Aperture Selector Assembly, contained within the Aperture Cover Assembly, is activated. The aperture selector is a two-phase stepper motor that moves an opaque slide over a row of small to increasingly larger slit openings, exposing the diffuser to increasing amounts of sunlight. Fully open, the aperture selector then reverses the slide motion to eventually block all light. Two LEDs are used to monitor the position of the selector (fully extended, fully retracted). Additionally, a resolver is used for continuous position readout. During solar calibration the reflectively scattered sunlight exposes the FPA to an irradiance that is equivalent to earth-reflected sunlight for an earth albedo ranging from 0 to 90%.

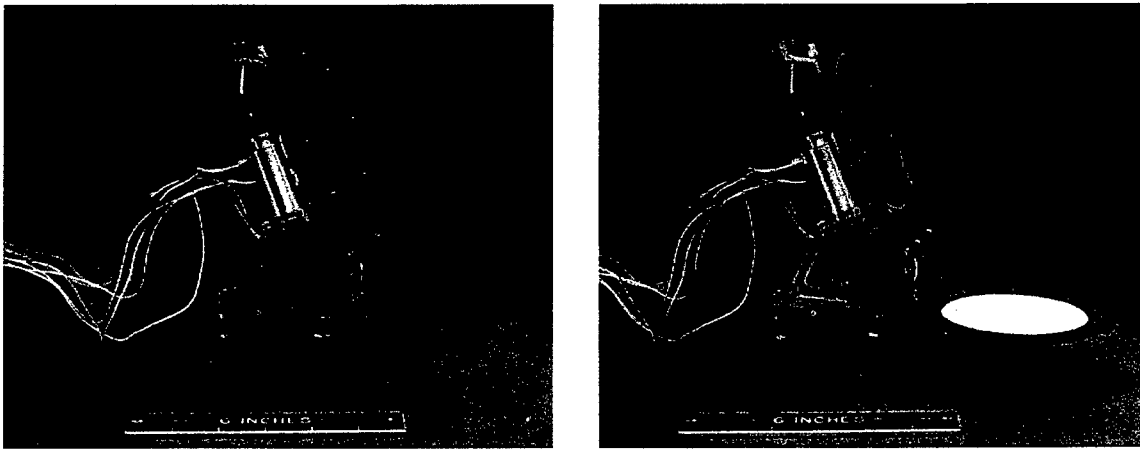


Figure 2-13. Photograph of the Spectralon diffuser plate and motor. The diffuser is stowed in the left image and deployed in the right image.

2.5 HIGH OUTPUT PARAFFIN ACTUATORS

The ALI employs six high output paraffin actuators or HOPAs. Four of the HOPAs are used as launch latches and fail safe latches for the aperture cover (Figure 2-14). The remaining two HOPAs are used as a single string launch latch and fail safe latch for the solar diffuser. The launch latches are used to secure the aperture cover and solar diffuser during ascent. The fail safe latches are only to be used if the aperture cover or solar diffuser motors fail and cannot be recovered. Once the fail-safe latches are fired, the associated mechanism can never be used again.

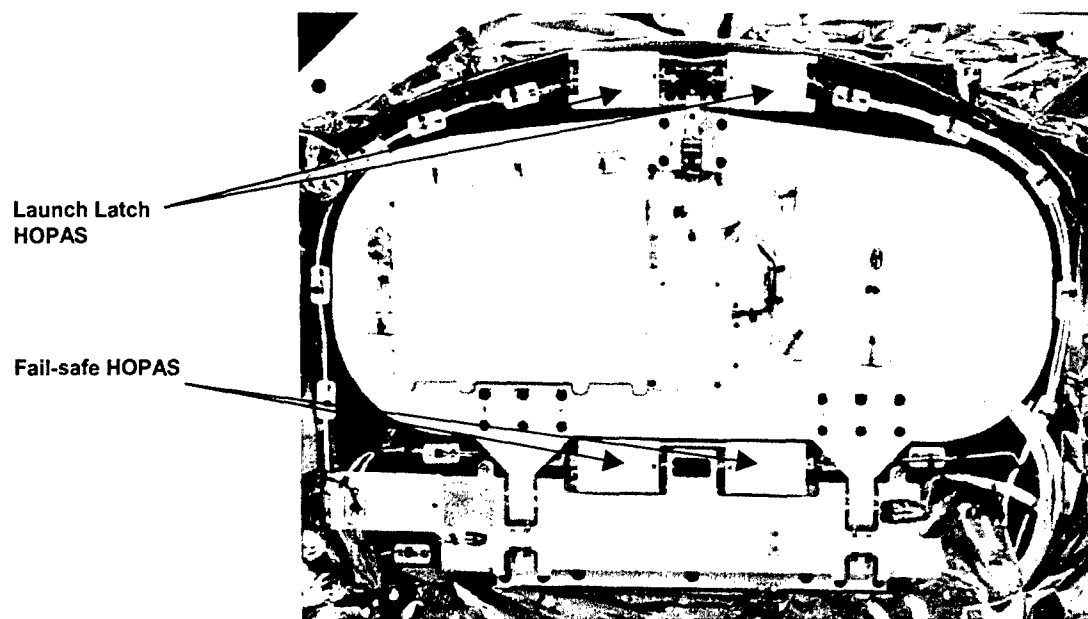


Figure 2-14. Location of aperture cover HOPAs.

3. ADVANCED LAND IMAGER VALIDATION

3.1 GROUND TEST VERIFICATION

The ALI instrument was thoroughly tested and calibrated at Lincoln Laboratory prior to delivery to GSFC for integration with the spacecraft. The following sections describe first, the functional verification tests, then the various calibrations: spatial, spectral, and radiometric. Some of the functional tests and all of the calibrations took place in a Class 1000 clean room at Lincoln Laboratory. Most of the calibrations were performed with the instrument at nominal operating temperatures in a thermal vacuum chamber.

3.1.1 Functional Verification

Functional verification tests are intended to show that the instrument or subsystem operates as intended, and produces results within nominal design limits. The functional tests described here include assembly and engineering tests; detector tests for dark current, noise, and anomalous detectors; a description of the Leaky Detector phenomenon; contamination; focus adjustment; and end-to-end imaging.

3.1.1.1 Instrument Assembly

The flight telescope was delivered by SSG to MIT Lincoln Laboratory in April 1998. The Focal Plane System was delivered by Raytheon SBRS in June 1998. ALI sub-systems were assembled, integrated, and tested over a 9-month period in preparation for delivery to the spacecraft integrator (Swales Aerospace) in March 1999. The integration and assembly followed a set of NASA processes specially tailored for quality control, documentation, and cleanliness of space-qualified components and sub-systems. During this time period, testing was undertaken for subsystem alignment, for space flight qualification, and for performance measurement.

3.1.1.2 Thermal and Mechanical Testing

A number of successful tests were conducted to establish the qualification of the ALI for launch and space operation (Table 3-1).

To facilitate testing, an ALI Structural Thermal Model (STM) and an Engineering Development Unit (EDU) of the ALICE and mechanisms were developed during the course of fabrication and assembly of the instrument. The STM was subjected to qualification level testing, while flight box and instrument level testing was restricted to protoflight levels.

Table 3-1
Thermal and mechanical tests during development

Test	Test Conditions
Sine burst acceleration along each axis <ul style="list-style-type: none"> • ALI Structural Thermal Model • Flight units box level Sine sweep <ul style="list-style-type: none"> • Flight units box level • ALI flight unit Random vibration along each axis <ul style="list-style-type: none"> • Flight units box level • ALI Flight Unit Note: Acceleration spectrum was notched as necessary to insure 3 σ acceleration loads did not exceed Qualification Level loads at any frequency for non-electronics box level testing. Mechanism Life Testing <ul style="list-style-type: none"> • Mechanism's Engineering Development Unit Thermal Cycle Testing <ul style="list-style-type: none"> • ALI Flight Unit 	<ul style="list-style-type: none"> • Qualification* • Protoflight(†) <ul style="list-style-type: none"> • Protoflight(†) • Protoflight(†) <ul style="list-style-type: none"> • Protoflight(‡) • Protoflight(‡) 1.5 times design life Aperture Selector and Calibration Diffuser: 240 cycles Aperture Cover: 3900 cycles Survive 50°C – -10°C thermal cycle before & after test 50°C to -30°C survival hot-to-cold soak cycle Four thermal cycles 40°C to -10°C Checked operation before, during, & after each cycle.

* Qualification levels = 1.5 × flight levels (2 oct/minute)

‡ Protoflight levels = flight level + 3 dB (1 minute/axis)

† Protoflight levels = 1.25 × flight levels (4 oct/minute)

After being fully assembled, the ALI also underwent thermal vacuum testing to 1) validate the ALI thermal model and 2) demonstrate survivability of the instrument within an environment more severe than expected on orbit. This testing included thermal soaking and thermal cycling while under vacuum. Figure 3-1 shows the instrument being placed into the thermal vacuum test chamber. Figure 3-2 provides a summary of ALI thermal vacuum testing, compared to on-orbit expectations. Testing at Lincoln Laboratory is included in the ALI I&T region of this figure.

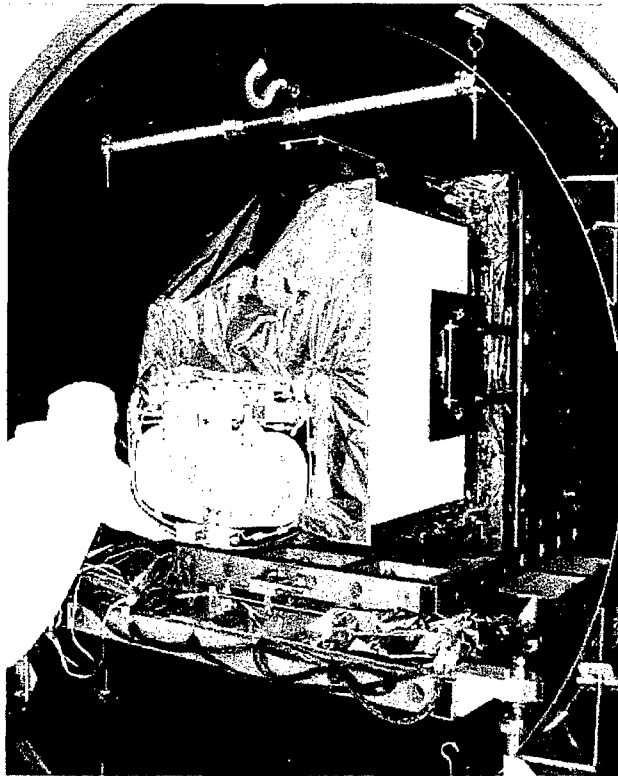


Figure 3-1. ALI being placed into thermal-vacuum test chamber.

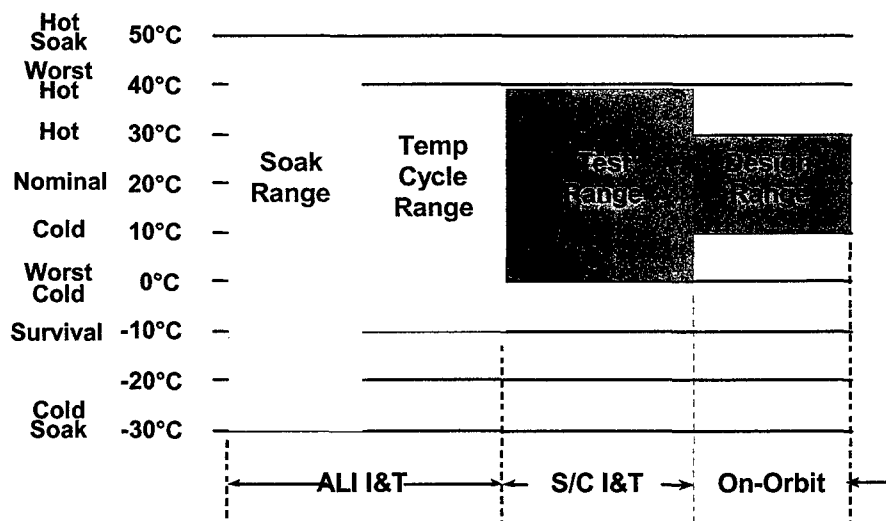


Figure 3-2. ALI thermal vacuum testing temperature ranges.

3.1.1.3 Dark Current, Noise, and Anomalous Detectors

This section provides a review of three key Advanced Land Imager instrument performance parameters: dark current, noise, and anomalous detectors. The dark current and noise of the ALI are closely coupled. The dark current defines the background level for each detector, and frame-to-frame fluctuations of this current is a major contributor to the noise of the instrument.[†] Results obtained while operating the focal plane at the nominal integration times (4.05 ms for multispectral bands and 1.35 ms for the panchromatic band) at 220 K are provided. Additional results with the focal plane operating at 215 & 225 K may be found elsewhere [3]. It should also be noted that all results are referenced to the 12-bit system the ALI employs.

This section also provides a review of anomalous detectors of the instrument. These detectors have been selected based on unusual dark current and noise characteristics, as well as gain and cross-talk peculiarities. The behavior of anomalous detectors should be carefully considered when selecting targets of small spatial extent or scientifically assessing the quality of particular scenes.

3.1.1.3.1 Dark Current and Noise Characterization

3.1.1.3.1.1 Dark Current

The ALI dark current is a measure of the background level of each detector. It is a combination of thermally excited electrons within the detector and the gain of the associated electronics. The dark current for each detector of every band has been calculated as the mean of 450 multispectral and 1350 panchromatic frames (2 seconds). The dark current levels calculated from data collected during ground calibration are provided in Figures 3-3 and 3-4. The focal plane was operating at 220 K during this period. Expected detector to detector and Sensor Chip Assembly to Sensor Chip Assembly (SCA to SCA) variations are present. Five of the six ALI inoperable detectors are clearly evident in the dark current data and are listed in Table 3-2. Nine ALI detectors have been identified as having excessive dark current (>1.25 times the mean dark current for that band and SCA) and are listed in Table 3-3. The observed large dark current offsets between odd and even detectors on SCA 4 band 2 and SCA 3 band 3 are the result of two 'leaky' detectors. Detector 1149 on band 2 and detector 864 on band 3 have significant cross-talk with neighboring odd and even detectors respectively. As a result, even under dark conditions, over 300 digital number (DN) units (out of 4096) of induced signal are present on the corrupted detectors. This effect is covered in more detail elsewhere [(Section 3.1.1.4, [3]). Finally, bands 5p, 5, and 7 exhibit large increases in dark current centered on detector 1200. These regions of enhanced dark current, otherwise referred to as 'hot spots', are stable and repeatable, and may be accounted for by using normal dark current subtraction techniques.

[†] All SWIR detectors have a transient effect associated with the initial data collected following the focal plane turn-on. As a result, the first ten frames from all data sets have been excluded from dark current and noise analysis

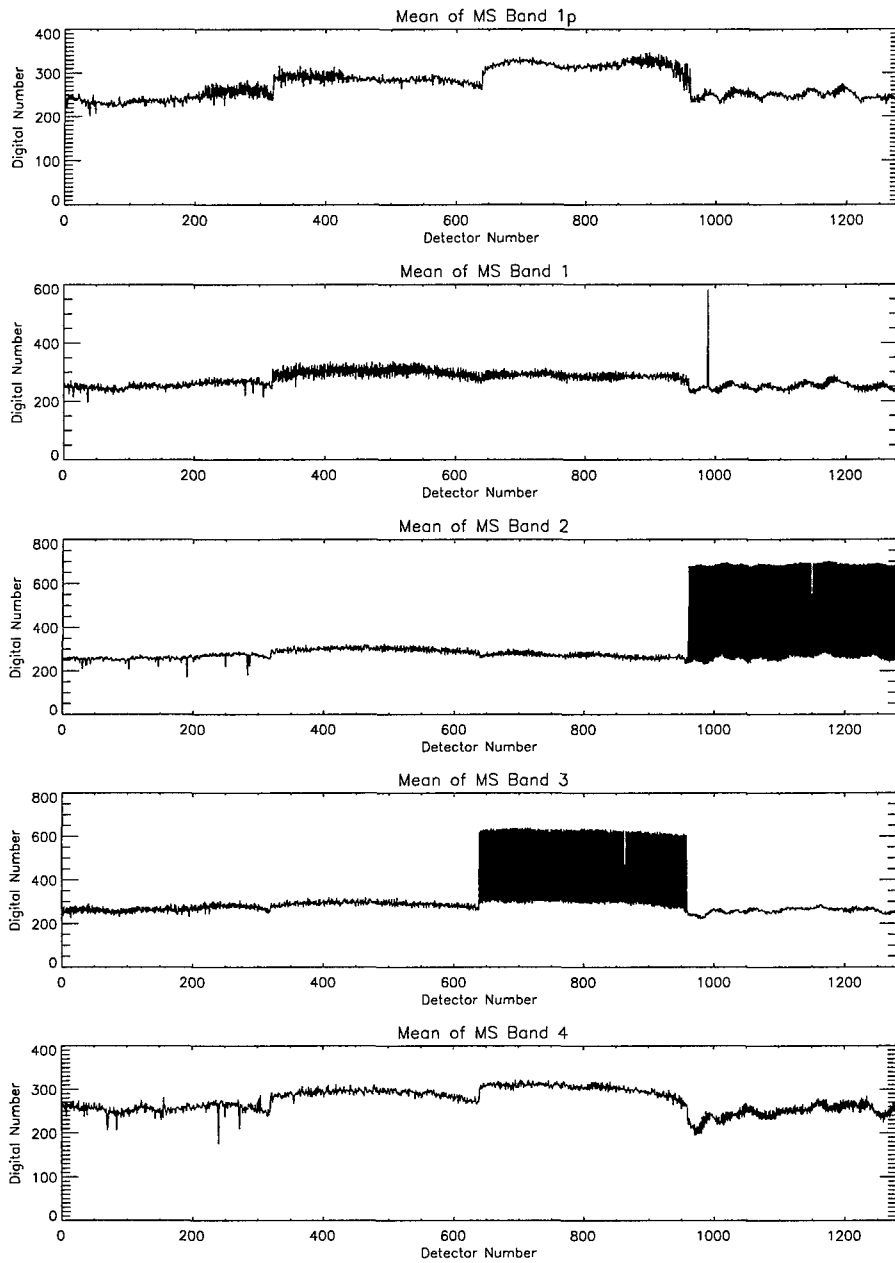


Figure 3-3. Band 1p, 1, 2, 3, 4 dark current values at 220 K.

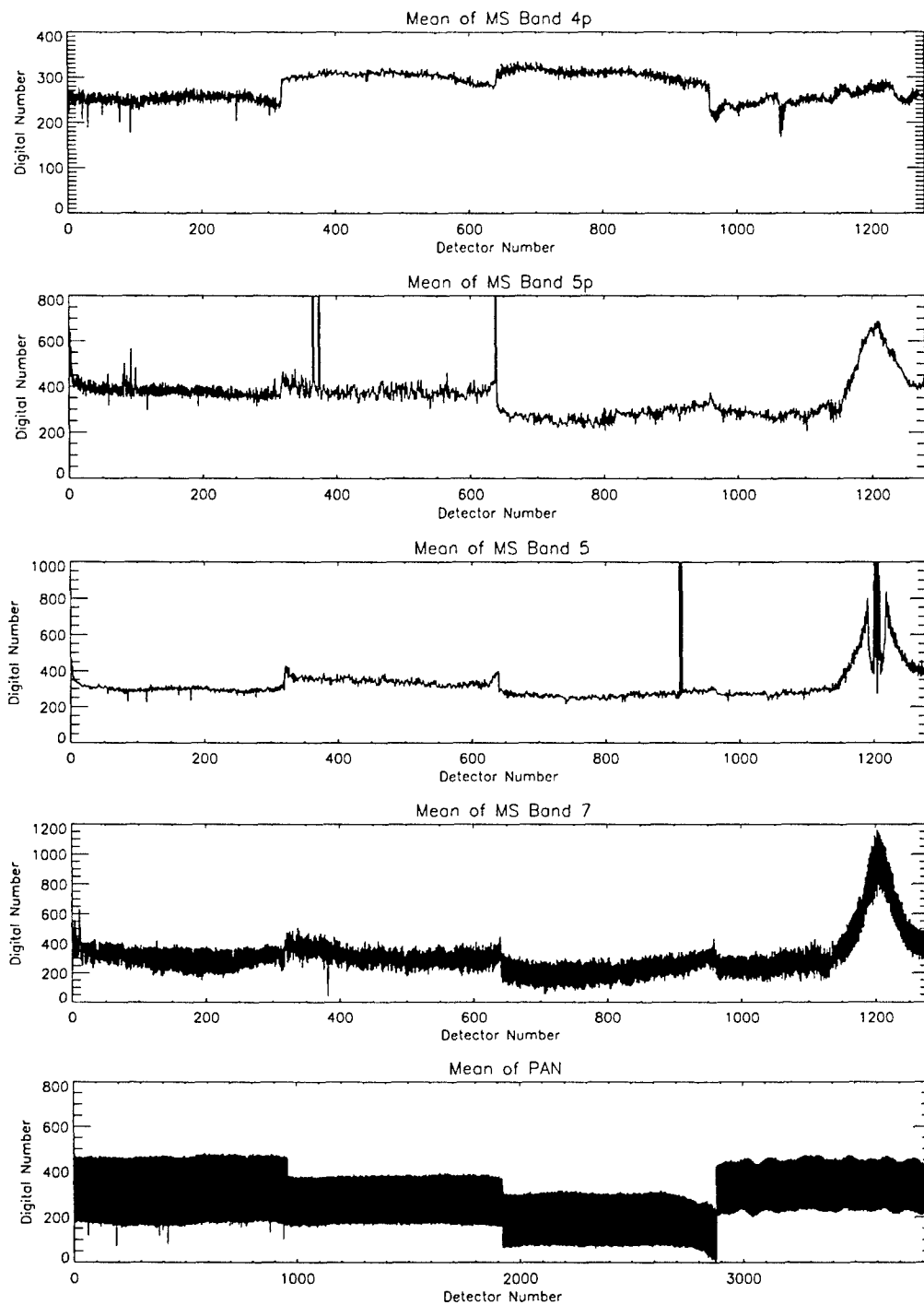


Figure 3-4. Band 4p, 5p, 5, 7 and pan band dark current values at 220 K.

Table 3-2
Inoperable detectors with marked dark current

Band	Detector	Comment
5p	374	HOT
5p	638	HOT
5	1202	HOT
5	1204	HOT
5	1206	HOT

Table 3-3
Detectors with marked dark current

Band	Detector	Comment
1	989	--
5p	365	Excessive noise
5p	374	Excessive noise, Inoperable detector
5p	638	Excessive noise, Inoperable detector
5	911	Excessive noise
5	913	Excessive noise
5	1202	Excessive noise, Inoperable detector
5	1204	Inoperable detector
5	1206	Excessive noise, Inoperable detector

3.1.1.3.1.2 Noise

The overall noise of the ALI is a combination of random, coherent, and pseudo-random fluctuations (PRF) in a detector's dark current value. For a standard Earth scene, the effects of these noise sources will be varied. The random or white noise component will establish the overall noise floor on a detector-to-detector basis. Coherent or pick-up noise will manifest itself as recognizable rippling or patterns in an otherwise 'clean' image. Pseudo-random or drifting dark current could affect the quality of an image on a frame-by-frame (high frequency) basis and as a function of time (low frequency) during an observation. For this document, only the white noise contributions will be discussed. A discussion of pseudo-random and coherent noise contributions may be found elsewhere [3].

The random or white noise of the ALI has been calculated for each detector as the standard deviation of ground calibration dark current data collected over 450 multispectral and 1350 panchromatic frames (~2 seconds). Results from these calculations are provided in Figures 3-5 and 3-6 for the focal plane operating at 220 K. The mean of white noise values is ≤ 1.2 DN for all bands and all sensor chip assemblies. Detectors with white noise values greater than three times the mean noise value for each sensor chip assembly or detectors with zero white noise, have been flagged as unusual. Fifteen ALI detectors have more than three times the average white noise values for all three focal plane operating temperatures and are listed in Table 3-4. All but one of these detectors are SWIR detectors and are associated with high dark current and/or high pseudo-random noise.

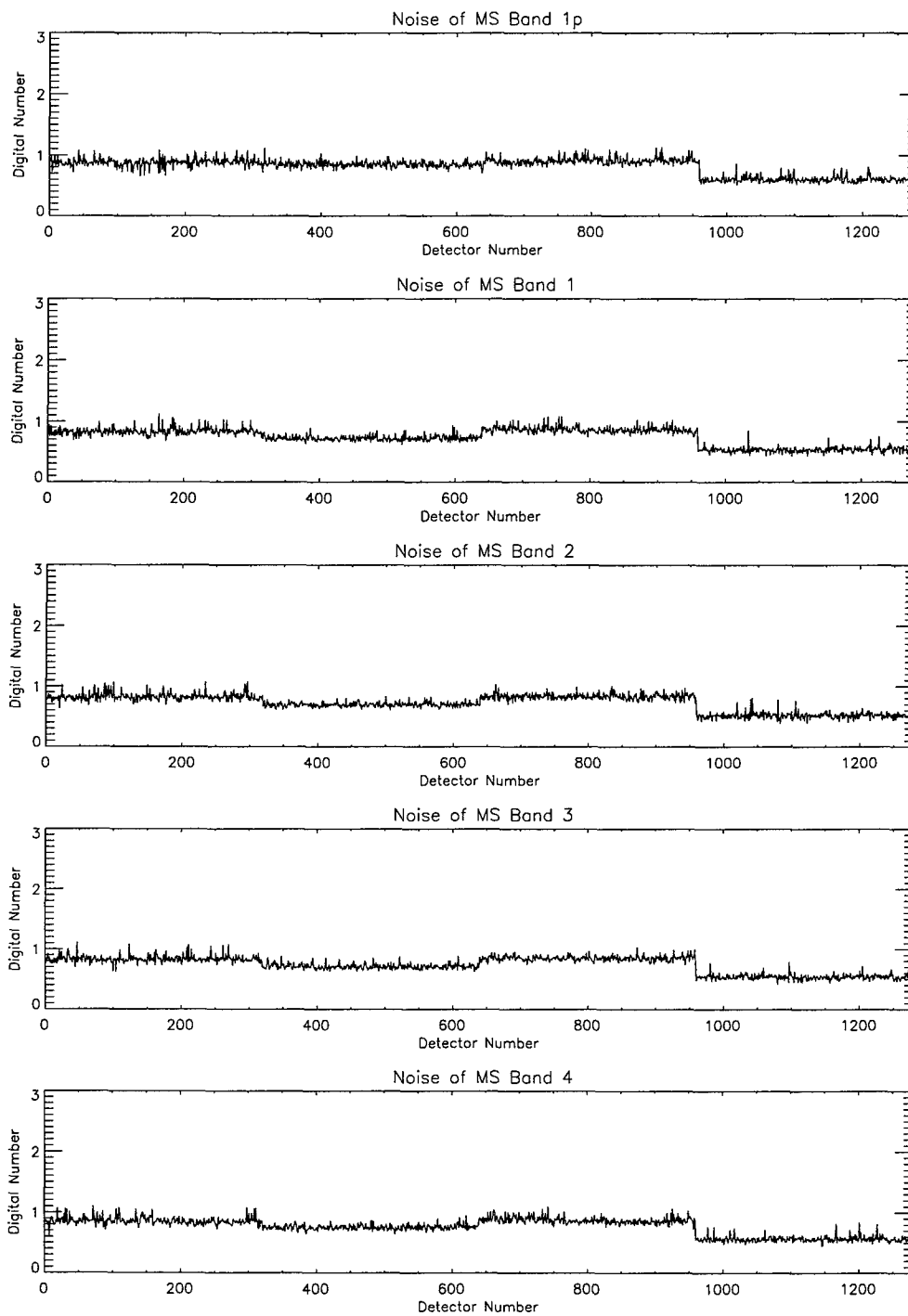


Figure 3-5. Band 1p, 1, 2, 3, 4 noise values at 220 K.

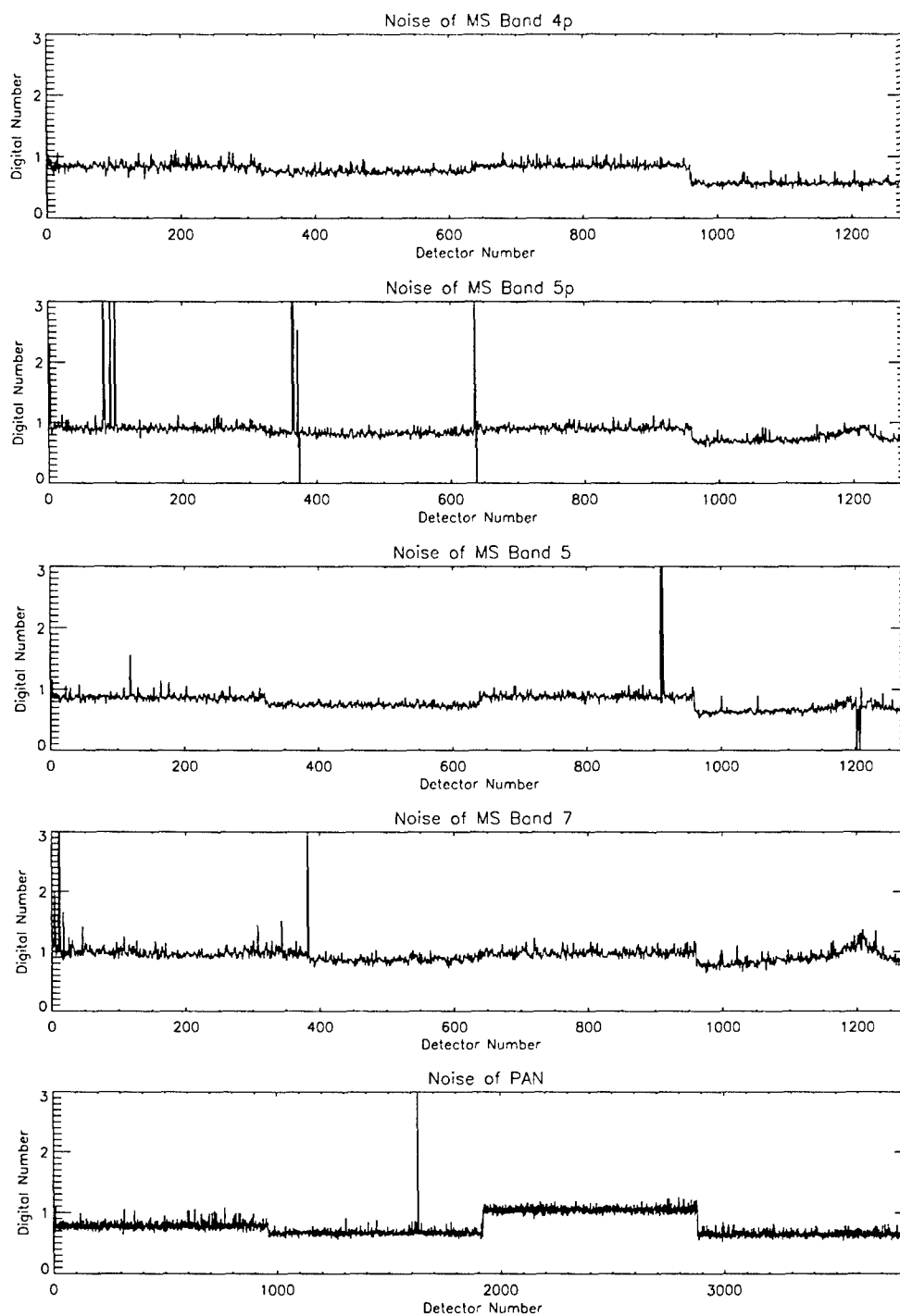


Figure 3-6. Band 4p, 5p, 5, 7 and pan band noise values at 220 K.

Table 3-4
Detectors with marked random or white noise

Band	Detector	Comment
5p	82	--
5p	92	--
5p	99	--
5p	365	Excess dark current
5p	372	--
5p	374	Excess dark current, Inoperable
5p	636	Noise value <3x mean with FPA @ 225 K
5p	638	Excess dark current, Inoperable
5	911	Excess dark current
5	913	Excess dark current
5	1202	Excess dark current, Inoperable
5	1206	Excess dark current, Inoperable
7	11	--
7	382	--
Pan	1631	--

3.1.1.3.1.3 Repeatability

Focal planes with highly repeatable dark current and noise properties are very desirable. This repeatability simplifies the normalization of background signal and the prediction for future scenes' signal to noise ratios. The Advanced Land Imager repeatability has been characterized by measuring the dark current and noise of each detector for ten data sets spanning ten days during ground calibration. For each of these data, the focal plane was maintained at 220 K, and the nominal integration time (4.05 ms for multispectral detectors, 1.35 ms for panchromatic detectors) was used.

Plotted in Figures 3-7 and 3-8 are the overlaid differences between dark current for each band collected during the ten-day period. The dark current was found to be repeatable to within ± 2 digital numbers for all VNIR and panchromatic detectors. SWIR detectors are repeatable to within -20/+100 digital numbers. Of particular interest are the sensitivities of the SWIR bands on SCA 1 and the good repeatability of the hot spot centered on detector 1200 of bands 5p, 5 and 7.

Plotted in Figures 3-9 and 3-10 are the overlaid differences between mean white noise levels for data collected over a ten-day period during ground calibration. The mean noise levels were found to be repeatable to within 0.1 digital numbers for all bands. Fourteen ALI detectors demonstrating noise differences $> \pm 0.5$ digital numbers are listed in Table 3-5. All but two of these detectors have been previously flagged as having high dark current or excessive noise values.

The above results indicate the VNIR and panchromatic dark current values and all detector noise levels of the ALI are highly repeatable. However, SWIR dark current levels have shown up to 100 DN variability. It is therefore recommended that dark reference scenes should be used to determine actual dark current and noise levels at the time of each Earth scene such that small day-to-day variations will not add to the uncertainties of the measurements.

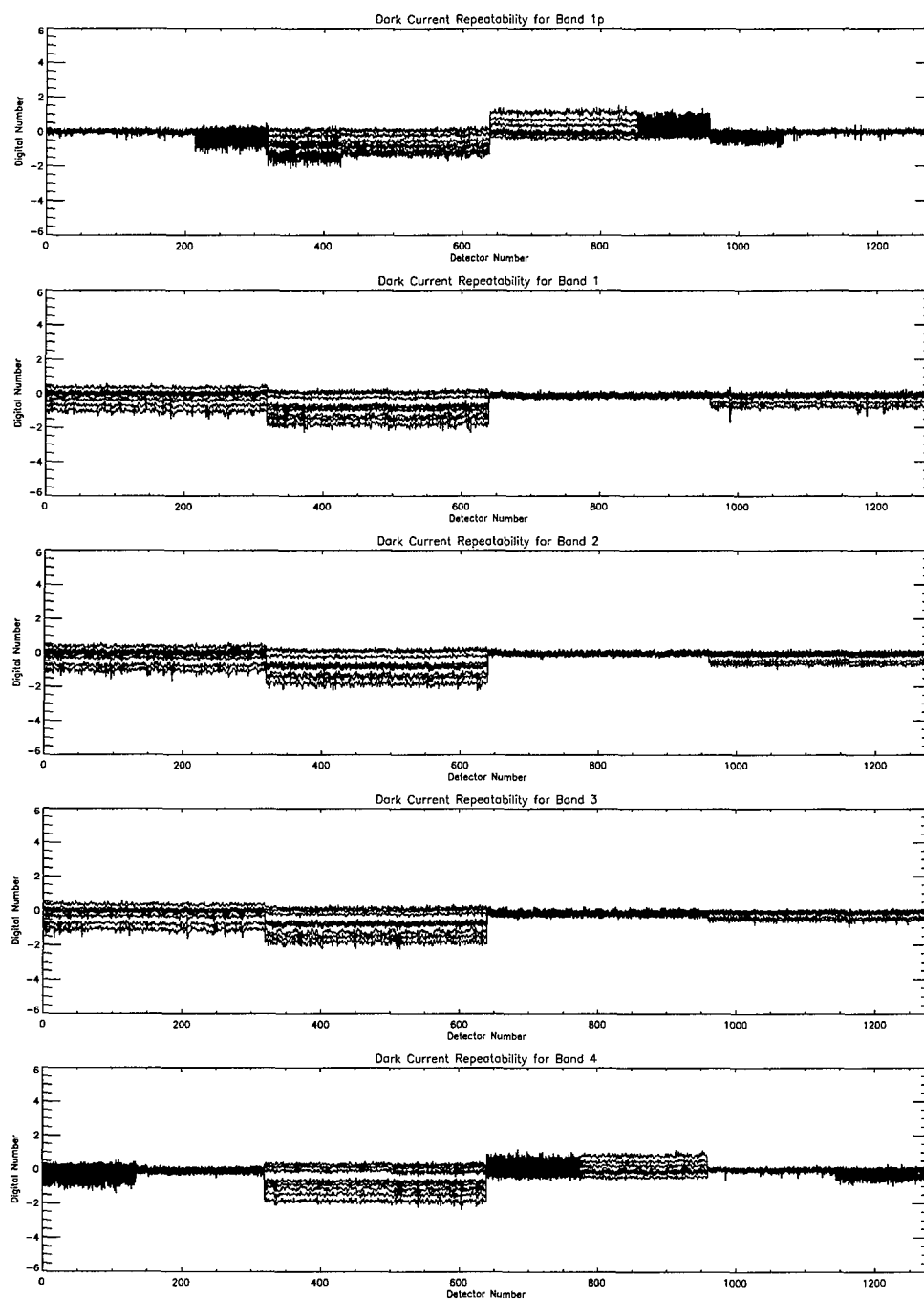


Figure 3-7. Bands 1p, 1, 2, 3, 4 dark current repeatability at 220 K.

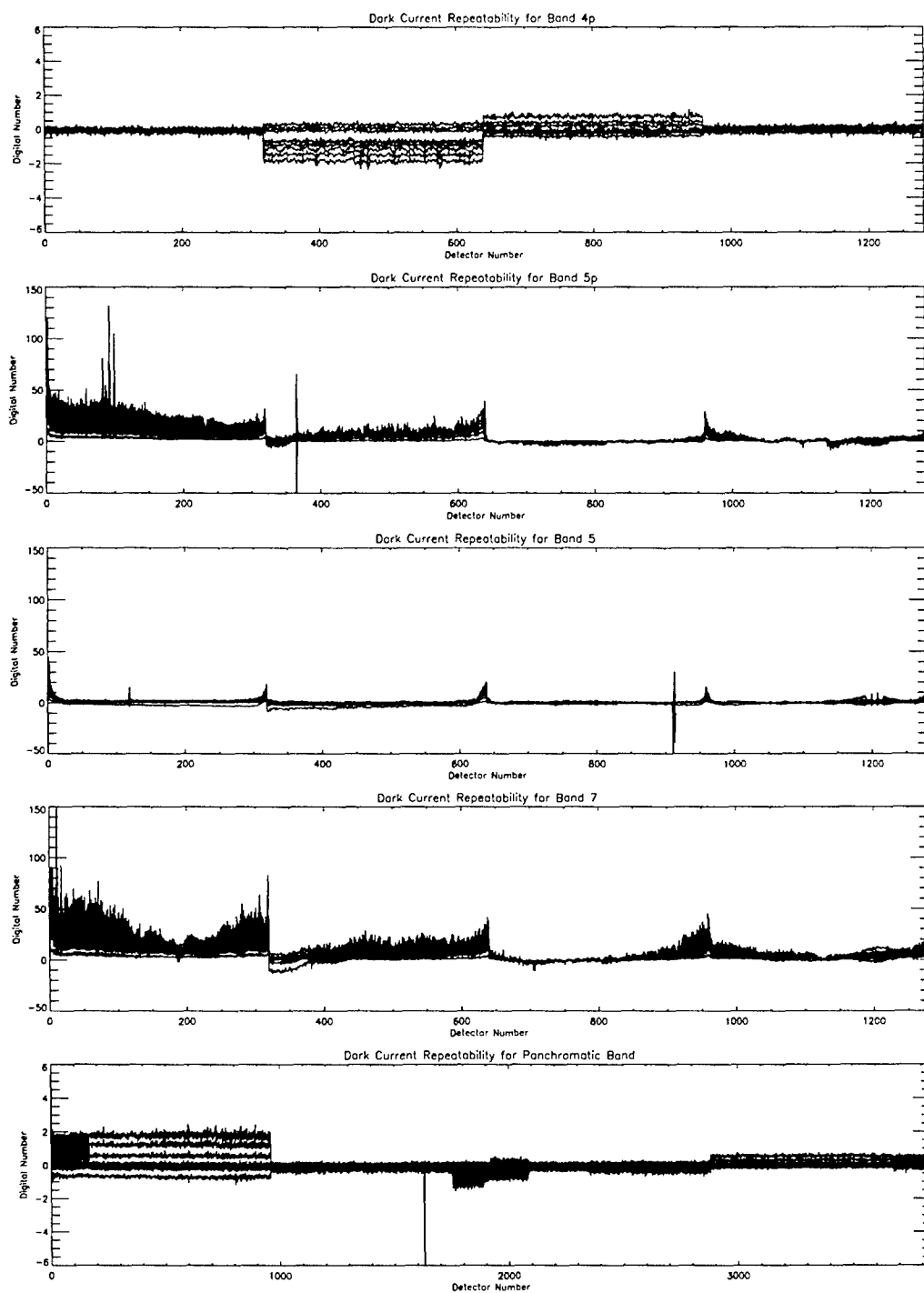


Figure 3-8. Bands 4p, 5p, 5, 7 and pan band dark current repeatability at 220 K.

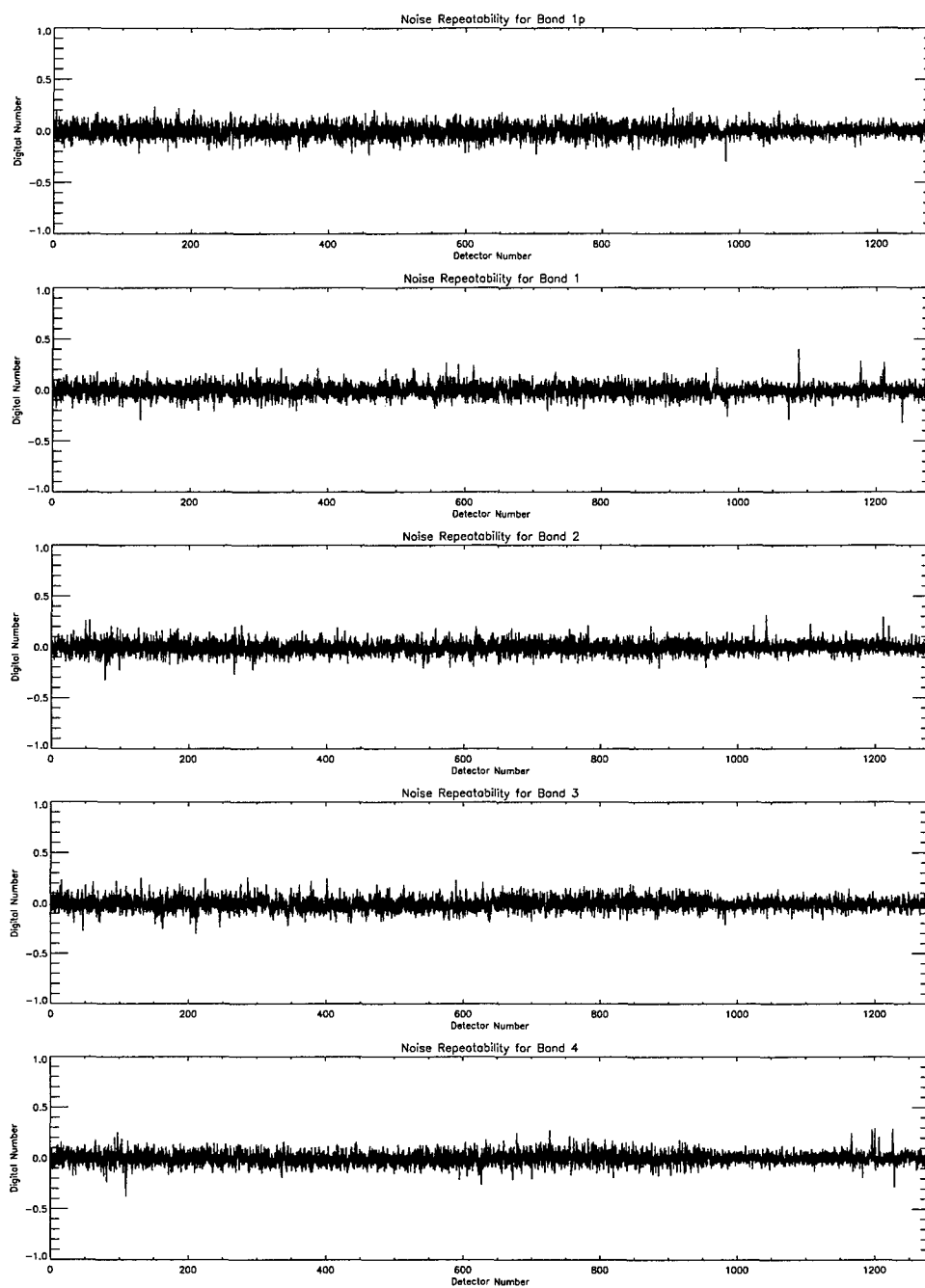


Figure 3-9. Bands 1p, 1, 2, 3, 4 noise repeatability at 220 K.

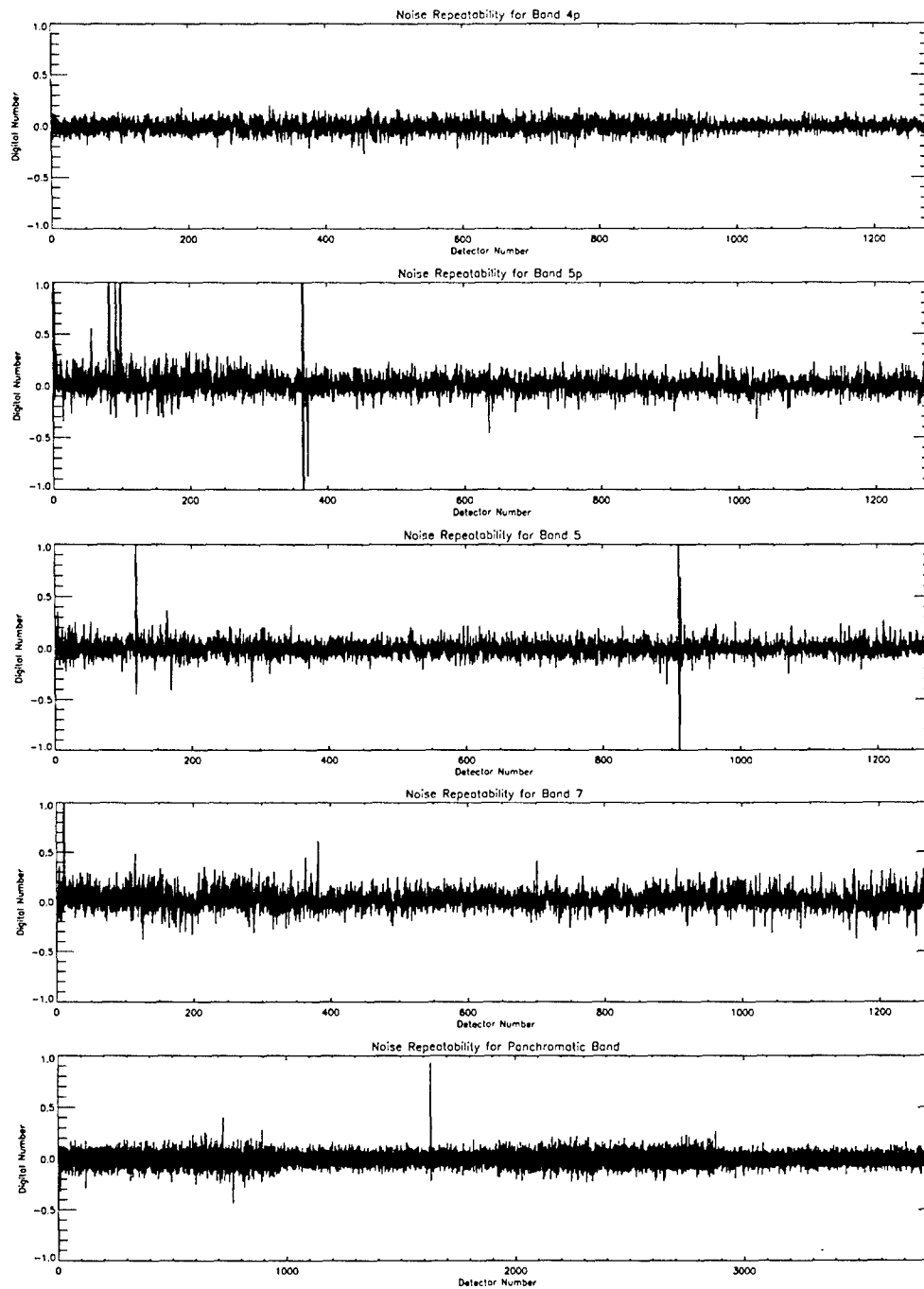


Figure 3-10. Bands 4p, 5p, 5, 7 and pan band noise repeatability at 220 K.

Table 3-5
Detectors with noise repeatability > ± 0.5 DN

Band	Detector	Comment
5p	2	Excess PRF [*]
5p	56	--
5p	82	Excess PRF, Excess white noise
5p	83	Excess PRF
5p	92	Excess PRF, Excess white noise
5p	99	Excess PRF, Excess white noise
5p	365	Excess dark current, Excess PRF, Excess white noise
5p	372	Excess PRF, Excess white noise
5	119	Excess PRF
5	911	Excess dark current, Excess PRF, Excess white noise
5	913	Excess dark current, Excess PRF, Excess white noise
7	11	Excess PRF, Excess white noise
7	382	Excess PRF, Excess white noise
Pan	1631	Excess white noise

^{*}PSR = Pseudo-Random Fluctuation.

3.1.1.3.1.4 Dark Current and Noise Characterization Summary

The dark current and noise characteristics for the EO-1 Advanced Land Imager have been characterized. Six inoperable detectors were identified indicating that 99.96% of the ALI focal plane is functional.

All SWIR detectors have a transient effect associated with the initial data collected following the focal plane turn-on. As a result, the first ten frames of the first dark image should be excluded from on-orbit dark current and noise analysis.

Ground calibration data indicate the VNIR and panchromatic dark current values and all detector noise levels of the ALI are highly repeatable. However, SWIR dark current levels have shown significant day-to-day variability. Additionally, the dark current is dependent on focal plane temperature, more particularly for the SWIR bands. It is therefore recommended that concurrent dark reference scenes should be used to determine actual dark current and noise levels at the time of each Earth scene.

The noise levels of the ALI focal plane are excellent (less than 1.2 digital number for the mean of all bands and sensor chip assemblies). Twenty-two detectors were identified as having higher than average noise values. All but one of these are SWIR detectors and associated with high dark current or pseudo-random noise.

It is recommended that a single one-minute dark scene be collected once every 14 days to characterize and track the dark current and noise of the Advanced Land Imager. Repeatability may be characterized by assessing the dark scenes obtained with each observation over a two-week period.

3.1.1.3.2 Anomalous Detectors

This section provides a summary listing of all Advanced Land Imager detectors that exhibit anomalous behavior. Anomalous detectors have been selected based on the following criteria:

1. Inoperable detector
2. Excessive dark current
3. Excessive noise
4. Anomalous gain value
5. High cross-talk

Detectors identified for each of the above criteria are listed in subsequent sections. All data used to generate this list were taken with the focal plane at 220 K and the nominal integration times: 1.35 ms for panchromatic detectors and 4.05 ms for multispectral detectors. Some detectors may be listed in several sections (e.g., a high noise detector may be temporally unstable). It must also be noted that although detectors may be marked 'anomalous', most of the characteristics identified in this section are accounted for during instrument calibration. Only the inoperable detectors are definite problems that need to be addressed by nearest neighbor interpolation or other schemes during image reconstruction. However, in the interest of fully understanding the ALI instrument, it is important to list all interesting focal plane array characteristics.

3.1.1.3.2.1 Inoperable Detector

An inoperable detector is one that has zero dark current or zero gain ('dead') or is saturated at all times ('hot'). Six ALI detectors have been identified as inoperable and are listed in Table 3-6.

Table 3-6
Inoperable Detectors

Band	Detector	Comment
5p	374	HOT
5p	638	HOT
5	982	Gain = 0
5	1202	HOT
5	1204	HOT
5	1206	HOT

3.1.1.3.2.2 Excessive Dark Current

Detectors with dark current values greater than 1.25 times the mean dark current for that band and SCA are flagged as having excessive dark current. Nine ALI detectors have been identified as having excessive dark current and are listed in Table 3-7.

Table 3-7
Detectors with marked dark current

Band	Detector	Comment
1	989	--
5p	365	Excess white noise, Excess PRF*
5p	374	Excess white noise, Inoperable
5p	638	Excess white noise, Inoperable
5	911	Excess white noise, Excess PRF
5	913	Excess white noise, Excess PRF
5	1202	Excess white noise, Inoperable
5	1204	Inoperable
5	1206	Excess white noise, Inoperable

* PSR = Pseudo-Random Fluctuation.

3.1.1.3.2.3 Excessive Noise

Detectors with noise values (standard deviation of dark current) greater than three times the mean noise value for that band and sensor chip assembly or detectors with more than 1 DN shift in dark current over a forty-second period have been flagged as having excessive noise. Twenty-two detectors have been noted as having excessive noise by the above criteria and are listed in Table 3-8. Fifteen ALI detectors have higher than average random (white) noise values, and sixteen ALI detectors have been noted as temporally unstable (low frequency pseudo-random fluctuations or high frequency pseudo-random fluctuations).

Table 3-8
Detectors with marked noise

Band	Detector	Comment
5p	2	Excess PRF
5p	82	Excess white noise, Excess PRF
5p	83	Excess PRF
5p	92	Excess white noise, Excess PRF
5p	99	Excess white noise, Excess PRF
5p	365	Excess white noise, High dark current, Excess PRF
5p	372	Excess white noise
5p	374	Excess white noise, Inoperable, Excess dark current
5p	636	Excess white noise, Excess PRF
5p	638	Excess white noise, Inoperable, Excess dark current
5	119	Excess PRF
5	911	Excess white noise, Excess dark current, Excess PRF
5	913	Excess white noise, Excess dark current, Excess PRF
5	1202	Excess white noise, Inoperable, Excess dark current
5	1206	Excess white noise, Inoperable, Excess dark current
7	4	Excess PRF
7	11	Excess white noise, Excess PRF
7	17	Excess PRF
7	126	Excess PRF
7	307	Excess PRF
7	382	Excess white noise, Excess PRF
Pan	1631	Excess white noise

3.1.1.3.2.4 Anomalous Gain Value

An anomalous gain value will either lead to lower dynamic range of the detector (early saturation), if too high, or low signal to noise ratios over the range of scene radiances expected, if too low. Four ALI detectors are found to exhibit anomalous gain values and are listed in Table 3-9.

Table 3-9
Detectors with anomalous gain values

Band	Detector	Comment
5p	365	Gain too high
5	911	Gain too high
5	913	Gain too high
5	982	Gain = 0

3.1.1.3.2.5 High Cross-Talk or Leaky Detectors

Detectors with high cross-talk are problematic in that they add signal to adjacent detectors. Correcting for this effect may be difficult, especially for scenes with high spatial frequencies covering a large dynamic range. Two ALI detectors have been identified as being leaky, i.e., having high cross-talk characteristics, and are listed in Table 3-10.

Table 3-10
Detectors with marked cross talk

Band	Detector
2	1149
3	864

3.1.1.3.2.6 Anomalous Detectors Summary

Six inoperable detectors were identified, indicating 99.96% of the ALI focal plane is functional. Twenty-one additional detectors have been observed with degraded performance due to such effects as noted dark current values and/or white, low frequency pseudo-random fluctuation, or high frequency pseudo-random fluctuation noise. The remaining 99.82% of the focal plane have excellent dark current stability and noise characteristics. A master list of anomalous detectors is provided in Table 3-11.

Table 3-11
Master anomalous detector list

Band	Detector	Inoperable	Excess Dark Current	Excess Noise		High Cross-Talk	Anomalous Gain
				White	PRF		
1	989		X				
2	1149					X	
3	864					X	
5p	2				X		
5p	82			X	X		
5p	83				X		
5p	92			X	X		
5p	99			X	X		
5p	365		X	X	X		X
5p	372			X			
5p	374	X	X	X			
5p	636			X	X		
5p	638	X	X	X			
5	119				X		
5	911		X	X	X		X
5	913		X	X	X		X
5	982	X					X
5	1202	X	X	X			
5	1204	X	X				
5	1206	X	X	X			
7	4				X		
7	11			X	X		
7	17				X		
7	126				X		
7	307				X		
7	382			X	X		
Pan	1631			X			

3.1.1.4 Leaky Detector

The Earth Observing-1 Advanced Land Imager focal plane contains two *leaky* detectors (1149 of Band 2 and 864 of band 3). When illuminated, these detectors leak or induce signal onto detectors of the same band and row. By row, we mean the odd or even detector row in which the *leaker* is contained (odd row for band 2 and even row for band 3). Detectors of the opposing row are not affected. Additionally, when the leaky detector is not illuminated, residual cross-talk remains but is effectively removed by dark-current subtraction. Detectors that are affected by leakage will be referred hereafter as *corrupted* detectors. Detectors that are not affected by leakage will be referred hereafter as *standard* detectors.

The optical or electrical cross-talk of leaky detectors results in the corruption of portions of images when the leaky detector is illuminated. Figures 3-11 and 3-12 depict images of Lincoln Laboratory in bands 2 and 3 respectively, before the effects of the leaky detectors are accounted for. The approximate location of the leaky detector column is indicated by an arrow. Furthermore, abutting sensor chip assemblies are included in these images to demonstrate the quality of the data in non-leaky regions.

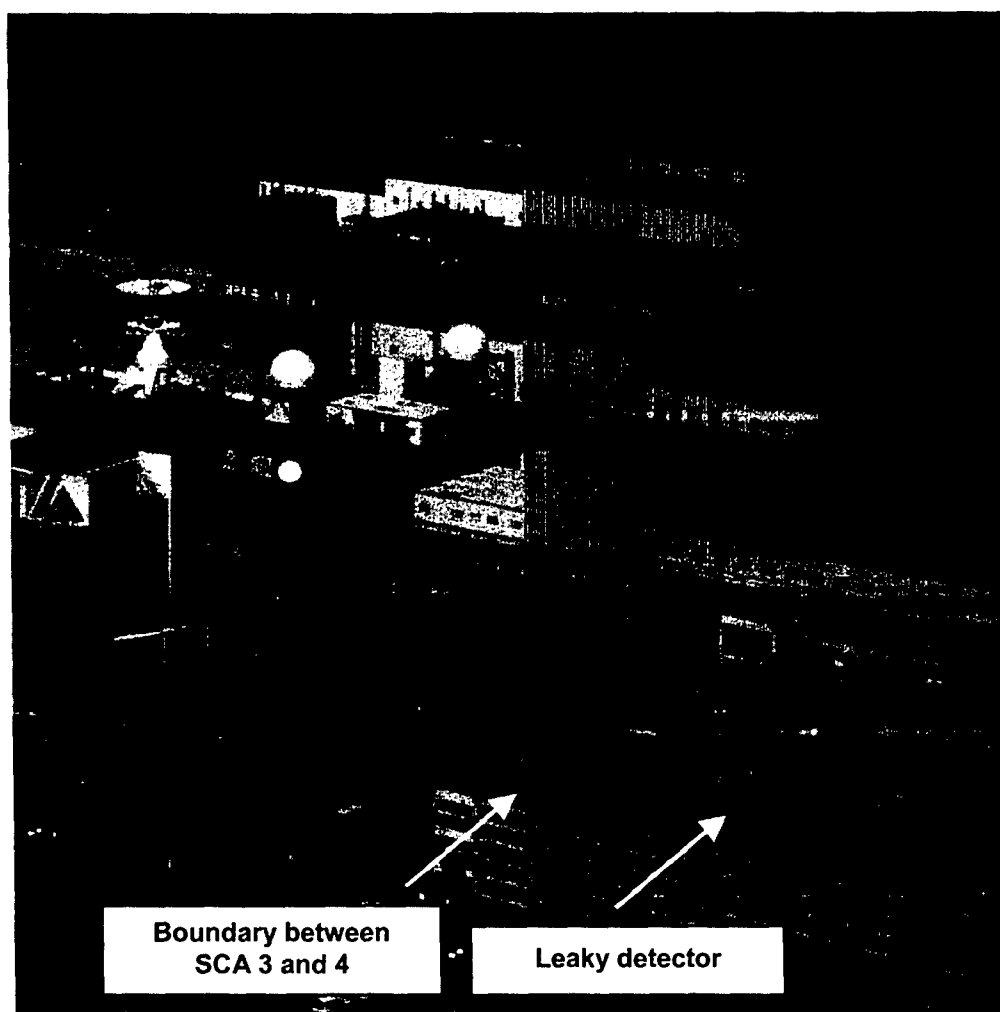


Figure 3-11. Band 2 image of Lincoln Laboratory before the effects of the leaky detector (1149) are corrected. The left portion of the image is from sensor chip assembly 3, which does not contain a leaky detector for this band.

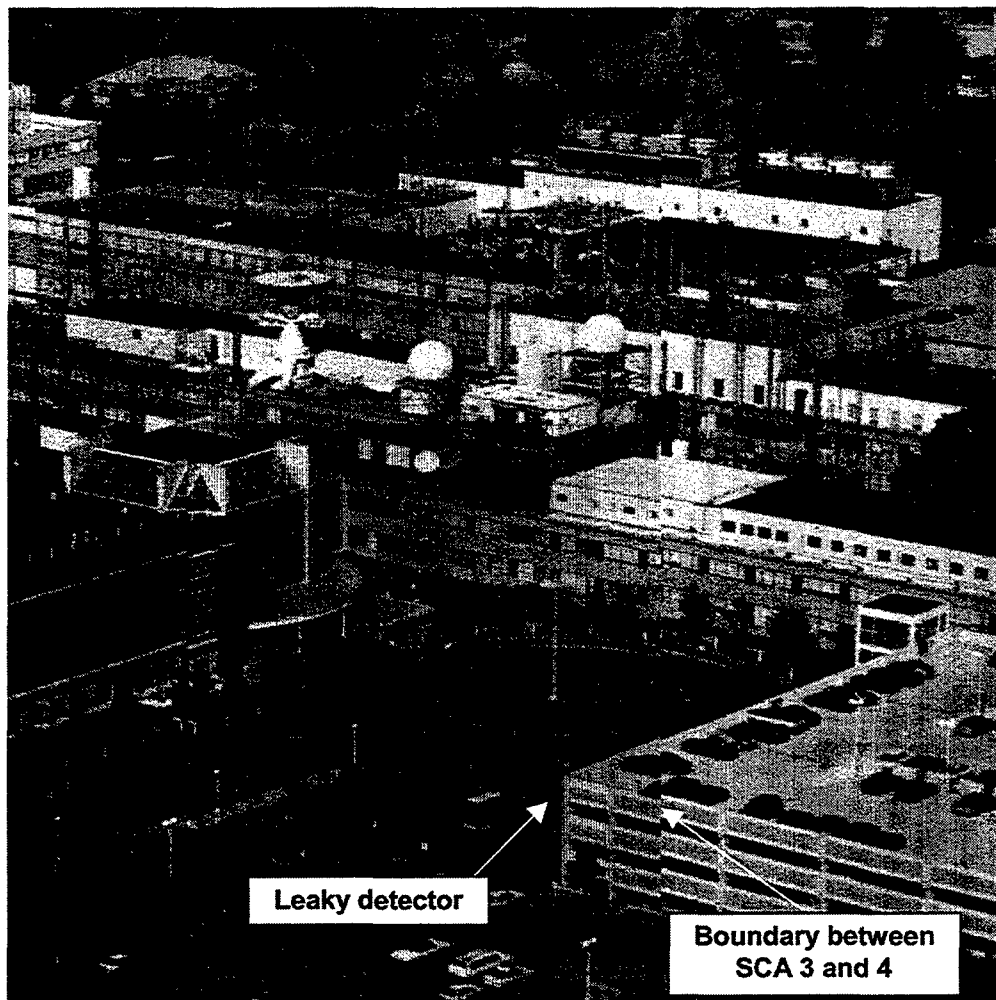


Figure 3-12. Band 3 image of Lincoln Laboratory before the effects of the leaky detector (864) are corrected. The right portion of the image is from sensor chip assembly 4, which does not contain a leaky detector for this band.

3.1.1.4.1 Radiometric Correction Methodology

The radiometric response of corrupted detectors is highly dependent on leaky detector illumination. As a result, a correction procedure must be followed to radiometrically account for the effects of leakage on affected regions. Initially, an algorithm was developed to correct images for leaky detector artifacts by associating the amount of leakage with the dark subtracted value of the leaky detector on a frame-by-frame basis. This algorithm may be represented analytically as

$$L_N = ADN_N + BDN_L \quad (1)$$

Where L_N is the apparent radiance of corrupted detector N , DN_N is the true detector value for detector N , A is the radiometric gain coefficient for detector N , DN_L is the detector value for the leaky detector, and B is a constant which describes the fraction of the leaky detector corrupting detector N . This algorithm correctly accounted for leaky detector effects for most portions of

images. However, it was quickly realized that all regions where the algorithm failed were associated with sharp edges crossing the leaky detector during the push-broom imaging of a scene. This led to the conjecture that the leak is caused by a localized defect in the detector area. For scenes with uniform illumination, the leaky detector (good and defective regions) are fully illuminated and Equation 1 is correct. For scenes with no illumination, no leakage exists and Equation 1 is again correct. However, if the leaky detector is partially illuminated, the defective region within this detector may have none, partial, or full illumination. As a result, the dependence on the leaky detector illumination is no longer valid and the original image correction process breaks down. *This leads us to the conclusion that the amount of leakage for any frame is dependent on the illumination of the leaky detector defective region and not of the entire leaky detector. Additionally, since we do not know the precise illumination of the defect a priori, we have adopted an empirical correction method to eliminate the effects of leaky detectors on ALI images.*

The empirical correction method we have adopted is implemented on a frame-by-frame basis and uses the differences between each corrupted detector and its nearest uncorrupted (standard) neighbor to derive a leakage function. The leakage function is then used to correct corrupted detectors while maintaining the unique detector-to-detector radiometric variations for that frame. This method is then repeated for all frames. The empirical correction method is implemented in the following manner:

- Correct geometrically odd and even detector offsets and SCA to SCA offsets for the entire image.
- Correct radiometrically entire image using calibration coefficients.
- Begin frame-by-frame loop
 - Generate difference array between corrupted detectors and nearest neighbors
 - Compute leakage function
 - Correct frame
- End frame-by-frame loop
- Save corrected image

3.1.1.4.1.1 Geometrically Correct Image

The first step in correcting the effects of leaky detector corruption is to geometrically correct the entire image for odd and even detector and SCA to SCA offsets. The ALI focal plane is composed of four sensor chip assemblies, positioned in a staggered formation to provide overlap between arrays (Figure 3-13). Within each array, detectors are aligned in odd and even rows for each band (Figure 3-14). The SCAs are offset by 5 mm and each odd and even row is separated by 80 μ m.

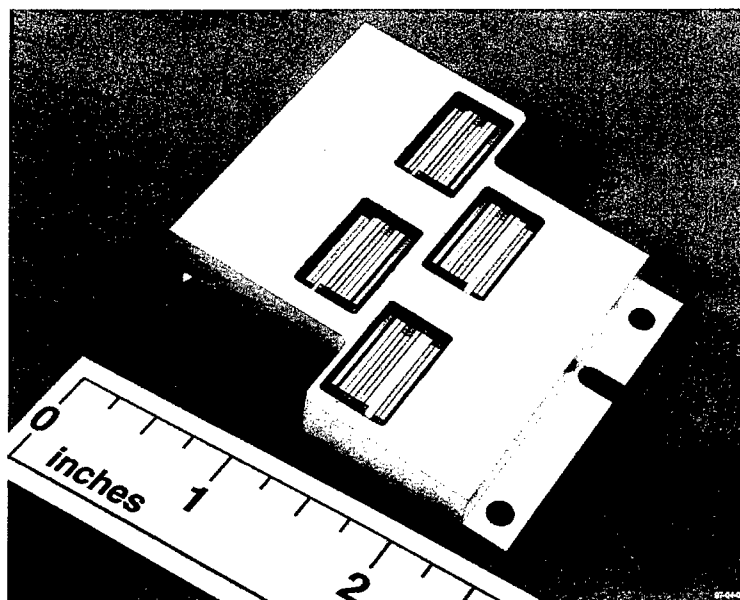


Figure 3-13. Photograph of ALI filter assembly.



Figure 3-14. Photograph of detector rows for Bands 1-4p. Odd and even rows for each band are evident.

To reconstruct an ALI image, even numbered SCAs and detector columns are shifted down an integral number of frames (correction factor is different for SCAs and columns), depending on the frame rate used during the data collection. Small effects from telescope distortion must also be accounted for when properly reconstructing an image but these effects are second order when correcting for leaky detector corruption. To illustrate the effects of detector offset shifting, subframes of the Band 2 image of Lincoln Laboratory are displayed in Figure 3-15.

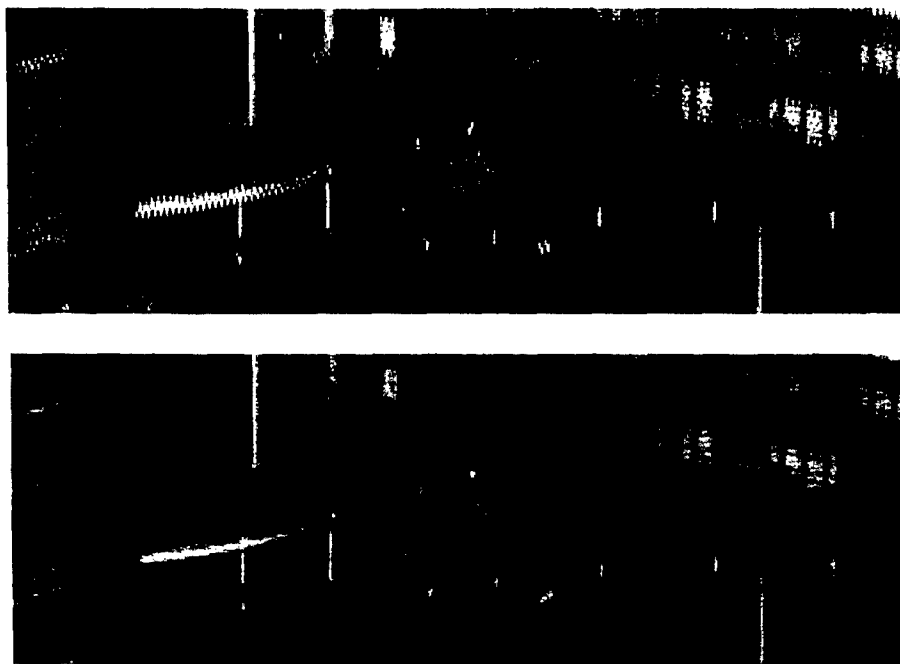


Figure 3-15. Example of geometric correction performed on images before the leaky detector correction is implemented. The top figure is before correction. The bottom figure is after correction.

3.1.1.4.1.2 Radiometrically Correct Image

The second step in accounting for leaky detector effects is to radiometrically calibrate the image. This involves applying radiometric calibration coefficients to transform data from digital numbers to $W/cm^2/sr/\mu$. For ALI data, this transform is linear and maybe expressed analytically as

$$L_N = A_N + B_N DN_N \quad (2)$$

Here, L_N is the radiance observed by detector N , A_N and B_N are the offset and gain calibration coefficients for detector N , and DN_N is the dark subtracted focal plane response for detector N . The calibration coefficients have been derived from laboratory measurements of the radiometric response of the focal plane to diffuse scenes of varying radiance (see *Earth Observing-1 Advanced Land Imager: Radiometric Response Calibration* [4]). Although the response of corrupted detectors is influenced by the leaky detectors, we have found the adoption of incorrect radiometric response coefficients for these detectors are effectively accounted for during leaky detector correction. As an example of this step in the leaky detector correction process, frame 1050 of the Band 2 Lincoln Laboratory image, before and after radiometric correction, are graphically displayed in Figure 3-16.

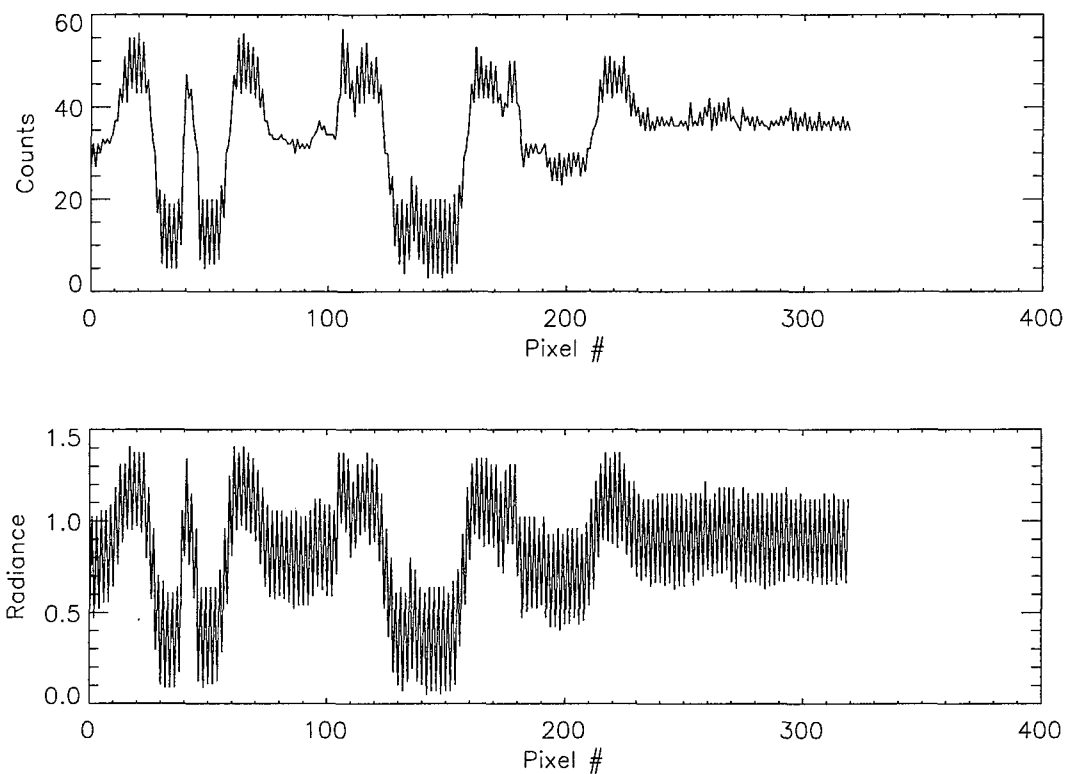


Figure 3-16. Effects of leaky detector corruption of frame 1050 of the Band 2 image of Lincoln Laboratory. The top figure is dark subtracted data. The bottom figure has been radiometrically corrected.

3.1.1.4.1.3 Generate Difference Array Between Corrupted Detectors and Nearest Neighbors

Once an image has been geometrically corrected and radiometrically calibrated, the leaky detector correction methodology focuses on a frame-by-frame correction. This correction begins with the generation of a *difference* array between corrupted detectors and nearest uncorrupted or *standard* neighbors. After an image has been geometrically corrected, each corrupted detector is abutted on either side by an uncorrupted or standard detector. A difference array between corrupted and standard detectors creates a database of leakage for a given frame. A trend of leakage versus radiance is then formed if the standard detector radiance is plotted against the difference array. The difference array against radiance for frame 1050 is plotted in Figure 3-17.

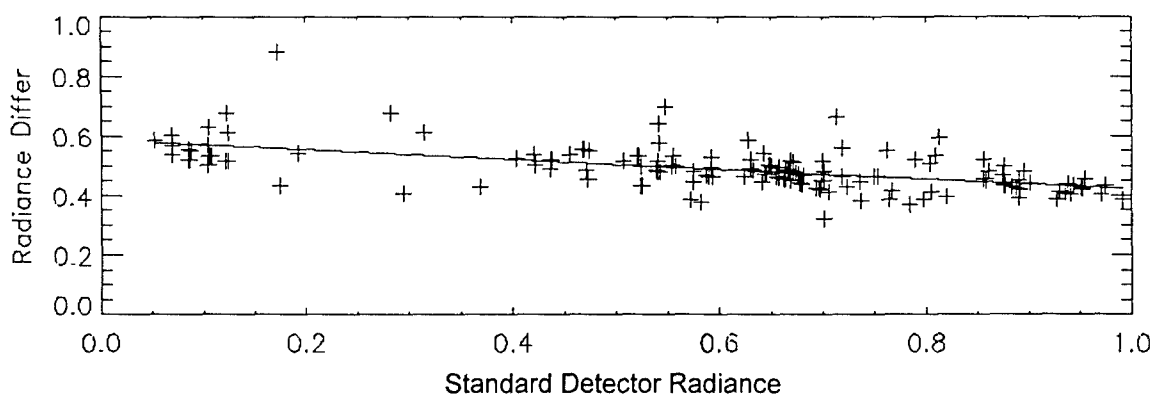


Figure 3-17. Frame 1050 difference array as a function of standard detector radiance.

3.1.1.4.1.4 Compute Correction Function

The leakage correction function for each frame is calculated as a polynomial fit to the standard detector radiance and difference array data. This fit identifies the leakage observed as a function of radiance by statistically averaging the inherent standard-to-corrupted detector variations in geometrically varying scenes. The correction function for frame 1050 is shown in Figure 3-18.

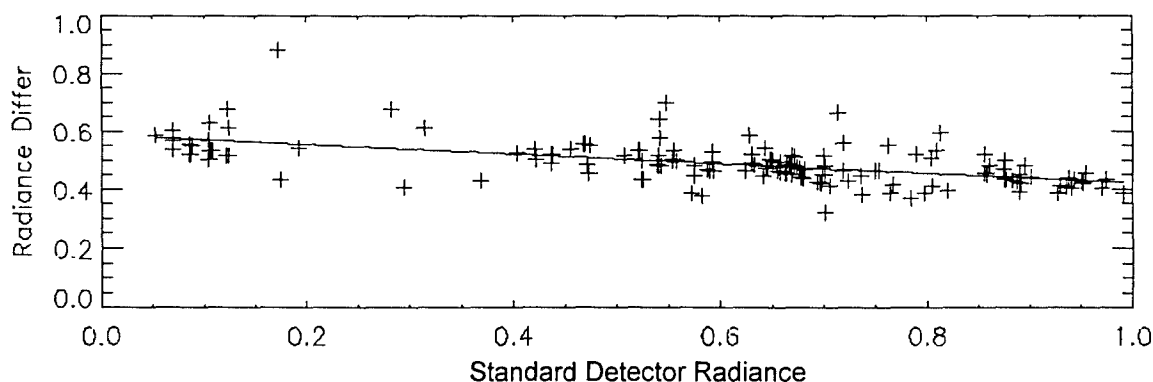


Figure 3-18. Frame 1050 difference array as a function of standard detector radiance. Overlaid is the leakage function that is used to correct corrupted detectors for this frame.

3.1.1.4.1.5 Correct Image

The final step in leaky detector correction is the application of the leakage correction function to individual detectors. For a given corrupted detector, a correction factor is calculated, based on the correction function and neighboring standard detector value:

$$C_N = A_{CF} + B_{CF}(R_S) + C_{CF}(R_S)^2 \quad (3)$$

Here, C_N is the correction factor for detector N, A_{CF} , B_{CF} , C_{CF} are the correction factors generated from the fitting procedure described above, and R_S is the radiance of the neighboring standard

detectors. Once a correction factor has been calculated, it is simply subtracted from the original radiometrically calibrated corrupted detector value. Figure 3-19 depicts the effects of leaky detector correction for frame 1050. As one may see, the leakage has been effectively removed, while maintaining the intrinsic detector to detector variability of the scene. This is demonstrated graphically in Figures 3-20 and 3-21. The images on the left are the original corrupted Band 2 and Band 3 images respectively. The images on the right are the images after leaky detector correction has been implemented.

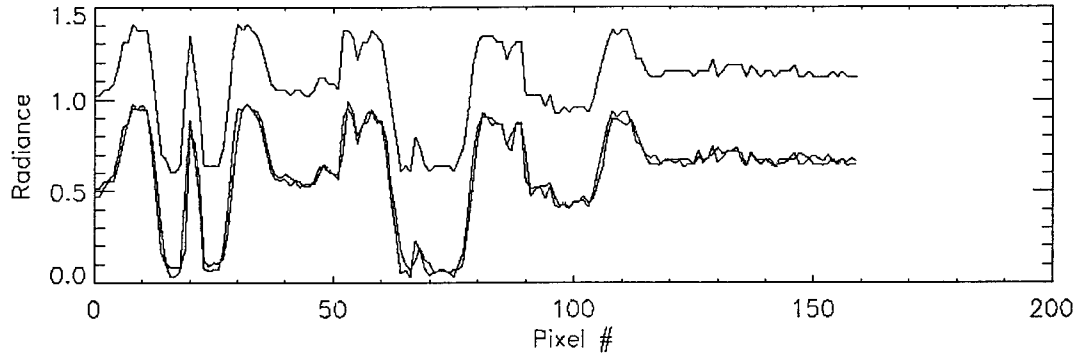


Figure 3-19. Frame 1050 with leaky detector correction applied. The data set at the top is the original radiometrically corrected corrupted detector data. The data at the bottom is an overlay of uncorrupted detector data and leaky detector corrected data.



Figure 3-20. Band 2 image of Lincoln Laboratory before (left) and after (right) leaky detector correction applied.



Figure 3-21. Band 3 image of Lincoln Laboratory before (left) and after (right) leaky detector correction applied.

3.1.1.4.2 Discussion

The radiometric responses of corrupted detectors are highly dependent on leaky detector illumination. As a result, an empirical correction method has been developed to effectively eliminate the addition of optical or electrical cross-talk induced by leaky detectors. This method centers on the generation of a *difference* array between corrupted and neighboring *standard* detectors. This array is used to fit a correction function on a frame-by-frame basis and calculate correction factors on a detector-by-detector basis. This method has been used on various scenes collected during ground calibration and flight operations with excellent results.

Using the above method on a variety of flight scenes, one area of concern has been identified: scenes with uniform high (low) radiance levels, sparsely intermixed with a very low number of small, low (high) radiance regions. Examples of these scenes include snow covered scenes with a single road cutting across the image or ocean scenes with small, sparsely distributed clouds. The root of the problem lies in the generation of the correction function. For the above examples, an overwhelming number of detectors will have nearly the same high (low) radiances with only a handful of detectors exhibiting low (high) radiances. If the difference array for the handful of detectors cluster is not correctly calculated or has a large scatter, the resulting correction function

will not be valid, resulting in poor correction for those detectors. This danger only exists for scenes where the distribution of radiance across the scene is split into large and small groups. Fortunately, by the nature of the problem, only the handful of detectors whose correction function is invalid will be affected.

3.1.1.5 Contamination

Contamination of the focal plane by an unknown substance was recognized in October 1998 during the characterization and calibration of the Advanced Land Imager at Lincoln Laboratory. This contaminant may be completely eliminated by raising the temperature of the focal plane above 260 K. Prior to launch, several bake outs occurred in an attempt to eliminate the source of the contaminant. In January 1999, the entire instrument was baked out at 303 K while under vacuum for one week and then later for an additional two days. The focal plane was also baked out for three hours at 273 K in October 1999 and for one day at 273 K in July 2000 during spacecraft thermal vacuum testing at Goddard Space Flight Center.

In the event that on-orbit bake outs would become necessary, an additional heater was added to the focal plane radiator in February 1999. This heater, along with others on the instrument, raises the temperature of the focal plane to 270 K on orbit.

3.1.1.5.1 Detection

The monitoring of contaminant deposition on the ALI focal plane during ground testing and on-orbit is performed using the internal reference lamps mounted on the telescope metering truss. These lamps provide three levels of stable, repeatable reference illumination of the focal plane (Figure 3-22). However, because the internal reference lamp assembly has a much higher f-number (40) compared to the telescope (7.5), the assembly acts as a microscope for detecting contamination effects. This magnification must be considered when assessing the impact of focal plane contamination on image quality and radiometry. Generally, any apparent spatial variations in the internal lamp data caused by focal plane contamination should be reduced by a factor of 4 when applied to imagery collected by the ALI.

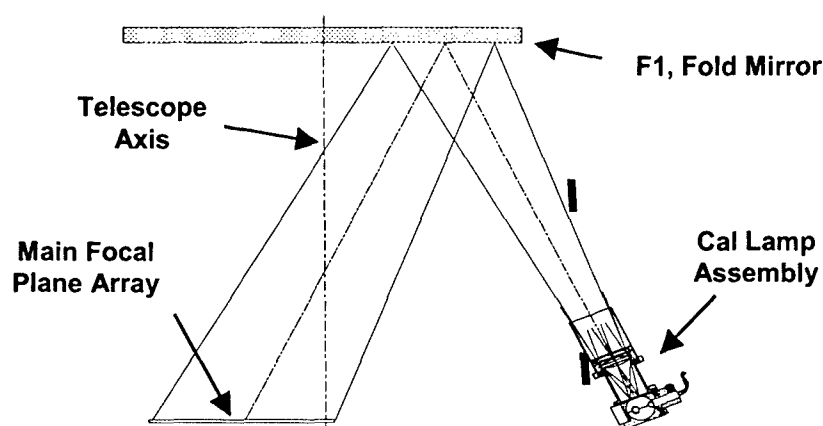


Figure 3-22. Illumination of the ALI focal plane using the internal reference lamp assembly.

The first step in detecting contaminants is to collect data using the internal reference lamp assembly when the focal plane is considered 'clean'. The dark current subtracted response of the focal plane for each band using the clean data is considered the baseline. Data is then collected once per day over a period of interest. All data are then divided by the baseline data, and the mean and standard deviations of the ratios are then computed for each band. The mean and standard deviations are considered figures of merit for focal plane contamination. If the reference lamps and focal plane are stable, and if no contamination occurs, the mean of the ratios for each day should be unity and the standard deviations should be equivalent to the noise of the detectors.

3.1.1.5.2 Location of Contamination

The location of ALI contamination has been isolated to the top surfaces of the spectral filters overlaying the focal plane detectors. During ground calibration at Lincoln Laboratory, a CCD camera was placed at the focus of an imaging collimator and images of the filter surfaces were obtained. The left side of Figure 3-23 shows a portion of the focal plane filters during a period when contamination had been detected. The image on the right is of the same portion of the filter after the instrument had been baked out. Clearly, a residue had formed on the surface of the filters during contamination build-up. Additionally, all evidence of the residue has been eliminated as a result of the bake out. This conclusion is supported by the levels of post-bake out data returning to baseline levels once the focal plane had been cooled to 220 K.

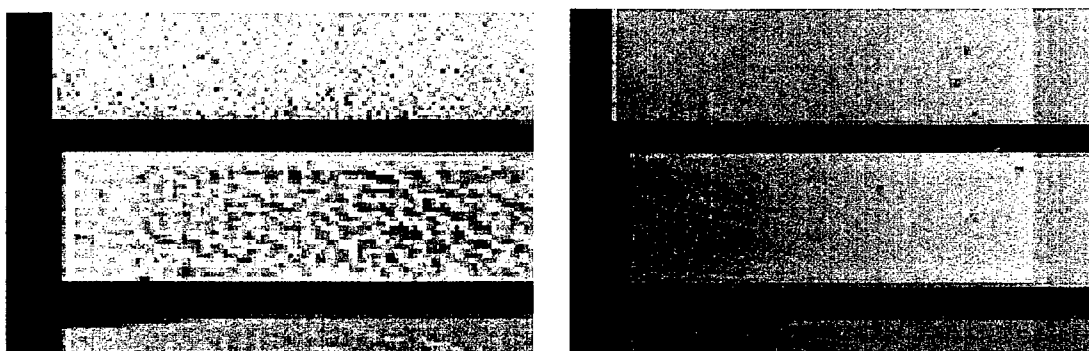


Figure 3-23. Image of a portion of the top surface of the focal plane filters when contaminated (left) and after a bake out (right).

3.1.1.5.3 Characteristics

Focal plane contamination appears in three forms: pixel-to-pixel variation, mean level shifts, and bowing. Pixel-to-pixel variation refers to an apparent random shifting in individual detector responses either above or below the original reference values. As deposition continues, the pixel-to-pixel variations increase and the standard deviations between observations increase.

Another characteristic of contamination is a mean level shift. This refers to the gradual shift of the apparent mean level response of an SCA as contaminants are accumulated on the filter surfaces. This shift usually lowers the mean level of the pixel response curve. However, in some instances, higher mean levels have been observed.

Bowing is also observed in cases of significant focal plane contamination. As an SCA becomes contaminated, the mean apparent response of the detectors may change as a function of detector position. Detectors near the edges of SCAs have a larger change in apparent response, relative to those near the middle of the SCA, resulting in a bowing appearance for some bands.

Figure 3-24 depicts history of focal plane contamination for Band 4 for two periods. The left column shows rapid contamination of the focal plane over a six-day period. Clearly evident are the effects of pixel-to-pixel variations, as well as mean level shifting and bowing. The right column reveals a significantly reduced contaminant build-up after the first instrument bake out at Lincoln Laboratory.

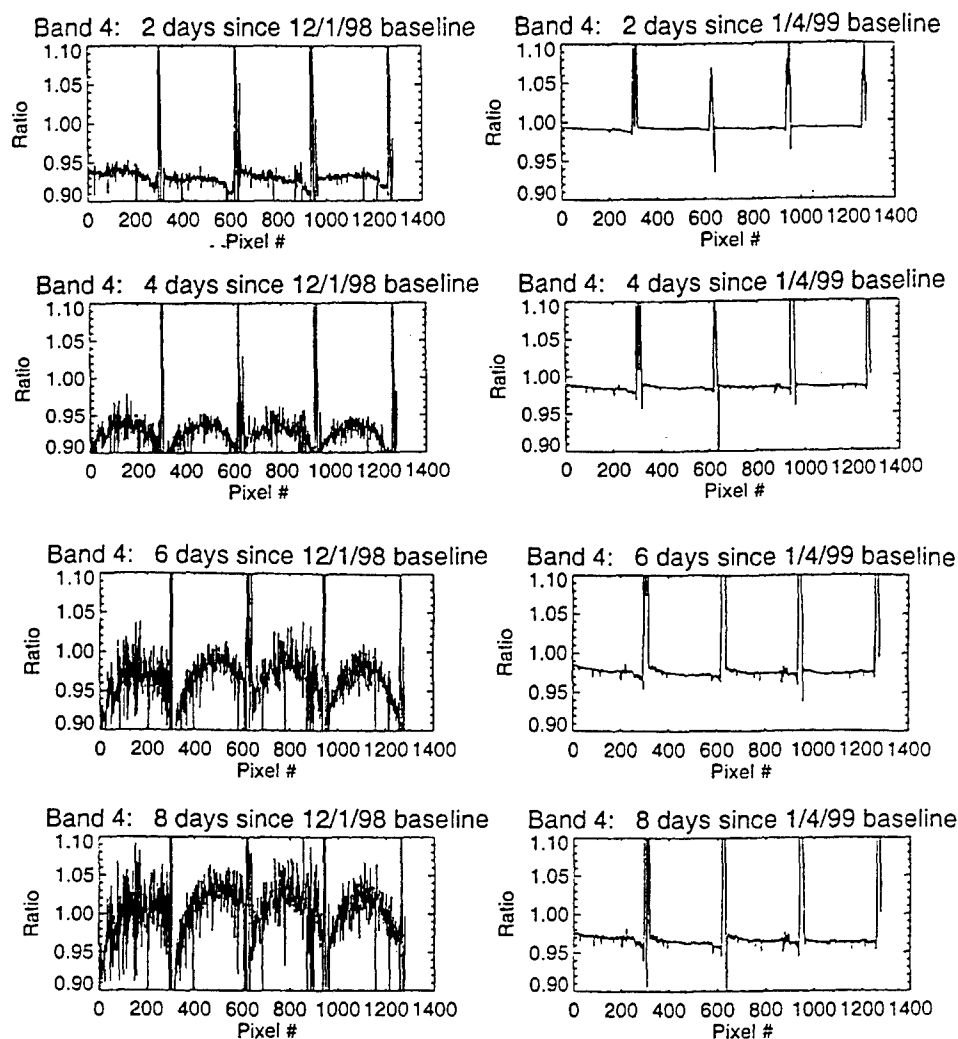


Figure 3-24. History of focal plane contamination for two periods during instrument characterization at Lincoln Laboratory.

3.1.1.5.4 Discussion

Much information pertaining to the contamination of the Advanced Land Imager focal plane has been obtained during ground testing between October 1998 and November 2001. The contaminant appears to condense on the surfaces of the spectral filters lying above the detectors when the focal plane is operated at 220K. However, once the focal plane is warmed above 260 K the contaminant 'boils off' and detector responses return to baseline levels. This implies that mirror surfaces, maintained above 273 K at all times, will not collect contaminants during ground testing or during orbital operations.

Although the source of the contamination is not known, the leading suspect is the black paint (Z306) coating the inside of the telescope to reduce stray light. Bake out of the telescope surround structure was limited to 70 hours and it is possible that residual outgassing of the paint may be sticking onto the filter surfaces when the focal plane is cold.

3.1.1.6 Focus Shim Adjustment

Following integration of the Focal Plane System with the instrument optics, a set of measurements were made to determine what correction, if any, was needed to the focus shim in order to put the focal plane detectors at the best focus. For these measurements, the ALI was supported on a fixture in a Class 1000 clean room, with its Z axis horizontal. In front of the ALI was the imaging collimator developed for imaging simulations and MTF testing (see Figure 3-25).

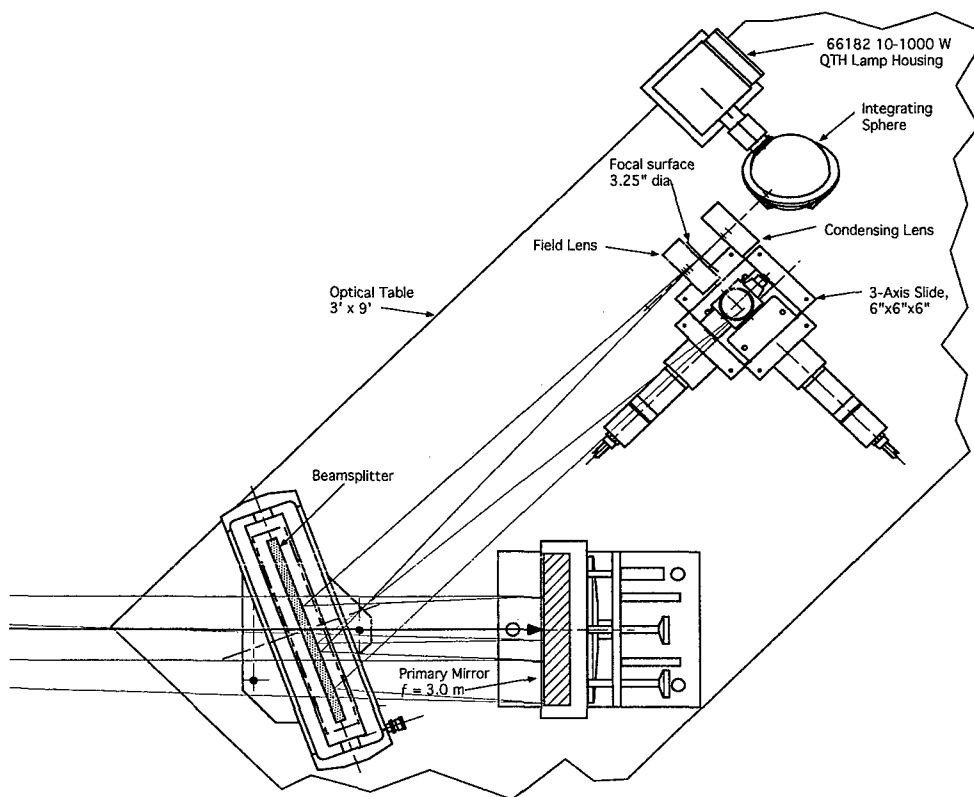


Figure 3-25. Top view of Imaging Collimator. A LUPI takes the place of the lamp, integrating sphere, and condensing lens during collimation testing.

The procedure was as follows: After the collimator had been set up for infinite focus, a series of knife-edge scans were performed as described under MTF calibration below. Data from a detector were recorded as the image of the knife edge passed across the detector. The scan was repeated with the knife edge shifted along the axis of the collimator at a series of positions known distances from the infinite focus reference position.

For each knife-edge scan, the sharpness of the edge in the detector data was computed. In this case, the figure of merit was the length (in frames at a constant speed) of the transition from dark to light. The figure of merit was plotted vs. the focus offset of the collimator. The value of focus offset at the minimum of the curve was determined. The corresponding ALI focus error was proportional to this collimator focus offset.

The ALI focus error was estimated for many of the VNIR detectors at widely-separated locations on the focal plane. From this set of data, a best shim correction was derived. A large piston correction of 823 μm was required, but no tip or tilt correction was necessary. The shim was then removed and corrected, and the focal plane re-installed. The focus tests were repeated. No further corrections were found to be necessary.

3.1.1.7 End-to-End Imaging Tests

A major functional verification test of the ALI was the End-to-End Imaging test. For this test, a reticle or target, typically the negative "USAF 1951" target, was mounted at the focal plane of the collimator. A vertical slide moved the target at the correct speed to simulate apparent ground motion from orbit. Focal plane data were recorded at the nominal frame rates and integration times. The data were then processed and reconstructed as planned for on-orbit data. The resulting digital images from all of the VNIR bands were examined, and the instrument was found to be working correctly. In the process, it was also found that two detectors caused significant cross-talk. Those "leaky detectors" (in band 3 of SCA 3 and band 2 of SCA 4) were the cause of a major effort in calibration to correct the resulting artifacts.

The original End-to-End Imaging tests were performed soon after the instrument was integrated at Lincoln Laboratory. A final test was performed in a clean room at GSFC after integration with the spacecraft and thermal vacuum testing. A starburst pattern was scanned in the early tests and in the final test. There was no perceptible difference between the original images and the final image.

3.1.2 Spatial Calibration

3.1.2.1 Modulation Transfer Functions

The spatial response of the ALI instrument was calibrated in the laboratory during the period July to December 1998, prior to its integration with the spacecraft. This section presents the final results for the calibrations of the Modulation Transfer Function (MTF). Details of the MTF model developed for the instrument are described. Results for selected bands are shown graphically. Fuller details of the MTF calibration, including numerical values of the MTFs have been reported elsewhere [5].

Spatial response is fully characterized by a spatial transfer function (STF). The full STF of the instrument is a two-dimensional complex function, which depends on the wavelength band, and to a lesser degree, on the position within the field of view. The STF is the Fourier transform of the point-spread function (PSF). The modulation transfer function is normally defined as the magnitude of the STF, a real, non-negative quantity. An additional phase transfer function (PTF) is then required to describe the spatial response completely.

In the ALI, as in most good imaging instruments, the PSF is essentially symmetrical. As a result, the imaginary part of the STF ($\text{Im}(\text{STF})$) is very small, compared to the real part ($\text{Re}(\text{STF})$). The conventional MTF then looks like the absolute value of $\text{Re}(\text{STF})$. For simplicity, we prefer to work with the STF, rather than the MTF and a PTF. We have habitually called the STF the "complex MTF," or simply the MTF while working on the ALI calibration. In the rest of this document, the terms have been used interchangeably.

The approach we used to measure the MTFs of the ALI was to project the image of a knife-edge into the instrument, and scan the edge slowly across a selected set of detectors while the instrument records the image data at its nominal rates. The knife-edge was physically located at the focus of a collimator and the scan was performed by translating its support stage slowly in the plane of best focus. For each pixel in the set, the detected signal vs. time, after normalization, yields an edge-spread function (ESF). Differentiation of the ESF gives the line-spread function (LSF). Fourier transformation of the LSF results in the STF, or complex MTF, along one axis.

All measurements reported here were made while the instrument was in a thermal vacuum chamber, at its normal operating temperatures. For each of the four sensor chip assemblies (SCAs), the knife-edge was scanned across a set of pixels near the middle of that SCA, for each band. Scans were performed in both the cross-track and in-track directions of the instrument by using two sides of the 9 mm open square in a negative "USAF 1951" target as our knife-edges. (The rest of the target was covered by black plastic.) When switching from one SCA to the next, the instrument was re-positioned on an azimuthal rotation stage in the vacuum chamber in order to scan each SCA with the knife-edge within $\sim 0.5^\circ$ of the collimator axis.

The knife-edge was moved at 200 $\mu\text{m/s}$, which translates to 127.4 $\mu\text{m/s}$ at the ALI focal plane. The frame rates were 226 s^{-1} for the multispectral (MS) bands, and 678 s^{-1} for the panchromatic (Pan) band. The spatial sampling intervals were 0.564 μm and 0.188 μm for the MS and Pan bands, respectively, or approximately 70 samples per pixel width in all cases.

Analysis of the data from the knife-edge scans proceeded in several steps. While the scans were being performed in the thermal vacuum chamber in the clean room, a portion of the data was analyzed and graphically displayed on a monitor next to the control computer. The data files were stored on the hard drives of a Silicon Graphics R-10000 workstation (called the Performance Assessment Machine (PAM)), and periodically backed up on DLT cartridges.

After all of the knife-edge scan files were recorded, preliminary processing was done on the PAM. A program was run to de-scramble the raw data. Next, running under IDL^{*}, a procedure read the full MS or Pan data file and wrote a much more compact file (*.kes)[†], containing only the data from the SCA and bands of that particular scan.

The next step was to analyze the signal from each detector to derive its edge-spread function. A sigmoid curve (hyperbolic tangent) was fitted to each pixel's ESF, in order to resample the ESFs to co-align all of the edge-crossing times. In the process, automatic selection criteria were applied to reject pixels that had data artifacts or incomplete scans. An intermediate file (*.kes.fit) was written to facilitate the further processing steps.

To transform the ESFs to MTFs, another procedure was developed to read the *.kes and *.kes.fit files, then derive the LSF and MTF functions from them. For each SCA and band combination, the complex MTF was computed on a pixel-by-pixel basis, then the mean and standard deviation was derived. These are written to an IDL data file (*.mtf) for further reference, and plots are generated to display the results of each step in the analysis.

Finally, for each band the complex MTFs for the individual SCAs are averaged and plotted together, along with a curve representing the MTF model. Again, the results are written to an IDL data file. A typical page of plots generated in the analysis of one scan file is shown in Figures 3-26 to 3-29.

* Interactive Data Language, from Research Systems, Inc., 4990 Pearl East Circle, Boulder, CO 80301, (see www.rsinc.com).

† In this context, * represents a "wildcard," substituting for the root name of the data file.

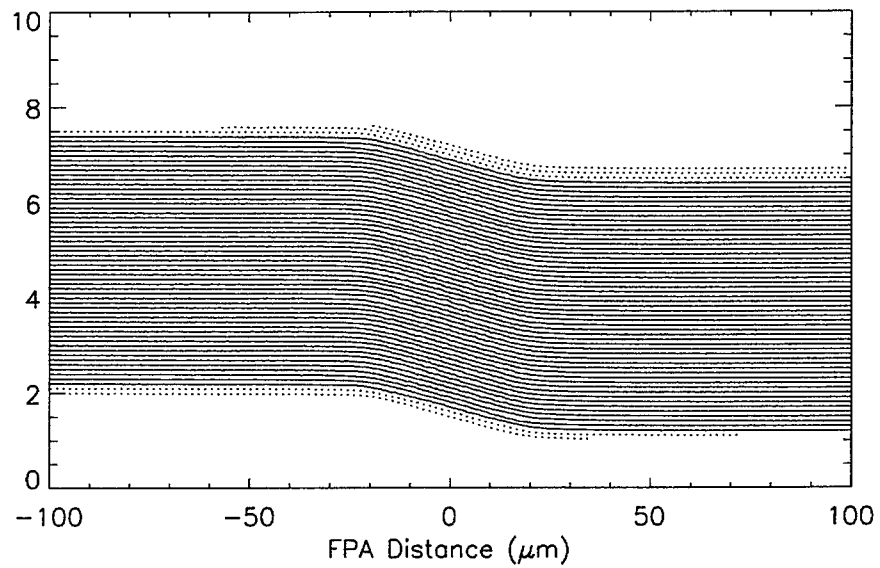


Figure 3-26. Edge-spread functions of SCA2, Band 4 pixels scanned in the cross-track direction, from file no. 16638. Pixels not used in further analysis are shown with dotted lines

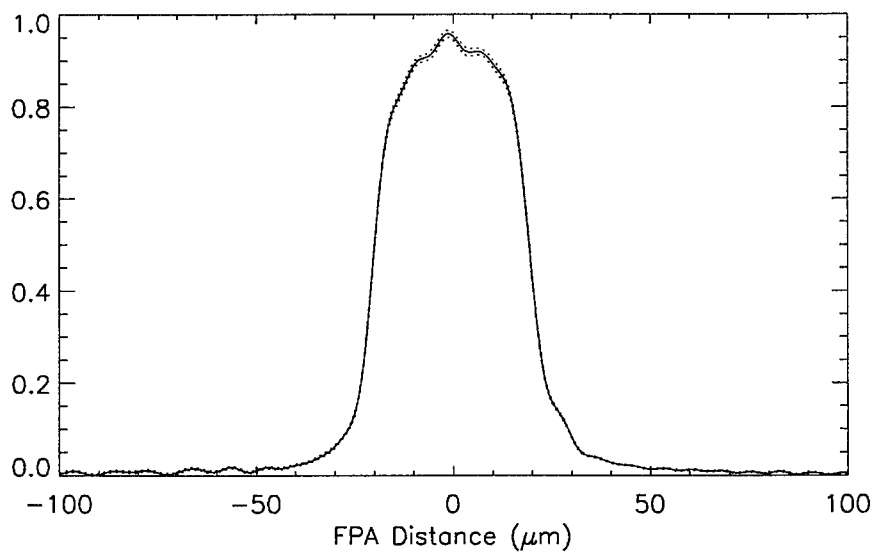


Figure 3-27. Average line-spread function derived from the data shown in Figure 3-26. The dotted lines are one standard deviation above and below the mean

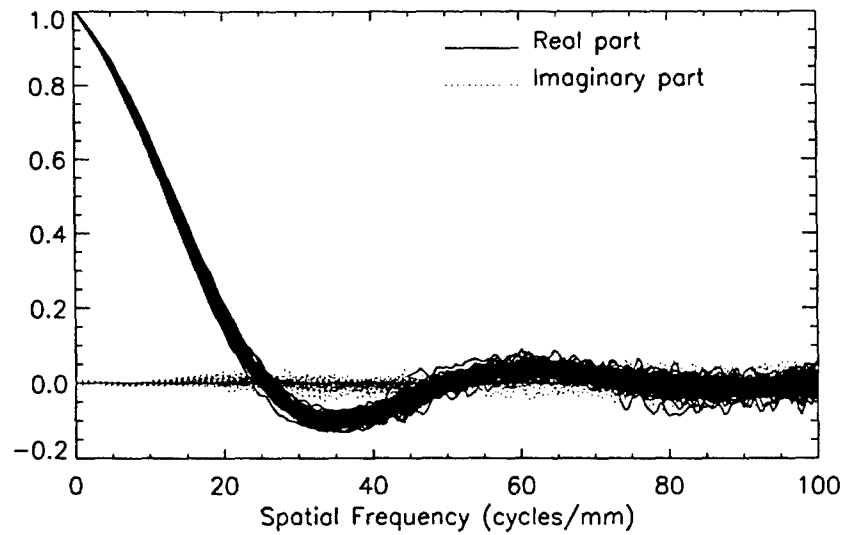


Figure 3-28. Normalized transfer functions derived from the data shown in Figure 3-26.

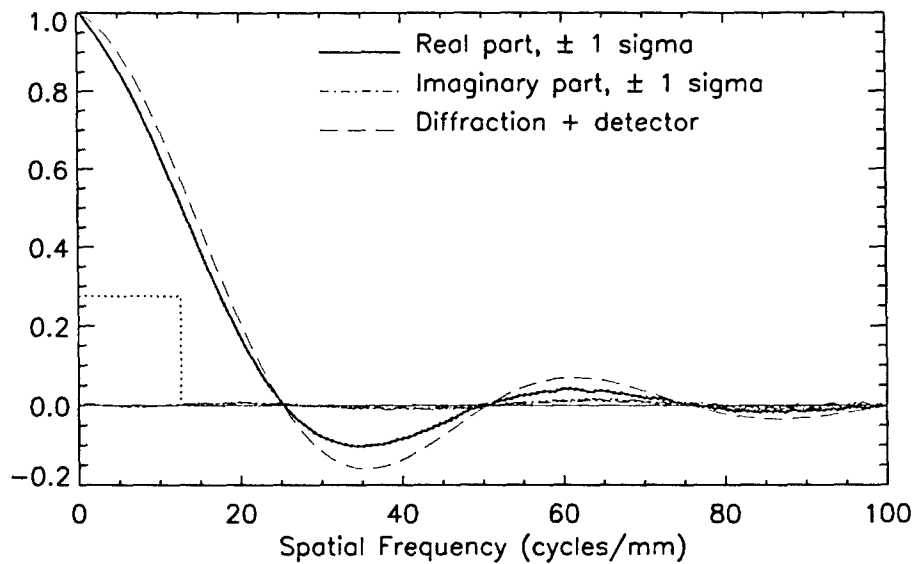


Figure 3-29. Average normalized transfer function derived from the data shown in Figure 3-26. The dotted lines are one standard deviation above and below the mean. The curve labeled "Diffraction + detector" is computed from the simplest model of diffraction by a circular aperture and a sharp-edged detector response. The specified MTF at the Nyquist frequency is indicated with dotted lines.

We describe the MTF of the instrument with a model which contains only enough parameters to fit the measurement data within the experimental uncertainties, and which will enable other investigators to compute the MTF for their own needs. It is important to have a model for the MTF, since the knife-edge scan measurements can only produce one-dimensional cross-sections of the MTF, which is a two-dimensional function. The following subsections describe the various factors which, when multiplied together, yield the system MTF of the ALI instrument. These are the optical system MTF, the detector MTF, and the MTF of the scan motion of the instrument as it collects images on orbit.

The optical MTF estimated from our laboratory measurements results from the combined optical transfer functions (OTFs) of the ALI telescope and the collimator. It is modified by the effects of light scattering from the imperfect surfaces of the ALI mirrors.

SSG, Inc., the builder of the ALI optical system, has used a laser unequal-path interferometer (LUPI) to characterize the wave front error (WFE) of the ALI. They obtained interferograms at a dozen points distributed over the $1.26^\circ \times 15^\circ$ field of view of the optical system. The WFE derived from each interferogram was fitted with a set of 37 Zernike polynomials. The first three Zernike polynomials, representing piston, tip, and tilt, are set to zero. The fourth coefficient represents a focus error. We use the Zernike coefficients from SSG to obtain an interpolated set of coefficients for any given point within the MS/Pan array of the ALI.

To ascertain the amount of focus error in the integrated system, MTF scans were performed with varying amounts of defocus applied at the collimator. The figure of merit (FoM) chosen to test the defocus was the integral of the MTF from zero to the detector sampling frequency of the FPA. A plot of this FoM as a function of the axial displacement of the knife-edge from the collimator focus is shown in Figure 3-30. The plot also shows a parabola fitted to the highest values, to derive the focus error. These results indicate that the ALI FPA, at operating temperature, is approximately $75 \pm 20 \mu\text{m}$ away from the optimum focus position. This does not seriously degrade the optical resolution, but must be taken into account when modeling the system MTF.

The spherical aberration of the collimator is calculated to be $0.007 \mu\text{m}$ rms, when the collimator and ALI pupils are correctly aligned. The remaining rms WFE, caused mainly by the beamsplitter, is approximately $0.032 \mu\text{m}$.

The spatial response of the detectors was initially modeled as unity within a defining rectangular mask ($39.6 \mu\text{m} \times 40 \mu\text{m}$ for the MS pixels, and $13.2 \mu\text{m}$ square for the Pan pixels), and zero outside of that area. The corresponding pixel MTF is a product of two sinc functions: $\text{MTF}_{\text{PIX}}(f_x, f_y) = \text{sinc}(w f_x) \text{sinc}(h, f_y)$ where w and h are the width and height of the detector mask, respectively, and (f_x, f_y) are the components of the spatial frequency.

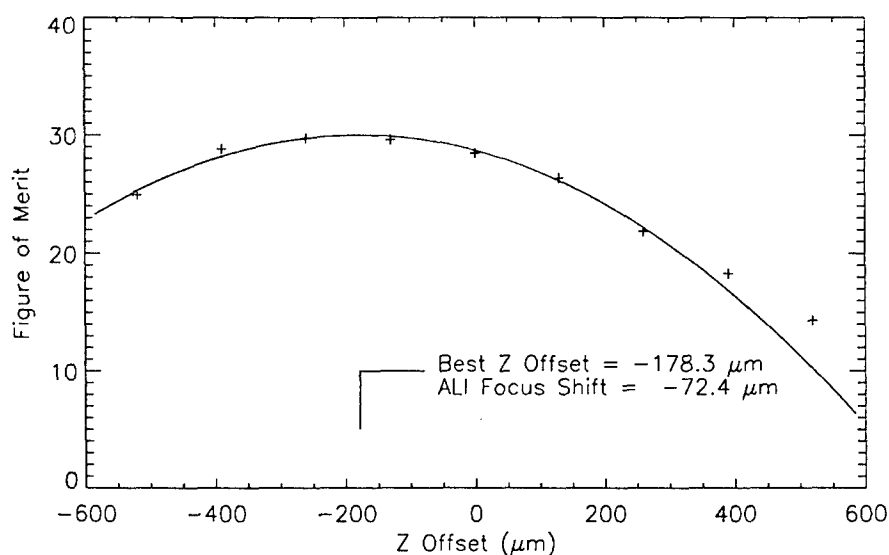


Figure 3-30. ALI focus figure of merit vs. axial displacement of the knife-edge from the collimator focus (Z Offset). Data symbols represent individual MTF scans. The curve is a parabola fitted to the points within 500 μm of the peak.

Measured values of the ALI system MTF tended to decrease approximately linearly, in comparison with the system MTF computed using this simple detector model, after adjustment of the free optical parameters. Good fits between measured and modeled MTFs are only obtained when a *carrier diffusion MTF* is included in the model.

Motion of the satellite as it collects image data in push-broom mode causes a slight smearing of the image in the in-track direction. The geometric footprint of each detector on the ground is convolved with a vector representing the motion of the view axis during the integration time of a single frame. The MTF of this motion is another sinc function in the in-track direction only: $\text{MTF}_{\text{INT}} = \text{sinc}(\alpha\nu)$ where ν is the angular frequency and α is the angle subtended by the ground motion vector.

Procedures written in IDL are used to construct the ALI WFE from the adjusted set of Zernike coefficients derived from interferograms by SSG. From the WFE, the optical point-spread function (PSF) and MTF of the ALI telescope are obtained, by use of the Fourier transform procedure in IDL.

A surface plot of the WFE near the middle of the MS/Pan array, excluding tip, tilt, and focus, is shown in Figure 3-31. There are small differences in WFE from place to place on the focal plane, caused by the fact that the beam footprint covers different parts of the M1 and M3 mirrors for different points in the field of view.

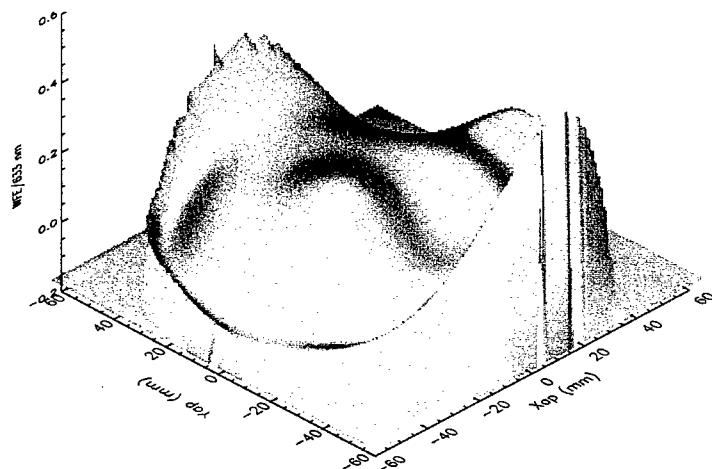


Figure 3-31. Surface plot of the wavefront error near the middle of the MS/Pan array.
The focus term is not included here.

The optical point-spread function of the Pan band, computed from the WFE, is shown in Figure 3-32. The real part of the corresponding OTF is shown in Figure 3-33.

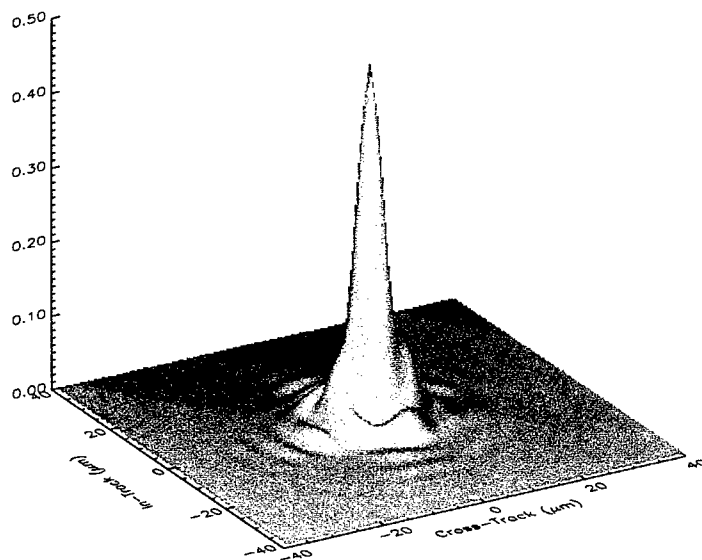


Figure 3-32. Optical point-spread function of the Pan band, computed from the full wavefront error, including the focus term.

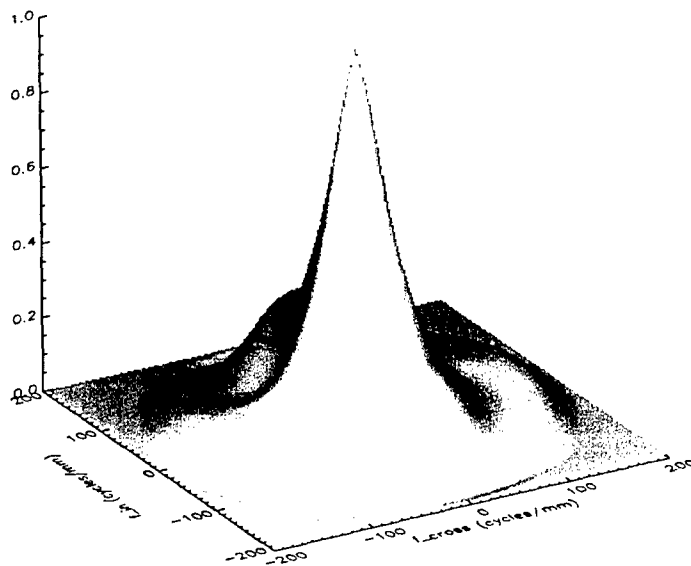


Figure 3-33. Optical transfer function of the Pan band (real part), computed from the wavefront error, including the focus term.

Figure 3-34 shows the MTF curves derived from scans of the four Pan arrays, along with the average, modeled MTF curve.

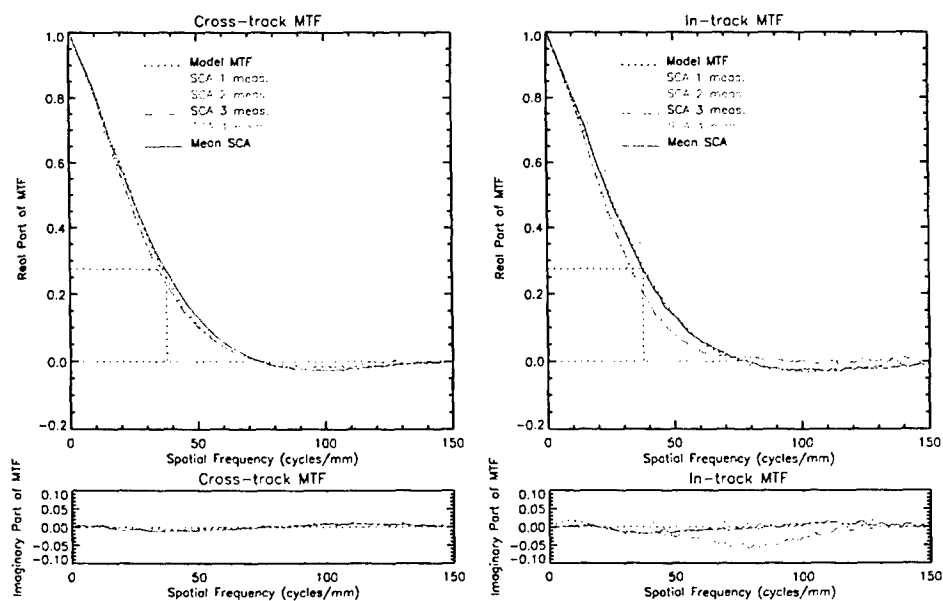


Figure 3-34. Measure and modeled Average MTFs for the Pan band, and measured MTFs for the individual SCAs.

The real part of the two-dimensional Pan MTF at the center of the array computed from our model is shown in Figure 3-35. The small imaginary part can be neglected, given the uncertainties in our fitting of the model to the measurements. The real part of the MTF is symmetric in both axes, the imaginary part anti-symmetric.

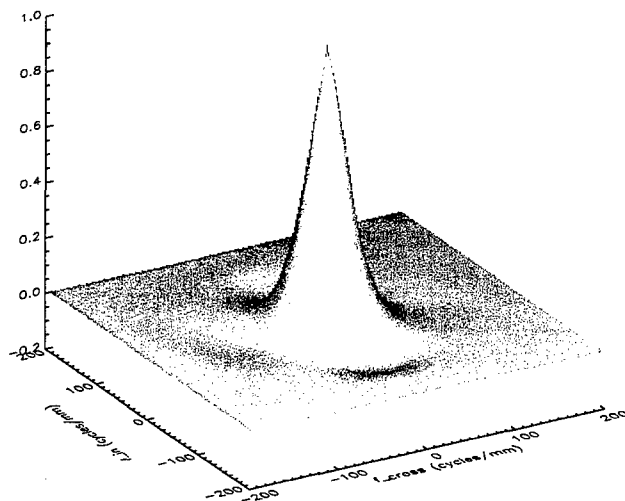


Figure 3-35. System MTF of the Panchromatic band near the center of the detector array.

Figure 3-36 gives a representation of the Panchromatic system point-spread function (PSF), not including scan motion spreading.

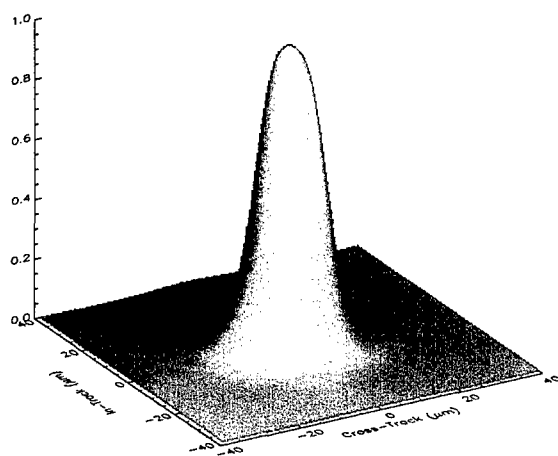


Figure 3-36. System PSF of the Panchromatic band near the center of the detector array.

The real part of the two-dimensional average MTFs for bands 1', 4', and 7 are plotted in Figures 3-37 to 3-39.

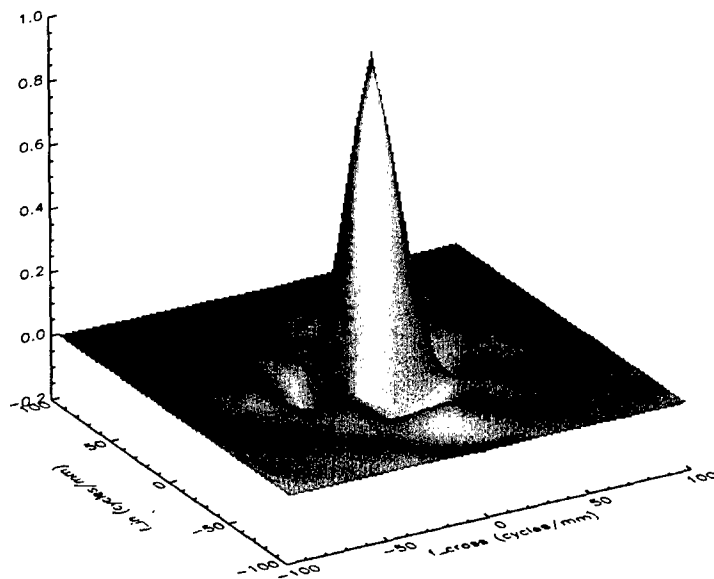


Figure 3-37. System MTF of band 1' near the center of the detector array.

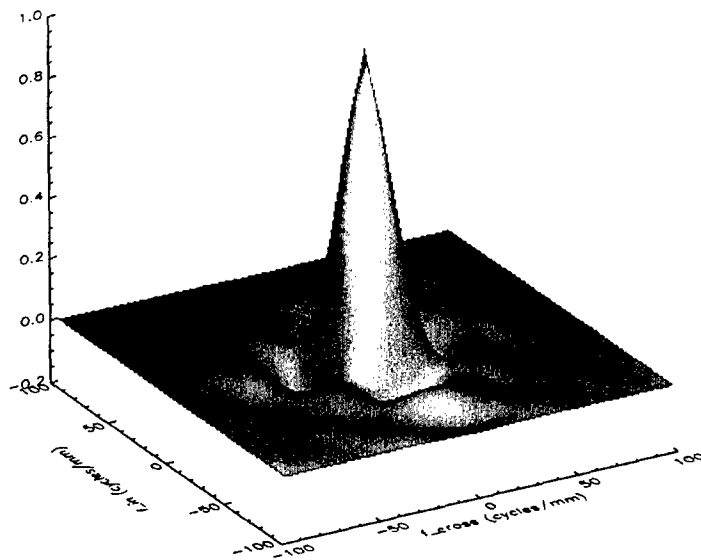


Figure 3-38. System MTF of band 4' near the center of the detector array.

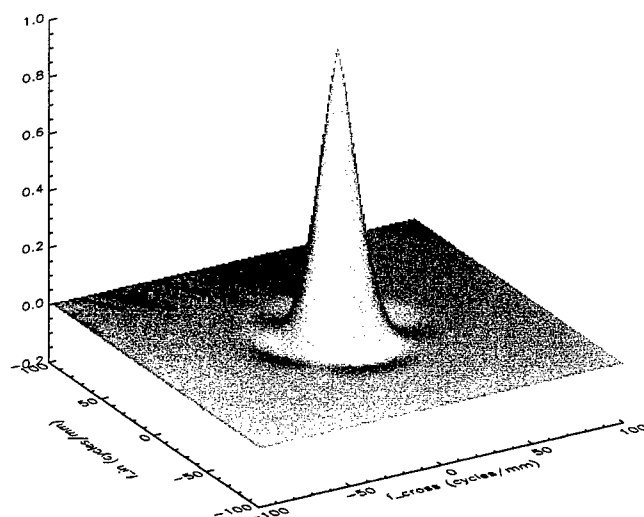


Figure 3-39. System MTF of band 7 near the center of the detector array.

Representative point-spread functions computed from the model MTFs are shown in Figures 3-40, 3-41, and 3-42. The in-track spreading caused by scan motion is not included in these PSFs.

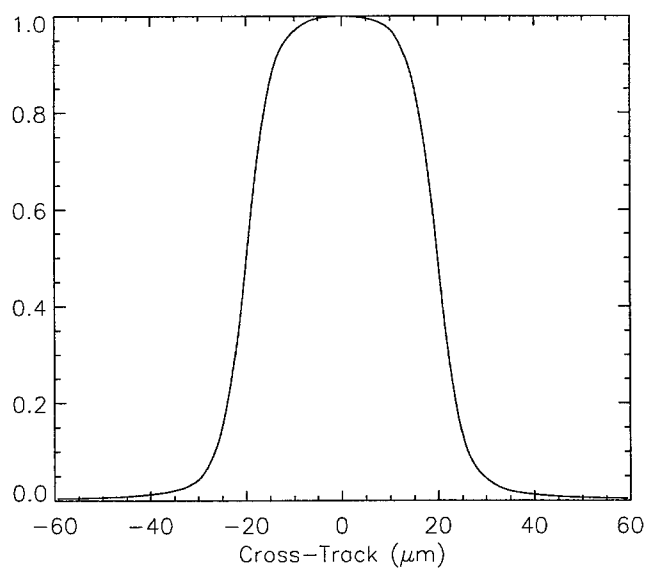


Figure 3-40. System PSF of band 1' near the center of the detector array. This cross-section is through center in the cross-track direction.

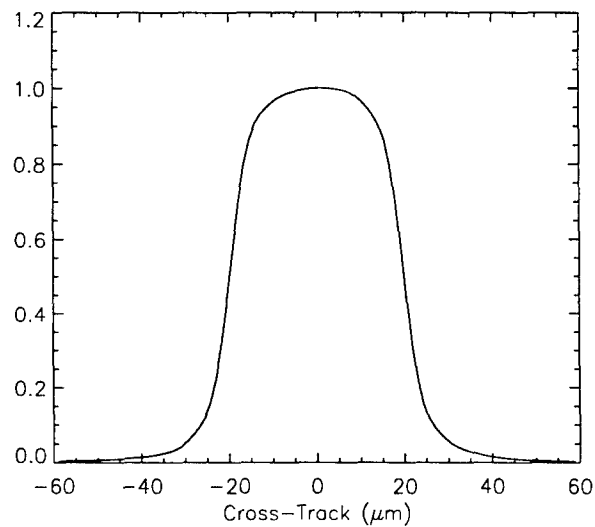


Figure 3-41. System PSF of band 4' near the center of the detector array. This cross-section is through center in the cross-track direction.

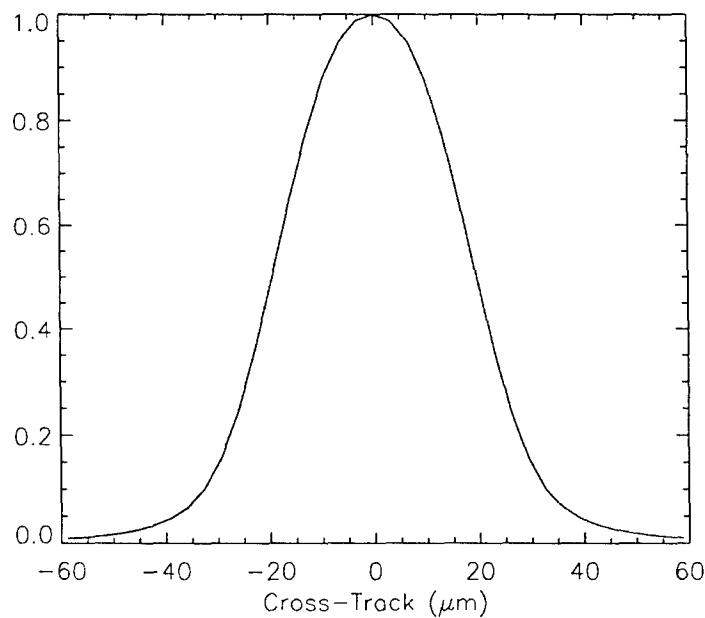


Figure 3-42. System PSF of band 7 near the center of the detector array. This cross-section is through center in the cross-track direction.

3.1.2.2 Detector Lines of Sight

In order to reconstruct the ALI image data in reference to the geographic coordinates of the land scene, the lines-of-sight (LOS) of the many detectors relative to the satellite body axes must be known. That information is contained in the LOS map. The LOS map is a tabulation of the sight

direction of each detector on the ALI focal plane, relative to a set of reference axes. A parameterized model was developed to describe the apparent position of each detector on the focal plane, as seen through the telescope. The detector LOS map is a tabulation of those apparent positions. To obtain the angular LOS of any detector, we treat the telescope as an ideal imaging system, with a given focal length. The LOS calibration performed at Lincoln Laboratory was reported by Hearn [6].

The focal length of the telescope is one key parameter. The physical position of a detector on the focal plane is described by the positions of fiducial marks on the SCA, and the layout design of the SCA. Here, we assume that the geometric precision of the photolithographic process used to make the ROIC/detector chip is on the order of $0.1\text{ }\mu\text{m}$, far greater than our ability to discern errors. Each VNIR detector thus far has four uncertain parameters to determine its position: focal length of the telescope, X-offset, Y-offset, and rotation offset of the SCA. In the case of the SWIR bands, three additional parameters describe the offset of the SWIR detector array chip relative to the ROIC.

The ALI telescope design produces some optical distortion. Owing to the asymmetry of the design, the distortion is not axisymmetric. Thus we are unable to apply a simple radial distortion model. Instead, we resort to a general third-order polynomial in X (the in-track axis) and Y (the cross-track axis). There are actually two polynomials, one for the X component of the distortion, and one for the Y component. This leads potentially to 32 polynomial coefficients to be determined. Some of the coefficients can be eliminated, such as the zero-power term, representing a fixed offset.

The ALI includes an optical reference cube fixed to its base pallet. The measurements that were made by theodolite to determine the orientation of the optical axes of the ALI telescope relative to this ALI reference cube are described in a following section. After final integration with the spacecraft, additional theodolite measurements were made to relate the ALI reference cube to the other sensors on board the spacecraft.

3.1.2.2.1 Subsystem Measurements

Four distinct sets of measurements were made in order to estimate the values of the line-of-sight parameters. This section describes the measurements made on the major subsystems of the instrument. Section 3.1.2.2.2 describes the end-to-end calibration measurements of the complete instrument to establish the detector lines-of-sight relative to the telescope axes. Finally, Section 3.1.2.3 discusses the theodolite measurements at Lincoln Laboratory to establish the angles from the reference cube to the telescope axes.

Santa Barbara Remote Sensing (SBRS) measured the locations of the SCAs on the assembled MS/Pan module. The measurements on the assembled focal plane used a coordinate-measuring machine to establish the locations of fiducial marks in the metallization of each SCA, to an accuracy of $\sim \pm 1\text{ }\mu\text{m}$. The location of the pixels within each SCA, determined by photolithography, is believed to have an accuracy of $\sim \pm 0.1\text{ }\mu\text{m}$.

SSG used a theodolite to measure the telescope for focal length and distortions. For this purpose, a fixture bearing scribed lines was mounted at the focal plane location. These lines were measured at Lincoln Laboratory on a coordinate-measuring machine. A precision theodolite was used to measure the angles of the scribe-line intersections when seen through the telescope, to ± 1 arc sec. These angular readings were then fitted to cubic polynomial functions to describe the cross-track and in-track optical distortion. A vector map of the measured distortions is shown in Figure 3-43. The axes are labeled in millimeters and encompass the entire $15^\circ \times 1.2^\circ$ field of view of the telescope. The residuals from the fits are shown in Figure 3-44. The fitted focal lengths are 942.41 mm and 945.15 mm in the cross-track and in-track directions, respectively. The scale of the vectors is greatly enlarged in comparison with Figure 3-43.

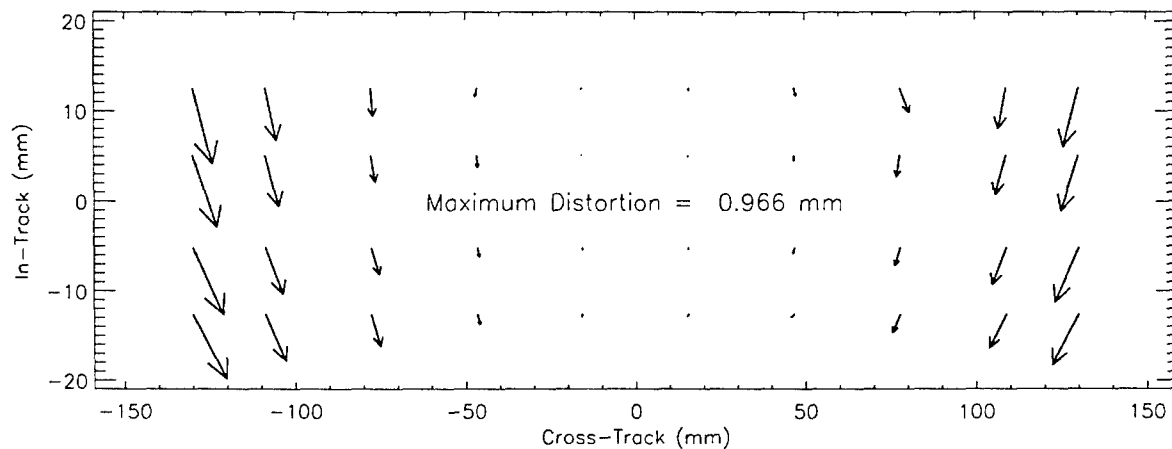


Figure 3-43 ALI telescope optical distortion, from SSG measurement data

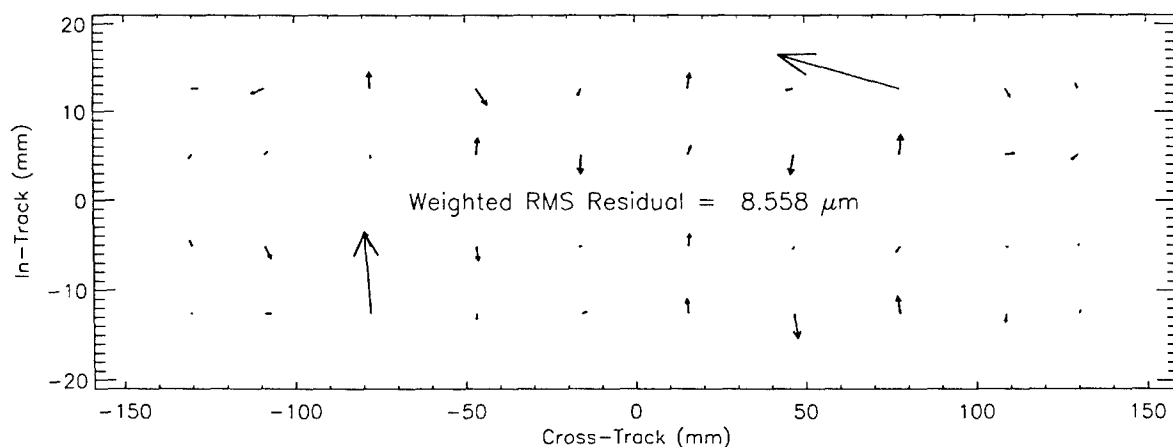


Figure 3-44. Residual ALI optical distortion, after subtracting a cubic polynomial fit from the measurement data.

3.1.2.2.2 End-to-End LOS Calibration

A precision target was placed at the focal plane of the imaging collimator. Ordinarily, a standard grid target would be used, giving apparent displacements of the grid points as seen by the instrument. The ALI detectors are arranged on the focal plane in staggered rows, not in a simple two-dimensional grid. It is only capable of forming two-dimensional images by scanning. It was undesirable to scan the target with the vertical slide, as was done to test end-to-end image formation, since that would introduce the uncertainties of the scan speed and direction. The approach chosen was to record static images of a Ronchi ruling placed at the collimator focal plane. The orientation of the ruling was changed from one image to the next. First, the lines were vertical, in the in-track direction to the ALI. Two more images were recorded with the lines at approximately 60° and 120° from vertical. The three static images of the Ronchi ruling which were later analyzed consisted of averages of 1,000 frames of MS/Pan detector signals. An image was also recorded with the Ronchi ruling removed from the collimator, to establish the "white" level signals. Similarly, dark levels were recorded, with the aperture cover of the instrument closed.

Relative lines of sight of the detectors were estimated from the Ronchi ruling images by using a linearized, least-squares fitting process to adjust the LOS parameters until numerically modeled detector signals matched the measured signals. The frequency of the Ronchi ruling target mounted in the collimator was 2.000 mm^{-1} . At the ALI focal plane, this became approximately 3.18 mm^{-1} . Thus there were 40.2 cycles of the ruling across each SCA detector row for the vertical ruling, and 20.1 cycles for the 60° and 120° rulings. This was expected to provide great precision in determining the relative detector lines-of-sight.

The data from the ALI were recorded and pre-processed on a Silicon Graphics workstation. The raw files were archived to digital linear tape. Additional analysis was performed with the IDL language, running on a 500 MHz Power Macintosh G4.

Results from the laboratory modulation transfer function measurements [5] were used to predict the appearance of the Ronchi ruling to the ALI. In IDL, the product of the detector transfer function with the component amplitudes of the square-wave was inverse-Fourier transformed to construct the detector response as a function of phase within the Ronchi cycle. This was stored as a look-up table. The remainder of the calculations then used vector algebra to find the expected phase of the Ronchi cycle at each detector.

The raw detector signals were radiometrically corrected with a two-point calibration. A normalization was performed on the detector signals to cause the peaks to be near one, and the valleys near zero. The theoretical response vs. Ronchi phase array (which did not range from zero to one) was modified to match.

In the standard IDL package is a linearized, least-squares fitting procedure called *curvefit.pro*. It requires the user to supply a function of the independent variables to be fitted to a given set of measured data values. Any number or type of parameters may be used to describe the user's function. In this case, the data values are the (normalized) measured detector signals for *all three* static Ronchi images, and the independent variables are the identities of the detectors to be fitted.

The SCA 4 fiducial position was selected to be fixed, to anchor the coordinate system of the telescope.

Vector algebra was used to trace the ray from the center of each detector through the ALI telescope, and through the collimator to its intersection with the Ronchi ruling target. Both the ALI optical system and the collimator were treated as ideal imaging systems with added distortion. Angular rotations of the vectors to different reference frames were accomplished in IDL by matrix multiplication.

It proved essential to plot the modeled detector signals over the measured ones, in order to verify whether or not the fitting process was converging to a valid set of parameters. This we did for each static image, one band at a time. All four SCAs were plotted, but the odd and even-numbered detectors were plotted separately, making eight plots per band. Samples of these diagnostic plots are shown in Figure 3-45.

The focal length of the ALI telescope cannot be determined from the image fits independently of the collimator focal length. The fits can only tell us that the ratio of the ALI focal length to the collimator focal length is 0.63445. If we use the design value of the collimator focal length, which is 1485.94 mm, then the ALI focal length is 942.761 ± 0.003 mm. Theodolite measurements of the ALI telescope indicated a focal length of 942.436 ± 0.005 mm. The discrepancy between these two values probably arises from an error of 0.5 mm in the collimator focal length. Analysis of images from on-orbit operations may permit a refinement of the ALI focal length determination.

Distortion polynomial coefficients for the linear terms in X and Y are highly correlated with the telescope focal length. We have generally fixed those terms at zero. The telescope however, could be anamorphic. In the final analysis, the in-track (X) distortion term linear in X position was left free.

To visualize the meaning of the parameters resulting from the fit to the Ronchi images, plots have been constructed to show the vector difference between actual LOS positions on the focal plane and corresponding ideal LOS positions in the absence of distortions or alignment errors. The scales of the vectors are much larger than the position scales, and are generally indicated by drawing a multispectral detector at the scale of the vectors. There is excellent agreement between the subsystem measurement and the Ronchi fit.

Figure 3-46 is a plot showing only the region of the focal plane near the MS/Pan array. It shows locations of the detector rows, the offsets of the SCAs, and the optical distortion field, all at the same scale, indicated by the $40 \mu\text{m}$ square detector "pixel." The offsets of the SCAs from their nominal locations are shown as vectors. The origins of the SCA vectors are at the positions of fiducial marks. The black arrows are from the subsystem measurement, and the red arrows resulted from the end-to-end fit.

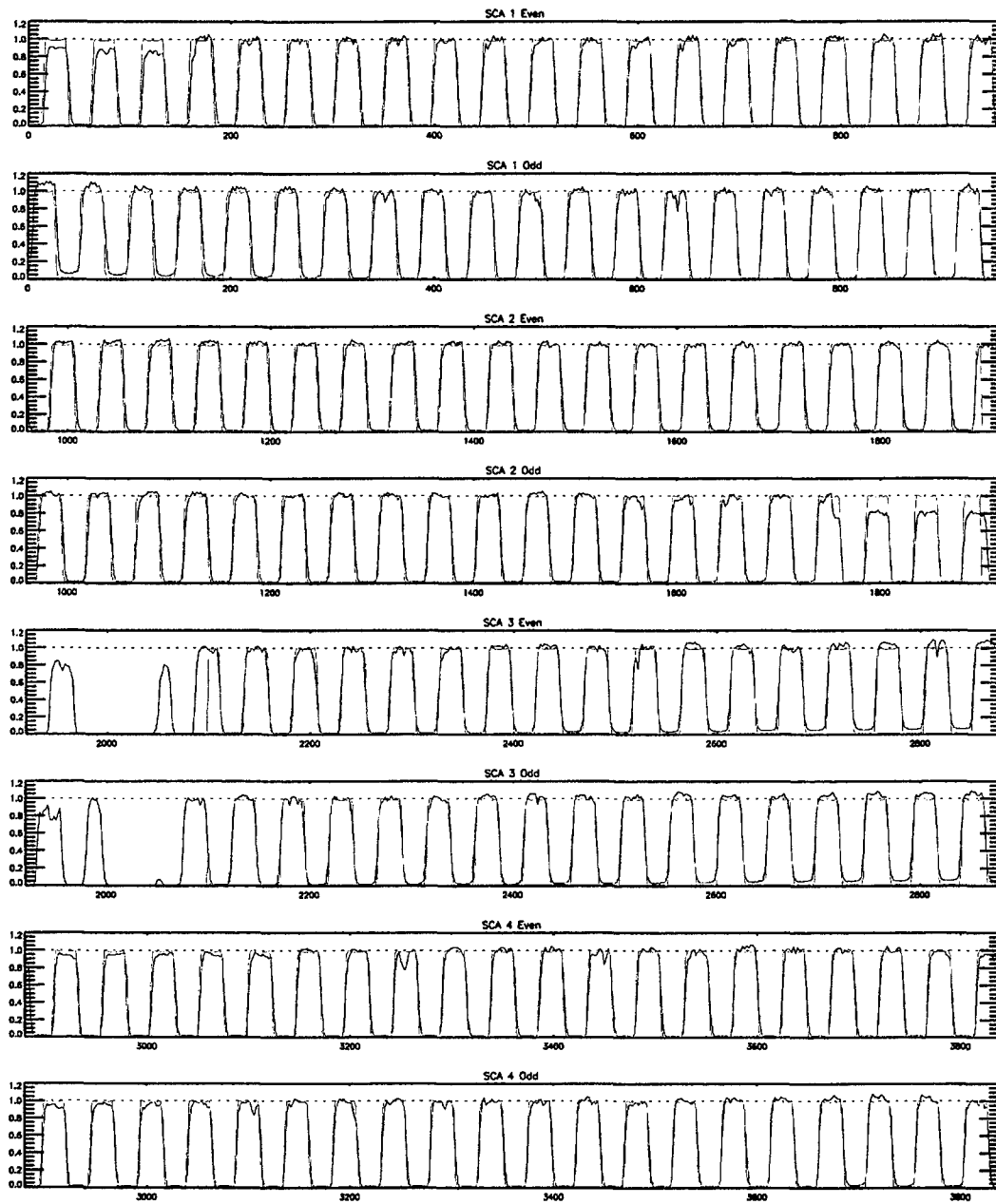


Figure 3-45. Measured detector signals and modeled signals (in red) for the Pan Band, 59.47° Ronchi orientation.

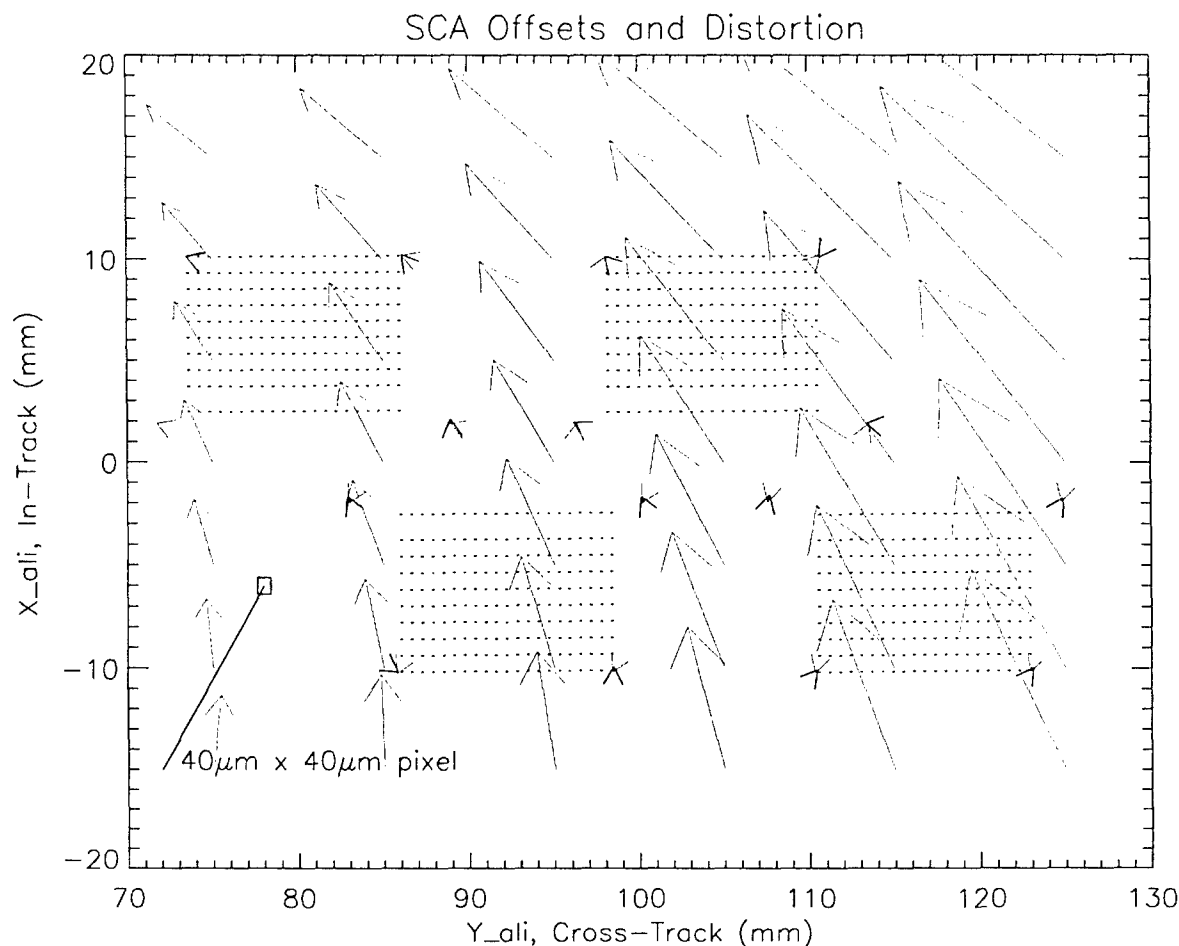


Figure 3-46. Vector plot of the MS/Pan end of the focal plane.

3.1.2.2.3 Detector Line-of-Sight Map

The end product of our line-of-sight calibrations is a data file to be used for the reconstruction of ALI images. An IDL procedure was developed to read the output data from the end-to-end parameter fitting procedure, and apply those parameters to reconstruct the LOS of every detector. The LOS map file lists the ALI focal length, and the *apparent* positions of the detectors on the ALI focal plane, in units of millimeters. The angular lines of sight are constructed as vectors. For example, given a detector position (x_d, y_d) on the focal plane, the corresponding (non-normalized) line-of-sight vector is $(-x_d, -y_d, f_{ALI})$. Such vectors are used in image reconstruction and geo-referencing procedures.

3.1.2.3 Reference Cube Alignment

The end-to-end measurements described in the preceding sections provided the detector lines of sight relative to the ALI telescope axes. This section describes the measurements made on the ALI instrument to determine the angular relationships of the telescope axes relative to the external reference cube. That cube is mounted on the ALI pallet, and is intended to provide an

angular reference during satellite integration for alignment with the inertial reference unit and the other optical instruments.

All measurements took place with the ALI in a fixed position in the clean room. It was placed on the Flotron fixture under the Class 100 hood, with the X-axis pointing down and the Z-axis horizontal. The reference cube was approximately 43 inches above the floor, and the center of the entrance pupil approximately 51 inches from the floor.

Equipment used for these measurements included an electronic autocollimating theodolite (Zeiss model Eth 2), a sturdy tripod for the theodolite, a 12-inch flat mirror in a gimbaled mount, and a stable portable platform for the mirror. A pair of Maglite flashlights were also mounted to a bar supported on a tripod in front of the theodolite in order to illuminate the focal plane. A plan view of the equipment positions is shown in Figure 3-47.

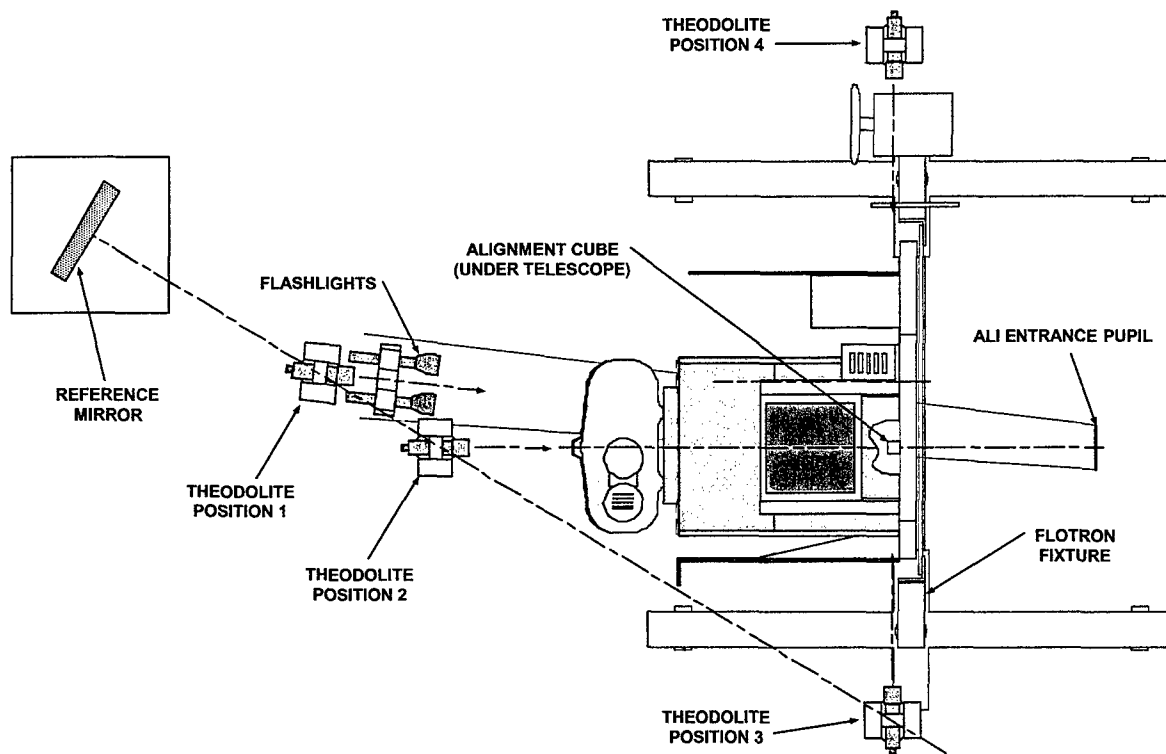


Figure 3-47. Plan view of clean room setup to measure alignment of the ALI reference cube

There were four distinct positions of the theodolite. Positions 1, 2, and 3 were along a line normal to the center of the reference flat mirror, which was kept in a fixed position. The detectors were sighted from position 1. The front of the reference cube was sighted from position 2, and the right side of the cube from position 3. The left side of the cube was sighted from position 4.

In position 1, the focal plane was sighted through the telescope. Each end of the Pan array of each SCA was measured. From positions 2, 3, and 4, the reference cube was measured in

autocollimation. In positions 1, 2, and 3, the fixed reference mirror was also measured in autocollimation. This provides an azimuth reference for those measurements. All elevation measurements are referred to the local vertical, which is automatically determined by the theodolite to an accuracy of 0.5 arc seconds. The azimuth accuracy is the same as for the elevation axis. Experience of the operators has shown that sightings of the same target are repeatable to approximately ± 1 arc second.

For the purpose of alignment, the frame of reference for the detector lines of sight is defined as follows: The Z-axis is the normal to the +Z face of the reference cube. The Y-axis is in the plane determined by this normal and the normal to the +Y face of the cube (which is orthogonal to the +Z normal to within 1 arc-second). The X-axis is orthogonal to the other two, forming a right-handed coordinate system.

Since the ALI was not situated with its X-axis exactly vertical during the present measurements, the angular readings had to be transformed to the cube frame of reference. Angular readings are first converted into vectors in the laboratory frame. The vectors in the laboratory frame were transformed to the reference cube frame by a rotation matrix. Application of the rotation matrix to the sighting vectors results in the cube-referenced vectors as listed in Table 3-12. For convenience, the corresponding azimuth and elevation angles are listed as well.

Table 3-12
Direction vectors in the cube frame

Vectors	Reference Axis			Angles (degrees)	
	X	Y	Z	Azimuth	Elevation
Pan Points					
1 Right	-0.003259	-0.133084	0.991099	7.6479	-0.1867
1 Left	-0.003270	-0.119690	0.992806	6.8743	-0.1873
2 Right	-0.008552	-0.120270	0.992704	6.9080	-0.4900
2 Left	-0.008561	-0.106914	0.994231	6.1377	-0.4905
3 Right	-0.003295	-0.107339	0.994217	6.1620	-0.1888
3 Left	-0.003309	-0.093965	0.995570	5.3918	-0.1896
4 Right	-0.008577	-0.094509	0.995487	5.4233	-0.4915
4 Left	-0.008586	-0.081046	0.996673	4.6488	-0.4919
Cube Faces					
+Z	0.000000	0.000000	1.000000	0.0000	0.0000
+Y	0.000000	1.000000	0.000000	-90.0000	0.0000
-Y	0.000052	-1.000000	-0.000035	90.0020	0.0030

The positions sighted on the focal plane through the theodolite are all within the MS/Pan detector array, and do not correspond with the axes of the ALI telescope. In contrast, the *relative* lines of sight derived from the end-to-end Ronchi images are based on the telescope axes. We next needed to relate the telescope axes to the ALI reference cube axes.

We see Table 3-12 a set of eight vectors called "Pan points." These correspond with relative lines of sight of detectors at the ends of the Pan array of each SCA. From the LOS map file, we take the *Y* (cross-track) position of each end detector, and the average *X* (in-track) position of the odd and even end detectors to be the nominal sighted location. Using the fitted telescope focal length, the eight unit LOS vectors in the telescope frame were constructed. They are listed in Table 3-13.

Table 3-13
Direction vectors in the telescope frame

Vectors	Optical Axis		
	X	Y	Z
Pan Points			
1 Right	0.003131	-0.129842	0.991530
1 Left	0.003046	-0.116589	0.993176
2 Right	-0.002232	-0.117034	0.993125
2 Left	-0.002322	-0.103737	0.994602
3 Right	0.002957	-0.104093	0.994563
3 Left	0.002883	-0.090775	0.995867
4 Right	-0.002385	-0.091222	0.995828
4 Left	-0.002463	-0.077870	0.996960

Vectors in the telescope frame should be related to vectors in the cube frame by a three-dimensional rotation of coordinates. To within measurement uncertainties, all eight vector pairs should be related by the same transformation. We employed matrix algebra to find a least-squares solution for the rotation matrix **R** that performs that transformation:

$$\mathbf{R} = \begin{pmatrix} 0.99915 & 0.00558 & -0.00570 \\ 0.00544 & 1.00072 & -0.00315 \\ 0.00689 & 0.00334 & 0.99999 \end{pmatrix}. \quad (1)$$

The **R** matrix is an approximation to the matrix for the small rotation from the telescope frame to the reference-cube frame. It represents small rotations about the *X*, *Y*, and *Z* axes, respectively.

Let us call the three rotation angles α , β and γ . In spacecraft terms, these angles represent roll, pitch, and yaw, respectively. We find the following estimates for the three angles:

$$\alpha = -0.186 \pm 0.005 \text{ degrees}$$

$$\beta = 0.361 \pm 0.034 \text{ degrees}$$

$$\gamma = 0.004 \pm 0.316 \text{ degrees}$$

The uncertainty in γ is much greater than for the other two angles, because that angle represents the rotation about the telescope axis, and the two ends of the MS/Pan array that was measured with the theodolite are separated by only 3° . Uncertainty in that angle also leads to greater uncertainty in the β angle about the Y (elevation) axis.

Finally, we construct a rotation matrix to transform vectors from the telescope frame to the reference cube frame:

$$\text{DCB} = \begin{pmatrix} 0.99998 & 0.00007 & -0.00630 \\ -0.00009 & 0.99999 & -0.00324 \\ 0.00630 & 0.00324 & 0.99997 \end{pmatrix}. \quad (2)$$

The three column vectors of the DCB rotation matrix represent the X , Y , and Z axes of the ALI telescope in the frame of the reference cube. This rotation matrix must be applied the detector LOS vectors to express them also in the reference cube frame.

3.1.2.4 Sample Images

This section presents a representative sampling of reconstructed ALI images—all have been system-corrected using the radiometric and line-of-sight calibrations of the detectors as described previously. The images are not geo-referenced, however. The images as shown here are selected from the JPEG-compressed browse image files. In our routine processing, the possible range of in-band radiances for each band is looked up, based on the solar zenith angle for the observation. For multispectral images, three bands are selected to be shown as red, green, and blue. True-color images use bands 3, 2, and 1 for the RGB triad. In order to bring out surface details with good contrast, but retain the wide dynamic range inherent in the data, a logarithmic scaling is applied for the 24-bit JPEG output. The radiances for 0% and 100% diffuse surface reflectance are used as scaling parameters for each selected color in the JPEG file. In this way, white surfaces (e. g. clouds) appear white in the browse images. The JPEG file can be opened in any good image-editing program, such as Adobe PhotoShop. We often make minor adjustments with the PhotoShop “Image > Adjust > Levels...” command, to further enhance surface detail, sometimes allowing bright clouds to saturate.

The first scene acquired by the ALI was of Alaska, just north of Anchorage, on November 25, 2000. It is shown in Figure 3-48. The solar zenith angle was approximately 85° for this data collection event. As a result, there is a very wide range of radiances in the scene, from the shadows

to the snow-covered slopes facing the sun. The resolution and dynamic range of the ALI are brought out by the portion of the panchromatic image of Sutton seen in Figure 3-49.

Another panchromatic image is presented in Figure 3-50. It shows the downtown portion of Washington, D.C. The shadow of the Washington Monument is clearly visible in this image. A similar panchromatic image of Boston appears in Figure 3-55. Figure 3-51 and Figure 3-52 show two typical presentations of an ALI image of Cape Canaveral, Florida. Figure 3-51 is the true-color image, and Figure 3-52 shows bands 4, 3, and 2 in false color. This selection is often used, since it highlights healthy vegetation in red. Additional true-color images are seen in Figure 3-53 (Yuma, Arizona) and Figure 3-54 (Oahu, Hawaii).

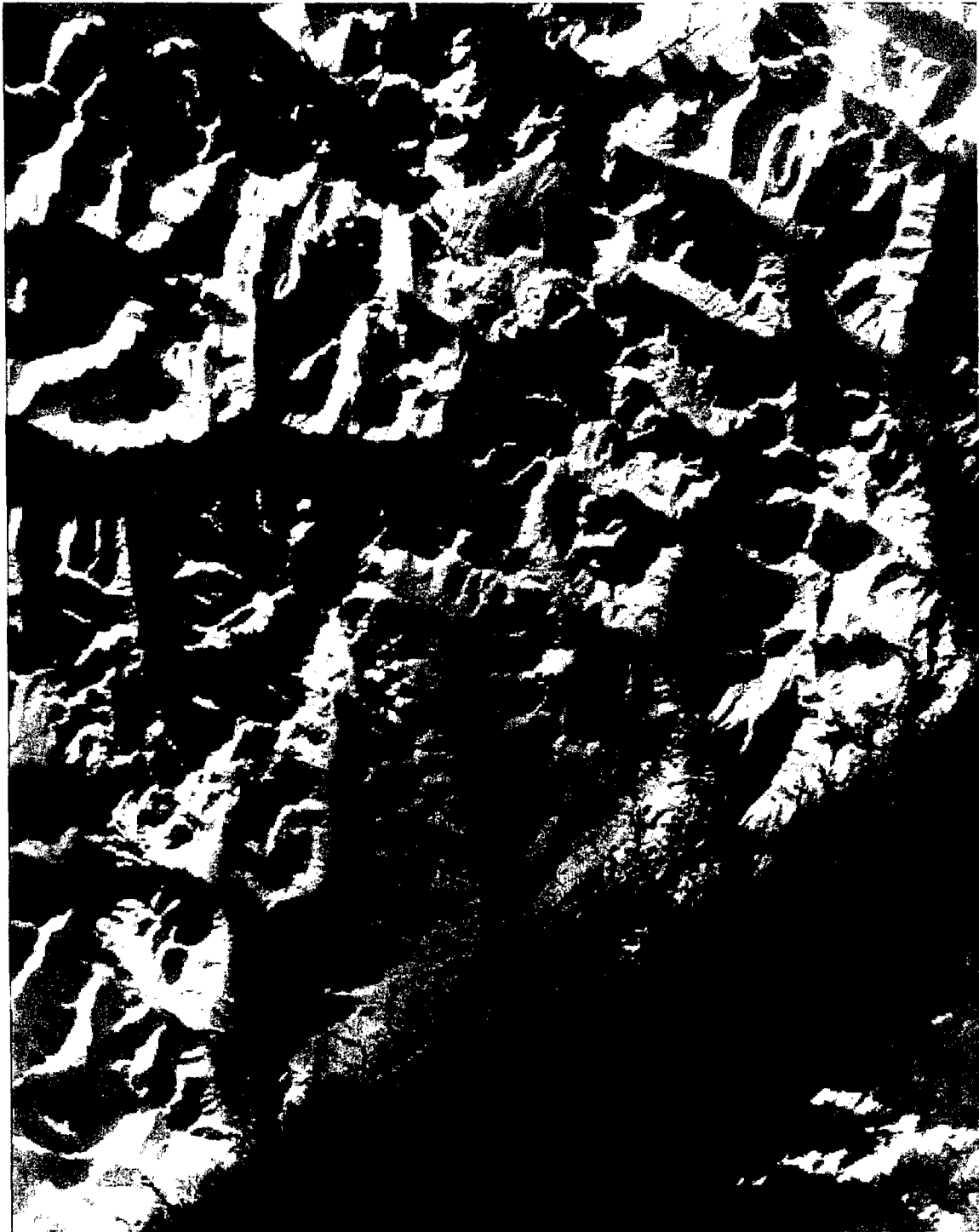


Figure 3-48. True-color image of Sutton, AK and the Matanooska River Valley.

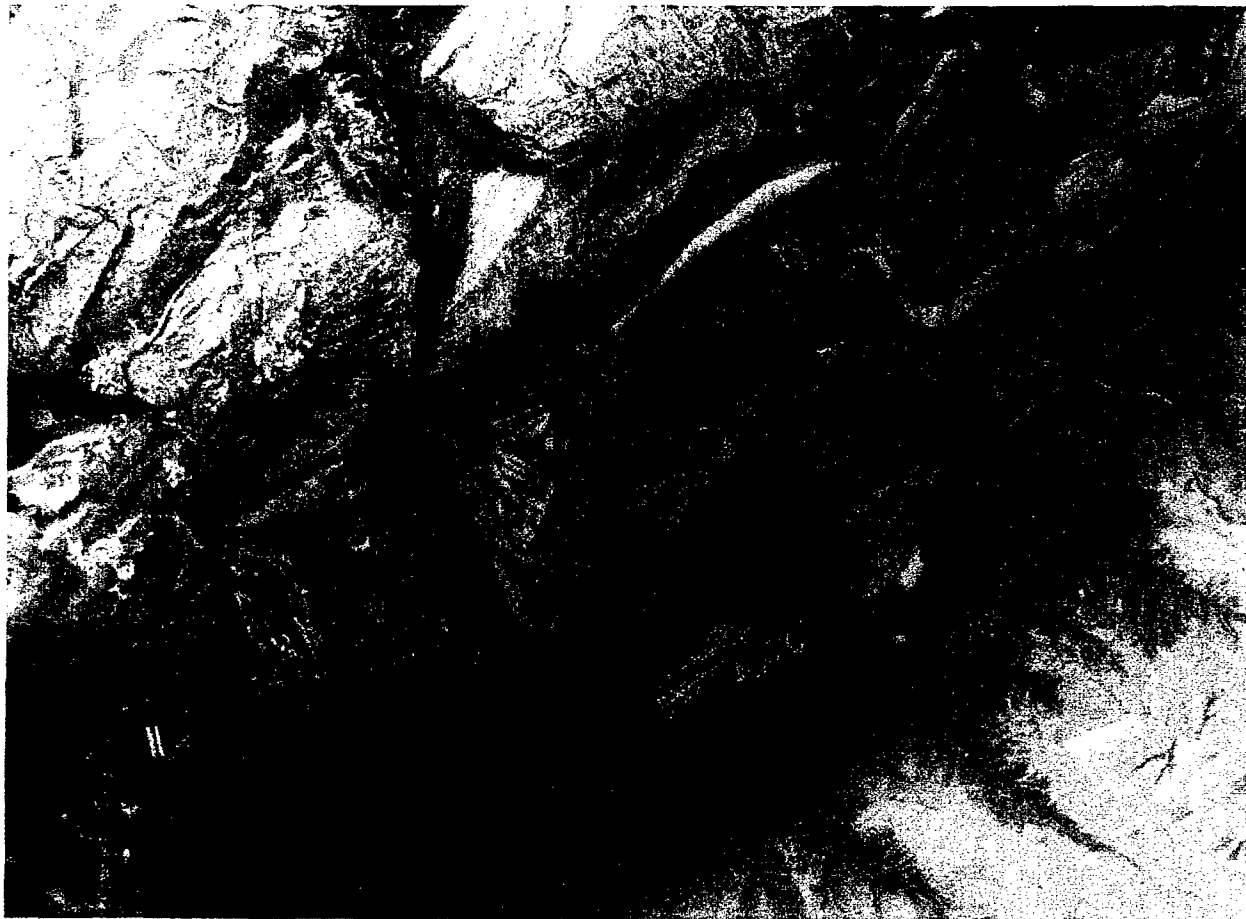


Figure 3-49. Selected portion of the panchromatic image of Sutton, AK



Figure 3-50. Panchromatic image of Washington, D.C.



Figure 3-51. True-color image of Cape Canaveral.



Figure 3-52. False-color image of Cape Canaveral. The red, green and blue components represent bands 4, 3, and 2, respectively. Healthy vegetation appears red.



Figure 3-53. True-color image of Yuma, Arizona and the Colorado river.

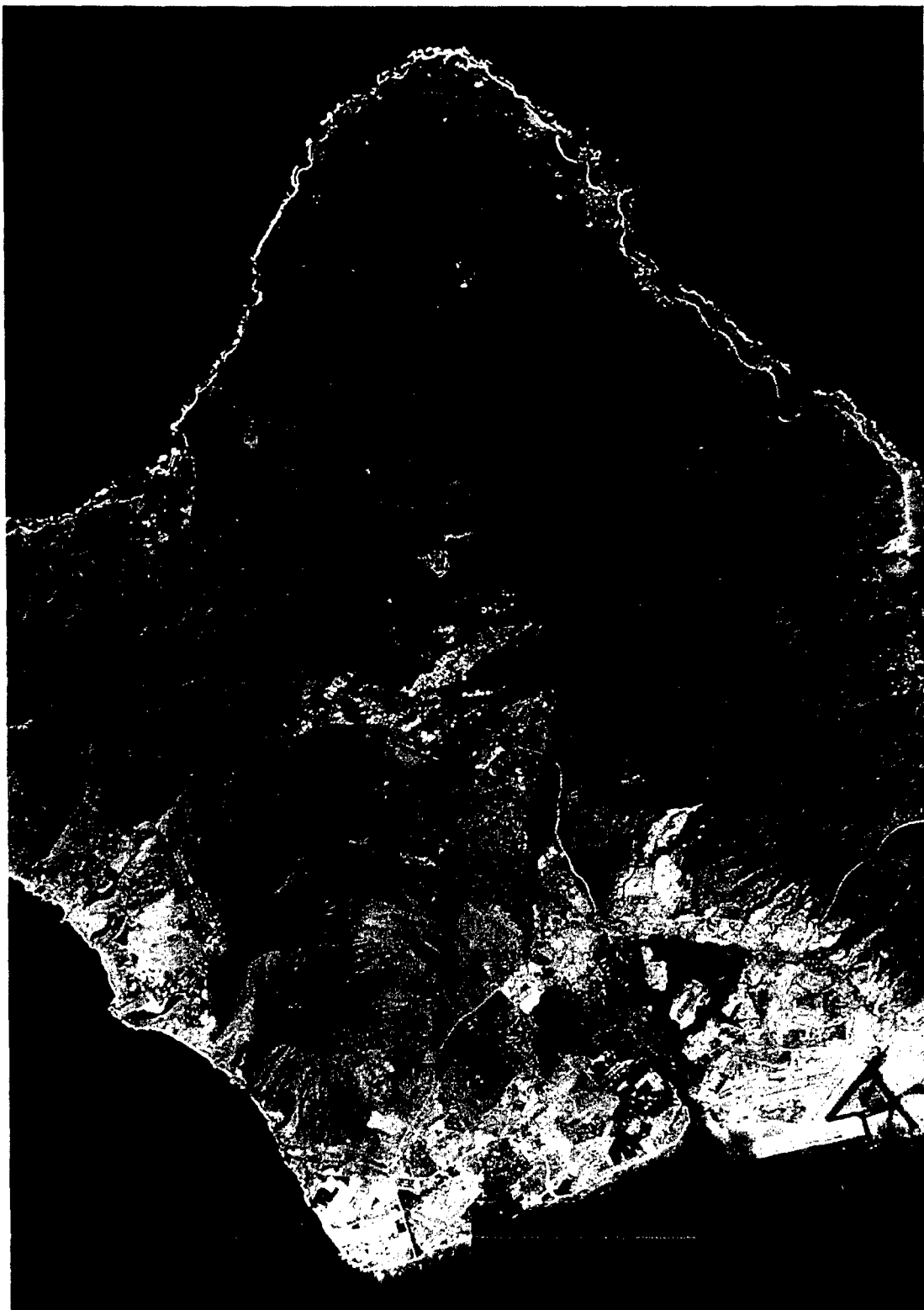


Figure 3-54. True-color image of Oahu, Hawaii



Figure 3-55. Panchromatic image of Boston.

In Figure 3-56, we present images of Lake Frome, South Australia in several different band selections. In the true-color image (bands 3-2-1), the dry lake bed appears in very light shades of gray. The SWIR bands 7-5-5' however, show dramatic variations as shades of blue, probably indicating the presence of water just below the surface.



Figure 3-56. Multispectral images of Lake Frome, South Australia. The spectral bands represented by red, green, and blue, respectively, are indicated at the top of each image.

Water in various forms appears in 3-57, which shows two views of Antarctica, near McMurdo Sound. In the true-color image on the left, it is difficult to distinguish snow, ice, and clouds. In the SWIR band image on the right however, snow and ice appear in shades of blue, while the clouds are white. A glacial stream appears distinctly darker, showing much less reflectance at the longer wavelengths.



Bands 3-2-1



Figure 3-57. Multispectral images of Antarctica, near McMurdo Sound. A true-color image (bands 3-2-1) is on the right. The image on the left of the short-wave infrared bands clearly distinguishes snow, ice, and clouds.

3.1.3 Spectral Calibration

Included in the ALI ground calibration period was the system level spectral characterization of one of four focal plane Sensor Chip Assemblies (SCAs). This section provides a review of the techniques employed during spectral calibration and the results for the VNIR, SWIR and panchromatic bands. These results are compared to subsystem measurements obtained before the instrument was assembled. Additional information may be found in the MIT/LL EO-1-2 project report [7].

Table 3-14
Spectral and spatial definitions for the ten EO-1 ALI bands

Band	Wavelength (μm)	Ground Sampling Distance (m)
Pan	0.48 – 0.69	10
MS-1p	0.433 – 0.453	30
MS-1	0.45 – 0.515	30
MS-2	0.525 – 0.605	30
MS-3	0.633 – 0.69	30
MS-4	0.775 – 0.805	30
MS-4p	0.845 – 0.89	30
MS-5p	1.2 – 1.3	30
MS-5	1.55 – 1.75	30
MS-7	2.08 – 2.35	30

3.1.3.1 Focal Plane Construction

The spectral bands for each multispectral channel are primarily defined by filters lying above the silicon and HgCdTe detectors. A cross sectional view of an individual SCA is provided in Figure 3-58 and a table of materials used in the filters is provided in Table 3-15. A three-piece sandwich design is used to construct the filters for bands 1p, 1, 2, and the panchromatic band. All other band filters use a single glass design. All glass segments are cemented together using Epotek 301 and the ten filters together form an assembly, which resides in a bezel, mounted directly above the detector arrays.

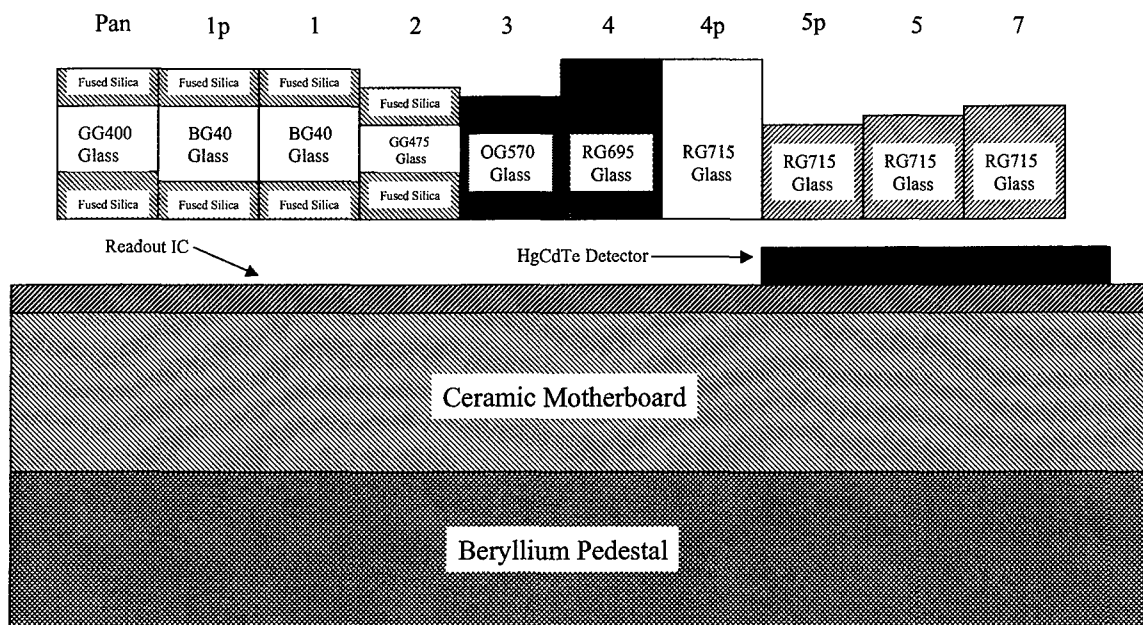


Figure 3-58. Focal plane array Sensor Chip Assembly cross-section.

Table 3-15
Materials used for focal plane filter construction

Band	Material
Pan	Fused Silica + GG400
1p	Fused Silica + BG40
1	Fused Silica + BG40
2	Fused Silica + GG475
3	OG570
4	RG695
4p	RG715
5p	RG715
5	RG715
7	RG715

3.1.3.2 Spectral Response Measurement Techniques

Spectral calibration of the Advanced Land Imager was conducted on both the subsystem and the system level.

3.1.3.2.1 Subsystem Level

The predicted system level spectral response for each band has been calculated analytically as the product of the spectral responses of individual ALI optical components. Component level spectral characterizations include measurements of witness sample detector responsivities by the Santa

Barbara Research Center (now the Ratheon Infrared Center of Excellence), filter transmissions by Barr Associates, and M1-3 and F1 mirror reflectivities by SSG Incorporated.

3.1.3.2.2 System Level

System level spectral calibration of the fully assembled flight instrument was performed at Lincoln Laboratory under vacuum and operating at expected flight temperatures. A spectral collimator was used to project a monochromatic beam into the vacuum tank via a quartz window. Data were collected from 400 nm to 2500 nm to map both in-band and out-of-band response for detectors in each of the multispectral and panchromatic bands of SCA 3.

The collimator used during system level spectral characterization of the ALI may be divided into three sections: source, collimating optics, and beam monitor (Figure 3-59). The source is composed of a quartz tungsten halogen lamp assembly, monochromator, integrating sphere, and condensing lens. The halogen lamp assembly provides a stable broadband source and is used to fill the $f/4$ entrance cone of the monochromator. The wavelength and spectral bandwidth passed through the system are defined by the order sorting filters, diffraction gratings and slit widths of the *Oriel* MS257 monochromator. Upon exiting the monochromator, the beam was randomized into a uniform 0.5" diameter spot using a 2" diameter (I.D.) *Labsphere Spectralon* integrating sphere. A condensing lens (01 LPX 245) was positioned to expand the output of the integrating sphere and provide a 3" diameter field for calibration.

The primary component of the spectral collimating optics was a 17" diameter, 100" focal length off-axis parabola. This mirror was mounted such that its focus was colocated with the virtual image of the integrating sphere output formed by the condensing lens. Collimated radiation reflected from the parabola was directed into the vacuum tank window using a large (18" diameter) flat mirror. A light tent was positioned around the spectral collimator and an intricate baffling scheme was adopted to prevent stray light from contaminating the dim monochromatic output for this measurement.

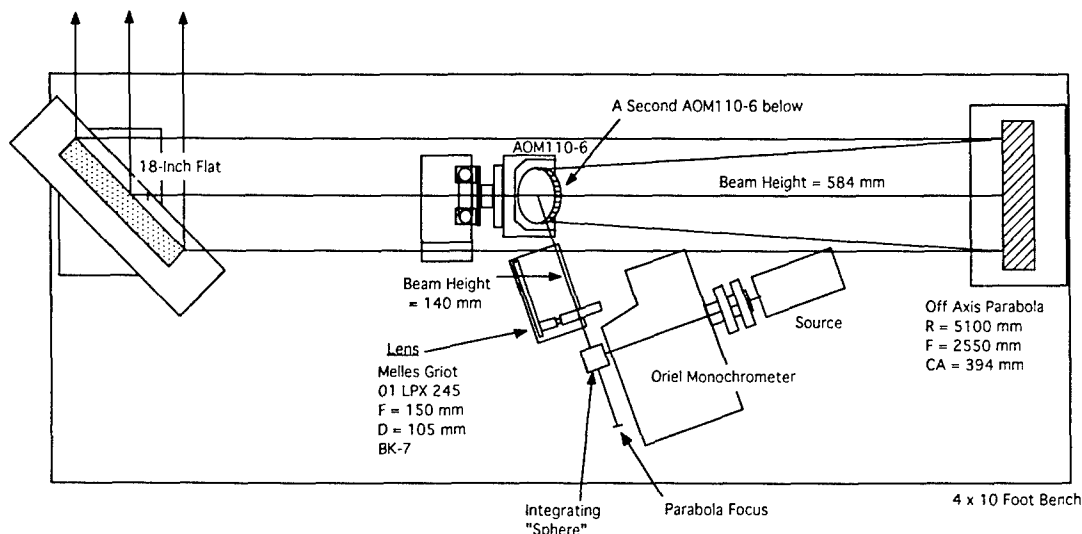


Figure 3-59. Collimator used during spectral calibration of the EO-1 Advanced Land Imager.

The collimator also contained two reference detectors, used to monitor the beam stability and flux throughout spectral calibration of the instrument: a silicon detector for VNIR measurements and a lead sulfide detector for SWIR measurements. Each detector, located between the 18" flat mirror and the vacuum tank window, was chopped and a lock-in amplifier was used to accurately subtract dark current drift and background radiation.

A DELL 266 MHz PC (Windows 95 platform) controlled the monochromator scanning and beam sampling using a GPIB interface and LabVIEW control software. For visible near infrared (VNIR) measurements (400–1000 nm) a spectral bandwidth and sampling interval of 2 nm was used. For short wave infrared (SWIR) measurements (1000–2500 nm) a spectral bandwidth and sampling interval of 4 nm was used.

Data collection consisted of iteratively sampling the beam with the reference detectors and the ALI at each wavelength interval. Initially, a wavelength and bandpass are set by the monochromator. A translation stage then positions the silicon or lead sulfide detector and chopper between the 18" flat mirror and vacuum tank window. After sampling the beam, the detector is moved to an out-of-beam position. All bands of the ALI then sample the monochromatic beam. Finally, a filter wheel, acting as a shutter between the light source and monochromator, blocks the incident beam to provide a dark ALI reference for each spectral sample.

3.1.3.3 Analysis

3.1.3.3.1 Subsystem Level

The generation of system level spectral response functions based on component level measurements must account for all elements that affect the response of an assembled instrument: mirror reflectivities, filter transmissions, and detector responsivities. Reduced witness sample data for each of these components were provided by each manufacturer as a part of MIT/LL quality control during instrument construction. Five VNIR and sixty SWIR detector responsivity measurements, 20 nm interval mirror reflectivity measurements, and 0.5 and 1nm interval filter transmission measurements were used in this analysis. Each of these data sets was interpolated onto a 1nm spectral sampling interval and the overall system level performance was calculated for each band as the product of component measurements as a function of wavelength, normalized to unity at the peak response.

3.1.3.3.2 System Level

Analysis of the ALI system level spectral calibration data was conducted at Lincoln Laboratory and centered on the normalization of a given detector's response (dn) to account for beam intensity and vacuum tank window transmission artifacts as a function of wavelength (λ). Initially, the ALI detector response is offset corrected by subtracting dark scene values for each wavelength. A plot of spectral transmission versus wavelength is then generated for a given detector by accessing data for a particular spectral calibration run and the wavelengths covered at that time. Artifacts induced by the vacuum tank window are then removed by dividing the detector's spectral response by the window's previously measured spectral transmission. Next, the varying intensity of the incident beam as a function of wavelength is accounted for by dividing the detector spectral response by the

beam intensity measured at each wavelength by the silicon or lead sulfide detector. Finally, the spectral response of the reference detector itself is removed by dividing the beam intensity measurement by the detector's responsivity for the spectral range of interest. The above technique may be shown analytically using the following relation

$$S_p(\lambda) = \frac{A_p(dn, \lambda) R_d(\lambda)}{T_w(\lambda) F(\lambda)}.$$

Here, $S_p(\lambda)$ is the derived spectral response for detector P as a function wavelength λ , $A_p(dn, \lambda)$ is the ALI focal plane response for detector P as a function of wavelength, $T_w(\lambda)$ is the spectral transmission of the vacuum tank window, and $F(\lambda)$ is the measured reference detector response to the beam as function of wavelength. $R_d(\lambda)$ is the spectral responsivity of the detector used to measure the beam.

Once the above corrections are applied, the resulting spectral response function for a given detector is normalized to unity at the peak response. Responses for 200 detectors are then averaged and compared to the theoretical spectral response of the ALI (generated from the component measurements).

3.1.3.4 Results

The system level spectral response function for each ALI VNIR, SWIR and panchromatic band have been measured for SCA 3. Figures 3-60 to 3-69 compare the measured spectral response functions near band cut-on and cut-off wavelengths to the theoretical response functions generated from component level measurements. We find excellent morphological agreement (<5% near peak transmissions) for all bands. The panchromatic band (Figure 3-69) in particular reveals good agreement between system and component level measurements despite intricate variability across this band's spectral bandpass. We also find the cut-on and cut-off wavelengths agree with subsystem level measurements to within 1 nm for VNIR bands and 2 nm for SWIR bands.

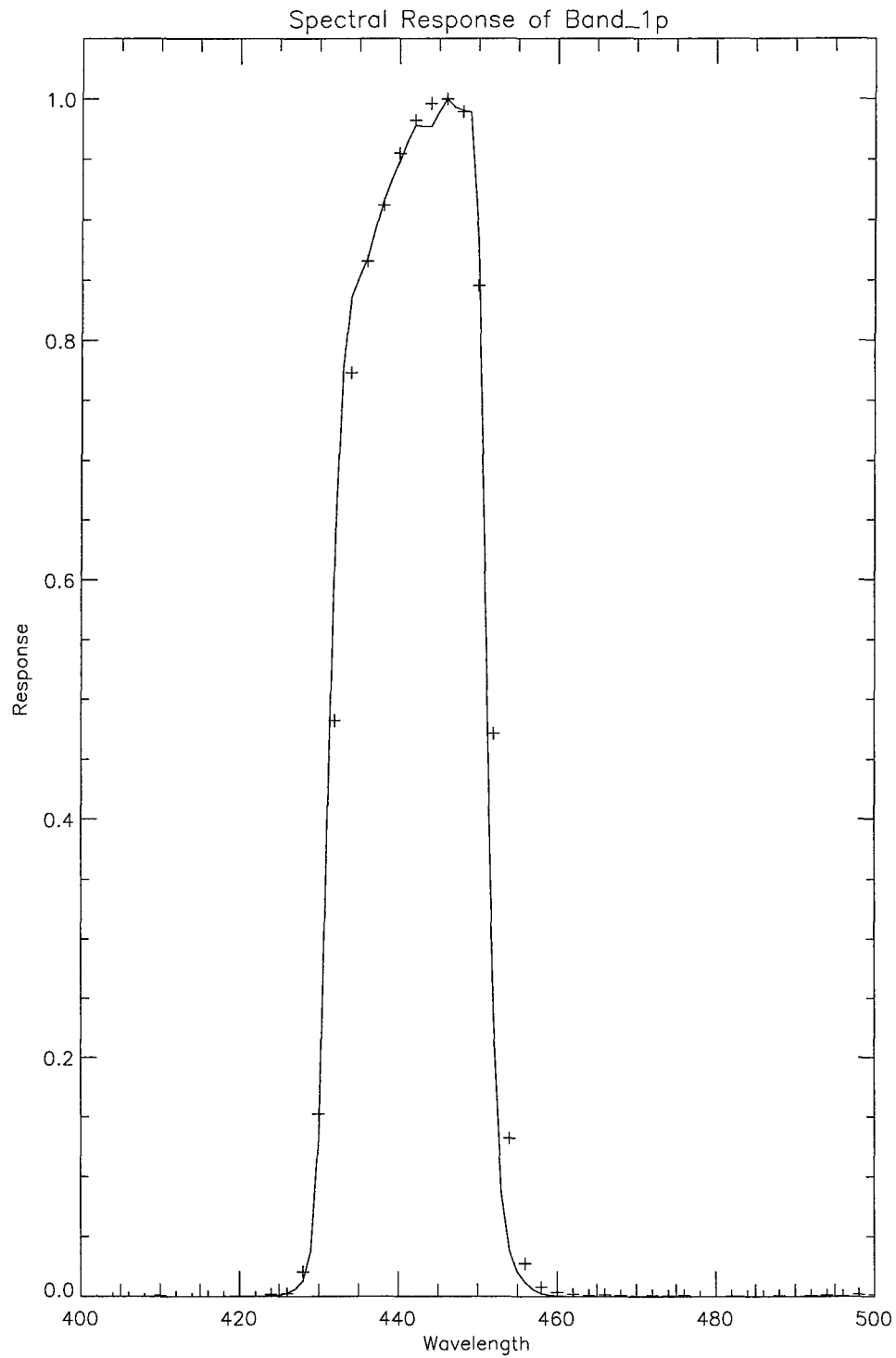


Figure 3-60. Spectral response of band 1p. The crosses represent the mean system level measured response for 200 detectors. The solid line represents data collected during subsystem level measurements.

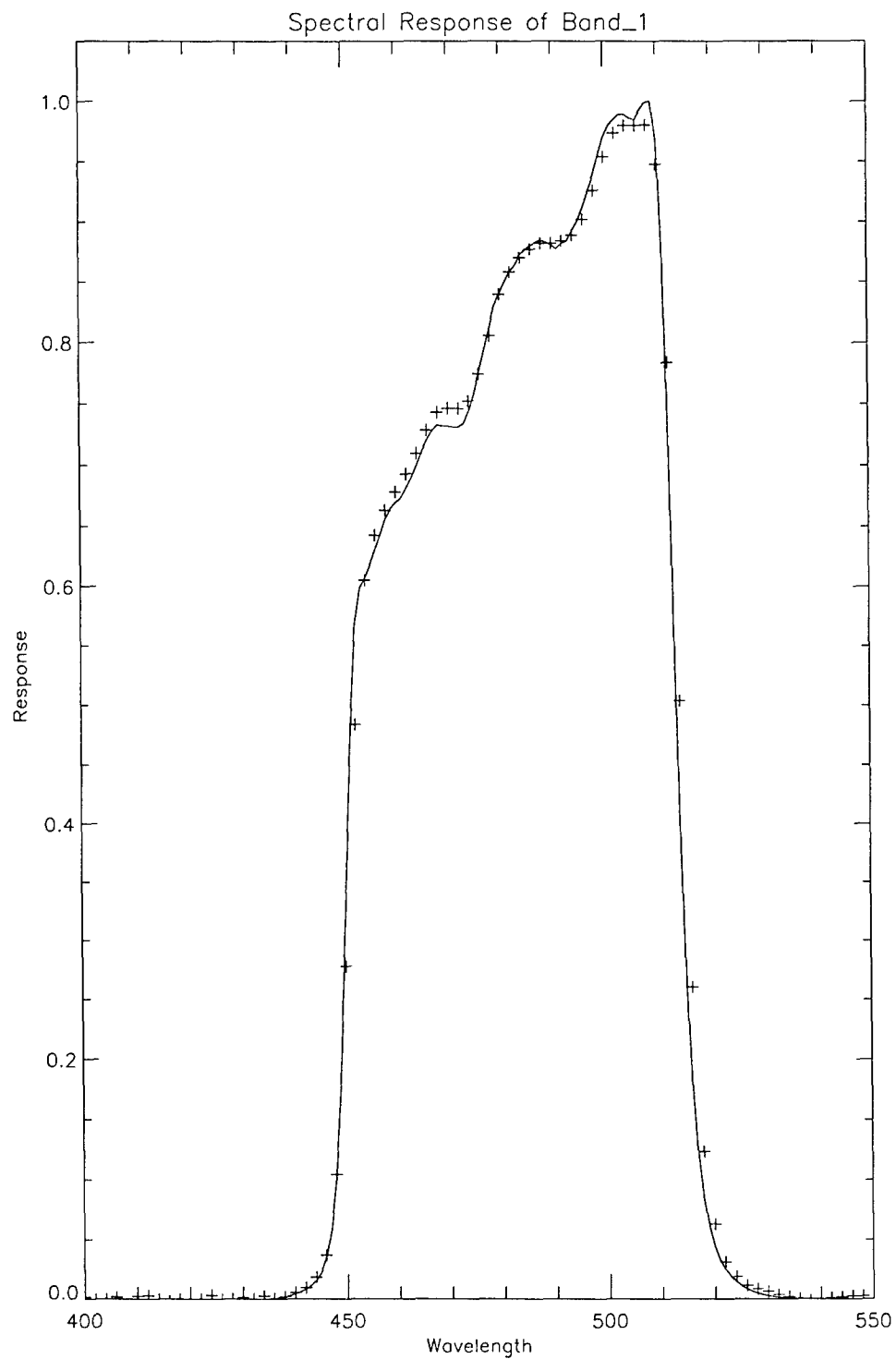


Figure 3-61. Spectral response of band 1. The crosses represent the mean system level measured response for 200 detectors. The solid line represents data collected during subsystem level measurements.

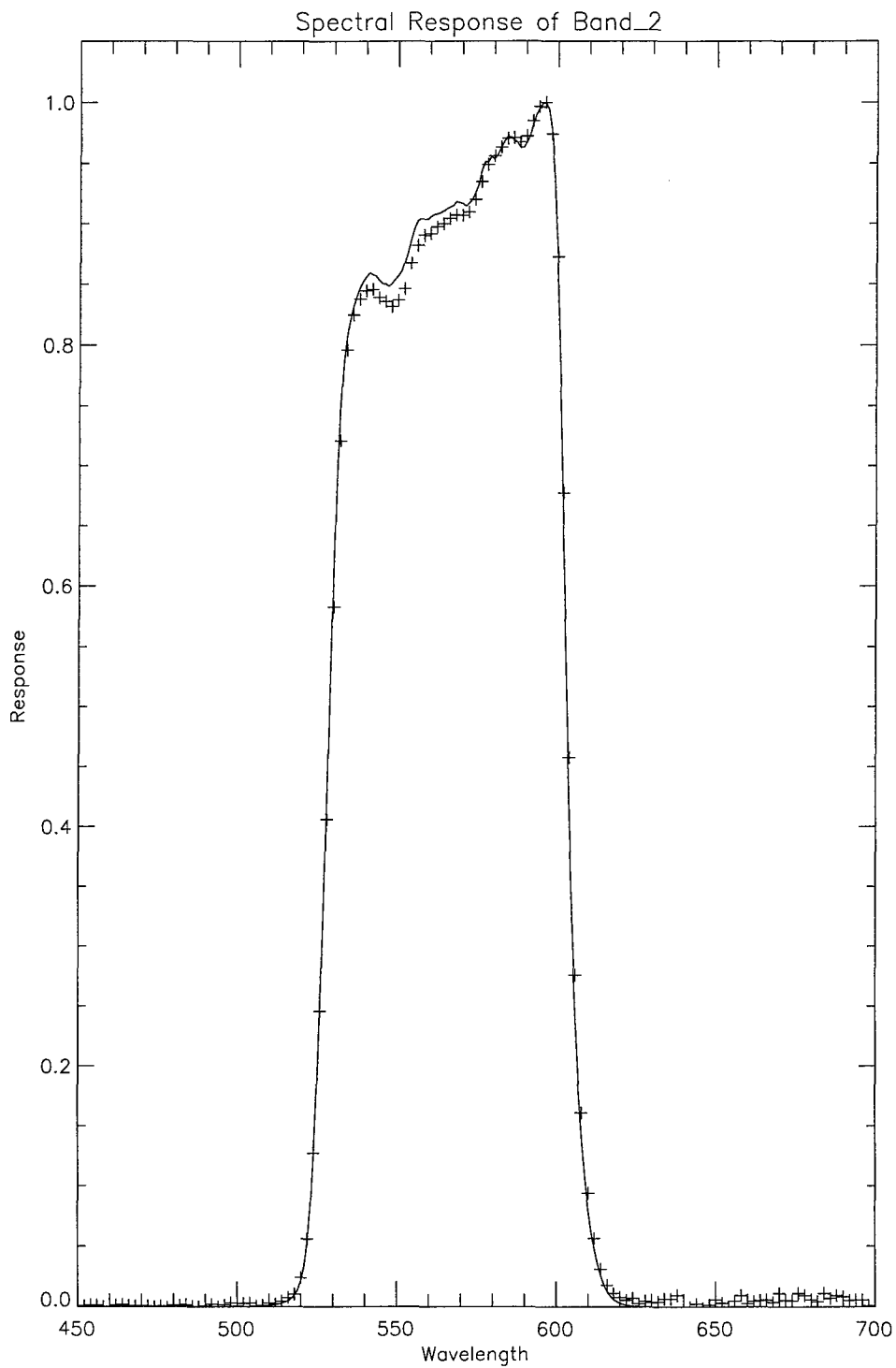


Figure 3-62. Spectral response of band 2. The crosses represent the mean system level measured response for 200 detectors. The solid line represents data collected during subsystem level measurements.

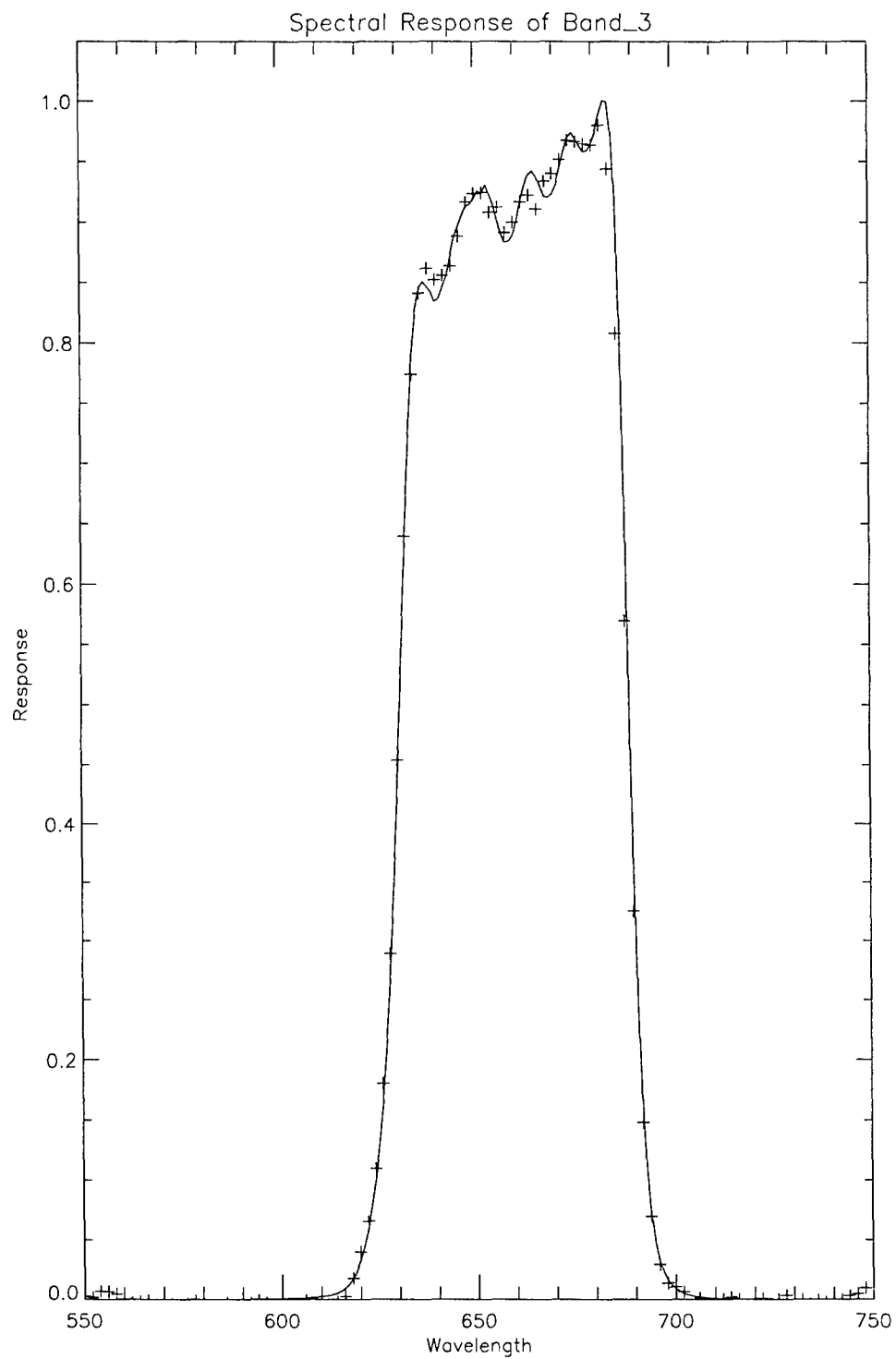


Figure 3-63. Spectral response of band 3. The crosses represent the mean system level measured response for 200 detectors. The solid line represents data collected during subsystem level measurements.

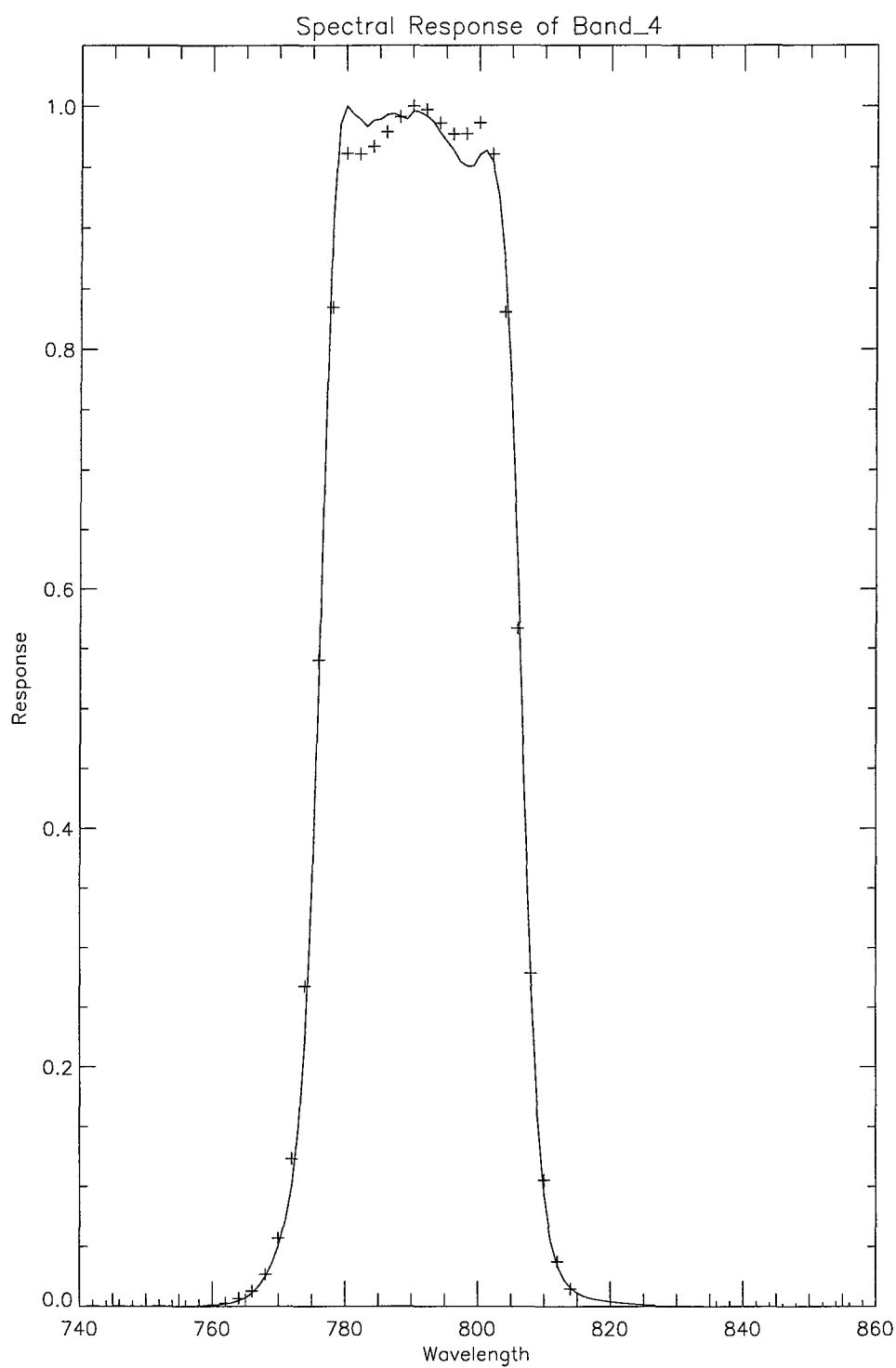


Figure 3-64. Spectral response of band 4. The crosses represent the mean system level measured response for 200 detectors. The solid line represents data collected during subsystem level measurements.

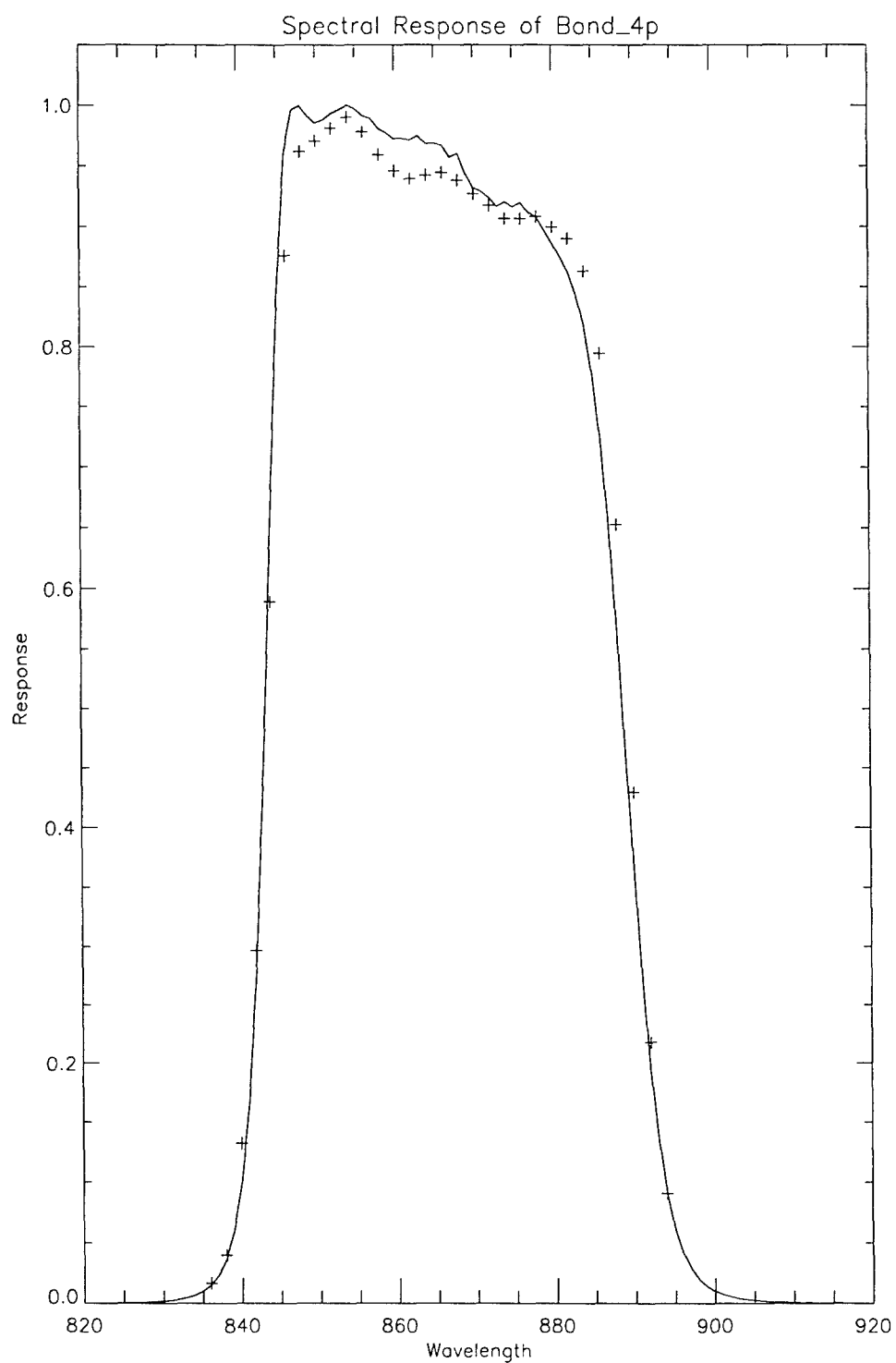


Figure 3-65. Spectral response of band 4p. The crosses represent the mean system level measured response for 200 detectors. The solid line represents data collected during subsystem level measurements.

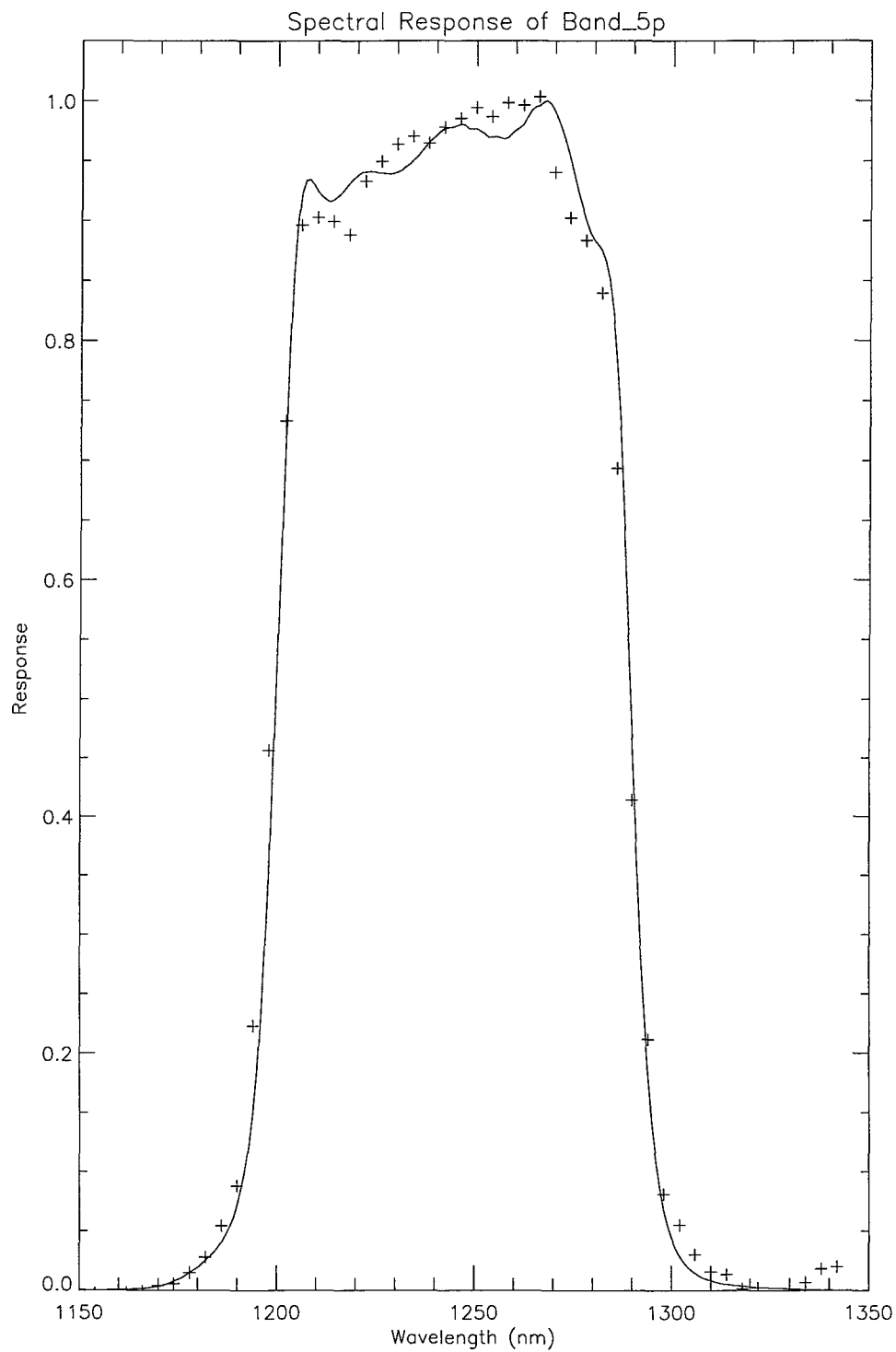


Figure 3-66. Spectral response of band 5p. The crosses represent the mean system level measured response for 200 detectors. The solid line represents data collected during subsystem level measurements.

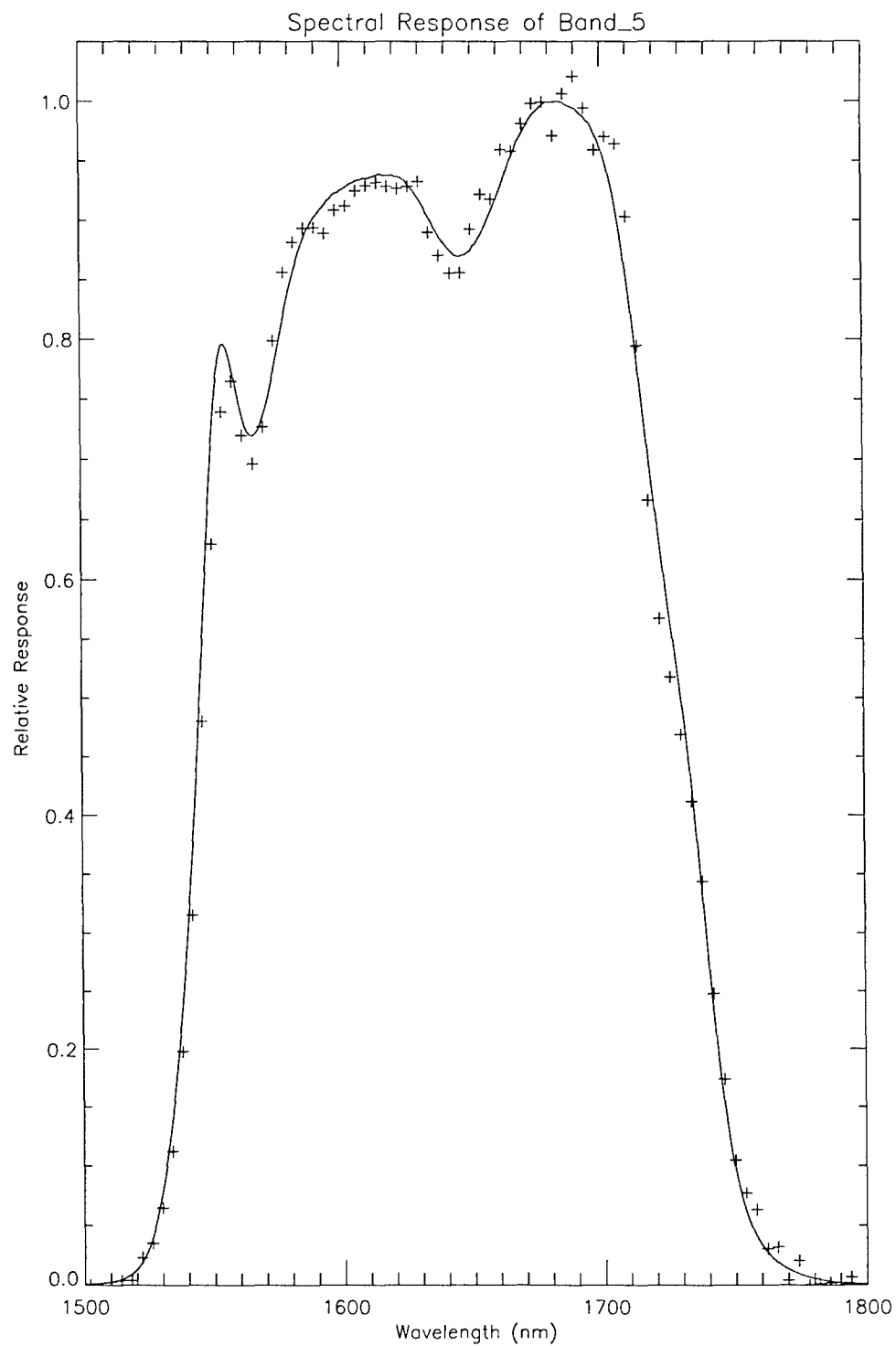


Figure 3-67. Spectral response of band 5. The crosses represent the mean system level measured response for 200 detectors. The solid line represents data collected during subsystem level measurements.

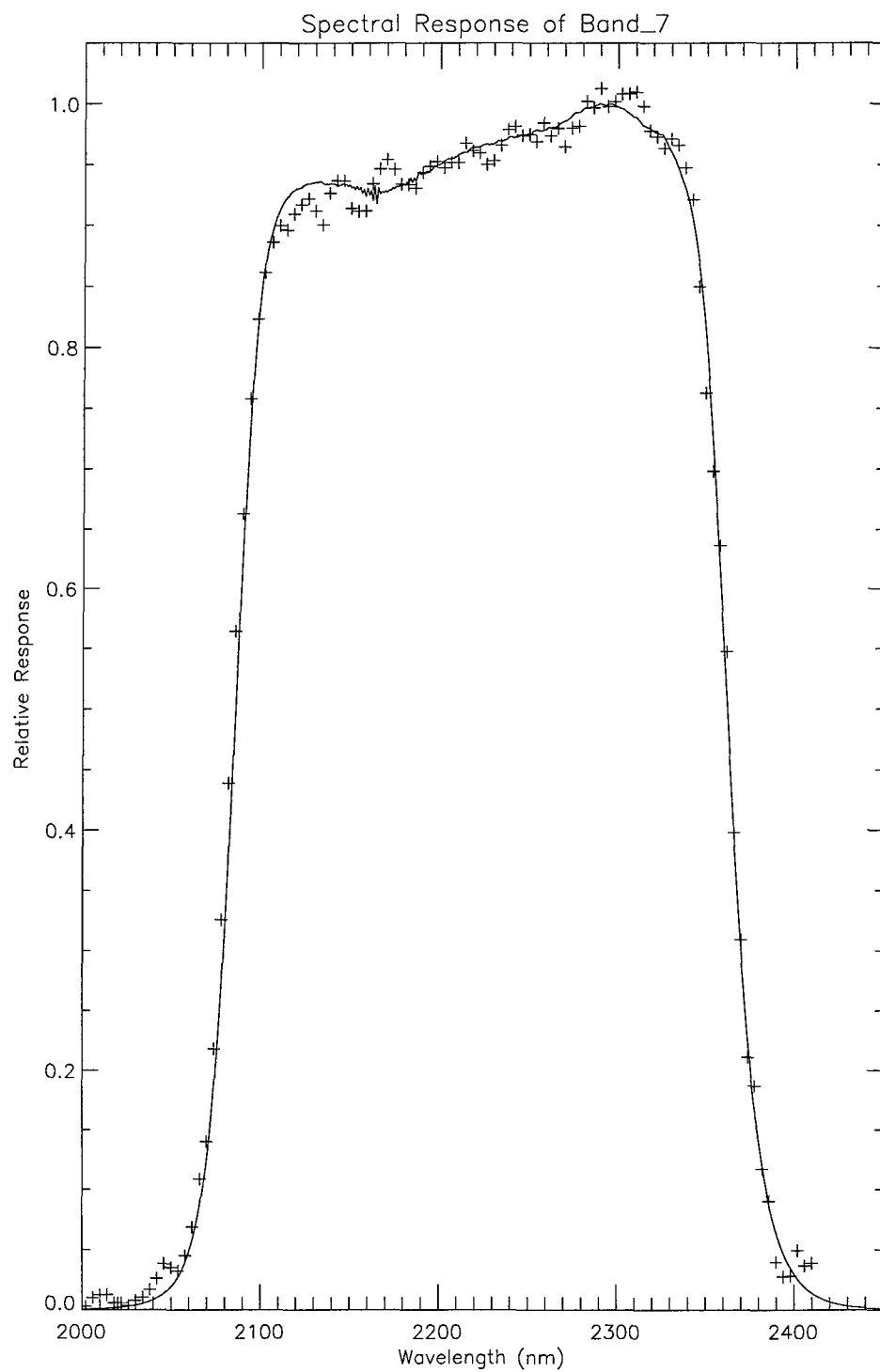


Figure 3-68. Spectral response of band 7. The crosses represent the mean system level measured response for 200 detectors. The solid line represents data collected during subsystem level measurements.

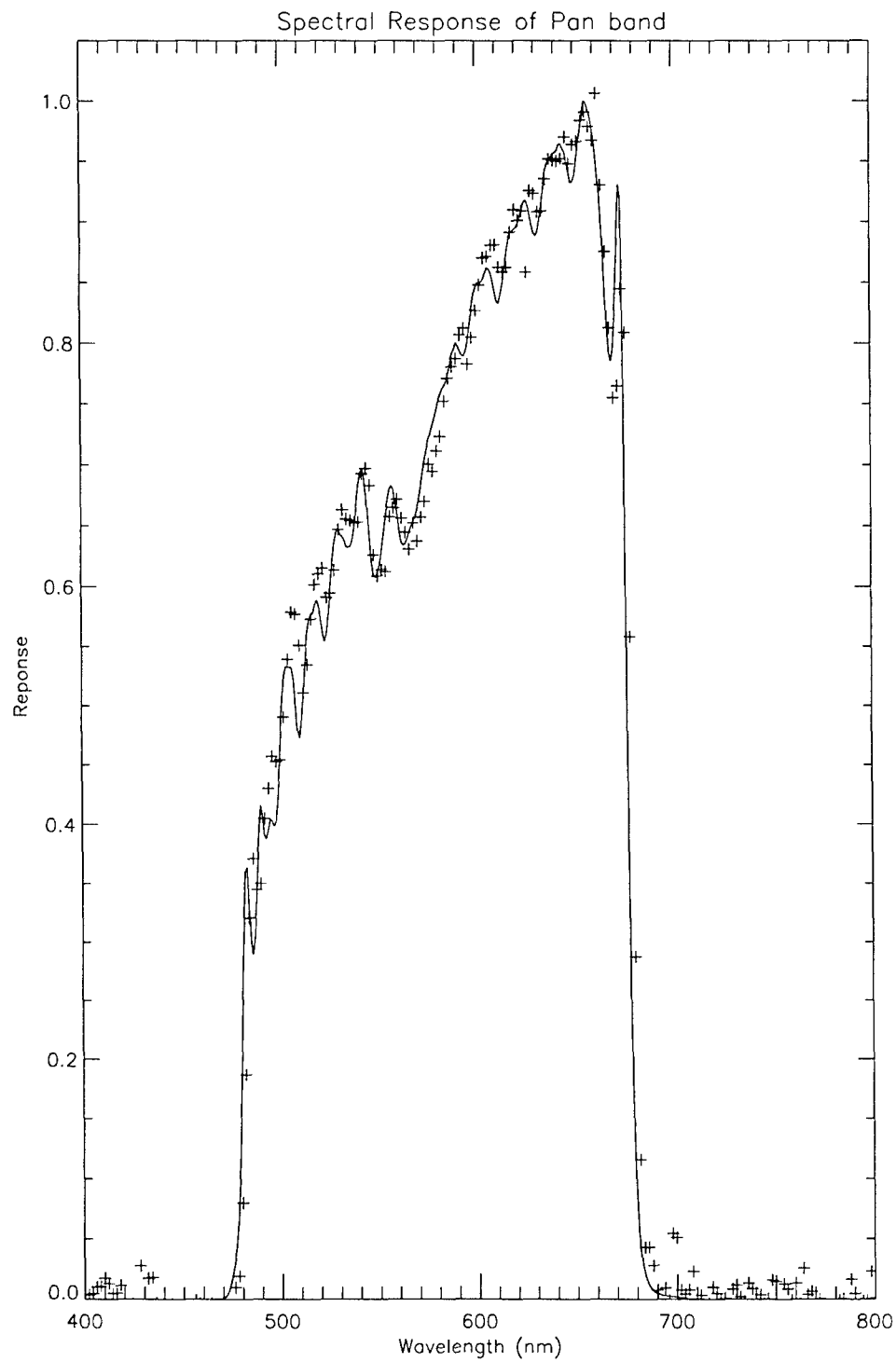


Figure 3-69. Spectral response of the panchromatic band. The crosses represent the mean system level measured response for 200 detectors. The solid line represents data collected during subsystem level measurements.

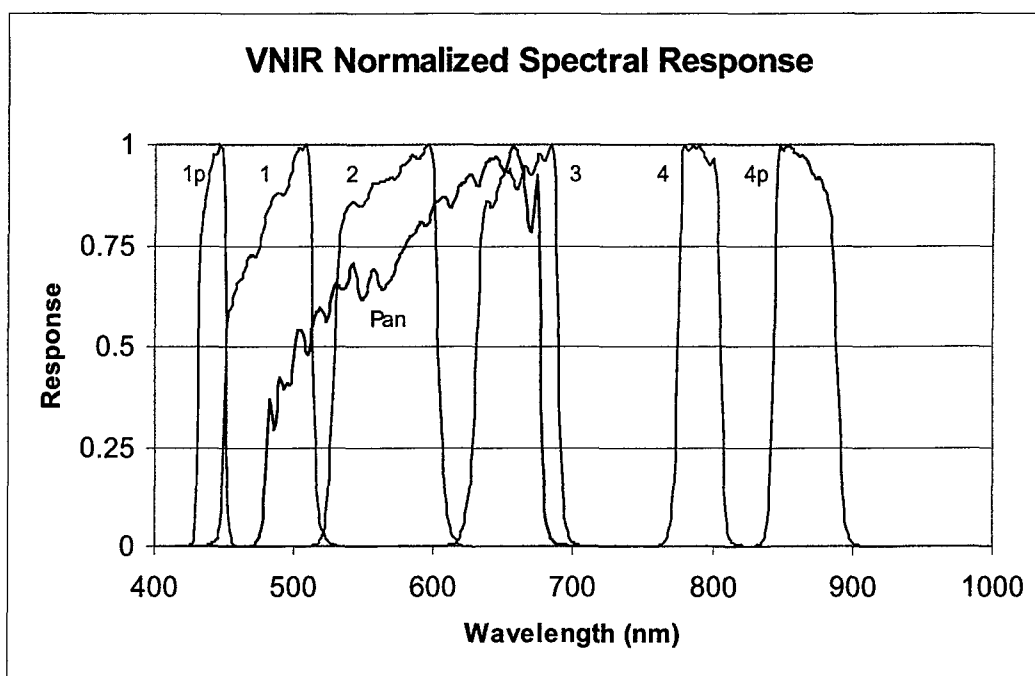


Figure 3-70. Normalized visible and near infrared spectral response functions based on subsystem level measurements.

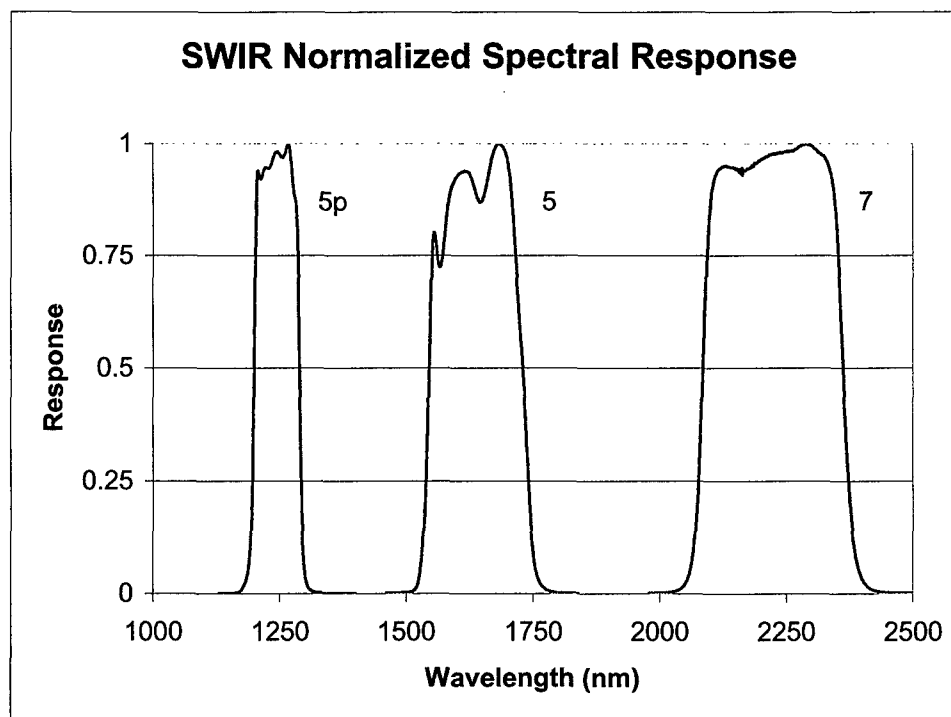


Figure 3-71. Normalized short wave infrared spectral response functions based on subsystem level measurements.

3.1.3.5 Discussion

We find the system level ALI VNIR, SWIR and panchromatic spectral response measurements are in excellent agreement with theoretical models generated from component measurements. We find the spectral response of the ALI to be primarily dependent on the spectral response of the band defining filters lying directly above the focal plane. Detector responsivities also have a small effect on the spectral response of this instrument. This is particularly true for bands with larger bandpasses, such as the panchromatic band. For this band, the gradually increasing efficiency of the silicon material must be accounted for to accurately predict the spectral response of the ALI. Finally, mirror response has little effect on the spectral response of the instrument above 500 nm, providing a global diminution of ~5% which is not a factor when band responses are normalized to unity. However, mirror reflectivities do fall off (down to 80%) below 500 nm and so must be properly accounted for when considering bands in this spectral range.

Response functions have been adopted based on the finer spectrally sampled component measurements as the spectral response of the Advanced Land Imager for the VNIR, SWIR and panchromatic bands. These responses are used to define the spectral bandpass for each band during the analysis of in-flight data. These responses have also been adopted for calculating the in-band radiance of each detector during radiometric calibration of the ALI (see *Earth Observing-1 Advanced Land Imager: Radiometric Response Calibration* [4].)

An Excel file entitled 'EO1_ALI_SPECTRAL_RESP.XLS' has been generated and is available through the GSFC EO-1 Project Office. This file contains the in-band and out of band response of each ALI band.

3.1.4 Radiometric Calibration

This section provides a review of the technique employed during radiometric calibration of the Advanced Land Imager and the results from the characterization of the radiometric response of each detector. Additional information may be found in MIT/LL EO-1-3 Project Report [4].

3.1.4.1 Radiometric Calibration Technique

The technique we have adopted for the measurement of the radiometric response of each ALI detector consists of flooding the entrance aperture with a diffuse source of stable, broadband emission at various radiance levels and recording the output of the focal plane at each level. The source of diffuse emission is a 76.2 cm diameter integrating sphere with a 25.4 cm diameter output port manufactured by *Labsphere Inc.* (Figure 3-72). The sphere contains three internally mounted 150 watt and one externally mounted 125 watt halogen lamps. These lamps provide a combined radiance equal to 100% Earth-equivalent albedo for Bands 3, 4, 4p, 5p, 5, and 7 and the panchromatic band. Four additional externally mounted 300 watt xenon lamps were used to provide 100% Earth-equivalent albedo for Bands 1p, 1, and 2. Eight intermediate radiance levels were obtained through a combination of sequentially extinguishing lamps and de-rating one internal lamp current. Exercising a linear attenuator mounted between the external halogen source and the integrating sphere provided an additional eight levels. This General Purpose Interface Bus (GPIB) commanded slide provided up to 256 aperture variations for an externally mounted source. A similar attenuator was also located between one of the externally mounted xenon sources and the sphere to provide more flexibility in selecting radiance levels for Bands 1p, 1, and 2.

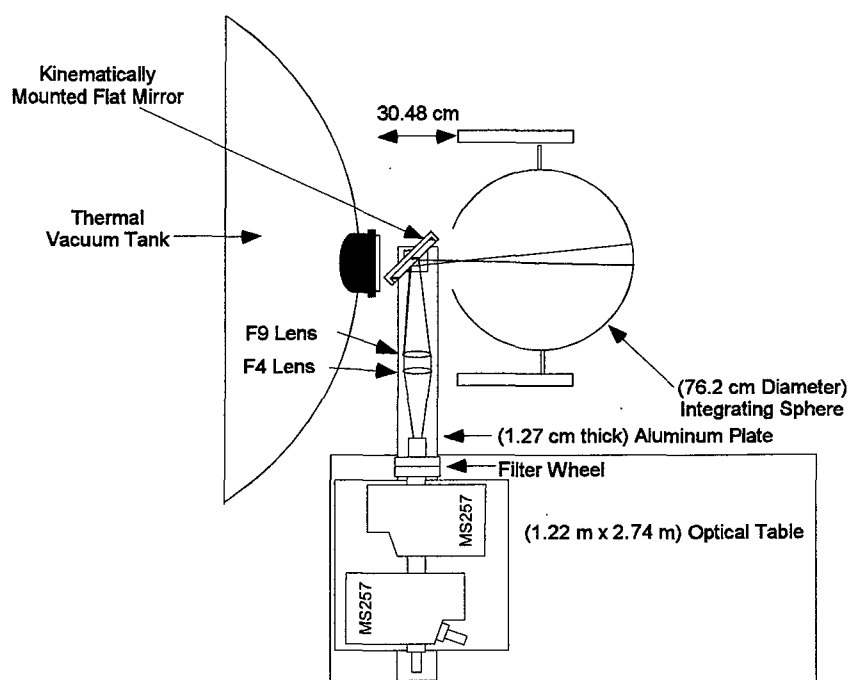


Figure 3-72. Integrating sphere and spectroradiometer used during radiometric calibration of the Advanced Land Imager.

3.1.4.1.1 NIST Traceability

In order to provide absolute radiometric traceability to other sensors, a radiometric transfer standard system was constructed at Lincoln Laboratory (Figures 3-72 and 3-73). The principal components of the system are an irradiance source, traceable to the National Institute of Standards and Technology (NIST), and an *Oriel MS257* monochromator used as a spectroradiometer. The 250 watt irradiance source was mounted on a post with proper baffling to control stray light from the room and reflections from the source off other surfaces. A standard radiance scene was generated by placing a *Labsphere Spectralon* sheet 50 cm from the irradiance source. The monochromator field-of-view was limited to a 6.45 cm² region of the diffuse scene to maintain the traceability of the radiance source. A (15.24 cm) flat mirror was placed between the *Spectralon* diffuser and entrance slit of the monochromator for convenient location of the source. Alternately scanning the radiance scene produced by the standard lamp and various radiance levels output by the large integrating sphere, radiometric NIST traceability was established for the Advanced Land Imager. Additional near real-time monitoring of the sphere radiance level was accomplished by mounting the flat mirror on a (30.48 cm) post between the vacuum tank window and the integrating sphere. During radiometric calibration of the ALI, the mirror was removed and the response of the focal plane recorded. Between ALI data collections, the mirror was kinematically mounted on an aluminum bar, redirecting a portion of the sphere radiance into the entrance slit of the spectroradiometer. The radiance of the integrating sphere was measured from 300 to 2500 nm

in 10 nm intervals with 5 nm full-width-half-maximum resolution. Finally, silicon and germanium detectors, mechanically mounted to the sphere wall, provided continuous broadband monitoring of the sphere stability.

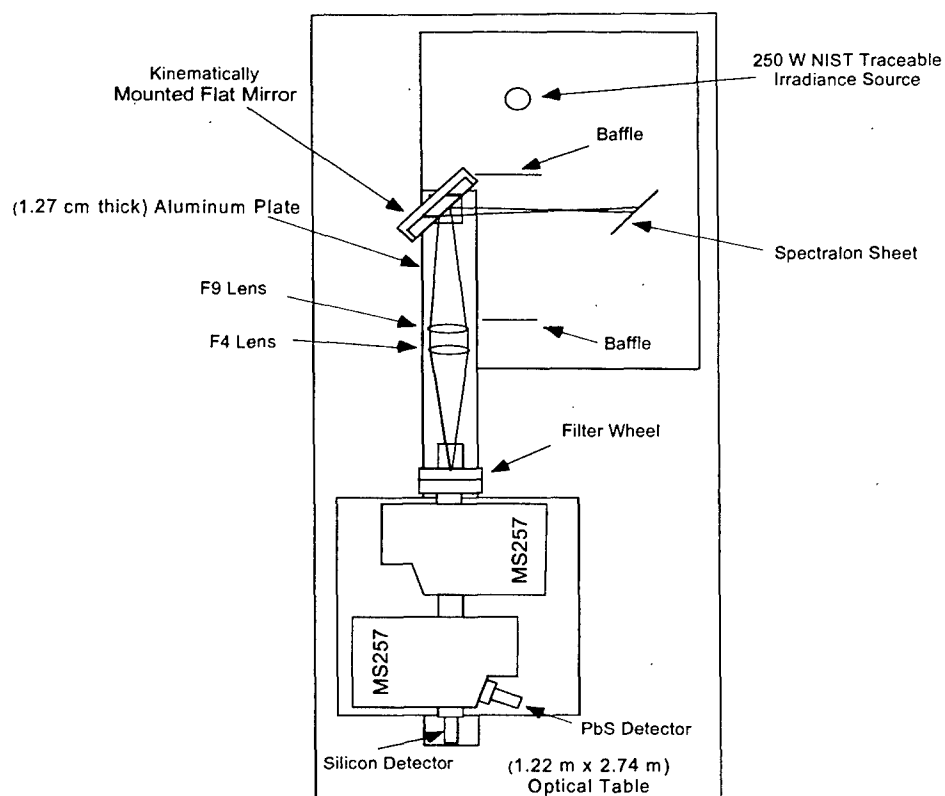


Figure 3-73. Radiometric transfer standard system built at Lincoln Laboratory.

3.1.4.1.2 Error Budget

A listing of contributing errors to the radiometric calibration technique at three wavelengths is provided in Table 3-16. The dominant factor in the VNIR spectral range is the NIST standard lamp. Near 1300 nm the repeatability of the lead sulfide spectroradiometer detector dominates the uncertainty in the measurement, followed closely by the standard lamp. Finally, at 2000 nm, the standard lamp again provides the largest degree of uncertainty in the measurement.

Table 3-16
Radiometric calibration error budget

Source	1 σ Error (%)		
	600 nm	1300 nm	2000 nm
NIST Standard Lamp	0.875	0.94	1.535
Spectralon Panel	0.67	0.67	0.67
Spectroradiometer Repeatability	0.67	0.67	0.67
Spectroradiometer Detectors	0.67	1.0	1.0
Integration Sphere Repeatability	0.33	0.33	0.33
Integrating Sphere Uniformity	0.67	0.67	0.67
Vacuum Window Transmission	0.33	0.67	0.67
ALI repeatability	0.33	0.33	0.33
Total (sum in quadrature)	1.7%	1.97%	2.32%

3.1.4.2 Data Collection

Radiometric data were collected in January 1999 in a Class 1,000 clean room at Lincoln Laboratory. This calibration was conducted with the ALI as a fully assembled instrument in a thermal vacuum chamber at operational temperatures.

Selection of the integrating sphere radiance level and monitoring of radiance stability was coordinated by the ALI Calibration Control Node (ACCN), a LabVIEW-based personal computer operating on a Windows 95 platform. Commanding and housekeeping monitoring of the ALI was also controlled by the ACCN via a Goddard Space Flight Center-provided RS2000 Advanced Spacecraft Integration and Systems Test (ASIST) computer. Data acquisition was performed by a Unix-based Electrical Ground Support Equipment (EGSE1) computer. A Silicon Graphics Performance Assessment Machine (PAM) stored and processed focal plane data in real time for quick look assessment.

For each radiance level selected, the sphere was allowed to stabilize for one hour. A spectroradiometric scan of the sphere output from 300–2500 nm was then conducted after placing a flat mirror between the sphere exit port and vacuum tank window to redirect the beam into the monochromator. After the mirror was removed, the response of the focal plane was recorded for several integration periods [0.81 (0.27), 1.35 (0.45), 1.89 (0.63), 2.97 (0.99), 3.51 (1.17), and 4.05 (1.35) milliseconds for MS (Pan) detectors]. Finally, the ALI aperture cover was closed and reference dark frames were recorded for identical integration periods.

Data were collected with the ALI illuminated by a combination of halogen sources only, a combination xenon sources only, and a combination of halogen and xenon sources. Additional data were collected using the halogen sources only with the focal plane operating at two other possible operating temperatures (215 K and 225 K) to assess the effects of temperature on focal plane response.

3.1.4.3 Analysis

Analysis of the radiometric response of the Advanced Land Imager has been divided into three categories: VNIR, *leaky*, and SWIR. The VNIR and SWIR analysis was separated due to the differing detectors used in these bands (silicon for VNIR, HgCdTe for SWIR). The *leaky* detector category refers to Band 2 of SCA 4 and Band 3 of SCA 3. Odd detectors of Band 2, SCA 4 exhibit substantial electrical cross-talk when detector 1149 is illuminated. Similarly, even detectors of Band 3, SCA 3 exhibit substantial electrical cross-talk when detector 864 is illuminated. An empirical correction methodology has been developed to effectively remove all traces of the cross-talk and transfer detector responses of these bands into units of radiance. As a result, calibration results for odd detectors of SCA 4 Band 2 and even detectors of SCA 3 Band 3 will not be reviewed in this section (See Section 3.1.1.4 for details of the leaky detection algorithm).

For VNIR and SWIR data, a linear function was fitted to the response of each detector to incident radiance after subtraction of the dark current. This fit may be expressed as

$$L_{\lambda}(B, I) = B_p [P_{illum, I} - P_{dark, I}].$$

Here, $L_{\lambda}(B, I)$ is the incident band weighted spectral radiance for Band B and sphere level I, B_p is the radiometric calibration coefficient for detector P ($\text{mW}/\text{cm}^2/\text{sr}/\mu\text{DN}$), $P_{illum, I}$ is the illuminated detector digital response for sphere level I, and $P_{dark, I}$ is the dark detector digital offset.

$L_{\lambda}(B, I)$ was calculated knowing the output radiance of the integrating sphere, the spectral response of each band, and the spectral transmission of the vacuum tank window. This may be expressed analytically as

$$L_{\lambda}(B, I) = \frac{\int L_{\lambda}(\lambda, I) T_w(\lambda) S(b, \lambda) d\lambda}{\int S(b, \lambda) d\lambda}$$

Here, $L_{\lambda}(\lambda, I)$ is the spectroradiometrically measured output radiance of the sphere for level I, T_w is the spectral transmission of the vacuum tank window, and S is the normalized spectral response for Band B. The spectral response of each band used in this analysis was determined during the spectral calibration of the ALI (see *Earth Observing-1 Advanced Land Imager: Spectral Response Calibration* [7]).

An example of a linear fit to the data for detector 100 of Band 3 is provided in Figure 3-74. In this figure, 20 radiance levels were used to fit the detector response. The top graphic is an overlay of the data points and best-fit linear function (the fit was anchored at zero incident radiance by inserting a synthetic data point of zero digital number (dn) for all detectors). The bottom graphic provides the errors to this fit for all radiometric levels. We find all VNIR, SWIR, and panchromatic radiometric response fits to agree with measurements to within $\pm 3.5\%$ (peak to peak). This is within the error budget specified in Table 3-16.

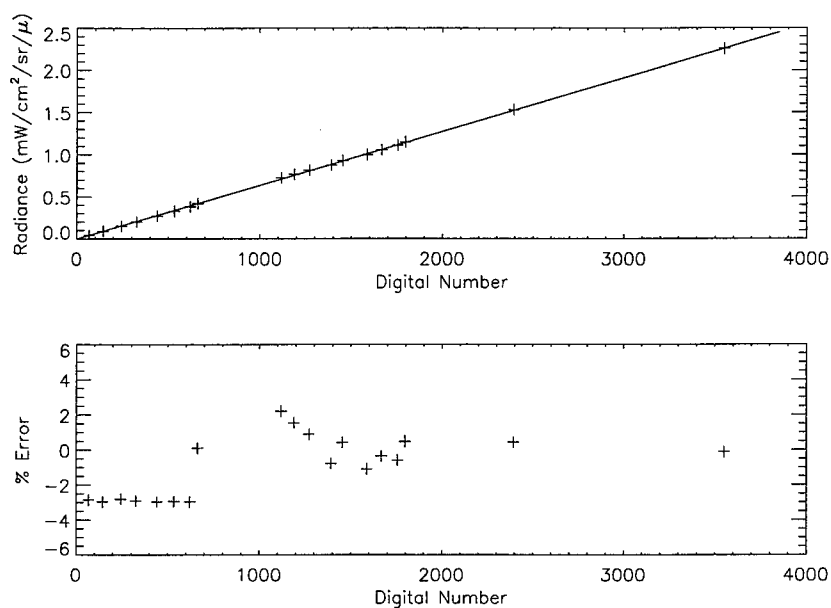


Figure 3-74. Example of linear fit to Band 3 detector 100 data.

3.1.4.4 Results

The radiometric response of each detector of every band was derived individually using the method defined above. From this calibration, the response coefficient, signal-to-noise ratio, saturation radiance, and dynamic range of the ALI focal plane have been determined. We report the results for a nominal integration time of 4.05 ms (1.35 msec for the Pan) and a focal plane temperature of 220 K.

The response coefficient of each band is provided in Figures 3-75 to 3-84. Detectors 0 through 319 belong to SCA1 (outboard), detectors 320 through 639 to SCA2, detectors 640 through 959 to SCA3, and detectors 960 through 1279 to SCA4. SCA-to-SCA and detector-to-detector variability are evident in these figures.

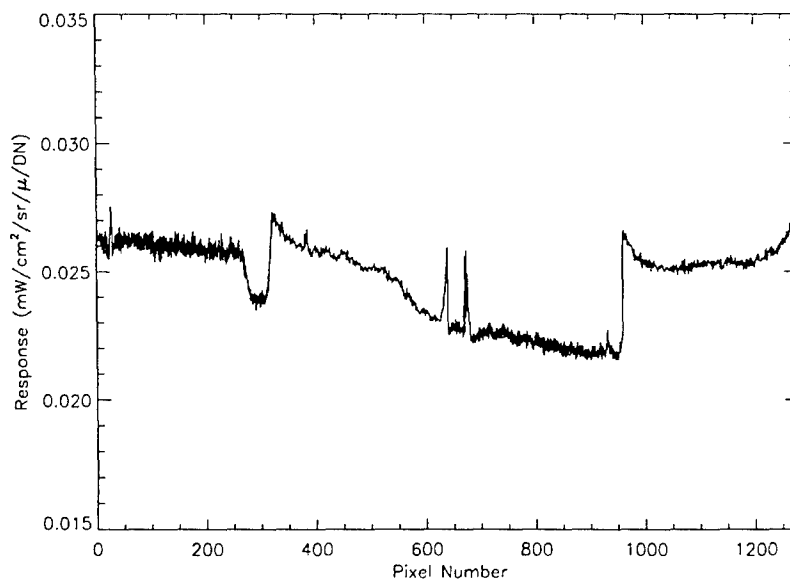


Figure 3-75. Radiometric calibration coefficients for Band 1p.

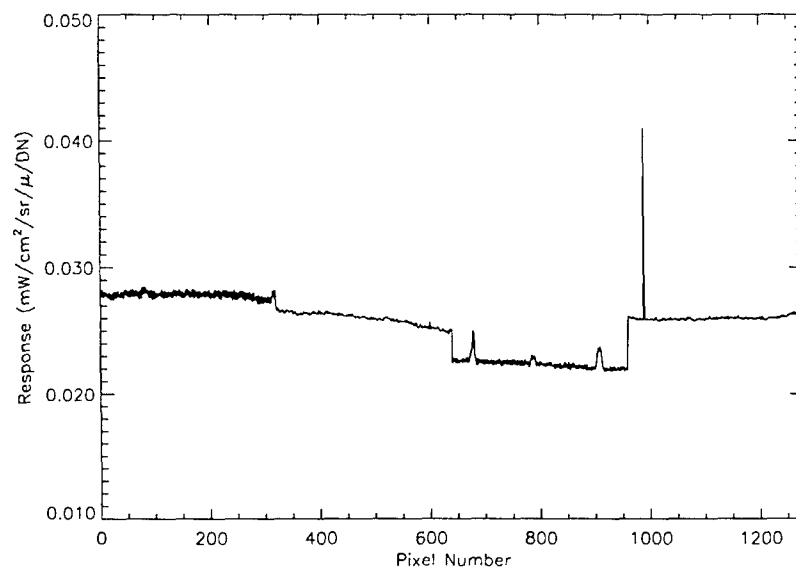


Figure 3-76. Radiometric calibration coefficients for Band 1.

Detector 989 of Band 1 has also been identified as having excessive dark current.

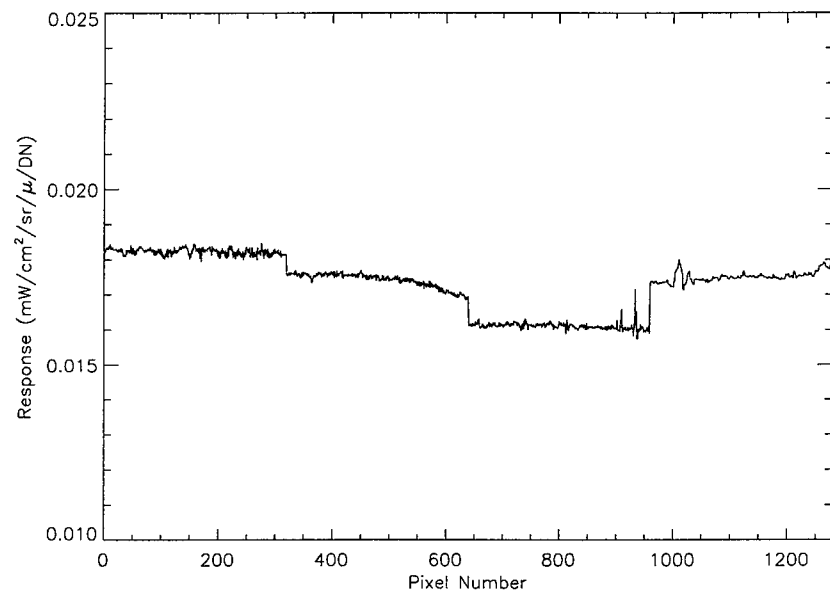


Figure 3-77. Radiometric calibration coefficients for Band 2.

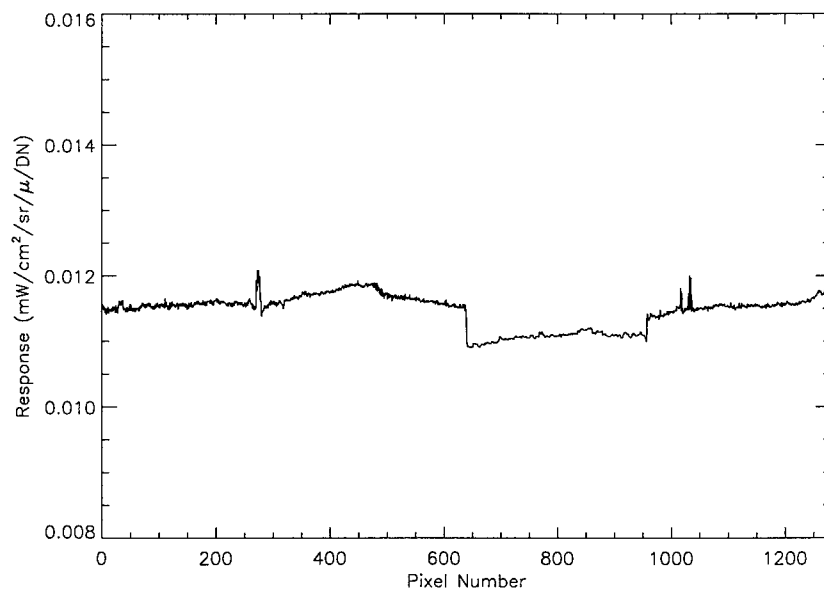


Figure 3-78. Radiometric calibration coefficients for Band 3.

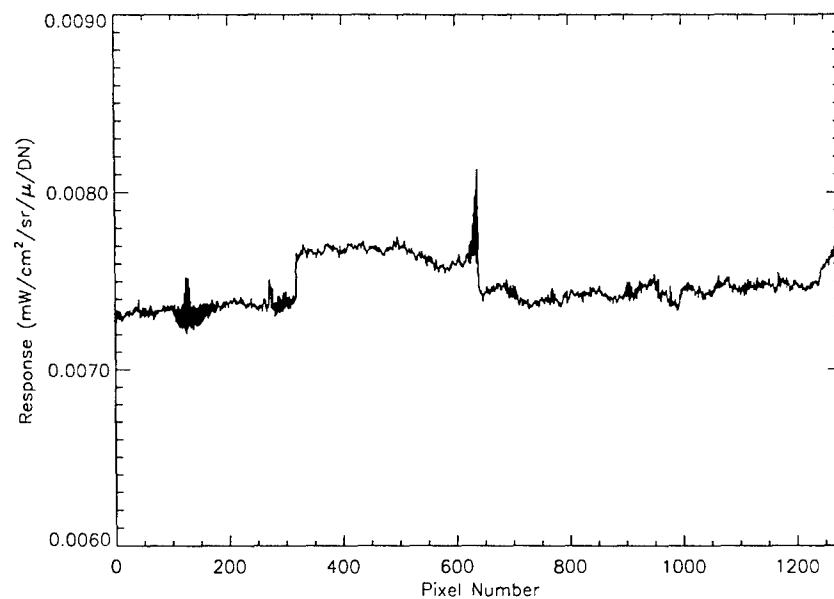


Figure 3-79. Radiometric calibration coefficients for Band 4.

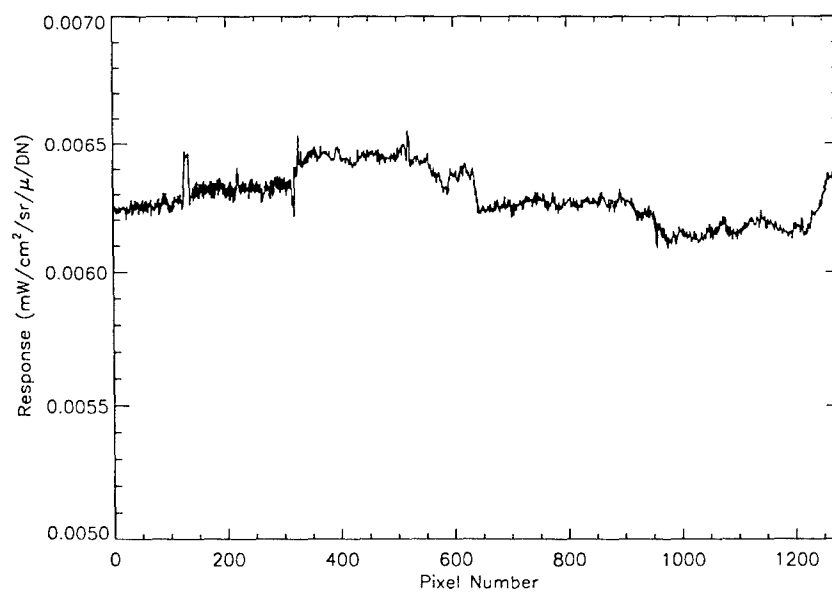


Figure 3-80. Radiometric calibration coefficients for Band 4p.

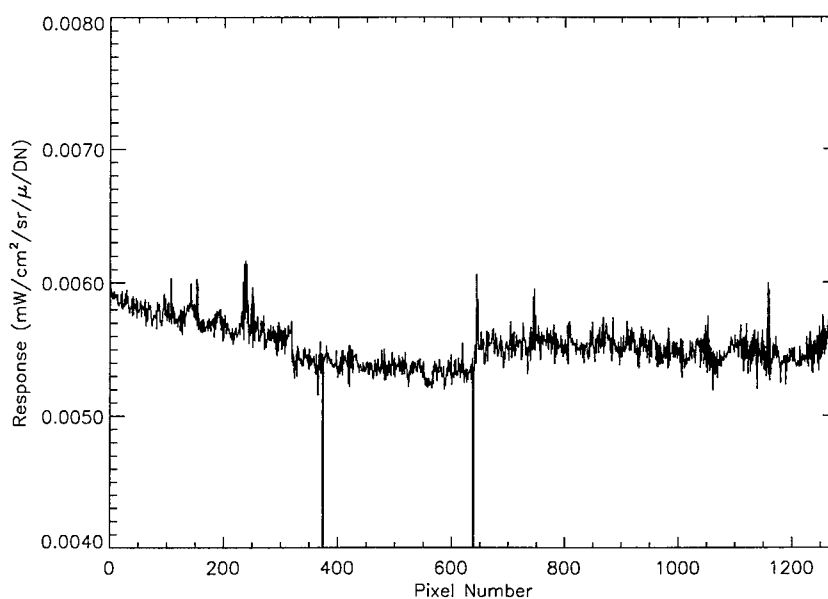


Figure 3-81. Radiometric calibration coefficients for Band 5p.

Detectors 374 and 638 of Band 5p have been classified as *inoperable detectors* that are saturated at all times. Detector 365 has a larger than average dark current value.

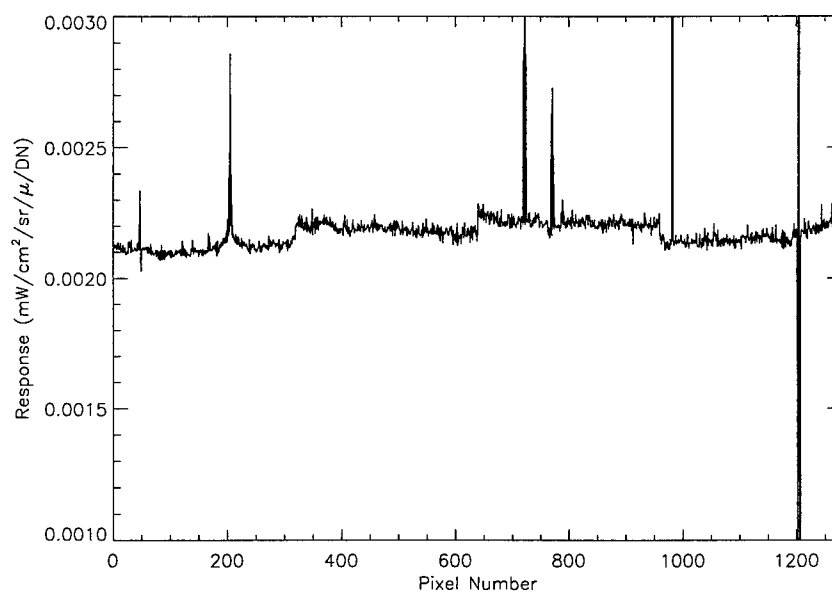


Figure 3-82. Radiometric calibration coefficients for Band 5.

Detectors 982, 1202, 1204, and 1206 are inoperable detectors.

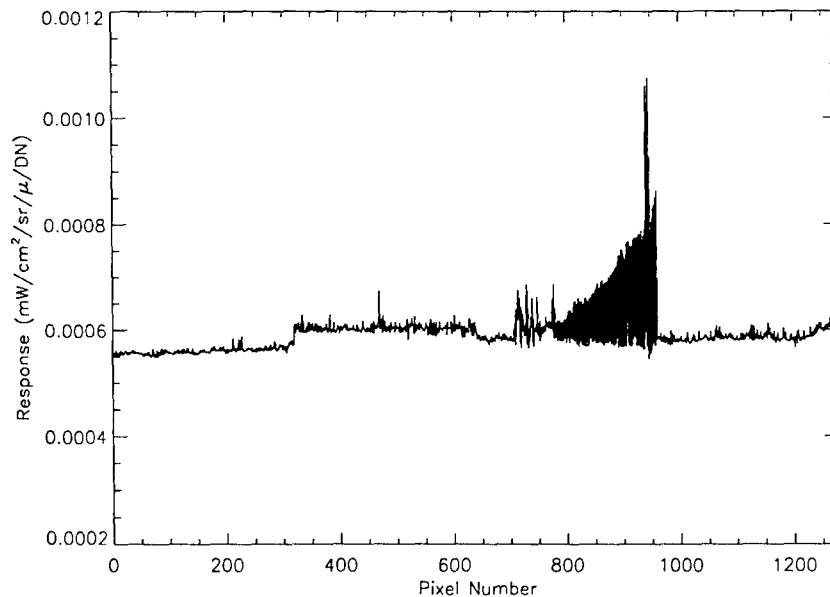


Figure 3-83. Radiometric calibration coefficients for Band 7.

The large differences present between odd and even detector calibration coefficients for SCA3 detectors 800-960 are not associated with any unusual noise or dark current characteristics of Band 7.

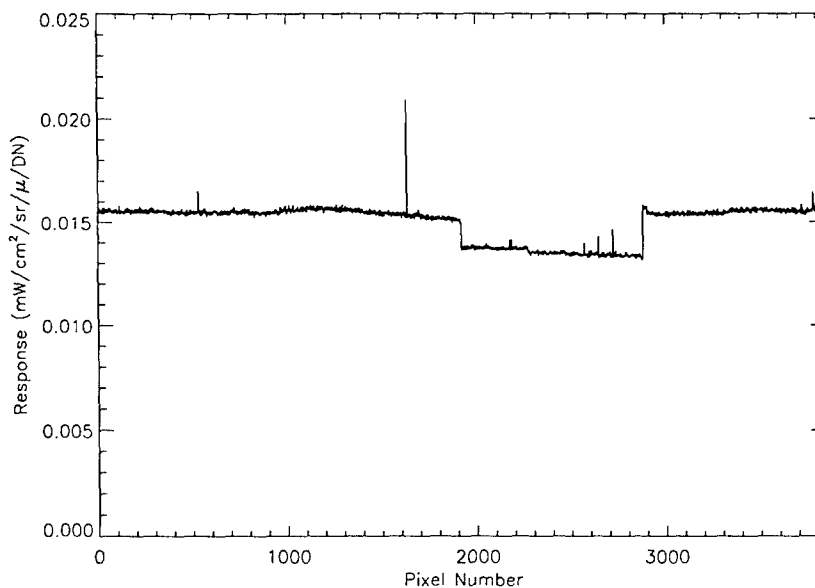


Figure 3-84. Radiometric calibration coefficients for the Panchromatic Band.

Detector 1631 of the panchromatic band has also been identified as having excessive noise.

3.1.4.5 Internal Reference Lamps

An internal reference source, located within the instrument telescope cavity, is used as a radiometric stability monitoring tool on orbit. This source consists of three Welch Allyn 997418-7

(modified) gas-filled lamps mounted on a small (2.03 cm) diameter integrating sphere (Figures 3-85, 3-86). Light emerging from the exit slit of the sphere passes through a BK 7 lens and infrared filter, is reflected off the ALI flat mirror, and floods the focal plane. The response of the ALI focal plane to these sources has been correlated to ground radiometric calibration. Additionally, extensive stability and lifetime testing for spaceflight operation was conducted at Lincoln Laboratory, and these sources have also been shown to be stable to within 1-2% over the two-year period between ground calibration and launch of the spacecraft.

Daily in-flight radiometric checks of the instrument are conducted by observing these internal reference sources. Following each observation, after the aperture cover has been closed, the three internal reference lamps are powered by the ALI Control Electronics. After an eight-second stabilization period the lamps are sequentially powered down in a staircase fashion, with two-second exposures between each step. In this manner, the focal plane receives a three point radiometric reference after each observation.

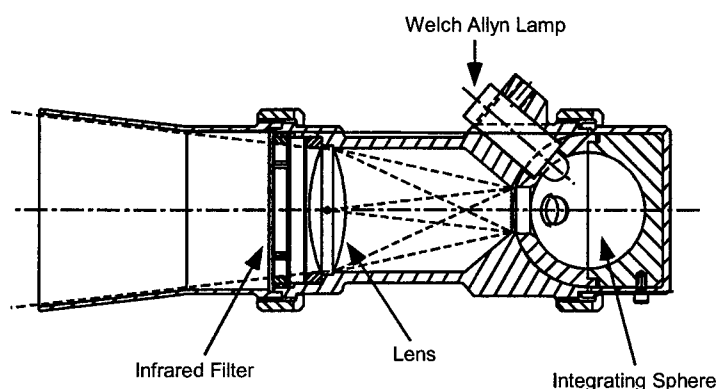


Figure 3-85. EO-1 ALI internal reference source.

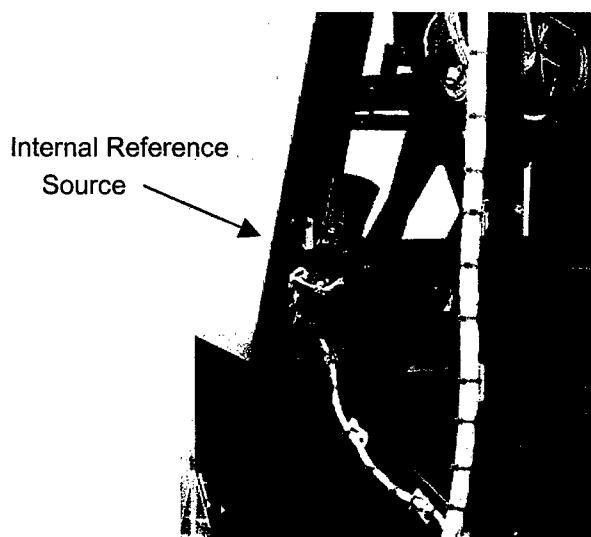


Figure 3-86. Photograph of internal reference source.

3.1.4.6 Discussion

The radiometric response of the Earth Observing-1 Advanced Land Imager has been calibrated during ground testing at MIT Lincoln Laboratory. This calibration includes the investigation of the response, signal-to-noise ratio, saturation radiance, and dynamic range of each detector of every spectral band.

The results obtained in the analysis outlined in this report, along with results from the *leaky detector* analysis (Section 3.1.1.4), have been incorporated into the calibration pipeline and are being used to radiometrically calibrate ALI flight data. As an example of this calibration, Figure 3-87 depicts a Band 4 image of Lincoln Laboratory before and after radiometric calibration is applied. Detector-to-detector and SCA-to-SCA variations, a result of dark current and response coefficient variations, are clearly evident in the data prior to calibration.



Figure 3-87. Band 4 image of Lincoln Laboratory. The image on the left is prior to radiometric calibration. The image on the right is after radiometric calibration.

Finally, the results presented here are being compared against data collected during on-orbit internal reference lamp monitoring and solar, lunar, and vicarious calibrations to track changes in ALI radiometric response over the lifetime of the mission (Section 3.2.2).

3.2 ON-ORBIT TEST VALIDATION

The objective of on-orbit test validation is to show that the technology performs on-orbit as well as it did before launch. This is to verify that the conditions of the launch or the orbital environment do not significantly degrade the performance. For the Advanced Land Imager, we divide the on-orbit test validation into the spatial and the radiometric performance categories. Spatial validation of the ALI technology consists of demonstrating that the instrument yields clear, sharp images that may be accurately registered with features on the ground. Radiometric validation is to show that the in-band radiances reported in the radiometrically-corrected (Level 1R) data accurately represent the top-of-the-atmosphere radiances of the scene imaged.

3.2.1 Spatial Validation

The major aspects of spatial validation are to verify the modulation transfer function (MTF) and the detector lines of sight.

3.2.1.1 Modulation Transfer Function

The MTF, or spatial transfer function (STF) which we prefer to use, was extensively calibrated at Lincoln Laboratory before integration with the spacecraft, as described in Section 3.1.2. In the laboratory, it is possible to present a precisely defined object to the instrument, and to sample the image data much more finely than is done on-orbit. Our approach to MTF validation on-orbit is to use the spatial calibration data to simulate the instrument response to simple models of certain well-defined objects imaged from space. The simulated response is then compared to the actual response. If the two match well, the MTF is validated.

Objects that we have used to date for MTF validation are bridges, the moon, and stars. Bridges can provide a roughly uniform strip of radiance contrasting with the uniform darker water on either side. The lunar limb presents a sharp edge against dark space. Bright stars are essentially point sources that yield the instrument's point-spread function, albeit at a low sampling frequency.

An example of a bridge scan is shown in Figure 3-88. It is the Bronx Whitestone Bridge, seen in a scan of New York City on March 20, 2001. The dotted rectangle delineates the pixels we used to test the MTF of the ALI. Those pixels were projected onto an axis perpendicular to the bridge. The result is shown in Figure 3-89. The radiance along that axis was modeled as a step function, including the bridge, the water on each side, and the shadow of the bridge on the water. The expected system response to this model was computed using the spatial transfer function from our laboratory calibration. After an initial estimate of the radiances and edge locations was made, those parameters were refined by performing a least-squares fit of the computed response to the average projected pixel data. The resulting fitted response is shown in Figure 3-90. The close agreement between the fitted response and the pixel data indicates the validity of the calibrated STF.



Figure 3-88. Portion of the panchromatic image of New York City, scanned on March 20, 2001.

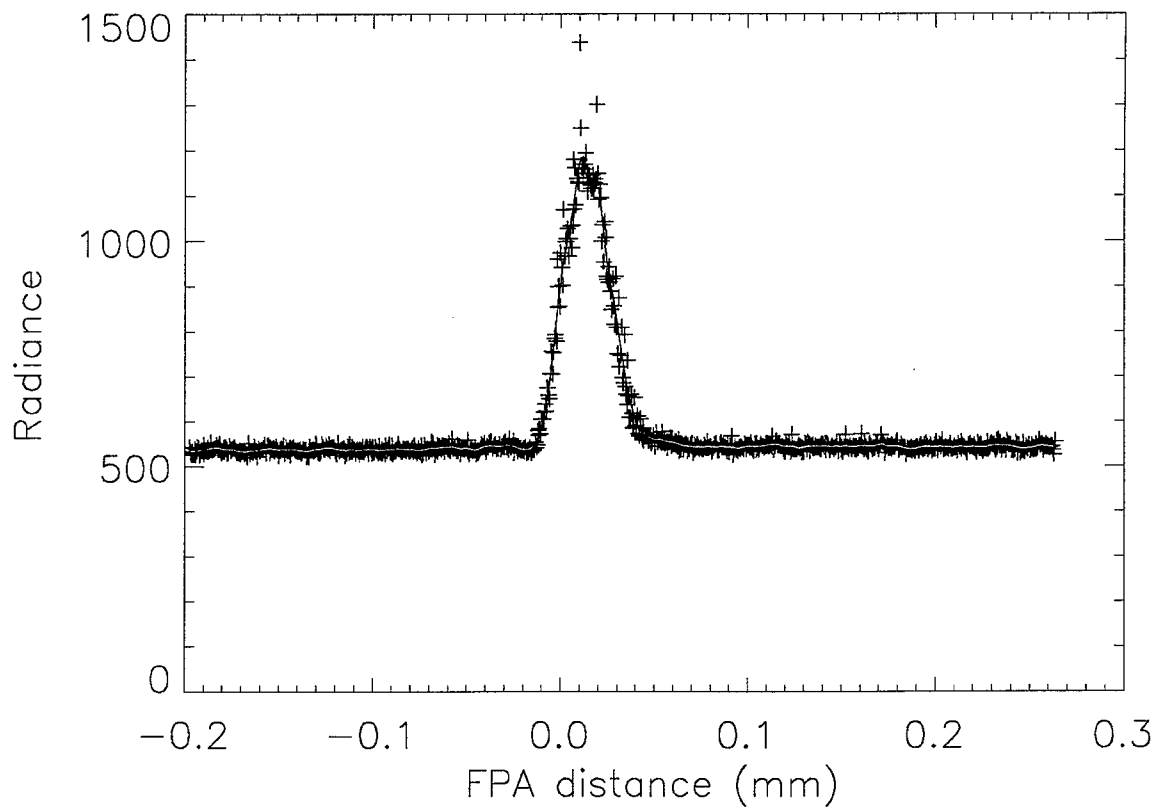


Figure 3-89. Panchromatic radiances of the region of interest shown in Figure 3-88, projected to the axis perpendicular to the Bronx Whitestone Bridge. Crosses are the individual pixel data, and the curve represents a slightly smoothed average of the radiance vs. distance.

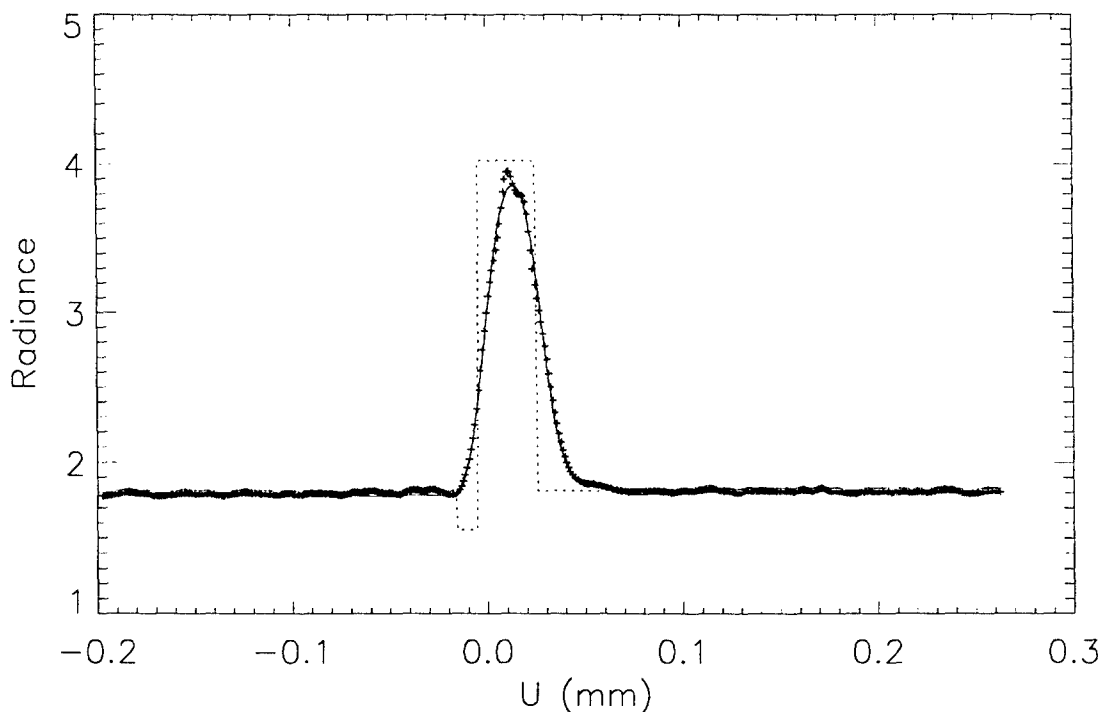


Figure 3-90. Radiance profile of the Bronx Whitestone Bridge. The crosses are the average panchromatic image data shown as the curve in Figure 3-89. The dotted lines show the fitted radiance model, and the smooth curve is the computed instrument response.

As a further check on the model, the apparent width of the bridge was compared to the actual width as reported on a website (<http://www.nycroads.com/crossings/bronx-whitestone/>). To make certain of the scale of the image, the distance from the bridge to a small point of land on Throgs Neck was measured both in the Pan image (3.013 mm) and on a USGS map of the Flushing quadrangle (2.279 km). The transverse scale factor is .7563 km/mm. The 29.3 μm fitted width of the bridge image corresponds to 22.15 m at the bridge. The reported width is 23.5 m.

A panchromatic image from a lunar calibration scan is seen in Figure 3-91. A small region of interest (ROI) along the southeast limb was selected. As for the bridge image, the pixel radiances in the ROI were projected onto an axis perpendicular to the limb. The result is shown in Figure 3-92. The figure also shows the panchromatic edge spread function computed from the MTF calibration data. Apart from a fall-off of lunar radiance inward from the limb, the agreement is close. In particular, the slope of the edge spread function matches the radiance data very well.



Figure 3-91. Panchromatic image of the first quarter moon, from a lunar calibration scan of Feb. 2, 2001.

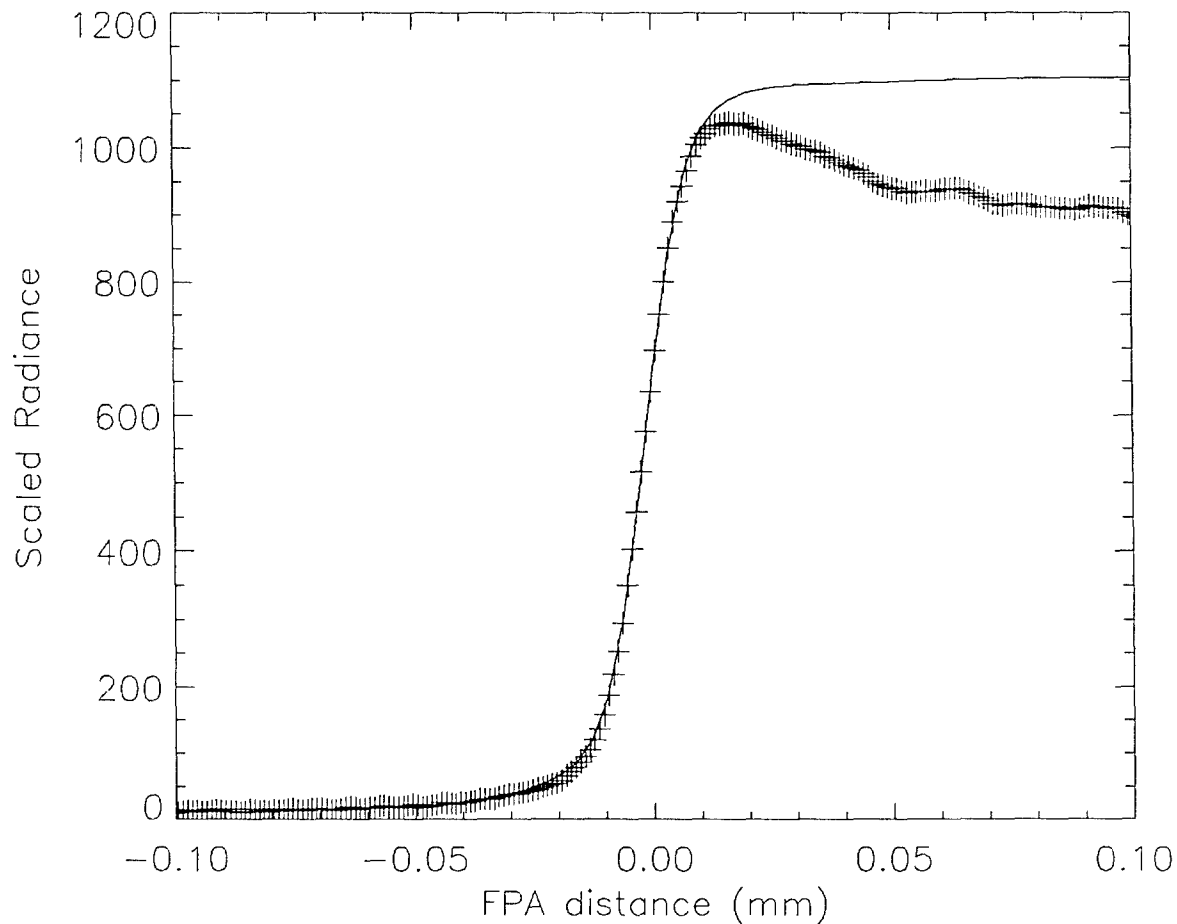


Figure 3-92. Scaled panchromatic radiance of the lunar limb as a function of distance perpendicular to the limb in the focal plane space. The crosses are the averaged data within the ROI, and the smooth curve is the computed ALI edge spread function.

A scan with SCA 4 across the 0.3 magnitude star Vega is presented in Figure 3-93. The scan was performed at one-fourth the nominal angular image speed of Earth scenes. Thus the data are sampled four times per detector height in the scan direction. Figure 3-94 shows the panchromatic radiance profiles through the star in the in-scan and cross-scan directions. The crosses are the calibrated scan data, and the curves represent the point-spread function computed from the MTF calibrations and fitted to the scan data.

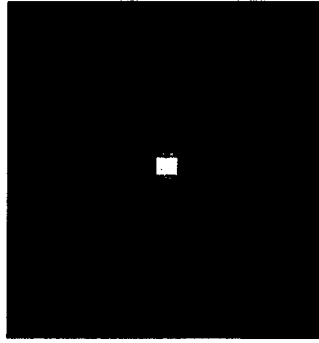


Figure 3-93. Panchromatic image of the star Vega. The scan direction is vertical here.

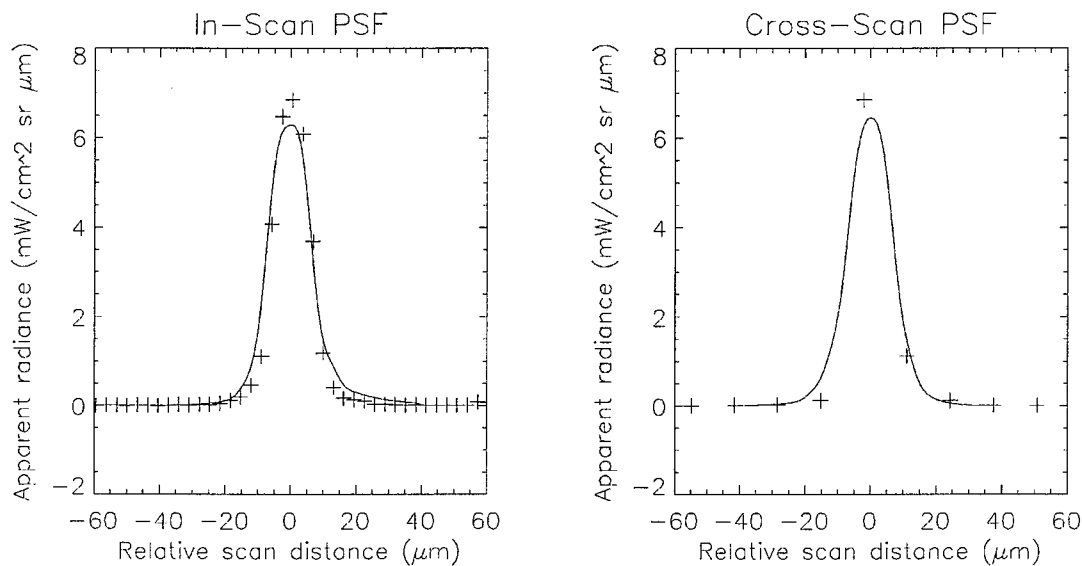


Figure 3-94. Panchromatic radiance profiles of Vega in the in-scan (left) and cross-scan directions. Only one row or column of pixels through the center of the star's image is shown in each case (crosses). The curve is a fitted Pan point-spread function.

In the case of the Vega scan, we observe from Figure 3-94 that the instrument performance may be better than indicated by the laboratory calibrations. The fitted point-spread function appears to be noticeably wider than the actual image. A possible explanation for this discrepancy is that the focus shim of the ALI may not have been cut with the correct wedge angles. During MTF calibration, the focus error was measured at one point of the focal plane array, and this value was incorporated in the MTF model. If the plane of the detectors is actually at a slight angle to the plane of best focus of the telescope, then images will be in better focus for some parts of the array than for others. This warrants further observations of a bright star, crossing different parts of the focal plane array, to ascertain if any truer estimate of the focus term should be incorporated in a revised MTF model.

3.2.1.2 Detector Lines of Sight

To date, the best indication we have of the validity of the detector line-of-sight map is the clarity of multispectral images reconstructed from the radiometrically-calibrated data. An example of these images is seen in Figure 3-95. Close inspection reveals no fringes of color that would indicate a misregistration of the spectral bands. There is also no sign of the boundaries of the individual SCAs. Thus the detector line-of-sight map is valid, at least down to the sub-pixel level.



Figure 3-95. False-color multispectral image of part of the South Island of New Zealand. Seen here are parts of the Rolleston Range, Lake Coleridge, and the Rakaia River. The red, green and blue components represent bands 7, 4, and 2, respectively. In this presentation, snow on the mountain peaks appears light blue, while clouds near the peaks are white.

The process we used to reconstruct images such as that in Figure 3-95 from Level 0 data is as follows: First, a radiometric calibration is performed on all of the data, to produce Level 1R files in HDF format. Next, the speed and direction of the image motion across the focal plane are estimated, assuming that they are constant. This is done by cross-correlating the overlapping portions of the Pan images in neighboring SCAs. The geometric re-sampling procedure reads in the Level 1R data and shifts the odd detector data in time (frame number) to restore synchronous sampling. (This step is necessary because the Data Processing System at GSFC applies an odd/even shift in the Level 0 data to offset the staggered locations of the detectors on the focal plane. That makes the Level 0 and Level 1R data easier to view.) Finally, the re-sampling procedure applies the detector line-of-sight map to re-sample the data to an output image, at the same nominal resolution. The outputs of this process are a Level 1G file in HDF format for each SCA. Another procedure produces browse files in JPEG format for selected triads of multispectral

bands or the Pan band. The JPEG images cover the full swath, and join the SCAs by omitting some redundant pixels that would otherwise overlap.

As previously stated, we see no evidence to date of errors in the detector line-of-sight map. The re-sampled images are clear and seamless. However, a full analysis of the band-to-band registration is yet to be done. If the bands were in perfect registration, then a satisfactory multi-band image could be constructed from the Level 1R data simply by shifting the bands by whole numbers of frames, representing their separations in the scan direction. This would not, however, take into account optical distortions or SCA location errors.

We have indirect evidence that the bands are in good registration. The procedure that estimates the image speed and direction generally finds the speed to be within a few percent of nominal, and the yaw angle to be a few milliradians or less. This is done solely with the Pan data. A multispectral image such as that in Figure 3-95 uses the speed and yaw from this Pan analysis, along with the line-of-sight map to place the other bands. Consider that the band 2 detectors are separated from the band 7 detectors by 4.8 mm in the scan direction. The band 7 detectors of adjacent SCAs are separated by 20.3 mm. Yet even at the line where the SCAs meet in the re-sampled image, the band-to-band and SCA-to-SCA registration is within 0.04 mm. For this to be true, both the line-of-sight map and the speed and yaw estimates have to be valid to better than two parts per thousand. This also indicates that the assumption of constant speed and direction is generally valid.

So far, Lincoln Laboratory has lacked the resources to produce geo-referenced Level 1G images. Our geometric re-sampling has relied on image data alone to estimate speed and yaw, rather than reading spacecraft telemetry. We have just begun to use the telemetry data for the simpler problem of deriving the Right Ascension and Declination of stars that were scanned. Apparent departures from the known positions are of order a few tenths of a degree. The discrepancies could result from pitch and roll offsets between the Attitude Control System (ACS) axes and the ALI axes, and from a temporal offset between the ACS readings and the image frame times. Further work should clear up these differences.

3.2.2 Radiometric Validation

The on-orbit radiometric performance assessment of the Advanced Land Imager consists of deriving radiometric performance characteristics of the instrument and comparing them to measured pre-flight or expected values [8,9]. This assessment not only assists in ensuring the radiometric accuracy of data collected on orbit, but also assesses ground calibration accuracy, cleanliness of the environment during ground testing, and changes of the instrument response induced by the stresses of launch.

Although the absolute radiometric accuracy of all data collected by the ALI is critical for Earth observations, sensitivity, saturation radiance, signal-to-noise ratio, and stray light are also key attributes when assessing the technical merit of this instrument for future Earth observing missions.

3.2.2.1 Sensitivity

The sensitivity of the ALI has been demonstrated by imaging several cities at night. Figure 3-96 depicts a panchromatic image of Las Vegas at night as seen by the EO-1 ALI and the Landsat 7 ETM+ instruments on January 22, 2001. Clearly visible are lights from various hotels and casinos. This scene demonstrates the ALI is capable of detecting events with radiances of $0.033 \text{ mW/cm}^2 \text{ sr } \mu\text{m}$ for this band. Table 3-17 lists the sensitivities of each band, as determined from this image.

The good sensitivity of the ALI also extends the sources of on orbit sensitivity measurements to include extra-Terran planets and stars. When observed from orbit, these sources can serve as ideal extended and point-like sources that may be used for instrument calibration without the troublesome effects of the Earth's intervening atmosphere inherent in all Earth observations. During the first twelve months of operations, the ALI has observed ten stars in the Pleiades star cluster as well as Vega and Rasalhague (Figure 3-97). The result of these measurements has demonstrated the ALI sensitivity to magnitude +6.5. Additional sensitivity observations include Venus, Saturn, and Jupiter (including the Jovian moons Io and Ganymede). Figure 3-97 is a collage of several celestial observations made to date. The stars detected by the ALI are represented as circles in this image.

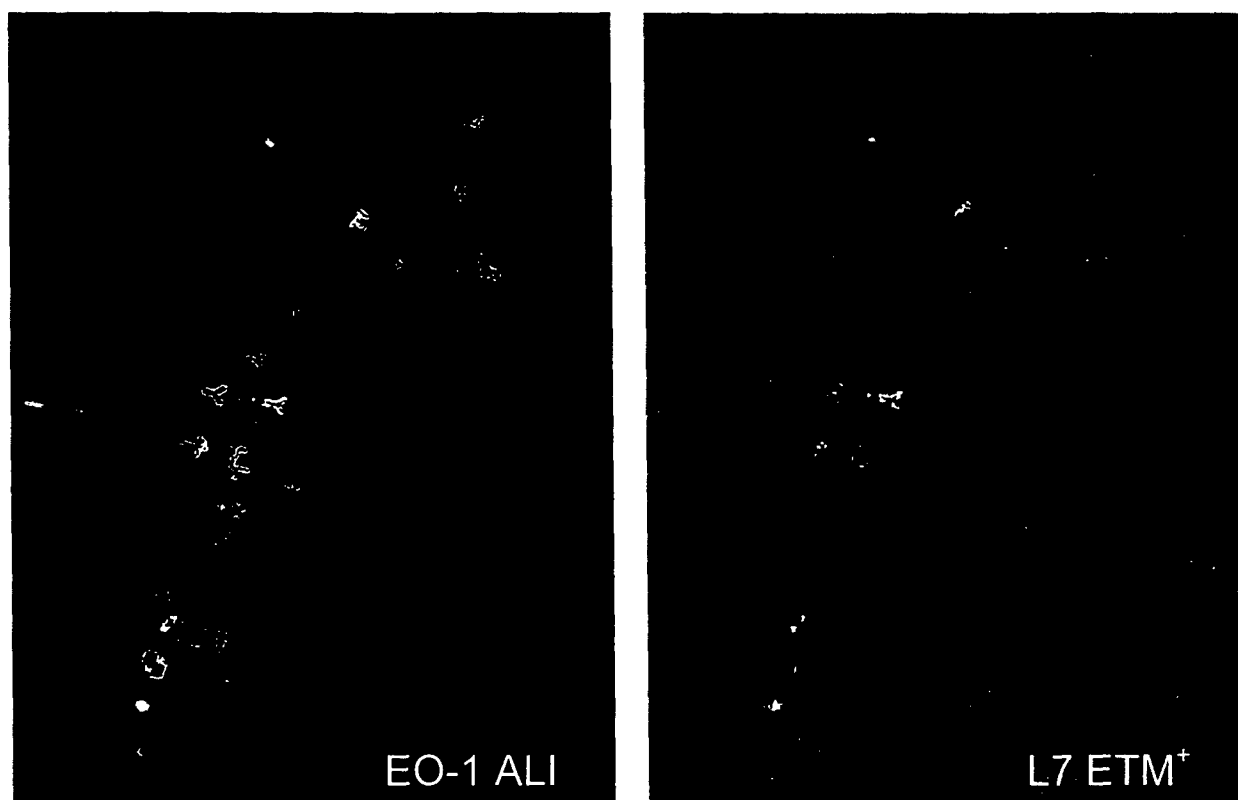


Figure 3-96. Panchromatic image of Las Vegas at night.

Table 3-17
ALI sensitivity

Band	Radiance (mW/cm ² sr μ)
1p	0.067
1	0.067
2	0.067
3	0.033
4	0.013
4p	0.013
5p	0.100
5	0.033
7	0.013
Pan	0.033

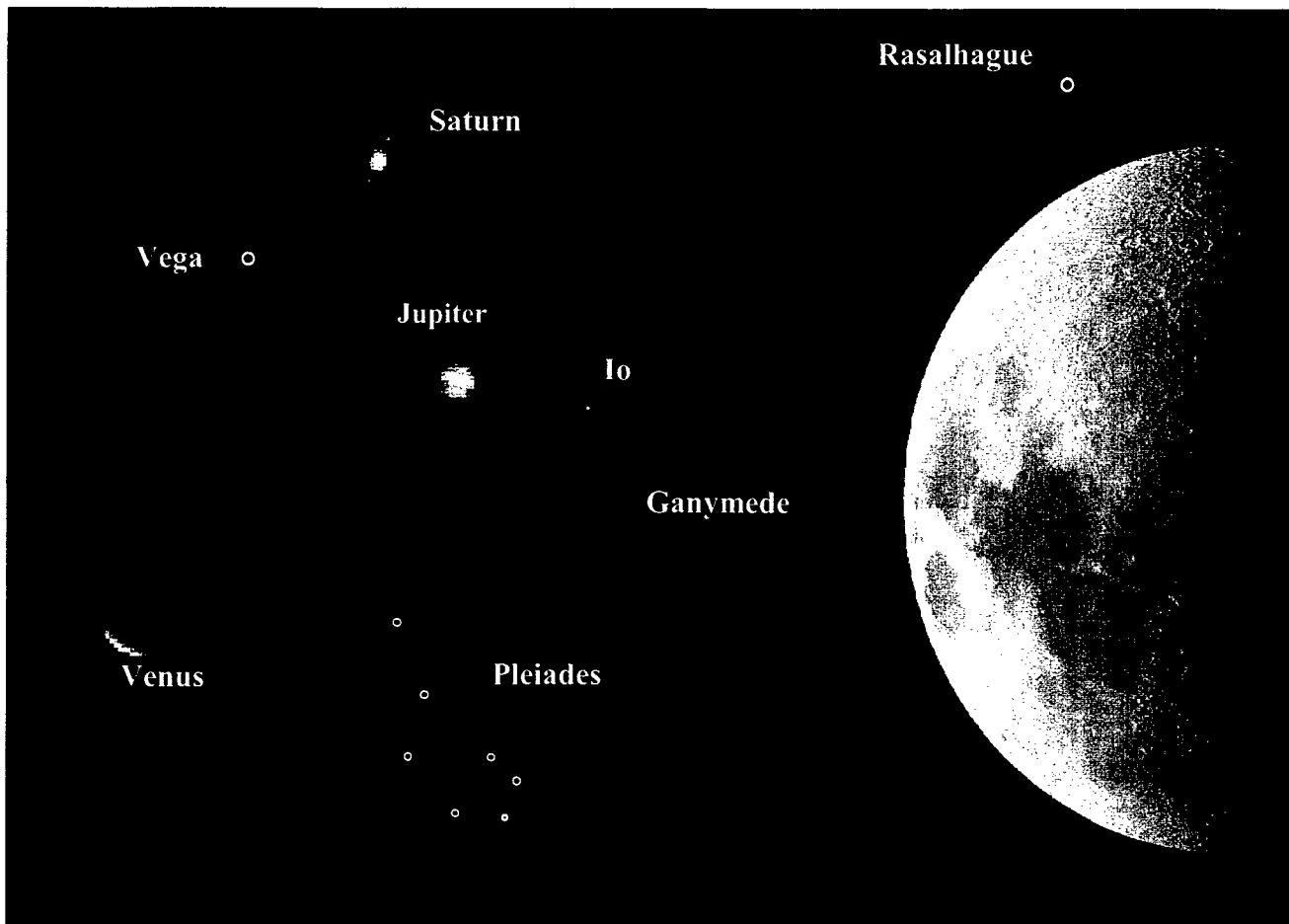


Figure 3-97. Celestial observations performed by the ALI.

3.2.2.2 Saturation Radiance

The ALI was designed such that the focal plane would not saturate for mid-latitude summer scenes with 100% Earth equivalent albedo. These high saturation radiances will allow for the direct observation of clouds, snowfields, frozen rivers, and glaciers. The saturation radiances of the ALI have been checked on orbit by observing scenes with high albedo. Figure 3-98 depicts a Band 4,3,2 ALI observation of Hawaii, HI under partially cloudy skies. Figure 3-99 depicts a Band 4,3,2 image of East Antarctica. In each observation, the high albedo regions are clearly resolved and not saturated. Table 3-18 lists the maximum radiance and number of counts in each band for each scene.



Figure 3-98. Band 4,3,2 image of Hawaii, HI.

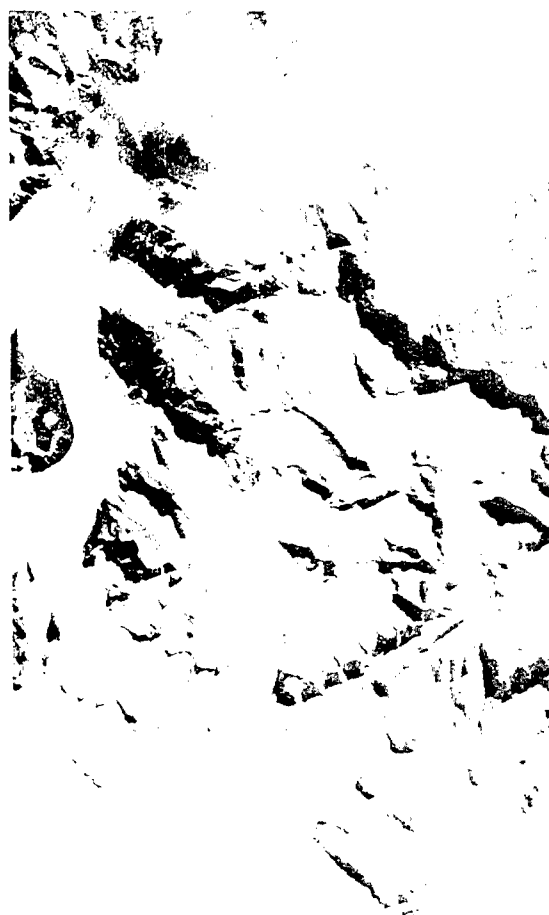


Figure 3-99. Band 4,3,2 image of East Antarctica.

Table 3-18
Response of ALI to high albedo scenes

Band	Hawaii HI (Clouds)		East Antarctica (Ice)	
	Radiance (mW/cm ² sr μ)	Counts ¹	Radiance (mW/cm ² sr μ)	Counts ¹
1p	24.52	1017	15.16	619
1	30.44	1189	18.25	705
2	28.36	1630	15.97	939
3	25.03	2052	13.71	1182
4	20.83	2705	10.68	1424
4p	17.83	2769	8.82	1423
5p	7.92	1492	1.85	342
5	3.43	1573	0.18	82
7	0.76	1246	0.043	72
Pan	27.67	1797	15.19	980

1=Maximum counts = 4095

3.2.2.3 Signal-to-Noise Ratio

The focal plane of the ALI has been designed to provide a signal-to-noise ratio for each band between four and ten times that of the Landsat ETM+. To check signal to noise ratios on-orbit, we have selected three regions of a data set, collected as a part of the on-orbit solar calibration sequence, representing low, medium, and high albedo scenes. Initially, these data are radiometrically calibrated using calibration coefficients derived during ground testing of the instrument at Lincoln Laboratory. Next, regions of constant radiance are identified. The signal to noise ratio for each region is then calculated for each band. Table 3-19 lists the derived signal to noise ratios for all bands.

Table 3-19
Signal to noise ratio for varying radiances

Band	Radiance*	SNR	Radiance*	SNR	Radiance*	SNR
1p	4.78	151	14.79	339	34.92	520
1	5.55	245	17.08	572	41.1	1263
2	5.11	310	16.10	1001	38.28	1536
3	4.29	343	13.37	1039	31.99	1933
4	3.34	358	10.44	722	25.03	1123
4p	2.80	350	8.73	710	20.93	1145
5p	1.40	263	4.42	662	10.66	1258
5	0.68	341	2.15	1040	5.13	1606
7	0.22	274	0.68	912	1.63	1636
Pan	4.82	215	15.04	348	36.01	703

* mW/cm² sr μ

3.2.2.4 Stray Light

The stray light of the ALI may be divided into three components: mirror scatter, black paint scatter, and filter scatter. The mirror and black paint scatter affect large regions (>3 degrees) and will be discussed first. The filter scatter affects much smaller regions (<0.25 degrees) and is discussed later.

3.2.2.4.1 Mirror and Black Paint Scatter

For a technology demonstration instrument, the first ALI optical fabrication priority was to produce mirrors with correct figuring to achieve the required image sharpness over the full 15×1.3 degree field of view. Mirror finish was lower on the priority list. The SiC mirrors produced by SSG Inc. for the ALI were of excellent figure quality but constrained by EO-1 programmatic considerations (budget, schedule) in obtaining optimum BRDF performance [10,11]. Based on mirror BRDF measurements performed by SSG Inc. and Schmitt Measurement Systems and analysis by Lambda Research Corp. [12], the EO-1 SiC mirrors did not meet the EO-1 adopted Landsat 7 specification for scattered light. It was concluded by the EO-1 project office [10,11] that the ALI telescope mirror surface quality was reasonably good and comparable to other Earth sensing instruments and that the full set of NMP technology validation objectives for ALI were realizable without additional mirror polishing. Lincoln Laboratory proceeded with integrating the ALI and performed a thorough instrument system calibration.

A separate NASA funded technology program was conducted by SSG Inc., which demonstrated component level BRDF consistent with the Landsat 7 stray light specification. Silicon clad SiC aspheric optics and uncoated SiC flat optical surfaces were demonstrated to have BRDF, which met all requirements. Multiple optics were demonstrated, including a full scale, ALI spare primary mirror.

3.2.2.4.1.1 Stray Light Modeling

A methodology for assessing the effect of telescope stray light on the measurement of scene radiance has been developed, based on a generalization of the Stray Light Analysis Report No. 3 by Lambda Research [12]. The analysis also included the effects of the reflective baffle, which defined the aperture stop, at the secondary mirror. The black paint used on the baffle was Aeroglaze Z-306. The stray light contribution from this effect amounted to 1%. The results provide a useful and simple tool for estimating the effects of stray light.

Assumptions:

1. The scene geometry is the same as for the Landsat specification, consisting of a large annular background region surrounding a small circular target region.
2. The scattered background radiance falling into the target region is due to both mirror scatter [12] and scatter from the reflective baffle. The major contribution from mirror scatter comes from approximately 3 degrees around the target region. The contribution from the black reflective baffle is defined as 1% of a 10-degree background region, centered on the target.
3. The fraction of background radiance falling into the target region is a constant.

4. The fraction of target radiance that is scattered out is also a constant and is the total integrated scatter (TIS) from the referenced report.
5. The radiometric calibration is based on a very low spatial frequency standard, e.g., a large extended near field source.

Definitions:

L_B = The true background radiance

\hat{L}_B = The estimated background radiance

L_T = The true target radiance

\hat{L}_T = The estimated target radiance

ΔL_T = The uncalibrated target radiance error due to the telescope stray light

ΔL_B = The calibrated background radiance error due to the telescope stray light

σ_B = The fraction of background radiance falling into any target region

σ_T = The total fraction of radiance that is scattered from any portion of the scene

ϵ = The scattering parameter

The resulting radiance errors are:

$$\Delta L_B = \hat{L}_B - L_B = 0$$

$$\Delta L_T = \hat{L}_T - L_T = [\sigma_B / (1 - \sigma_T + \sigma_B)] [L_B - L_T]$$

$$\Delta L_T / L_T = \epsilon [L_B / L_T - 1.]$$

Table 3-20
Stray light parameters

Band	$\sigma_T(\%)$	$\sigma_B(\%)$	$\epsilon(\%)$
Pan	6.5	3.6	3.5
MS-1	15.5	7.6	8.3
MS-2	10.9	5.5	5.8
MS-3	7.6	4.1	4.2
MS-4	4.4	2.7	2.7
MS-5	0.9	1.3	1.3
MS-7	0.5	1.2	1.2

This model suggests that stray light may be an issue for measurements on dark regions near very large and very bright regions and conversely for small bright scenes surrounded by large dark regions. This is especially true at the shorter wavelengths.

3.2.2.4.1.2 On-Orbit Stray Light Characterization

Two types of data have been used to characterize the ALI stray light performance on-orbit: limb scans and nominal Earth scenes containing uniform regions. The limb scans were used to evaluate the off-axis scatter of the ALI mirrors and black paint. The Earth scene data were compared to Landsat 7 ETM+ and ground truth data to evaluate the impact of stray light for a variety of scene contrasts.

3.2.2.4.1.2.1 Limb Scans

The off-axis stray light characteristics of the ALI have been investigated by scanning the Earth's limb across the telescope field of view. Four limbs scans were performed in 2001, scanning in the +pitch, -pitch, +roll, -roll directions. For each observation, the instrument begins collecting data with the Earth completely filling the ALI FOV. The instrument is then pitched or rolled until the Earth's limb is 50° off-axis and the ALI is viewing deep space. A plot of an individual detector's response over time traces the transition from Earth observing to space observing events. The Earth limb profile for a +roll scan as viewed by detector 100 for Band 3 is depicted in Figure 3-100.

The Earth's limb is located at the -7° position (angle of the detector FOV relative to the boresight). An instrument with zero stray light effects will observe a limb profile that is the product the limb's natural illumination falloff with altitude and the instrument edge spread function. The expected limb profile is overlaid in Figure 3-100. The effects of stray light are evident for angles up to 40 degrees off-axis. Also overlaid in Figure 3-100 is the expected limb profile for the ALI based on the stray light analysis of the mirrors conducted by Lambda Research Corporation [12]. Clearly, the expected falloff due to stray light effects from the mirrors alone does not match the observed profile. This data confirms the effects of scatter from the Z306 black paint inside of the telescope. These data are also useful for they define the angular dependency of all ALI stray light sources in the +pitch, -pitch, + roll, and - roll directions.

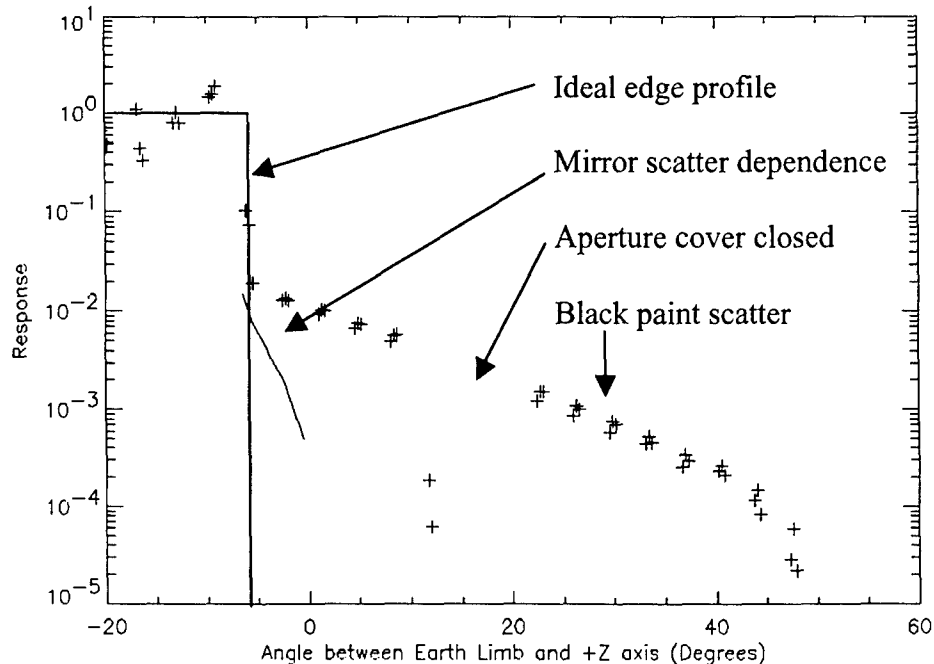


Figure 3-100. Earth limb scan history for detector 100, Band 3.

3.2.2.4.1.2.2 Earth Observations

The impact of stray light for typical Earth scenes and the validity of the stray light model discussed previously have been evaluated by comparing diffuse scenes as seen by the ALI, the Landsat 7 ETM+, and ground truth data. EO-1 and Landsat 7 are flying in formation, allowing for data from the same scene to be collected by the ALI and ETM+ with only a one-minute separation. The ground truth data are collected during both observations.

For the comparison, the radiance of a spatially uniform region of a scene is extracted from the ALI, ETM+, and ground truth data. The ratios of the ALI data to similar ETM+ data (bands 1, 2, 3, 5, 7) and ground truth data are then plotted as a function of the *radiance ratio*, t/b . The *radiance ratio* is calculated from the ETM+ data and is defined as the ratio of the mean target radiance to the mean background radiance, defined by a circle 3° in radius and centered on the target region. In this context, the *radiance ratio* is defined as the *true* contrast of the region being evaluated for stray light effects.

The predicted impact of stray light on the ALI data as a function of t/b for Band 3 is provided in Figure 3-101. For regions where the target radiance is greater than the background radiance, the expected stray light error is -3% and is dominated by the effect of light being scattered out of the target region into the surrounding background region due to the effects of total integrated scatter. For targets whose radiance is much lower than the mean background radiance, the impact of stray light is the result of light being scattered from the bright background into the dim target regions.

Also plotted in Figure 3-101 is the result of an ALI, ETM+, and ground truth comparison for scenes containing a variety of t/b values. The scenes used for this analysis included Maricopa, Arizona, Suez Canal, Antarctic Ross Ice Shelf, Cuprite, Nevada, Barreal Blanco, Argentina, and the San Francisco Salt Ponds. The model and data agree qualitatively and indicate a substantial rise in the expected radiometric error for targets with low radiance ratios for this band (3). This analysis was extended to also assess the effects of stray light for Bands 1, 2, 5 and 7 (these ALI bands are very similar to the corresponding ETM+ bands). The results for Bands 1, 2, and 3 are shown in Figure 3-102. The derived values of the scattering parameter ϵ , for all the bands, are summarized in Table 3-21.

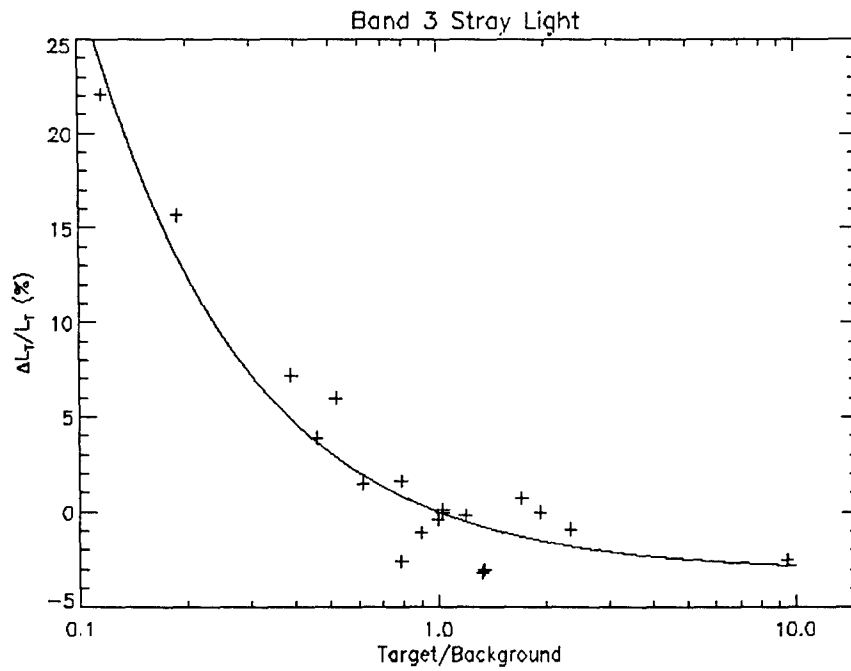


Figure 3-101. Stray light model and flight data for Band 3.

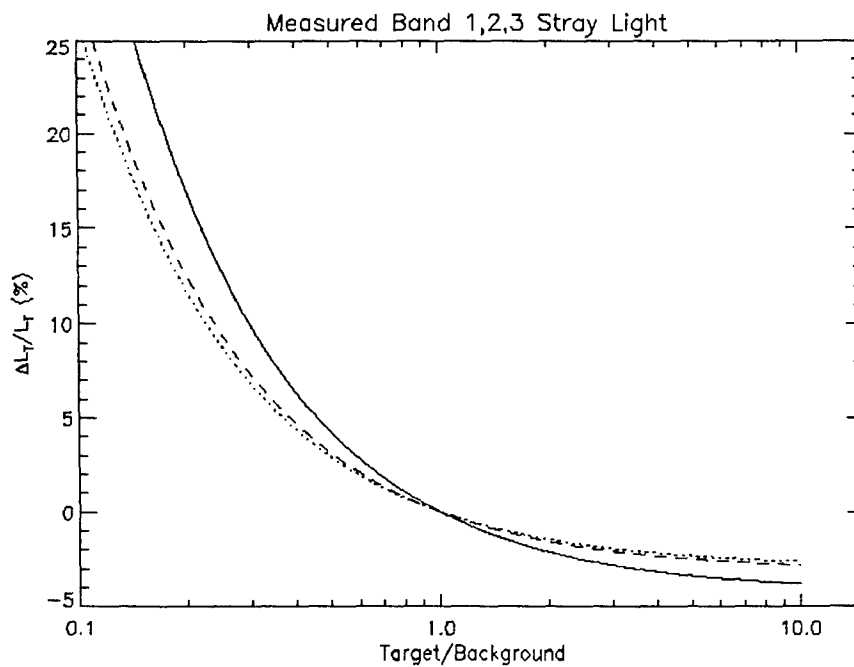


Figure 3-102. Effects of stray light for bands 1 (solid), 2 (dotted), 3 (dashed). These results have been derived by fitting the stray light model to flight data.

The SWIR stray light data suggest little impact for all radiance ratios $t/b > 0.75$. However, it must be noted that the stray light analysis could not be extended below $t/b = 0.75$ due to the large scatter in the ALI and ETM+ data as a result of low signal in these bands. Significant error due to stray light is expected and observed for SWIR data with $t/b < 0.75$ (e.g. small lakes). The data and model also indicate an increasing effect of stray light with decreasing wavelength, particularly for $t/b < 1.0$. However, the flight data suggest the magnitude of the stray light impact is less than predicted by the model for the VNIR bands (Table 3-21).

Table 3-21
Radiance errors derived from the stray light model and flight data

Band	Radiance Error ϵ (%) Theoretical	Radiance Error ϵ (%) Measured
1	8.3	4.2
2	5.8	2.9
3	4.2	3.1
4	2.7	-
5	1.3	<1.0
7	1.2	<1.0

3.2.2.4.1.3 Impact on Flight Data

In principle, the effects of stray light on a particular target could be assessed if the radiance ratio for the target was known. However, the effects of large off-axis scattering by the black paint on the interior of the telescope cavity can be problematic in some instances. As an example of the utility of the stray light model and the effects of the black paint scatter, a scene of the West Coast of Africa is shown in Figure 3-103.

Panel A of Figure 3-103 is a true-color, Band 321, image that has been radiometrically calibrated. Regions 1 and 2 have radiance ratios near 1.0 and so the predicted radiometric error due to stray light is minimal. Panels B, C, and D are three-color images defined by bands 321, 432, and 755p respectively. These images have been stretched to enhance the region of water off the African coast. Although the radiometric model predicts minimal stray light in this region, clear 3-10% SCA-to-SCA banding is evident. The stray light effects observed off the African coast are the result of large off-axis angle scattering of the in-land region photons off the black-paint behind the secondary mirror. To properly account for this effect, a second background region, extending more than ten degrees, would be needed. Since the ALI field of view is only 3 degrees, an independent measure of the extended background radiance is required.

Finally, it should be noted that extended off-axis scattering by the black paint only becomes problematic for large regions with relatively low radiances. This is because the scattering effect of the paint is approximately 1% of the mean of the extended background. For small regions ($< 3^\circ$) the model discussed above is appropriate. For larger regions, the effects of the black paint scatter are small if the target radiance approaches or exceeds the extended background radiance. However, for large regions with low radiance levels (e.g. water) and a relatively high-extended background

radiance (e.g. land, clouds, ice), the 3° assumption for the background region breaks down and the 1% scatter effect of the black paint becomes significant.

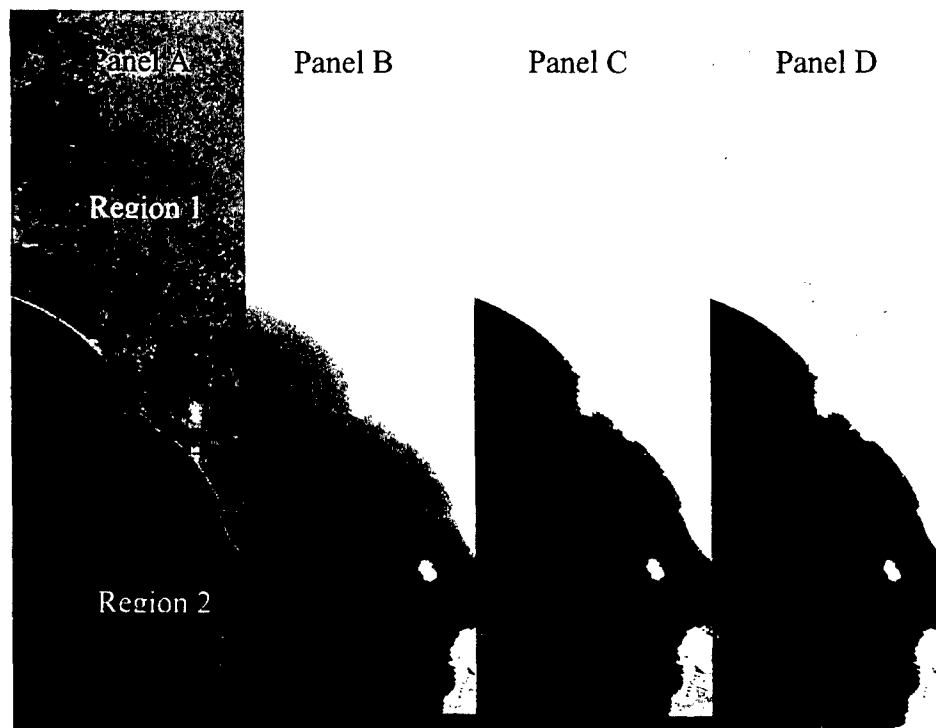


Figure 3-103. Stray light impact example for West Coast, Africa scene. The effects of black paint scatter in the water is evident in the enhanced images in panels B, C, D.

3.2.2.4.2 Filter Scatter

Evidence for a third source of stray light manifests itself as a 1% *echo* or *ghost* near the primary image for Bands 5p, 5, and 7. This artifact is clearly observed in lunar calibration and lava flow data.

3.2.2.4.2.1 Lunar Calibration

During an ALI lunar calibration, the Moon is scanned in each of the four sensor chip assemblies or SCAs. Figure 3-104 depicts the raster scanning technique used during a typical lunar observation. Figure 3-105 is a photo of the ALI SCA module with the scan path of the moon overlaid.

Lunar images, created from each of the ten ALI bands for SCA 1, are shown in Figure 3-106. After stretching the image and zeroing the main lunar image, any residual stray light effects are revealed (Figure 3-107). Clearly, an elongated secondary image of the Moon is observed after the primary image in Band 5p, 5, and 7. Another ghost image is also seen prior to the image for Band 1p. No obvious ghosting effects are seen in the VNIR bands.

The characteristics of the lunar ghost are:

1. Observed for Bands 1p, 5p, 5, 7
2. Restricted to in-track only
3. Band 1p effect on opposite side of the SWIR effects
4. Always occur after the main image
5. Band 7 ghost 62 frames long
6. Band 5 ghost 44 frames long
7. Band 5p ghost 18 frames long
8. Ghost intensities are $\sim 1\%$ of the average Lunar brightness

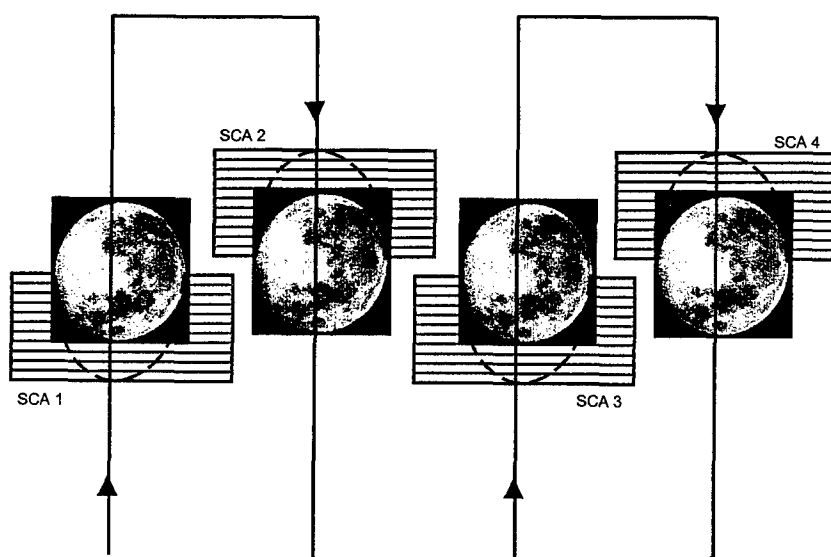


Figure 3-104. Raster scan for a typical ALI Lunar calibration.

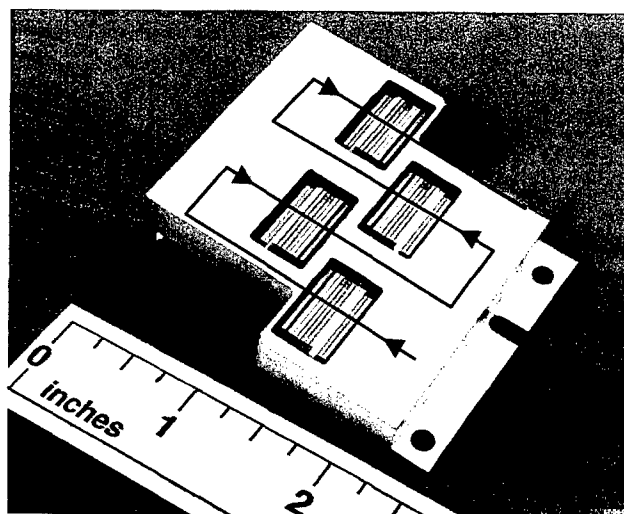


Figure 3-105. Direction of a typical Lunar calibration scan on the SCA module.

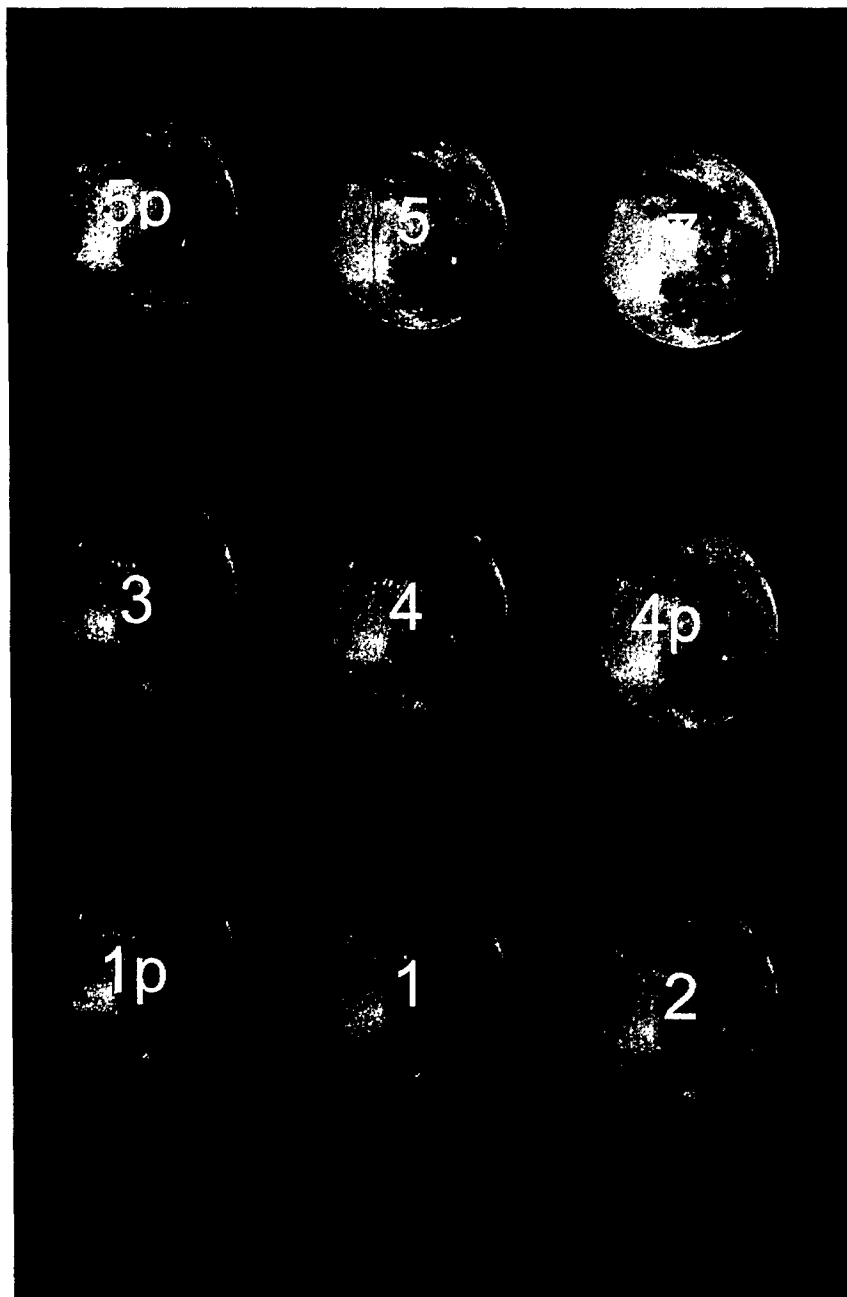


Figure 3-106. Images of the moon from a typical Lunar calibration.

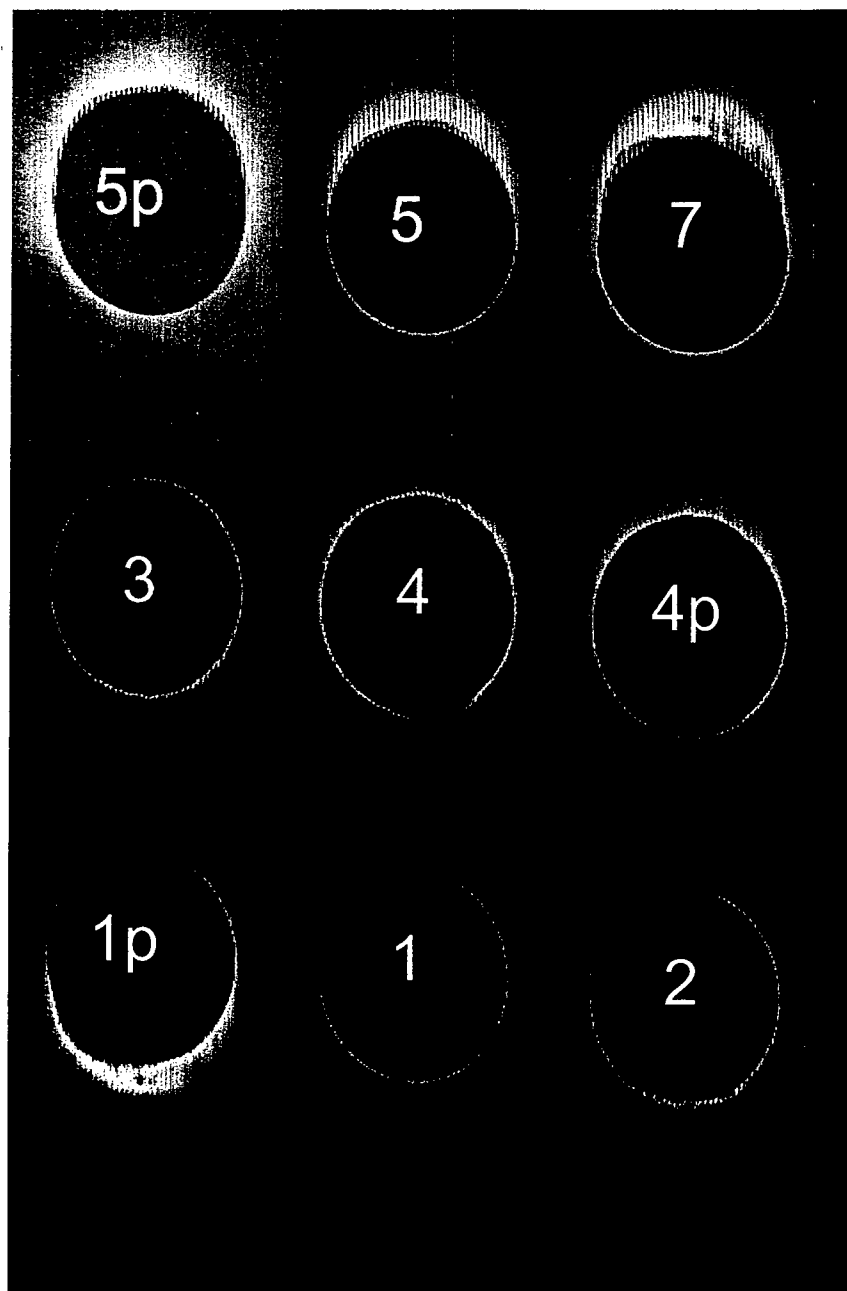


Figure 3-107. Stretched images from a typical Lunar calibration.

3.2.2.4.2.2 Lava Flow Observation

Ghost images have also been observed in the Mount Etna observation on 203091955. During this observation, active lava flows were visible and observed by the instrument. These flows are highly luminous and saturate the ALI in Bands 5 and 7. Additionally, ghost images appear after the primary lava flow images and are observed in Bands 5p, 5, and 7.

Figure 3-108 provides an example of the lava flow ghost images for Band 7. The characteristics of the lava flow ghosts are:

1. Observed for Bands 5p, 5, 7
2. Always occurs after the main image
3. Band 7 ghost 53-65 frames long
4. Band 5 ghost 43 frames long
5. Band 5p ghost 14-23 frames long
6. Restricted to in-track only
7. Odd and even pixels appear shifted by 15 frames within the ghost image

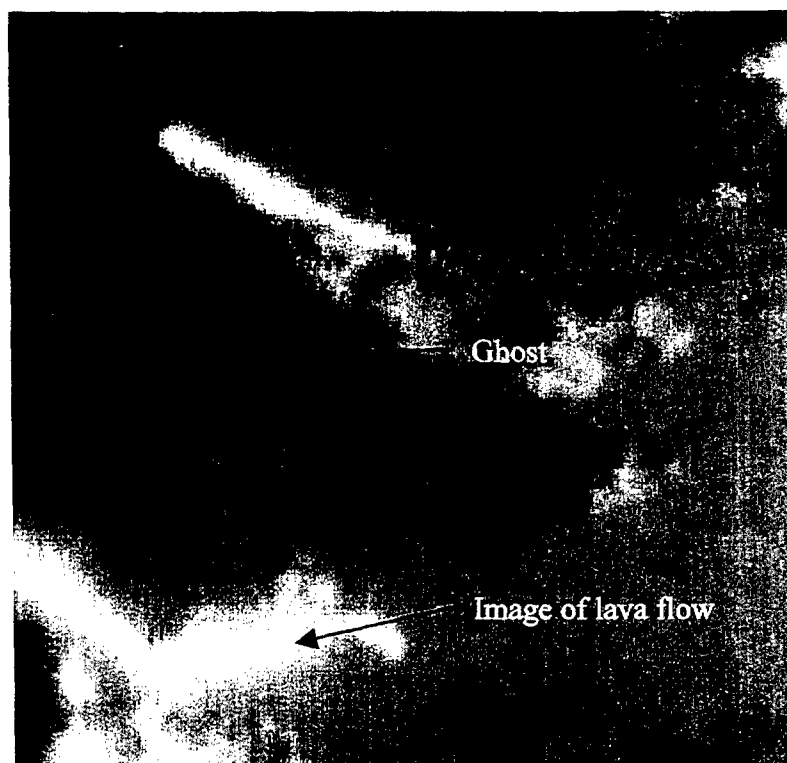


Figure 3-108. Ghosting effects observed in Mount Etna lava flows (Band 7).

3.2.2.4.2.3 Ghost Generation Model

The current ghost generation model is based on the scatter of light, at the interface of the VNIR and SWIR filter blocks located directly above the detector arrays, onto the SWIR filters. Figure 3-109 provides a cross-section of the focal plane filters and indicates the ghost generation scattering point.

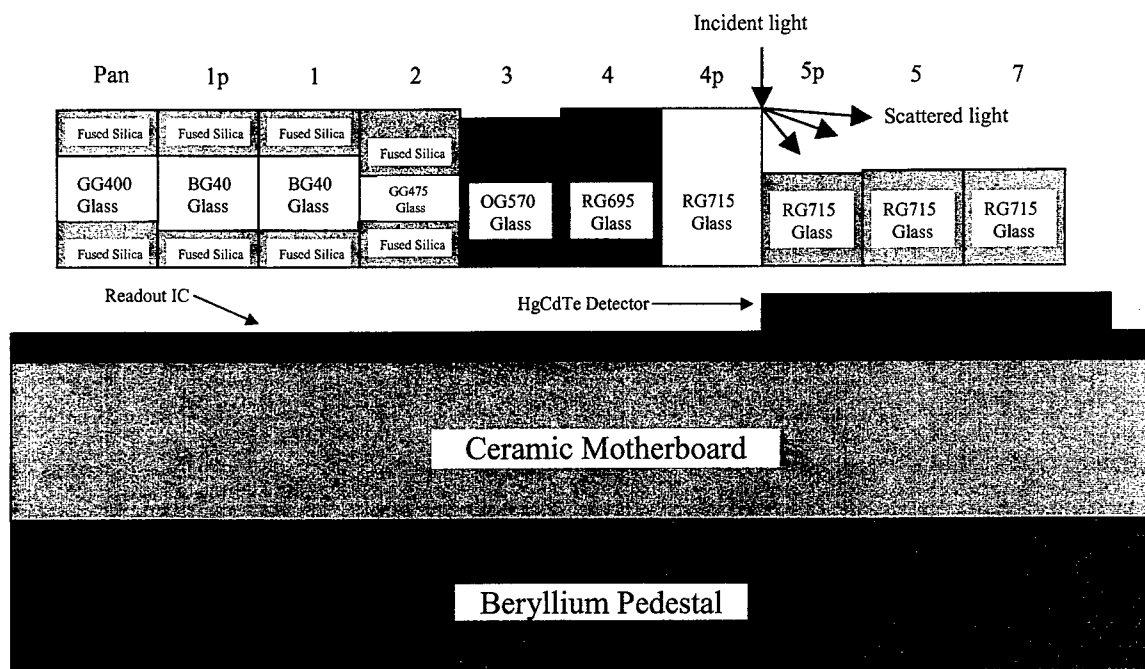


Figure 3-109. Cross section of ALI SCA. The ghost generation model assumes light is scattered from the discontinuity at the boundary between the VNIR and SWIR filter assemblies.

When considering the observed lunar calibration ghost, it is useful to separate the imaging processes into separate components (Figure 3-110). Initially, the image of the moon is projected onto the SWIR filter surfaces prior to being imaged by the VNIR arrays. No portion of the image of the lunar disk intersects the VNIR/SWIR filter boundary and no scattering occurs. Once the image reaches the VNIR/SWIR filter interface and the VNIR bands begin to record the image of the moon, a portion of the disk intersects the filter boundary, and in-track scattering occurs. However, as long as the portion of the lunar image intersecting the boundary is less than the width of the image intersecting the SWIR arrays, the scattered image will overlap the lunar disk image and no obvious ghost will appear. This ghosting effect will add a 1% uncertainty to the primary lunar image. Once, the extent of the lunar image interacting with the filter boundary exceeds the portion of the lunar image intersecting the SWIR arrays and the scattered light 'spills over' to the region outside the lunar limb and the ghost image begins to appear. However, the extent of the cross-track width of the ghost is limited to the extent of the lunar image intersecting the filter boundary. The ghost image will continue to develop, appearing to trace the lunar limb, until the down-track image of the moon passes the VNIR/SWIR filter boundary.

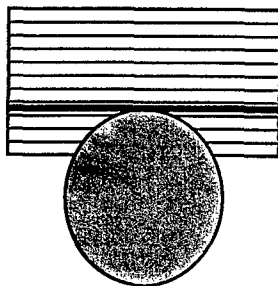
The generation of lava flow ghost images also relies on the in-track scattering of an image at the VNIR/SWIR filter boundary (Figure 3-111). Initially, the image of the flow is constrained to be within the SWIR filter region and no scattering occurs. However, once the flow image begins to intersect the boundary, light is scattered back into the SWIR filter region. If the scattered light cross-track dimension exceeds the image of the flow within the SWIR bands, a ghost effect

appears. In this manner, the intricate structure of the flow will be 'traced' in the down-track SWIR data as it did in the lunar data.

The ghost model, as defined above, predicts several characteristics that should be observable in the lunar and lava flow data. One of the key predictions is that the Band 7 ghost should have the largest separation distance and be 3 times that of Band 5p and 1.5 times that of Band 5. Additionally, odd and even detectors for each band should be illuminated simultaneously by the scattered light, resulting in an odd-even effect in reconstructed images. Both of these effects are observed in the lunar and lava flow data. All of the ghost model predictions are listed in Table 3-22, along with the status of the verification using ALI data.

Position

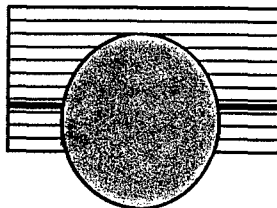
Limb approaches
Boundary.



Results

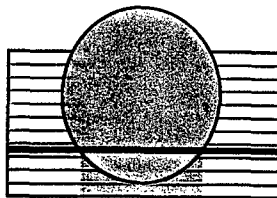
Reflections begin but
are contained within the
lunar image.
No ghosting observed.

Intersection of image
with boundary exceeds
intersection of image
with Band 7 array.



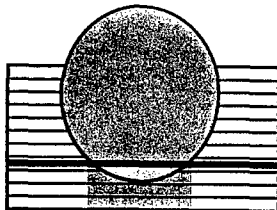
Reflections begin to
exceed lunar image
for Band 7 - Ghost image
begins near center of
lunar image for this band.
Constrained to width of
lunar image.

Limb crosses Band 7.



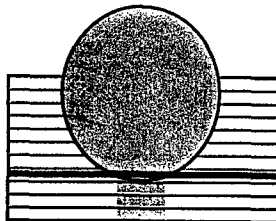
True image for Band 7
ending. Ghost for Band 7
reducing in cross-track to
extent of lunar image
intersecting with boundary.

Limb crosses Band 5.



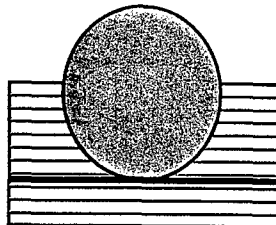
True image for Band 5
ending. Ghost for all SWIR
bands restricted to extent
of lunar image intersecting
with boundary.

Limb crosses Band 5p.



True image for Band 5p
ending. Ghost for all SWIR
bands restricted to extent
of lunar image intersecting
with boundary.

Limb crosses
boundary.



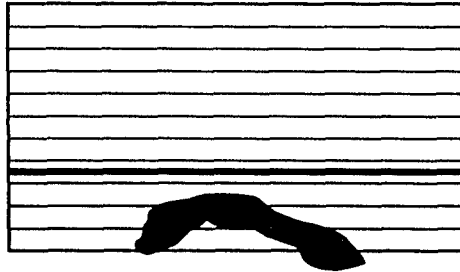
All reflections end.
No ghosting observed.

Figure 3-110. Generation of Lunar ghosts by scattering off the VNIR/SWIR filter boundary.

Position

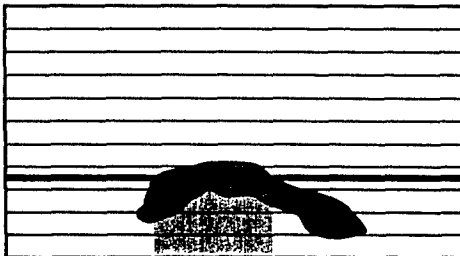
Results

Lava flow approaches boundary.



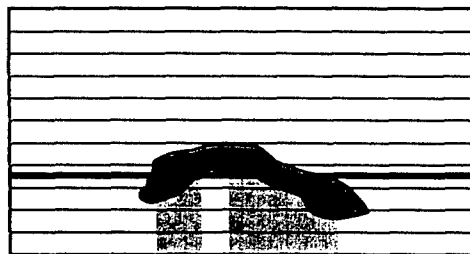
No reflections. No ghosting observed.

Lava flow image begins to cross boundary.



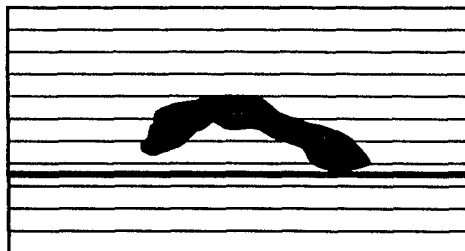
Reflections begin but are constrained to that part of the flow image interacting with the boundary.

One-half of flow beyond boundary.



Reflections continue but vary according to that part of the flow image interacting with the boundary, creating a "reflected image" of the flow.

Lava flow exits boundary.



All reflections end. No ghosting observed.

Figure 3-111. Generation of lava flow ghosts by scattering off the VNIR/SWIR filter boundary.

Table 3-22
Ghost generation model predictions

Prediction	Status
Band 7 ghost distance 3x that of Band 5p.	Confirmed – lunar/lava
Band 7 ghost distance 1.5x that of Band 5.	Confirmed – lunar/lava
Ghost will appear after primary image and will be limited to in-track.	Confirmed lunar/lava
Ghosts will appear to trace primary image's spatial signature.	Confirmed – lunar/lava
No ghosts will occur in the VNIR.	Confirmed – lunar/lava
Odd/Even effects will occur in the reconstructed image.	Confirmed – lunar/lava
Lunar ghost will occur before the primary image if the lunar scan direction is reversed.	Confirmed - lunar
Ghosts will occur before the primary image for SCA 1 and 3 for normal DCE.	Confirmed – nightflare

3.2.2.4.2.4 Discussion

The ghost image effects observed in the ALI lunar observations are approximately 1% of the mean lunar irradiance. The model developed to account for this effect predicts all data should have this effect to some degree. The impact of this effect will depend on the local SWIR contrast within a scene. For flat scenes with large diffuse regions, no radiometric impact will occur due to focal plane ghosting. This is because a uniform diffuse scene, which included the effects of ghosting, was used to calibrate the ALI in the laboratory. For other scenes with varying local contrast, the impact on the ALI absolute radiometry will be based on the ratio of the radiance impinging on the filter boundary to the radiance falling on the SWIR arrays from the scene. If the boundary radiance is small or equivalent to the scene radiance, the impact on the scene radiometry is minor. This is the case for the lunar observation when the intersection of the lunar disk with the boundary is smaller than the intersection of the image with the SWIR arrays. However, as the radiance falling on the boundary regions exceeds the radiance on the SWIR arrays, the impact on the absolute radiometry of a scene grows. The extreme cases of this are the lunar and lava flow ghosts. In the lunar image case, the irradiance of the lunar disk is infinitely greater than that of deep space, and an obvious ghost appears. For the lava flows, the radiance of the lava is much greater (saturates ALI detectors) than the surrounding terrain, resulting in the ghost images.

Although the ghost model does account for the observed SWIR effects, it does not explain the ghost observed in Band 1p. However, the reversal of the ghost to occur before the primary image indicated a different mechanism and requires further investigation. No resources have been used to investigate the Band 1p ghost at this time, but it is tempting to attribute the observed effect to a scatter off the bezel surrounding the SCA in much the same manner as was done for the VNIR/SWIR filter boundary described above.

If the ghost generation model is correct, this effect can be removed by manufacturing the ALI filter arrays such that no boundary occurs between filters. However, care must be taken to preserve the focus of the instrument when aligning filters with different indices of refraction.

3.2.2.4.3 Conclusion

The EO-1 Advanced Land Imager stray light from the telescope mirrors and black paint has been characterized on orbit using Earth limb scans and by comparing flight data to ETM+ and ground truth data. The stray light model for these components agrees qualitatively with the flight data for off-axis angles $< 3^\circ$. The stray light component caused by the black paint lining the inside of the telescope is the dominant source of stray light for larger off-axis angles and is difficult to assess using only ALI data.

Another stray light generation model, based on the scattering of incident light off the boundary between the VNIR and SWIR filter assemblies, has also been developed and is consistent with ghosting or echo effects observed in the SWIR bands in Lunar and lava flow observations.

For scenes with high contrast (e.g. coastlines, lakes in snow covered areas, mostly cloudy scenes over water) the impact of stray light on the ALI radiometry may become significant. It is therefore recommended that scientific inferences, developed using high contrast ALI data, should be carefully evaluated for stray light effects.

3.2.2.5 Absolute Radiometry

The absolute radiometric accuracy of the Advanced Land Imager defines the ability to make accurate, quantifiable measurements of a scene's radiance in each of the instrument's ten spectral bands. On-orbit, the absolute radiometric accuracy of any mission is challenged by stray light, instrument aging, and the space environment. We have adopted five independent calibration techniques in an attempt to establish and maintain the radiometric accuracy of the ALI over the duration of the mission: pre-flight calibration, solar calibration, lunar calibration, ground truth measurements, and intersatellite comparisons*. The basis for the on-orbit radiometric accuracy of the Advanced Land Imager is pre-flight calibration (Section 3.1.4). However, in order to assure the accuracy of these measurements and to assess changes in the instrument response over time, on-orbit calibration techniques are also required.

* Another source of on-orbit radiometric calibration for the ALI is an internal reference source mounted on the inside of the optical metering truss (Section 2.3). Initially, the internal reference source was to serve as a radiometric transfer standard between pre-flight and on-orbit calibrations of the ALI. However, a noticeable increase in lamp output in the VNIR was observed immediately after launch. This has been attributed to a loss of convective cooling of the filament in the zero-G environment. This increase in lamp output has resulted in invalidating any attempts at using the reference lamps as a calibration transfer standard between preflight and flight calibration of the ALI detector arrays. However, the lamp output has been very repeatable since launch and has proven to be invaluable at monitoring the stability of the focal plane during the first year of on-orbit operations (Section 3.2.2.6).

3.2.2.5.1 Solar Calibration

Solar calibration is the primary method of on-orbit radiometric calibration of the ALI. The solar calibration procedure, which is illustrated in Figure 3-112, involves pointing the ALI at the sun

with the aperture cover closed. A motor-driven aperture selector in the aperture cover assembly moves an opaque slide over a row of small to increasingly larger slit openings and then reverses the slide motion to block all sunlight. A series of seven discrete aperture areas can be obtained. Just prior to solar calibration, a space grade Spectralon® diffuser plate is swung over the secondary mirror by a motor-driven mechanism. The diffuser reflectively scatters the sunlight that would otherwise impinge on the secondary mirror. The scattered sunlight exposes the FPA to irradiance levels equivalent to Earth-reflected sunlight for albedos ranging from 0 to 100%.

The detector response during a solar calibration sequence consists of an approximately linear increase as the aperture opens, with a series of constant responses during those times when the slide passes over a reference bar. These bars provide a set of seven calibrated response points.

When the aperture cover reverses direction and closes, the pattern of response reverses and proceeds back down to zero. Typical examples of detector responses for each of the ten ALI spectral bands are shown in Figure 3-113. The flux level at the maximum or seventh level corresponds approximately to a 100% albedo at a 30° solar zenith angle.

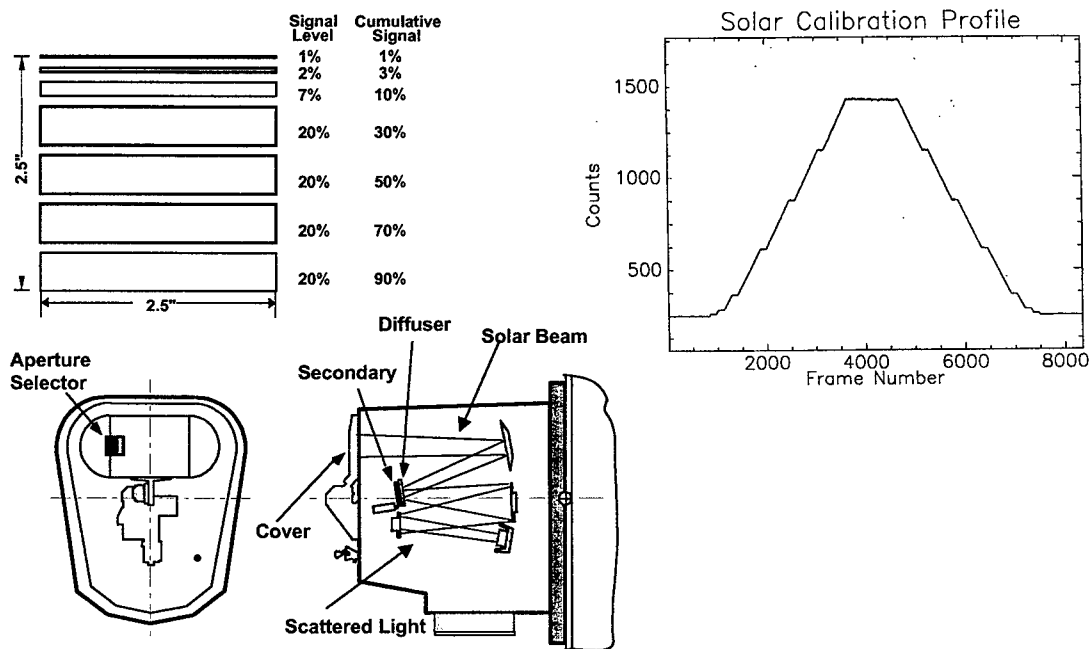


Figure 3-112. Illustration of the solar calibration mode and laboratory test data from a solar simulator.

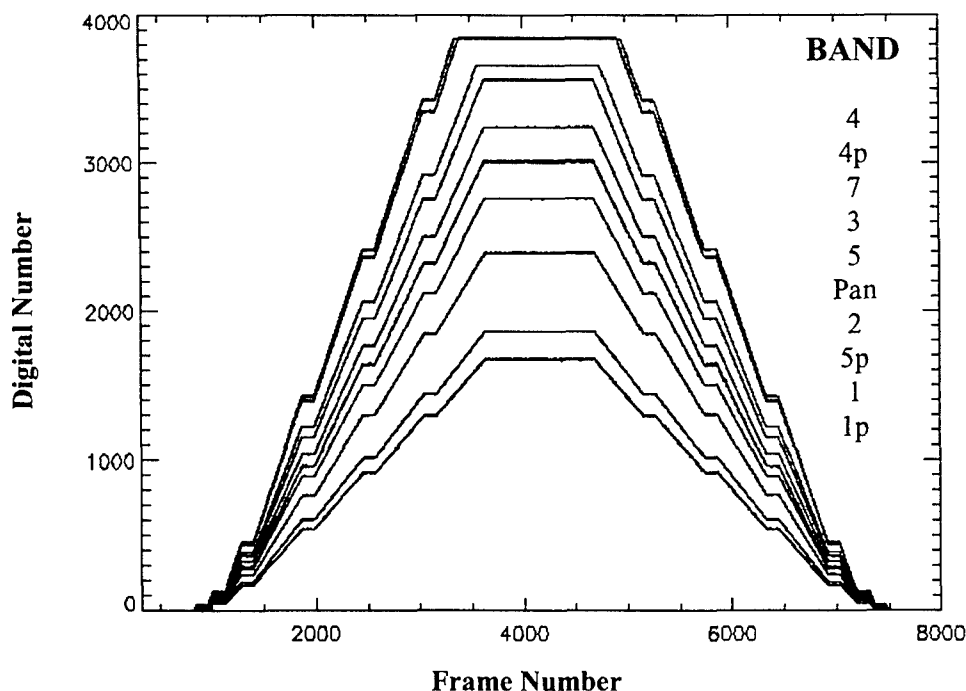


Figure 3-113. Measured detector responses for the ten ALI bands during a solar calibration.

During solar calibration, the optical throughput of the ALI differs from a normal data collection because the Spectralon BRDF replaces the reflectance of the secondary mirror. Measurements of the BRDF were made on a spare flight quality Spectralon disk over a spectral range of 400 to 900 nm and for the appropriate angles of incidence and reflection at NASA's Goddard Space Flight Center. Values outside this spectral range were estimated by assuming that they scale as the total hemispherical reflectance, which was measured by Labsphere®. The resulting BRDF is shown in Figure 3-114.

A detailed CODE V® optical analysis provided the ratios of the irradiance at the FPA to the solar irradiance at the sub aperture for each position of the aperture selector. For a given sub aperture the FPA irradiance was shown to vary by 2% over the full 15-degree field of view and by less than 1% over the region populated by detectors. The irradiance at the FPA is thus a known function of the aperture slot opening and solar irradiance. This FPA irradiance corresponds to a known effective radiance at ALI entrance. The detector channel output corresponding to this effective radiance provides the solar calibration.

The solar irradiance model used in the analysis is the MODTRAN 4.0-CHKUR model, which is currently being used for all Landsat 7 solar calibration derived gains.

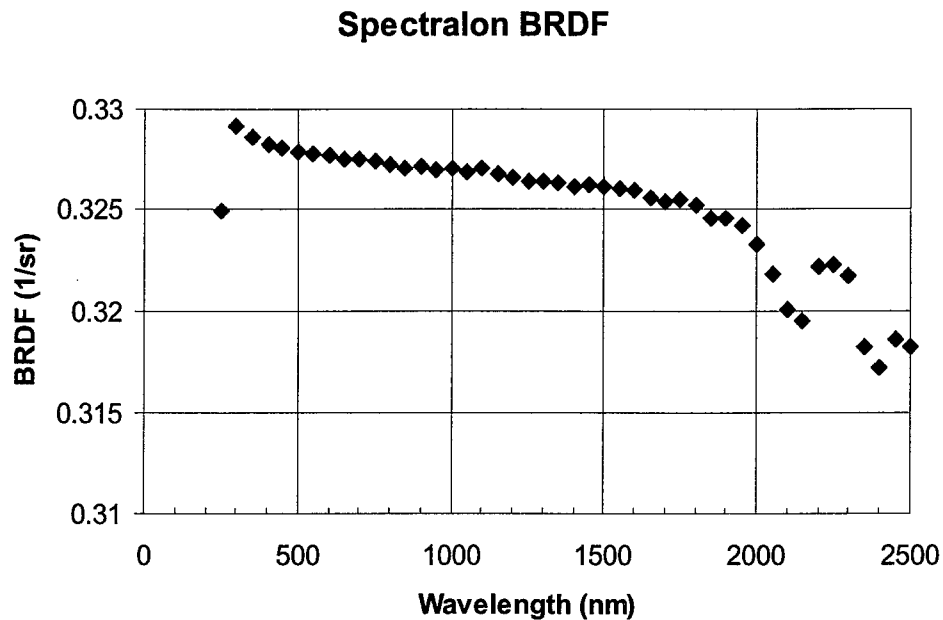


Figure 3-114. BRDF of diffuser located in front of the ALI secondary mirror used in the solar calibration model.

The results from a solar calibration measurement, performed on February 9, 2001, are provided in Figure 3-115. The measured radiances using pre-launch calibration coefficients for each band have been normalized to the expected values from the Code V analysis. These data are plotted at the mean wavelength of each band.

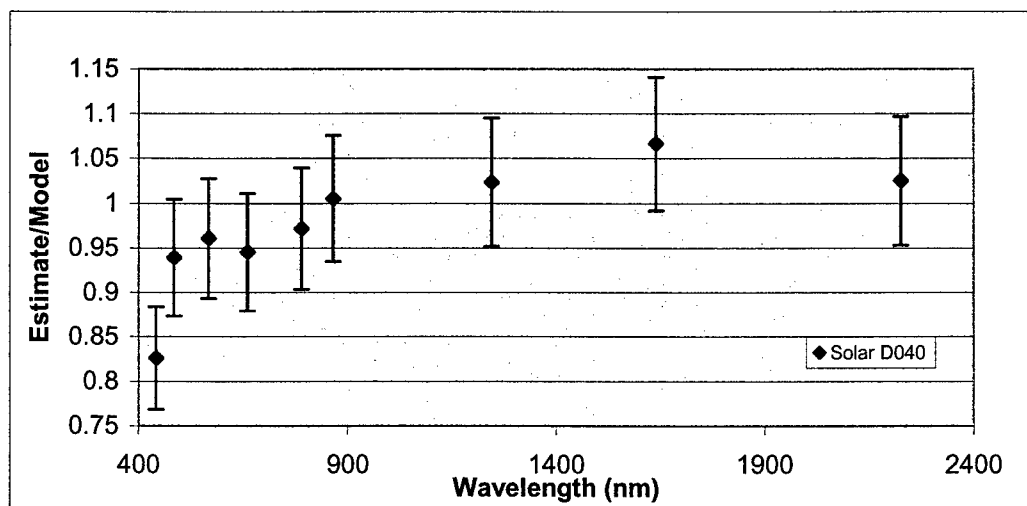


Figure 3-115. Results of solar calibration of the ALI from February 9, 2001. The ratio of observed to expected radiances for level 6 are plotted as a function of wavelength.

With the exception of band 1p, the solar and pre-launch calibrations agree to within the estimated uncertainties. The pre-launch calibration error combined with the additional on-orbit effects of contamination and stray light is estimated to be less than 5% for all bands. The solar calibration uncertainty is estimated to be 5% in the VNIR bands and 7% in the SWIR bands. The larger uncertainty in the SWIR bands is due to both the uncertainty in the solar irradiance models and the BRDF of the Spectralon. The low response in band 1p is a significant discrepancy between the two calibration techniques. A potential cause for this discrepancy is the degradation of the Spectralon diffuser, which is known to be highly susceptible to contamination. This hypothesis was ruled out by comparing the solar calibration results to lunar calibration measurements and ground truth observations.

The solar calibration data exhibit two other interesting trends, which are of lesser significance. There is a general increase in the ratios with increasing wavelength as can be seen in Figure 3-115. A second effect, not shown here, is a decrease in the ratio with decreasing aperture area. The effect has been attributed to a systematic error (within machining tolerances) in the aperture areas.

3.2.2.5.2 Ground Truth

The second method of assessing the radiometric accuracy of ALI data hinges on reflectance-based ground truth measurements [13]. The principle of this technique is to image a stable, high-altitude, flat, diffuse ground target using the ALI while simultaneously measuring the reflective properties of the target region and local atmospheric conditions. The ground measurements can then be used to predict the top of the atmosphere radiance observed by the ALI.

Throughout the first year of the EO-1 mission, ground truth campaigns were conducted by several groups, including the University of Arizona, the University of Colorado, the Australian CSIRO, and the NASA Jet Propulsion Laboratory. Ground truth sites include Barreal Blanco and Arizario Argentina, Lake Frome Australia, and complementary sites in the western United States (Railroad Valley, Ivanpah Playa, Walnut Gulch, and White Sands).

The first step of the reflectance-based approach is to measure the reflectivity of the site to be imaged by the ALI. This consists of obtaining several spectroradiometric measurements of a sample portion of the site by walking a backpack-mounted sensor in a grid-like manner and averaging the results. Immediately prior to and after these measurements, spectroradiometric measurements of a lambertian reference panel are obtained. The reflectance of the site is then obtained by ratioing the average site radiance to the average panel radiance and interpolating the result to the 1 nm level.

The second step of the reflectance-based approach is to measure the local atmospheric conditions at the time of the EO-1 overflight. Data obtained from a multispectral solar radiometer are used as input to atmospheric modeling tools to retrieve spectral atmospheric optical depths in 1 nm intervals from 400-2500 nm, aerosol size distribution, and column water vapor levels.

Once the surface reflectance and atmospheric conditions have been measured, a top of the atmosphere radiance is predicted at the time of the EO-1 overflight. First, the solar irradiance

impinging on the Earth's atmosphere is determined from a solar irradiance model and Sun-Earth distance. Next, the effects of atmospheric scatter and absorption are accounted for using radiative transfer modeling. The downwelling irradiance is then reflected off the site surface using the reflectivity measurements obtained previously. The atmospheric scatter and absorption effects on the upwelling radiance are accounted for by additional radiative transfer modeling, resulting in a predicted hyperspectral at-sensor radiance. Finally, the integrated product of the predicted hyperspectral radiance and ALI spectral response functions provides expected in-band radiances for the site for each spectral band. The predicted in-band radiances are then compared to the observed in-band radiances, based on pre-flight calibration, in order to evaluate the absolute radiometry of the instrument.

Figure 3-116 overlays the results of ground truth measurements of Barreal Blanco, Argentina and Ivanpah Playa, California obtained by the Remote Sensing Group of the University of Arizona with the solar calibration measurement presented earlier [14]. The errors associated with the ground truth measurements have been estimated to be $\pm 3\%$.

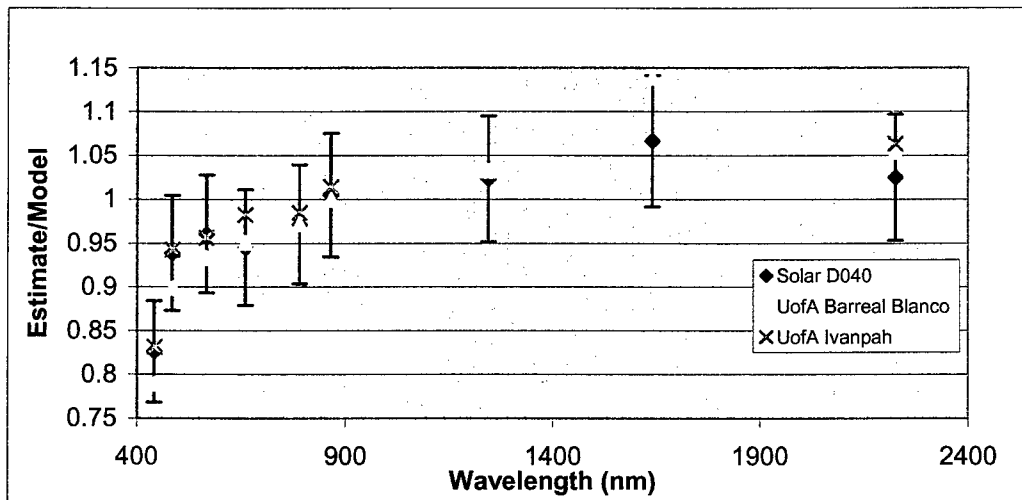


Figure 3-116. Overlay of ground truth results obtained by the University of Arizona and solar calibration data.

Examination of Figure 3-116 reveals good agreement between the ground truth and solar calibration measurements. The repeatability of the Band 1p offset and overall trend in the VNIR add confidence to the solar calibration model and indicate a change in the ALI radiometric response since pre-flight calibration for these bands. However, a 7% difference between the solar and ground truth data exists for Band 5 (1650 nm) and is not well understood at this time.

3.2.2.5.3 Lunar Calibration

A third method used to evaluate the absolute radiometry of the ALI on orbit is lunar calibration. This method involves observing the Moon with the instrument and comparing the measured lunar spectral irradiance with a predicted lunar irradiance for the time of the observation.

Lunar observations using the ALI have been conducted near a 7° phase angle each month since January 2001. For each observation, the spacecraft is maneuvered to scan the Moon in the in-track direction at 1/8 the nominal scan rate in order to oversample the disk. Because the Moon has ~ 1/2 ° diameter, the entire lunar disk may be imaged on an individual sensor chip assembly or SCA. As a result, four images of the Moon are obtained during each lunar calibration sequence—one per SCA.

To calculate the observed lunar irradiance, dark current levels are subtracted and the image is radiometrically calibrated using the pre-flight calibration coefficients. A region of interest, narrowly circumscribing the Moon, is then defined by locating the region of each column where the intensity falls to below 1% of the average lunar irradiance (Figure 3-117). Summing the response within the circumscribed region, the spectral irradiance of the Moon for each band may be calculated as

$$E_M(\lambda, day) = \frac{d\Theta \Delta}{fF} \Sigma L_P(\lambda)$$

Here, $E_M(\lambda, day)$ is the lunar spectral irradiance for a given mission day number, $d\Theta$ is the ALI pitch rate during the scan (radians/second), Δ is the detector pitch, f is the ALI focal length, F is the frame rate (Hz), and $L_P(\lambda)$ is the measured lunar spectral radiance for detector P ($\text{mW}/\text{cm}^2/\text{sr}/\mu\text{m}$).

Once the measured lunar irradiance has been determined for a given observation, the expected lunar irradiance is calculated by the USGS using data obtained from the Robotic Lunar Observatory (ROLO) in Flagstaff Arizona [15]. Since 1996 ROLO has been measuring the lunar irradiance between 350 and 2500 nm as a function of phase angle as often as weather and seeing permit. Contemporaneous observations of nearby bright stars provide absolute calibration of the Observatory, as well as a measurement of atmospheric extinction. The USGS has been able to use this database to predict lunar irradiance for most phase angles. As a result, lunar observations are emerging as an exciting new opportunity for radiometric calibration of space based VNIR/SWIR instruments.

The results of a lunar irradiance comparison for measurements obtained on February 7, 2001 required a normalization of 5% to the ROLO data for all bands in order to bring the results into agreement with ALI measurements. The source of this offset is unclear at this time but the leading candidate is an uncertainty in the absolute radiometric traceability of the ROLO measurements. In any case, once the 5% offset is applied, the lunar irradiance comparison result was overlaid with solar and ground truth comparisons in Figure 3-118. The lunar data agree well with the other techniques, supporting the hypothesis that the radiometric response of the instrument has changed significantly for Band 1p and has drooped slightly in the VNIR since pre-flight measurements were taken.

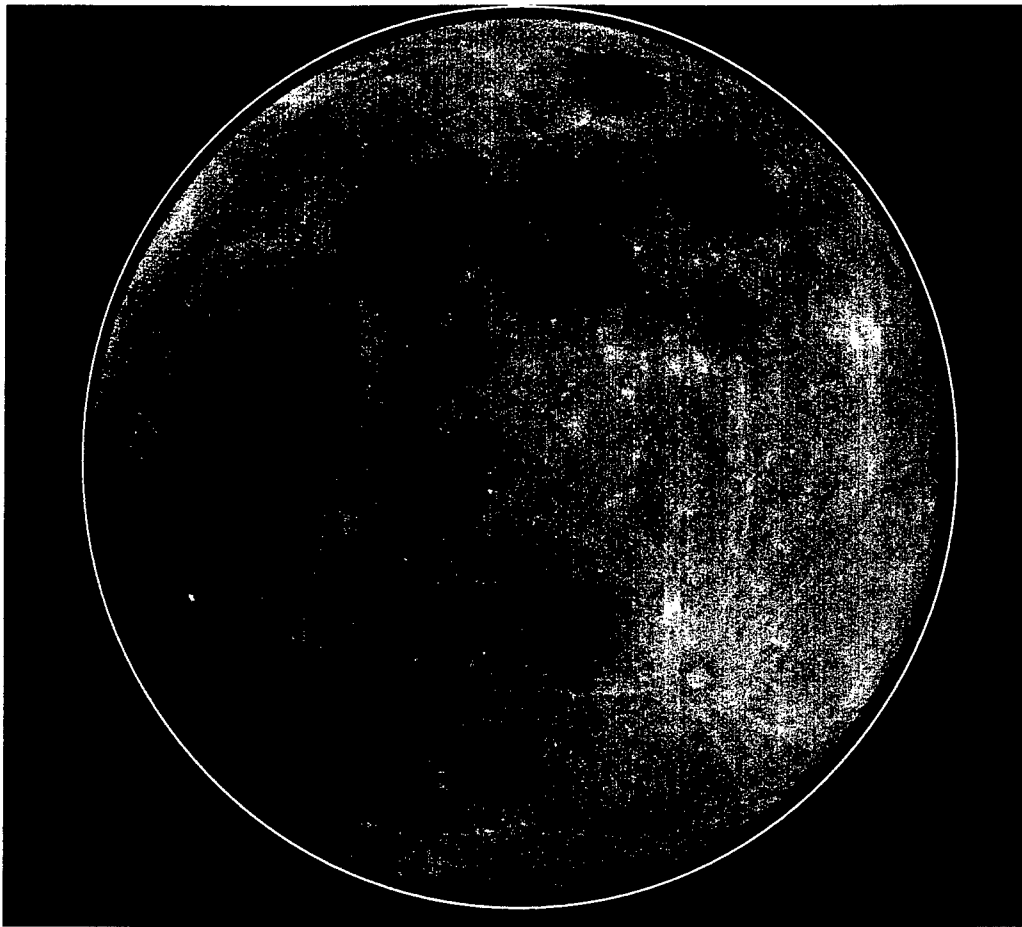


Figure 3-117. Image of the Moon taken by the ALI on February 7, 2001. The circle surrounding the Moon defines the regions used in the lunar irradiance calculations.

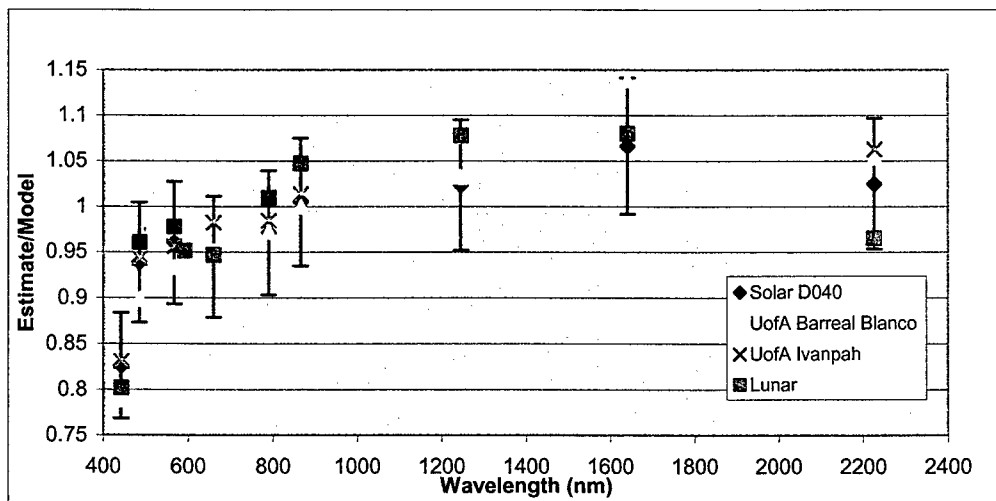


Figure 3-118. Results from solar, ground truth, and lunar absolute radiometric calibrations.

3.2.2.5.4 Internal Reference Lamp Illumination

Another source of on-orbit radiometric calibration for the ALI is an internal reference source mounted on the inside of the telescope. This source consists of three Welch Allyn 997418-7 (modified) gas-filled lamps mounted on a small (2.03 cm) diameter integrating sphere (Figures 3-119, 3-120). Light emerging from the exit slit of the sphere passes through a BK 7 lens and infrared filter, is reflected off the ALI flat mirror (M4), and floods the focal plane.

The internal reference lamps are activated during two data collection events per day, when the ALI aperture cover is closed. After an eight-second stabilization period the lamps are sequentially powered down in a staircase fashion, with two-second exposures between each step. In this manner, the focal plane will receive a daily three point radiometric reference.

Initially, the internal reference source was to serve as a radiometric transfer standard between pre-flight and on-orbit calibrations of the ALI. However, a noticeable increase in lamp output in the VNIR was observed immediately after launch. This has been attributed to a loss of convective cooling of the filament in the zero-G environment. This increase in lamp output has resulted in invalidating any attempts at using the reference lamps as a calibration transfer standard between preflight and flight calibration of the ALI detector arrays. However, the lamp output has been very repeatable since launch and has proven to be invaluable at monitoring the stability of the focal plane during the first year of on-orbit operations.

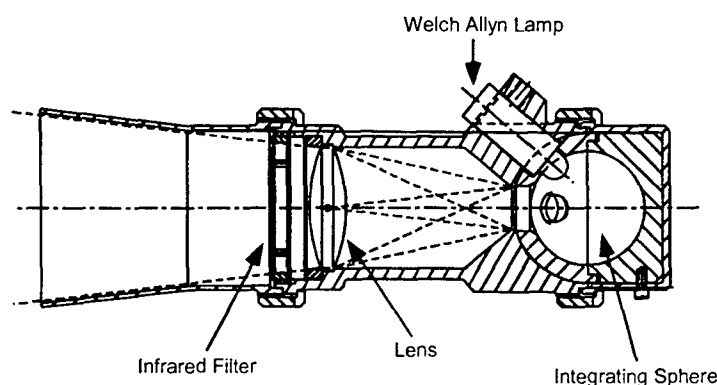


Figure 3-119. EO-1 ALI internal reference source.

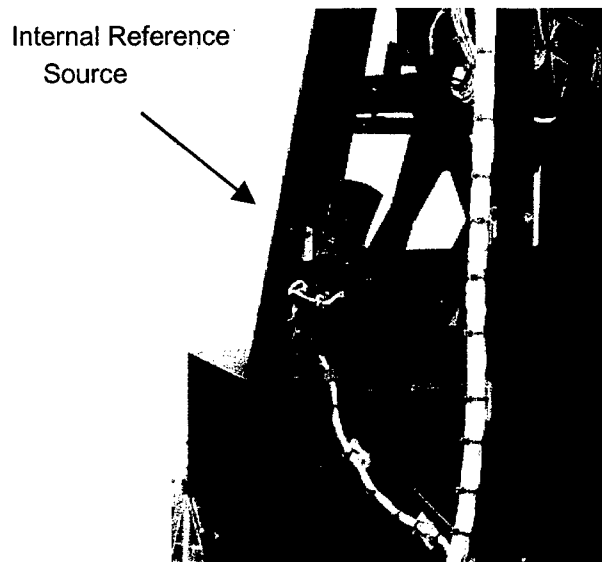


Figure 3-120. Photograph of internal reference source.

3.2.2.5.5 Intersatellite Comparisons

The final method used in assessing the radiometric accuracy of the Advanced Land Imager is intersatellite comparison. The EO-1 spacecraft is orbiting the Earth in a constellation of four spacecraft: Landsat 7 (10:01 AM descending node), EO-1 (10:02 AM), SAC-C (10:14 AM), and TERRA (10:42 AM). Since these spacecraft closely follow one another, a target can be imaged by instruments on all these satellites within a 41-minute period. This allows for an intercomparison of satellite data for flat, diffuse, stable regions.

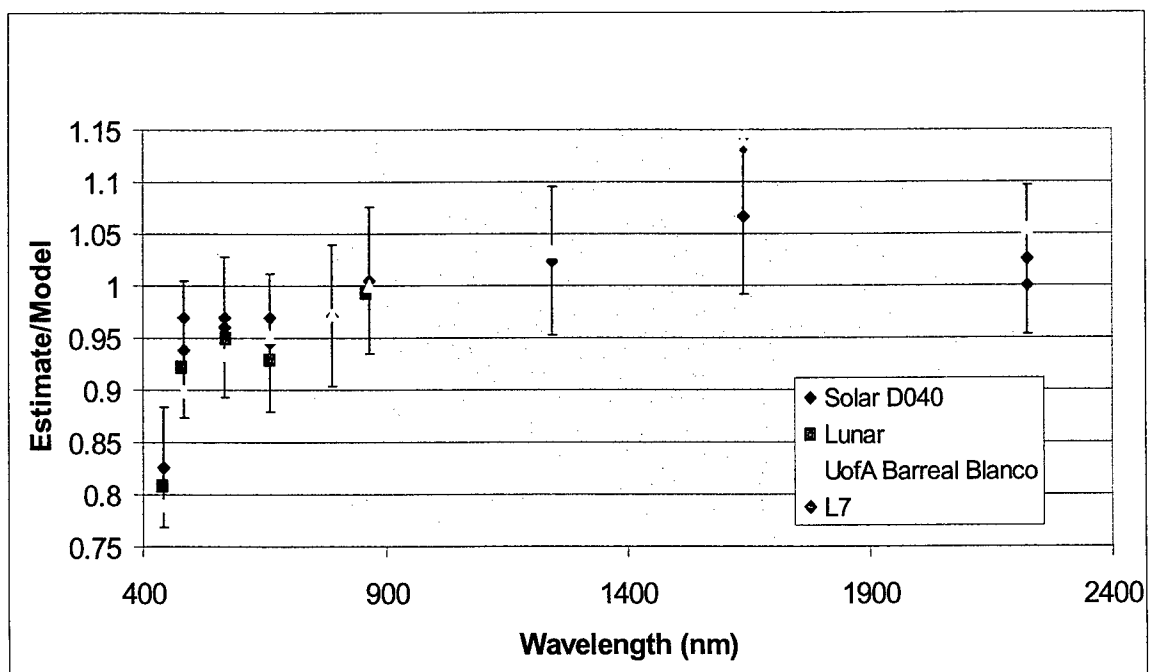


Figure 3-121. Results of solar, lunar, ground truth, and intersatellite radiometric calibrations.

To date, a comparison between EO-1 ALI and Landsat 7 ETM+ data have been conducted for three sights: the California Super Site (January 14, 2001), Railroad Valley (January 5, 2001), and Barreal Blanco (February 22, 2001). For each of these observations, Bands 1, 2, 3, 5 and 7 of the ALI and ETM+ may be directly compared, due to the similarity of each instrument's spectral response. For all observations, the ALI measured radiance is consistently 2-4% lower than the ETM+ radiances for Bands 1, 2, and 3. Band 7 is consistently with $\pm 2\%$ of the ETM+ measurements. Finally, ALI Band 5 measurements are consistently 12-15% higher than ETM+ measured radiances. The results of the EO-1, Landsat 7 intercomparisons, along with other results are displayed in Figure 3-121. The intercomparison results are consistent with solar, lunar, and ground truth measurements for Bands 1, 2, 3, and 7. The intercomparison also agrees with ground truth data but disagrees with the solar calibration data for Band 5.

3.2.2.6 Radiometric Stability

The radiometric stability of the ALI has been tracked since launch using the techniques outlined above. Solar calibrations occur every two weeks and began on January 9, 2001. Lunar calibrations occur monthly and began on January 28, 2001. Ground truth measurements occur approximately every 2 months and began on December 30, 2000. Internal reference lamp measurements have been taken daily since November 25, 2000. However, only internal lamp measurements taken one day after focal plane bakeouts are used in stability analyses. Table 3-23 provides the dates for each of the calibrations during the first year on orbit and Figure 3-122 graphically represents their distribution.

All solar, lunar, and ground truth calibration data presented here have had corrections applied to remove the radiometric effects of contamination on the instrument focal plane filter surfaces. Contamination of the focal plane has been observed throughout preflight and on-orbit testing of the instrument. However, it has been demonstrated that by raising the temperature of the focal plane above 250 K, the effects of contamination are removed. Furthermore, the effects of contamination on orbit have been monitored daily using the internal reference lamps. Figure 3-123 provides an example of the radiometric effects of contamination for Band 3 during the first year on-orbit.

Using the internal lamp data, a correction has been derived for each solar, lunar, and ground truth observation. This correction has been applied so that the intrinsic stability of the instrument may be tracked and compared using the various calibration techniques. Because the internal lamp data selected for trending is close to periods when the instrument is baked out, the effects of contamination are minimal for these data. The corrections applied to all bands are listed in Table 3-24.

Table 3-23
Dates of EO-1 ALI on-orbit radiometric calibrations during the first year on orbit

Mission Day Number	Technique	Mission Day Number	Technique
5	Internal Lamp	192	Solar
11	Internal Lamp	197	Lunar
29	Internal Lamp	199	Internal Lamp
39	Ground Truth	207	Ground Truth
50	Internal Lamp	207	Internal Lamp
50	Solar	211	Solar
56	Internal Lamp	223	Ground Truth
61	Internal Lamp	227	Internal Lamp
63	Ground Truth	228	Lunar
67	Internal Lamp	234	Solar
73	Solar	237	Internal Lamp
73	Internal Lamp	239	Ground Truth
79	Lunar	248	Internal Lamp
79	Internal Lamp	249	Solar
81	Solar	257	Lunar
87	Solar	259	Internal Lamp
87	Internal Lamp	264	Solar
93	Internal Lamp	270	Internal Lamp
101	Internal Lamp	278	Solar
102	Solar	280	Internal Lamp
106	Internal Lamp	286	Lunar
110	Lunar	286	Ground Truth
114	Solar	291	Solar
114	Internal Lamp	291	Internal Lamp
120	Internal Lamp	301	Internal Lamp
128	Solar	306	Solar
128	Internal Lamp	313	Internal Lamp
134	Internal Lamp	317	Lunar
138	Lunar	320	Solar
142	Internal Lamp	322	Internal Lamp
143	Solar	328	Internal Lamp
149	Internal Lamp	332	Internal Lamp
156	Solar	334	Solar
158	Internal Lamp	343	Internal Lamp
168	Internal Lamp	345	Solar
169	Lunar	346	Lunar
175	Ground Truth	353	Internal Lamp
179	Internal Lamp	360	Solar
180	Solar	366	Internal Lamp
188	Internal Lamp		

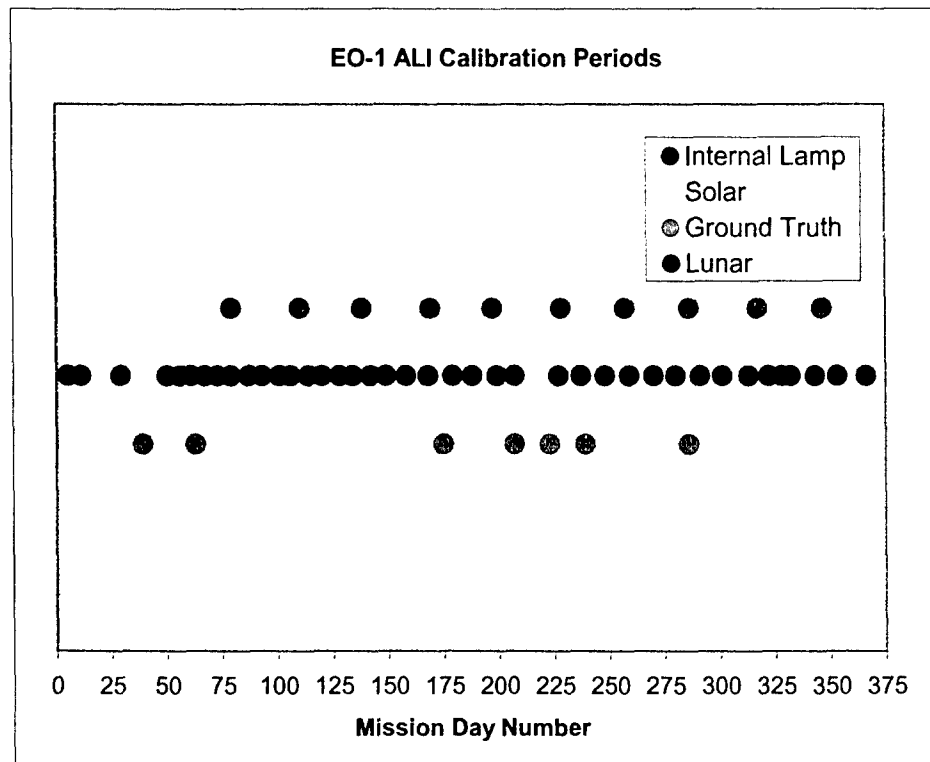


Figure 3-122. Radiometric calibration measurement periods during the first year on orbit.

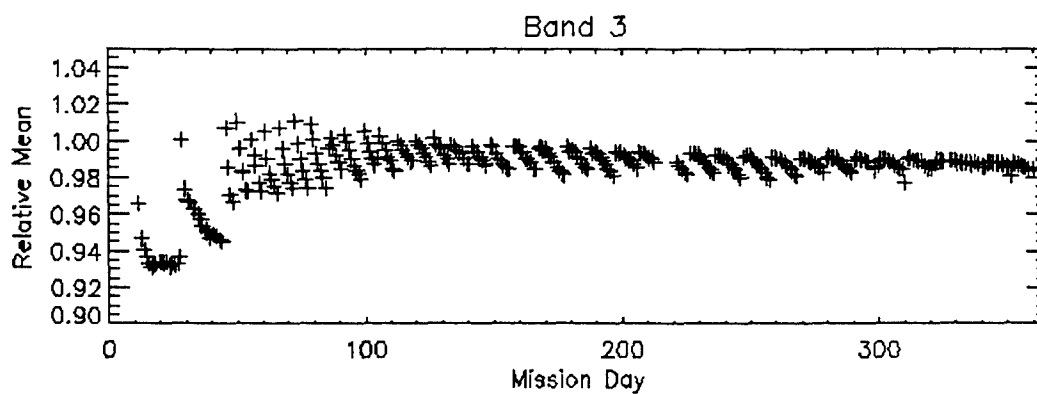


Figure 3-123. Effects of contamination on Band 3 data. Each point is derived from internal lamp data that has been ratioed to data obtained on Day 5 of the mission

Table 3-24
Radiometric corrections (%) used to remove contamination effects

Method	Day Number	Band									
		1p	1	2	3	4	4p	5p	5	7	Pan
Lunar	79	0.19	0.19	0.12	0.26	0.06	0.08	-0.09	-0.01	0.00	0.01
	110	0.86	1.18	1.19	1.70	1.47	1.65	0.47	0.90	0.75	1.71
	138	0.40	0.66	0.74	0.98	0.70	0.90	0.19	0.57	0.34	1.28
	169	0.03	0.17	0.00	0.35	0.13	0.33	0.17	0.30	0.30	0.58
	196	0.31	1.46	1.14	1.65	1.60	1.82	0.76	1.11	0.88	1.60
	228	-0.03	-0.14	-0.12	0.23	-0.02	0.19	0.01	0.15	0.08	0.36
	257	0.91	1.41	1.19	1.52	1.33	1.55	0.54	0.87	0.72	1.58
	286	0.15	0.52	0.47	0.58	0.24	0.49	0.32	0.58	0.47	1.02
	317	-0.37	0.49	0.45	0.42	0.11	0.36	0.39	0.59	0.36	0.80
	346	-0.47	0.18	0.14	0.11	-0.25	-0.06	0.31	0.29	0.05	0.37
Solar	50	-0.83	0.11	0.24	0.90	0.91	0.85	0.17	0.18	-0.04	0.53
	73	0.02	0.19	0.24	0.55	0.37	0.37	-0.14	0.04	-0.03	0.40
	81	1.00	1.23	1.11	1.62	1.37	1.49	0.32	0.61	0.45	1.29
	87	-0.52	0.43	0.60	0.57	0.48	0.54	0.29	0.26	0.03	-0.42
	102	0.68	0.84	0.83	1.21	1.00	1.12	0.31	0.57	0.37	1.19
	114	-0.30	0.40	0.40	0.64	0.47	0.62	0.12	0.32	0.05	0.67
	128	0.34	0.26	0.23	0.41	0.18	0.36	-0.03	0.16	-0.02	0.69
	143	0.45	0.50	0.42	0.61	0.33	0.54	0.15	0.37	0.19	0.86
	156	0.21	1.27	0.98	1.48	1.37	1.62	0.71	1.17	1.04	1.68
	180	-0.55	0.21	-0.07	0.35	0.25	0.45	0.25	0.35	0.06	0.41
	192	0.48	0.39	0.42	0.81	0.59	0.81	0.45	0.66	0.43	1.13
	211	0.22	0.28	0.24	0.58	0.31	0.58	0.31	0.56	0.37	0.92
	234	0.49	0.88	0.84	1.08	0.84	1.11	0.45	0.82	0.69	1.46
	249	-0.66	0.12	0.03	0.28	0.08	0.32	0.25	0.34	0.20	0.40
	264	0.07	0.72	0.61	0.71	0.48	0.73	0.50	0.70	0.47	1.05
	278	-0.11	0.94	0.81	0.96	0.78	1.03	0.47	0.83	0.52	1.31
	291	-0.09	-0.20	-0.06	0.13	-0.20	-0.04	0.08	0.11	0.16	-0.27
	306	-0.25	0.59	0.48	0.47	0.15	0.41	0.32	0.57	0.36	0.85
	320	0.82	0.94	0.62	0.60	0.17	0.42	0.26	0.57	0.42	1.06
	334	-0.56	0.18	0.12	0.15	-0.17	0.00	0.28	0.30	0.19	0.42
	345	0.41	0.28	0.15	0.11	-0.33	-0.14	0.27	0.19	0.03	0.39
	360	-0.20	0.58	0.57	0.49	0.13	0.34	0.51	0.66	0.32	0.88
Ground Truth	38	1.88	3.31	3.43	5.53	4.48	4.55	2.74	4.92	6.05	NA
	63	0.44	1.62	1.60	2.58	2.47	2.58	0.76	1.13	0.87	NA
	175	0.85	1.20	0.98	1.46	1.25	1.49	0.55	1.02	0.81	NA
	205	-0.04	0.87	0.80	1.15	1.05	1.29	0.54	0.91	0.69	NA
	223	0.84	1.09	0.85	1.07	0.81	1.08	0.54	0.87	0.69	NA
	239	-0.08	0.07	0.06	0.36	0.06	0.33	0.18	0.35	0.22	NA
	286	0.15	0.52	0.47	0.58	0.24	0.49	0.32	0.58	0.47	NA
	307	0.70	0.74	0.61	0.55	0.13	0.40	0.30	0.60	0.52	NA

*Ground truth Panchromatic data were not available for this analysis.

3.2.2.6.1 Solar Calibration

Solar calibration data have been trended at the SCA and pixel level. Initially, all solar calibration data for aperture selector position six are ratioed to the data obtained on July 12, 2001. The mean

of these ratios for each band and SCA is then plotted as a function of mission day number with standard deviations of the ratios used as 1-sigma error-bars. All data are normalized by the appropriate Sun-Earth distance correction factor corresponding to the day of the observation. The solar irradiance correction factor (F) is given by the approximation:

$$F = [1 + e \cos((d-4)360^\circ/365)]^2 / [1 - e^2]^2$$

where d is the day of the year and $e = 0.01671$ is the eccentricity of the Earth's orbit. The distance correction factors used in this analysis are shown in Figure 3-124. Figure 3-125 depicts solar calibration results for SCA 1 of Band 3 for the first year on orbit. The original data as a function of mission day number is provided in the top graph. Normalized data are depicted in the second graph, and the residual errors to a linear fit to the data in the lower graph.

In order to identify sub-SCA response changes, a linear fit is performed on the data of individual detectors as a function of mission day number. The slope of each fit is then displayed as a function of cross-track position and examined for sub-SCA trends. Figure 3-126 depicts instrument level response changes as a function of cross-track position for Band 3 using the solar calibration technique.

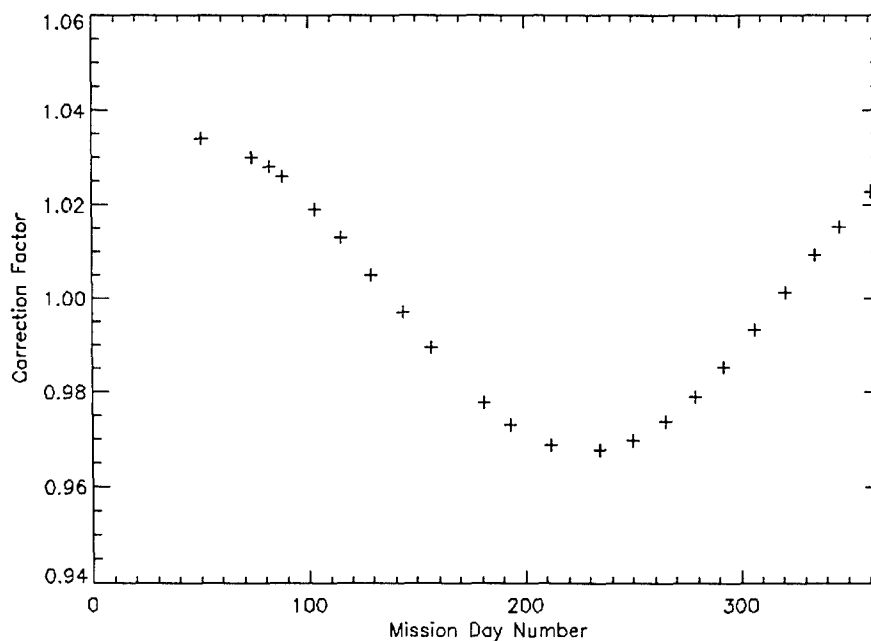


Figure 3-124. Solar calibration correction factors.

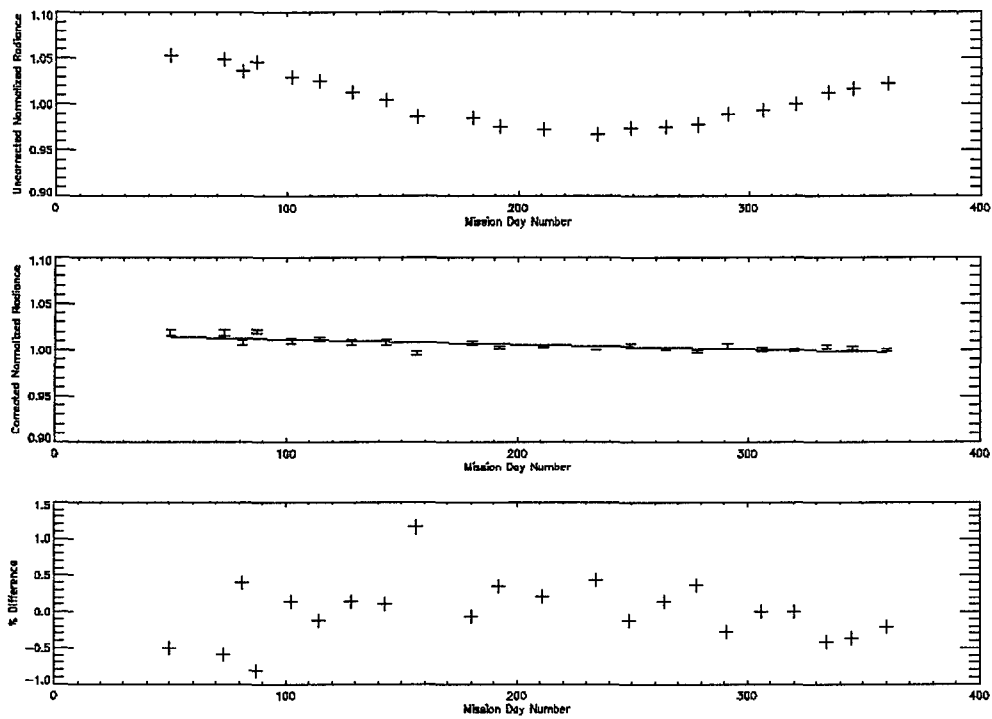


Figure 3-125. Instrument response stability for Band 3 based on solar calibration data.

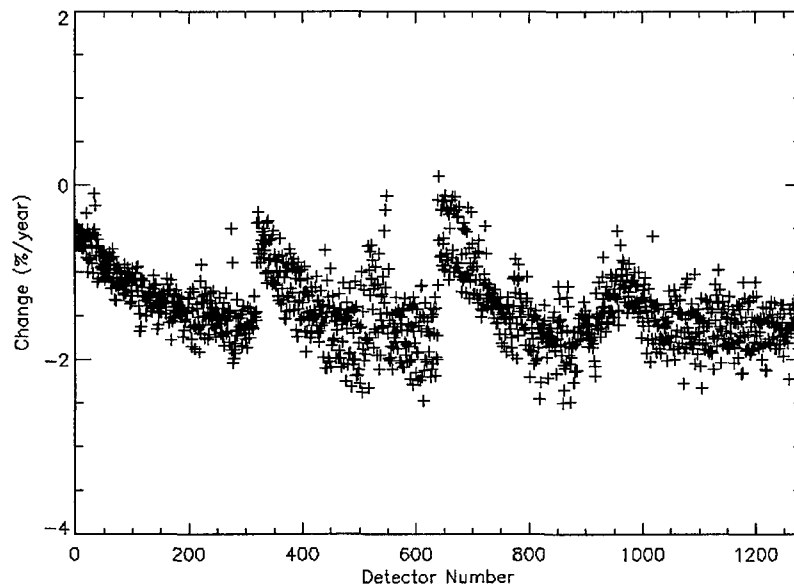


Figure 3-126. Change in instrument response for Band 3 derived from solar calibration data.

3.2.2.6.2 Ground Truth

No correction factors are required to trend ground truth data. All Sun-Earth separation, atmospheric, and site reflectivity corrections are accounted for in the University of Arizona analysis. Unfortunately, because only a small region of a target may be characterized for an overflight, only portions of the focal plane may be sampled using the ground truth reflectance-based calibration techniques. Figure 3-127 depicts the ground truth data for Band 3 as a function of mission day number for the first year in the top graph and the residual errors to a linear fit to the data in the lower graph.

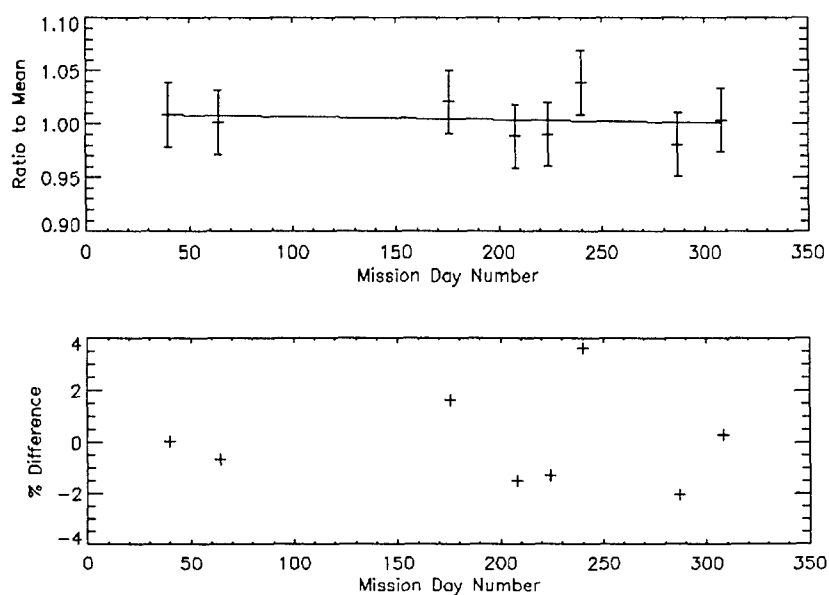


Figure 3-127. Instrument response stability for Band 3 based on ground truth measurements.

3.2.2.6.3 Lunar Calibration

No additional correction factors are required for lunar calibration trending. The spectral irradiance derived from ALI data is simply compared to the expected lunar irradiance, provided by the ROLO model. Because the Moon fills over 2/3 of an SCA, pixel level response changes cannot be monitored using this technique. However, SCA level trending may be accomplished and has been performed for the first year on orbit. Figure 3-128 depicts the lunar calibration data for Band 3 as a function of mission day number for the first year in the top graph and the residual errors to a linear fit to the data in the lower graph.

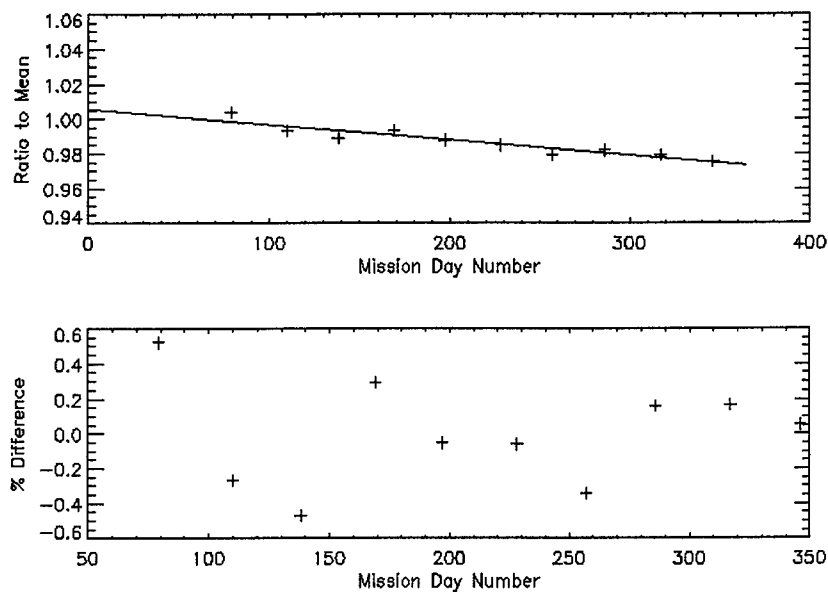


Figure 3-128. Instrument response stability for Band 3 based on lunar calibration measurements.

3.2.2.6.4 Internal Reference Lamp Illumination

Internal reference lamp data have been trended on the SCA and pixel level. Initially, all lamp data taken one day after each focal plane bakeout are ratioed to the data obtained on July 12, 2001. The mean of these ratios for each band and SCA is then plotted as a function of mission day number with standard deviations of the ratios used as 1-sigma error-bars. No correction factors are required to trend this data. Figure 3-129 depicts reference lamp results for Band 3 for the first year on orbit. The original data as a function of mission day number is provided in the top graph and the residual errors to a linear fit to the data in the lower graph.

In order to identify sub-SCA response changes, a linear fit is performed on the data of individual detectors as a function of mission day number. The slope of each fit is then displayed as a function of cross-track position and examined for sub-SCA trends. Figure 3-130 depicts instrument level response changes as a function of cross-track position for Band 3 using the reference lamp data.

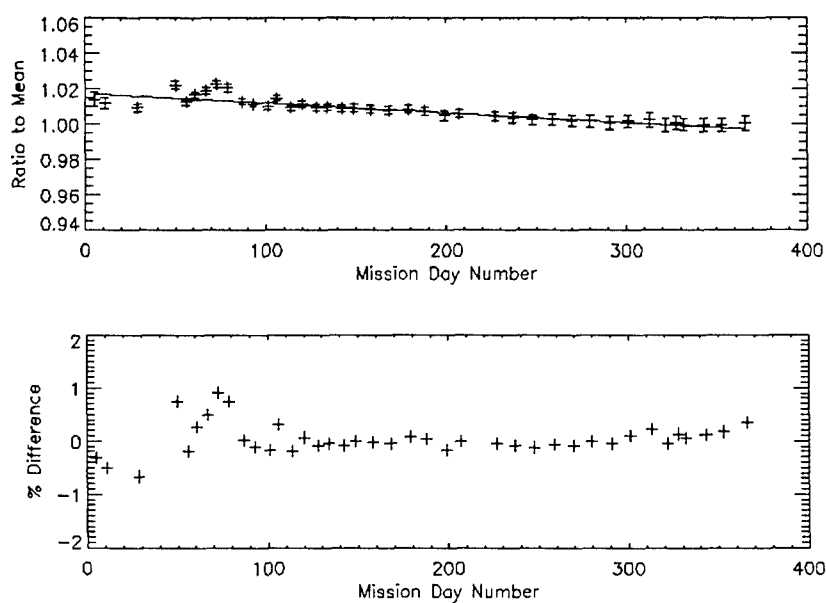


Figure 3-129. Instrument response stability based on internal reference lamp data.

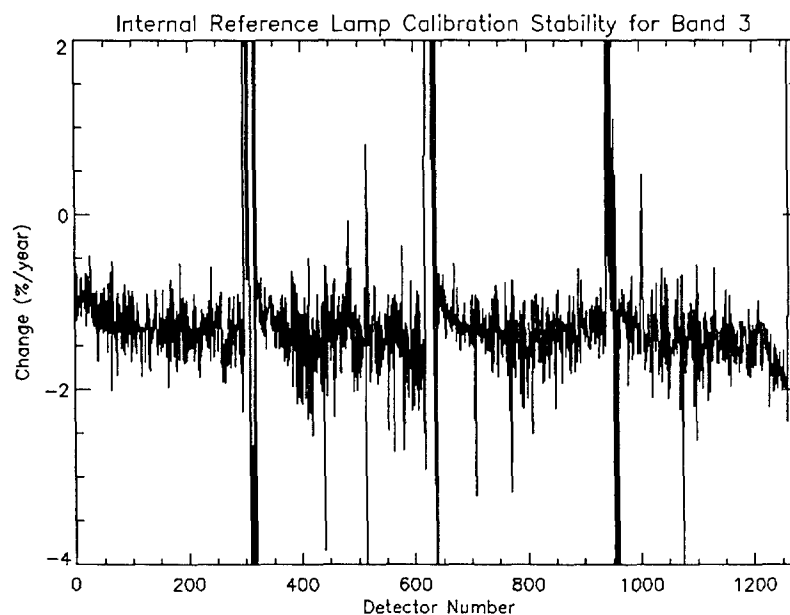


Figure 3-130. Change in instrument response for Band 3 derived from internal reference lamp data.

3.2.2.6.5 Comparison of Results

In an effort to demonstrate results at the SCA level and derive additional information pertaining to the radiometric stability of the instrument from the combination of various calibration techniques, SCA 1 data for Bands 2 and 3 for all of the techniques described above have been

overlaid in Figures 3-131 and 3-132. Linear fits to the data from combined internal lamp and solar calibration data are overlaid in each graph. Table 3-25 tabulates these results.

In order to demonstrate sub-SCA trending, cross-track solar calibration and internal reference lamp data for Bands 2 and 3 have been overlaid in Figures 3-133 and 3-134.

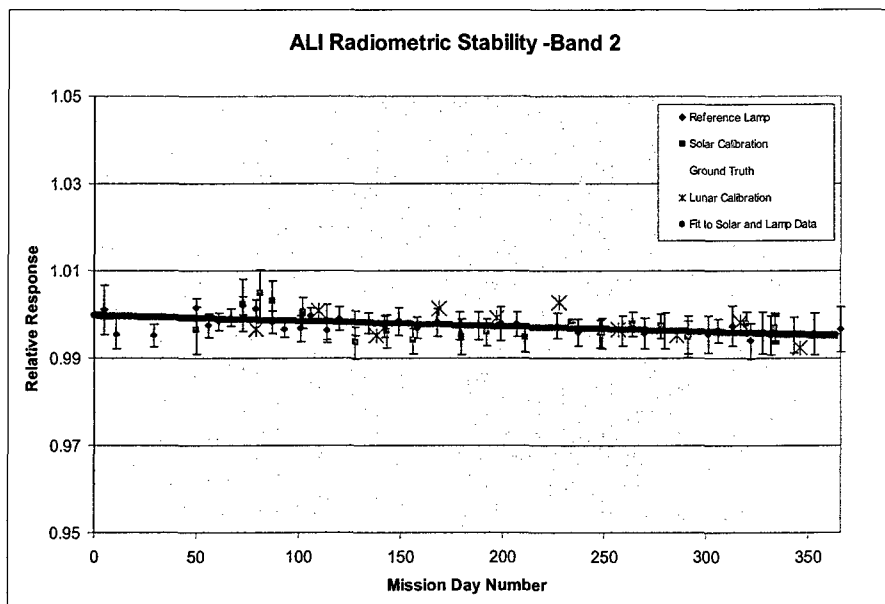


Figure 3-131. Trending of ALI radiometric calibration data for Band 2.

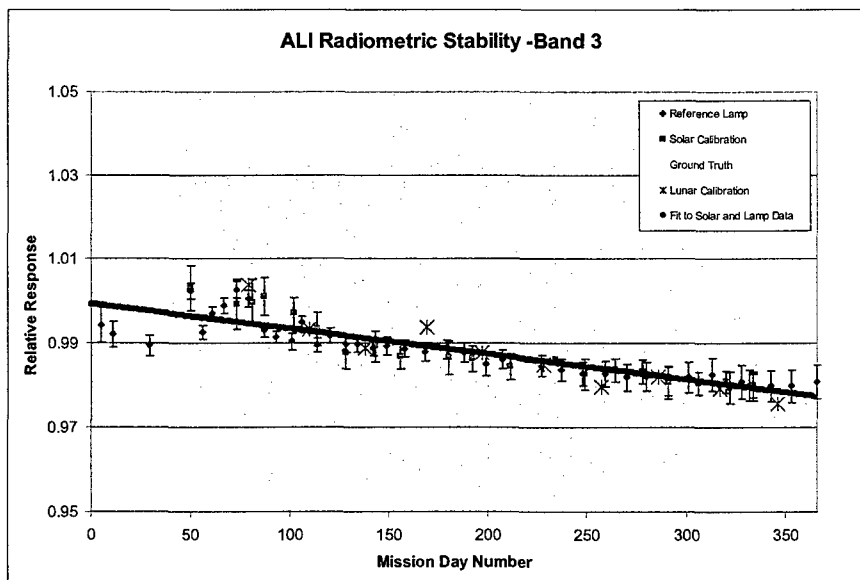


Figure 3-132. Trending of ALI radiometric calibration data for Band 3.

Table 3-25
Radiometric stability trending for the first year on-orbit

Band	Response Change (%/year)
1p	-0.80
1	-0.75
2	-0.45
3	-2.20
4	-3.04
4p	-3.10
5p	-0.72
5	-0.59
7	0.02
Pan	-0.71

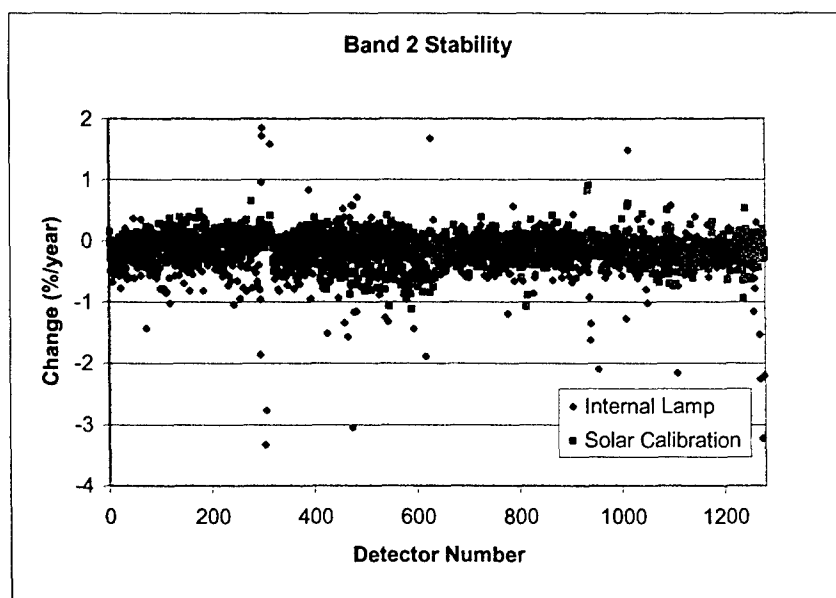


Figure 3-133. Radiometric stability of detectors for Band 2 as determined by internal lamp and solar calibration data collected during the first year on orbit.

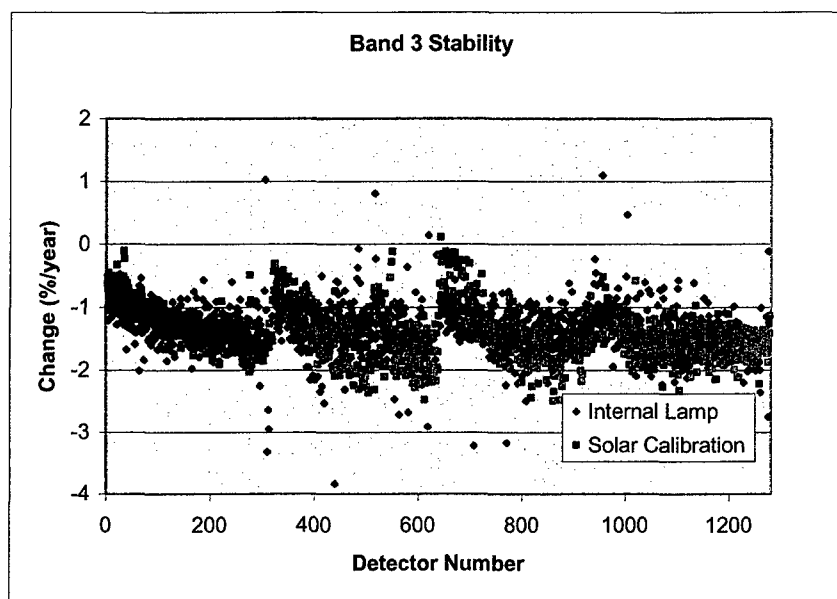


Figure 3-134. Radiometric stability of detectors for Band 3 as determined by internal lamp and solar calibration data collected during the first year on orbit.

3.2.2.6.6 Comments

The absolute radiometry of the Advanced Land Imager has been extensively examined during the first year the instrument was on-orbit, using solar, lunar, and ground truth calibration techniques. Results from each method agree within experimental errors and indicate an 18% drop in the Band 1p response of the instrument since pre-flight characterization. Although one could argue the Spectralon diffuser used in the solar calibration technique could have become contaminated during ground testing or launch, radiometric calibration data that do not involve the diffuser (e.g. ground truth and lunar observations) also observe a similar Band 1p change. This exonerates the diffuser and suggests the change has occurred elsewhere in the instrument. Additionally, because the solar calibration technique does not employ the secondary mirror, this component is the only element within the optical chain that cannot be responsible for the observed change.

The on-orbit calibration data also reveal a small drooping of the VNIR band responses (other than Band 1p) towards the blue. The highest of these is a 5% decrease in radiometric response for Band 1. Again, because ground truth, lunar and solar data reveal similar changes, only the diffuser and secondary mirror can be eliminated as sources for these changes.

Finally, the on-orbit Band 5 response is consistently 5-12% higher than the response measured during pre-flight calibration. It is interesting to note the change in response as measured by the solar calibration technique are consistently 7% lower than ground truth and lunar calibration data. The source of this difference is not understood at this time.

3.2.2.6.6.1 Sources of Radiometric Differences

There are several possible sources of the radiometric discrepancies between preflight and flight measurements. The three leading candidates are 1) errors in the preflight calibration of the instrument, 2) stray light, and 3) a change in the instrument response. The preflight radiometric calibration of the ALI is based on the knowledge of the radiance emitted by a 30" diameter integrating sphere at several emission levels. To validate this knowledge, the NASA/Goddard developed Landsat Transfer Radiometer (LXR) was brought to Lincoln Laboratory and used to measure the sphere radiance. The LXR measurements agreed with the pre-flight spectroradiometer measurements to within $\pm 2\%$ for all eight of the LXR VNIR bands for three sphere intensity levels. This agreement includes an LXR band 10 nm wide centered at 440 nm, equivalent to Band 1p of the ALI. The good agreement suggests the pre-flight calibration of the ALI was well understood and measurement uncertainties cannot account for the apparent radiometric changes on orbit in the VNIR.

Another possible source of error in ALI radiometry on orbit is stray light. One technology being demonstrated by the ALI is large, wide field-of-view silicon carbide optics. Extensive pre flight measurements of the BRDF for the optical elements were made. These data were used in a system level analysis to assess the impact of stray light on flight observations. A model was developed to estimate the error in measured scene radiance as a function of the ratio of scene radiance to background radiance. This effect can be significant for dim regions of scenes with high contrast. The details of the characterization and effects of stray light on flight data are presented in Section 3.2.2.4. However, it can be stated that the effects of stray light on absolute radiometric data presented here are small. Solar and internal lamp data are diffuse scenes obtained with the aperture cover closed. Ground truth and lunar observations are bright targets in dim backgrounds, minimizing the effects of stray light from outside the target field.

The final source of observed discrepancies between preflight and flight calibration measurements is a real response change within the instrument. This includes a change in the reflectivity of the mirrors, the spectral bandpasses of the filter assemblies, or the responsivity of the detector arrays. Contamination of the top surface of the focal plane filters has been detected since initial instrument thermal vacuum testing. Trending of internal lamp data indicate that a gradual build-up of material occurs when the focal plane is operated below 250 K. This data also reveals that the contaminant is virtually removed by raising the temperature of the focal plane for a 20-hour period every ten days on orbit. This chronic problem raises suspicions relating to the apparent permanent change in instrument response since preflight calibration. However, internal reference lamp trending indicates the reflectivity of flat mirror (M4) and the response of the focal plane remained stable to within 1% for bands 1p, 1, 2, 5p, 5, 7, pan, and within 3% for bands 3, 4, 4p since launch. Unfortunately, the observed increase in internal lamp intensity after launch prohibits one from extending focal plane response trending from preflight calibration to on orbit. However, trending does exist from preflight calibration at Lincoln Laboratory in December 1998 through the second spacecraft thermal vacuum test at Goddard Space Flight Center in July 2000 (4 months before launch). This data indicates M4 and the focal plane have remained stable to within 2% during ground testing. Furthermore, solar, lunar, and ground truth data trending, which exercise other elements of the optical train, suggest M1, M2, M3, and the solar diffuser have been stable to within 1% since the first on-orbit calibrations in late December 2000. As a

result, if a response change did occur within the instrument, it must be restricted to between July 2000 and November 21, 2000 if the change occurred on M4 or the focal plane or it must be restricted to between December 1998 and December 29, 2000 if the change occurred on M1, M2, or M3.

Although the cause of the preflight to flight radiometric calibration discrepancy is not clearly understood, the stability of the instrument suggests a single radiometric correction to the preflight calibration coefficients for each band will provide $\pm 5\%$ agreement between measured solar, lunar and ground truth data and expected values during the first year on orbit. Each band's correction factor has been derived by first developing a calibration error model as a function of the ratio of target to background radiances for a variety of scenes by comparing Landsat 7 ETM+ data to ALI data and including solar, lunar, and ground truth measurements. The target radiance is defined as the mean radiance of a small region of interest, usually only tens of pixels in diameter. The background radiance is defined as the mean radiance of a three degree region centered on the target. This error model includes effects of stray light and absolute radiometric offsets. A detailed description of the calibration error model is described in Section 3.2.2.4. Figure 3-135 depicts the calibration error model developed for Band 3, overlaid with flight data. Once the model is defined, a band's absolute radiometric correction factor is defined as the calibration error for a target to background ratio of 1.0. In order to account for the observed slight linear decrease in radiometric response as revealed in the stability data, the correction factors are then normalized to the predicted June 1, 2001 response level for each band.

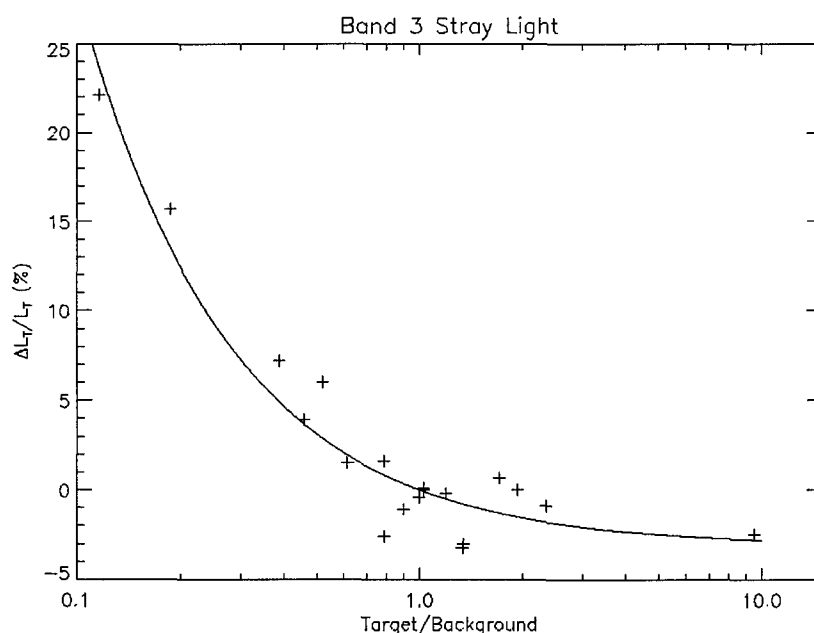


Figure 3-135. Band 3 radiometric error model and flight data.

Table 3-26 lists the radiometric correction factors derived using the above technique. These factors have been used to update the preflight radiometric coefficients residing in the EO-1 ALI Radiometric Calibration Pipeline. Figure 3-136 depicts the results of solar, lunar, and ground truth testing once the on-orbit data has been processed using the updated calibration coefficients. As one may see, the agreement between the methods of calibration outlined above to ALI observations using the new coefficients is within $\pm 5\%$ for all bands, except Band 5. For this band the solar calibration data still differ from ground truth and lunar data by 7%.

Table 3-26
Radiometric correction factors used to update preflight calibration coefficients

Band	Correction Factor
1p	1.21
1	1.07
2	1.05
3	1.04
4	1.02
4p	0.99
5p	0.98
5	0.87
7	0.98
Pan	1.05

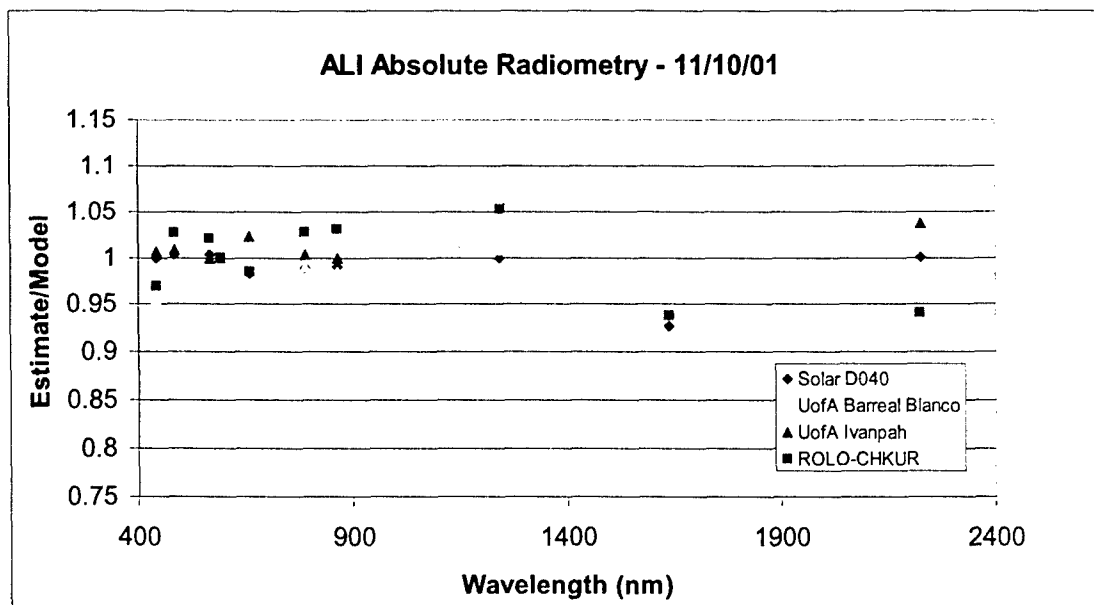


Figure 3-136. Results of ALI absolute radiometric calibration after the corrections to pre-flight calibration coefficients are applied.

3.2.2.6.6.2 Stability

The ALI stability measurements using solar, lunar, ground truth, and internal lamp data are in good agreement. All methods indicate excellent stability (<1 %/year) for Bands 1p, 1, 2, 5p, 5, 7, pan. However, solar and lunar data indicate a 2-3 % change per year for Bands 3, 4, 4p. Because the internal lamp data also track this trend, these changes can be isolated to the flat mirror and/or focal plane. Ground truth data also suggest these trends, but longer timelines are necessary to strengthen this result.

The Band 3, 4, 4p linear decrease in response should be monitored and correction factors applied to these data as a function of mission day number in order to preserve the absolute radiometric accuracy of ALI data for these bands.

Stability measurements also reveal 1 %/year long-term intra-SCA variations for Bands 3, 4, 4p (Bands 5p, 5, 7 to a lesser degree). These variations are consistent between solar and internal lamp data, isolating the source to the flat mirror and/or the focal plane. These variations appear similar to the effects of contamination build-up observed during preflight calibration of the instrument. This suggests a slow, low-level build-up of a contamination layer may be occurring on the focal plane filter surfaces for these bands. This effect will result in the degradation of the ALI detector-to-detector radiometric accuracy or 'flat-fielding' as a function of mission day number. This will manifest itself as 1) 'cupping' within an SCA and 2) SCA to SCA boundaries becoming evident for scenes that would normally be considered radiometrically flat. These effects can be mitigated by correcting the intra-SCA radiometric calibration coefficients every six months.

3.2.2.6.6.3 Calibration Methods

Of the four radiometric calibration techniques described above, the internal reference lamps and the solar calibration methods are the simplest. Although the internal reference lamps are very stable, the apparent increase in lamp brightness after launch resulted in the loss of the absolute radiometric transfer capability from preflight to on-orbit. Additionally, these lamps only sample the flat mirror and the focal plane and cannot be used as a monitor of the overall instrument stability. However, they have proven to be extremely valuable in tracking the build-up of contamination on the focal plane filters and also in monitoring the focal plane stability on a daily basis. Additionally, because the reference lamps illuminate most of the focal plane, analysis of these data may be used to identify sub-SCA radiometric response changes.

The solar calibration technique is particularly attractive since it requires only the Sun-Earth $1/r^2$ distance correction factor to trend data as a function of time. Additionally, this method provides a seven point radiometric linearity check for each detector for most bands and provides a means for identifying sub-SCA response changes at the instrument level. Although this technique does employ a Spectralon diffuser that is easily contaminated, the location of the diffuser within the telescope cavity helps to shield the diffuser surface from spacecraft contaminants as well as Solar and Earth-reflected ultraviolet radiation.

Lunar calibration is an attractive radiometric calibration method since the Moon is geologically stable, and spectrally flat. The data presented here also suggest lunar observations are a good tool for tracking the stability of the instrument. However, this technique is only now maturing and being integrated into spacecraft calibration plans. As a result, uncertainties related to the absolute calibration of the moon still exist at this time. Furthermore, the lunar calibration method can only be used to identify radiometric response changes for detectors illuminated by the lunar disk and for the region of the focal plane used to integrate the lunar signal.

Perhaps the most complex method of absolute radiometric calibration is the ground-based reflectance method. This requires precise field measurements, atmospheric modeling, and radiative transfer propagation in order to account for temporally varying surface reflectivities and atmospheric conditions. Furthermore, this method is restricted to the region of the scene characterized by the field measurements and cannot be used to identify response changes for the entire ALI field of view. However, this technique is critical for validating solar and lunar calibration data and in some cases is the only method available for monitoring the radiometric accuracy and stability of instruments whose on-board calibration systems had failed or become unreliable.

3.2.2.7 Discussion

The radiometric performance of the Advanced Land Imager has been investigated using several on-orbit techniques. Excellent sensitivity has been demonstrated by imaging cities at night as well as stars and extra-Terran planets. Stability measurements indicate the instrument has been stable to within 3% since launch for all bands.

Solar, lunar, ground truth, and intersatellite radiometric measurements all agree within experimental error in the VNIR and suggest a slight drop in the blue response from pre-flight calibration measurements. Additionally, solar and lunar calibration data indicate a significant drop in Band 1p response.

3.3 ON-ORBIT USAGE EXPERIENCE

The ALI has undergone significant testing during the first twelve months in orbit. This section provides a summary of the electrical and mechanical operations, detector trending, and contamination monitoring between November 21, 2000 and November 21, 2001.

3.3.1 Electrical and Mechanical Operations

3.3.1.1 ALI Electronics

On November 25, 2000 (Day 5 of the mission) the ALI was powered for the first time on orbit. As of November 21 2001, the ALI Control Electronics (ALICE) has been powered continuously for 8640 hours. The focal plane electronics (FPE) is only powered during data collection events or DCEs. 2271 DCEs have been collected for a total FPE powered time of 303 hours.

3.3.1.1.1 Mechanisms and HOPAs

The ALI has three mechanisms and six High Output Paraffin Actuators or HOPAs. The primary mechanism is the aperture cover. The aperture cover has been exercised 2361 times. During solar calibrations, the solar diffuser and aperture selector mechanisms are exercised. These mechanisms have been used 22 times. The HOPAs are used as launch latches for the aperture cover (2) and solar diffuser (1), and as failsafe latches for the aperture cover (2) and solar diffuser (1). One aperture cover and one solar diffuser launch latch were successfully deployed on November 25, 2000.

3.3.1.1.2 Internal Reference Lamps

The internal reference lamps are used as focal plane stability as well as contamination build-up monitors. Until May 15, 2001 these lamps were exercised as a part of each data collection event. In order to preserve the life of the Krypton bulbs in the event of an extended mission, the lamps are now exercised one or two times per day. As of November 21, 2001 the internal reference lamps had been exercised 1135 times. Trending data for periods when the focal plane is not contaminated indicate that the internal reference lamps have been stable to within 1% for all bands.

3.3.2 Detector Trending

The trending of focal plane dark current data has been used to assess detector stability. In this section, we present noise and dark current stability trending and contrast mean values, obtained in November 2000, with those determined from pre-flight characterization. Dark current stability over one-half orbit period is also investigated.

3.3.2.1 Dark Current and Noise Trending for the First 60 Days

This section provides detector noise and dark current trending results of the Advanced Land Imager during its first sixty days in orbit (November 21, 2000–January 19, 2001). Data are trended for each of the ten spectral bands and each of the four sensor chip assemblies. Additional information may be found on the EO-1-7 project report [16].

3.3.2.1.1 Methodology

The noise and dark current of the Advanced Land Imager have been trended using dark current data collected as a part of daily Earth scene observations. During a typical data collection event or DCE, two seconds of dark current are collected before and after the Earth scene is imaged. These dark currents are used to establish baselines for all detectors for the corresponding observation and are also used to monitor the noise of the focal plane over time. For each DCE, the data from the second two-second dark period is used for the trending in this report*.

* All SWIR detectors have a transient effect associated with the initial data collected following the focal plane turn-on. Additionally, ground processing sometimes requires fill data to be added to the end of each data set. As a result, the first and last twenty-five frames from all data sets have been excluded from trending analysis.

The focal plane has been divided into several sections for this analysis, owing to the different noise and dark current produced by different detectors. For the noise analysis, the focal plane is divided by band and SCA. For the dark current analysis, odd and even detectors are treated separately for all bands. Results for the Panchromatic band have been additionally divided by tri-reads (each Panchromatic detector is read three times for each Multispectral detector read. Each tri-read results in a different dark current value for each detector.). Finally, SCA 4 for the SWIR bands has been divided into four sections to account for the enhanced dark current values observed near detector 1200.

For each data collection event, the noise has been calculated as the mean of individual detector noise values and the dark current has been calculated as the mean of individual detector dark current values. Data collection event numbers, calendar dates and days since launch are provided as a reference in Table 3-27.

Table 3-27
Data collection event dates

Year	GMT Day	Day*	DCE Count
2000	330	5	1-3
	331	6	4
	336	11	5-6
	337	12	7-8
	338	13	9-10
	339	14	11-12
	340	15	13-14
	341	16	15-17
	342	17	18-20
	343	18	21
	344	19	22-23
	345	20	24-27
	346	21	28-29
	347	22	30-32
	348	23	33-36
	349	24	37-41
	350	25	42-44
	351	26	45-46
	352	27	47-51
	353	28	52-54
	354	29	55-59
	355	30	60-63
	356	31	64-66
	357	32	67-70
	358	33	71-74
	359	34	75-79
	360	35	80-87
	361	36	88-92
	362	37	93-98
	363	38	99-103
	364	39	104-110
	365	40	111-116
	366	41	117-119
2001	001	42	120-123
	002	43	124-129
	003	44	130-137
	004	45	138-143
	005	46	144-150
	006	47	151-154
	007	48	155-159
	008	49	160-164
	009	50	165-168
	010	51	169-172
	011	52	173-178
	012	53	179-185
	013	54	186-192
	014	55	193-198
	015	56	199-203
	016	57	204-207
	017	58	208-213
	018	59	214-217
	019	60	218-224

*Since launch.

3.3.2.1.2 Noise Trending

The results of the ALI focal plane noise trending are provided in Figures 3-137 to 3-146 and Table 3-28. Each figure depicts the results of an individual band. Within each figure, the results for each sensor chip assembly are provided. Table 3-28 lists the mean and standard deviation of noise values, grouped by bands, in a similar fashion.

The mean noise value levels for all bands and SCAs is less than 1 digital number, except for the Panchromatic Band on SCA 3 (1.15 digital numbers) and Band 7 SCAs 1, 2, and 4 (1.06, 1.09, and 1.01 digital numbers, respectively). The standard deviation of detector noise is less than 0.05 digital numbers for all VNIR bands and SCAs. The repeatability of some SWIR SCAs is slightly higher with a maximum standard deviation of 0.099 digital numbers for Band 7, SCA 2.

The apparent systematic increase in detector noise across several spectral bands for some particular DCEs is the result of focal plane outgassing performed at the times of those observations. All ALI detectors were heated to 270 K five times during the first sixty days in orbit to drive-off contaminant build-up on the focal plane filter surfaces. This heating resulted in increased detector dark current and noise, particularly in the short wave infrared bands (5p, 5, 7). Outgassing periods correspond to DCE numbers 55, 140, 160, 190, and 219.

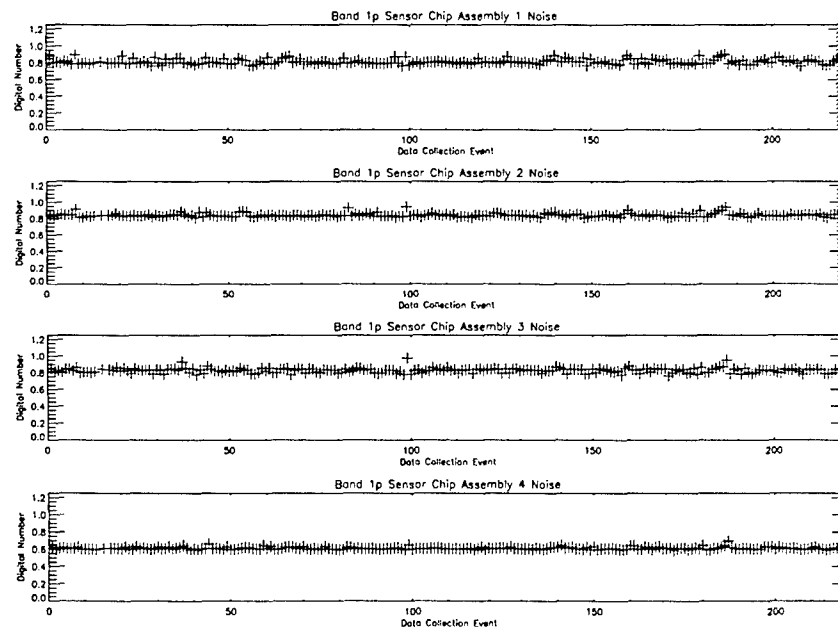


Figure 3-137. Noise trending for Band 1p. Detector outgassing occurred near DCE 55, 140, 160, 190, and 219.

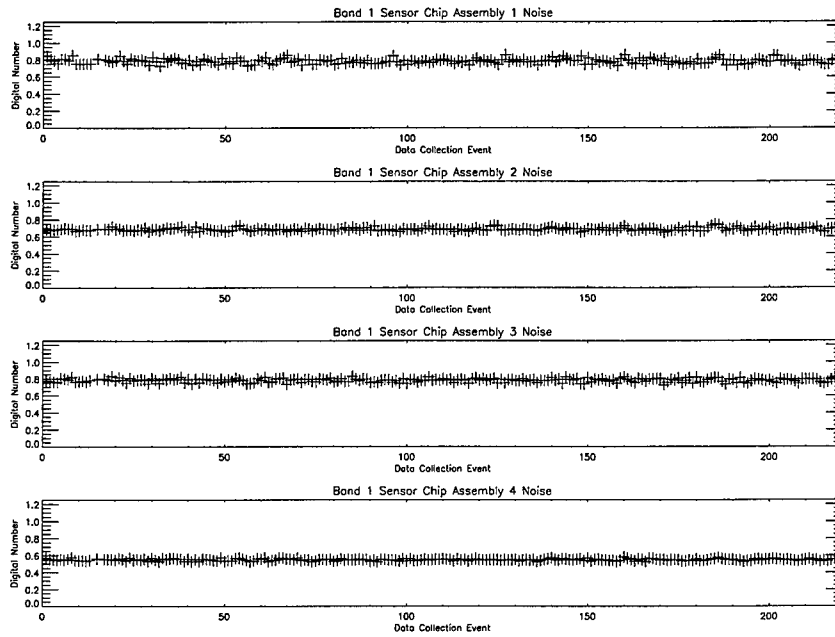


Figure 3-138. Noise trending for Band 1. Detector outgassing occurred near DCE 55, 140, 160, 190, and 219.

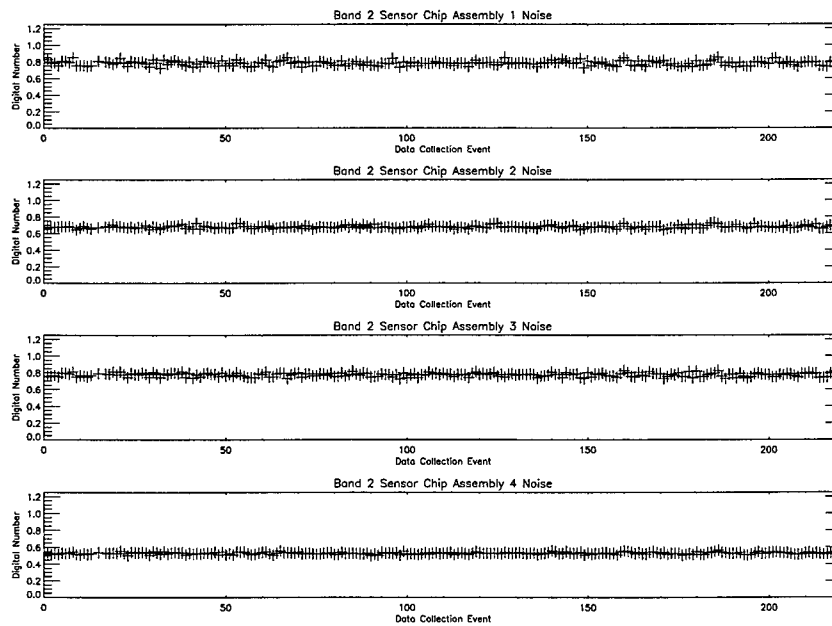


Figure 3-139. Noise trending for Band 2. Detector outgassing occurred near DCE 55, 140, 160, 190, and 219.

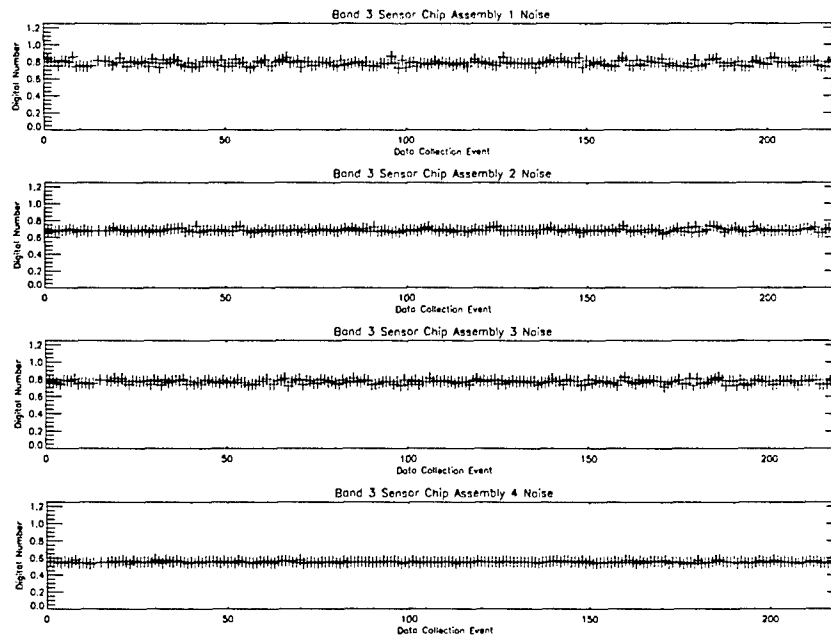


Figure 3-140. Noise trending for Band 3. Detector outgassing occurred near DCE 55, 140, 160, 190, and 219.

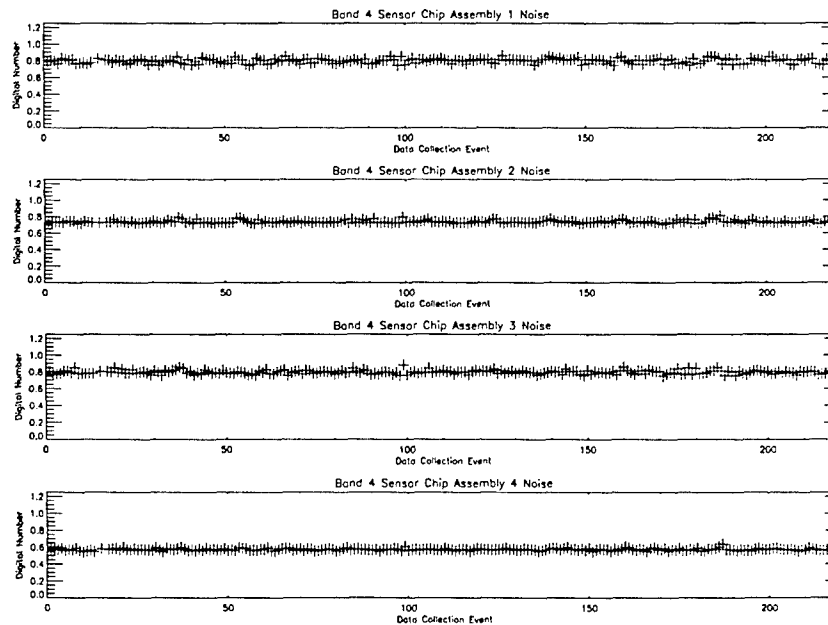


Figure 3-141. Noise trending for Band 4. Detector outgassing occurred near DCE 55, 140, 160, 190, and 219.

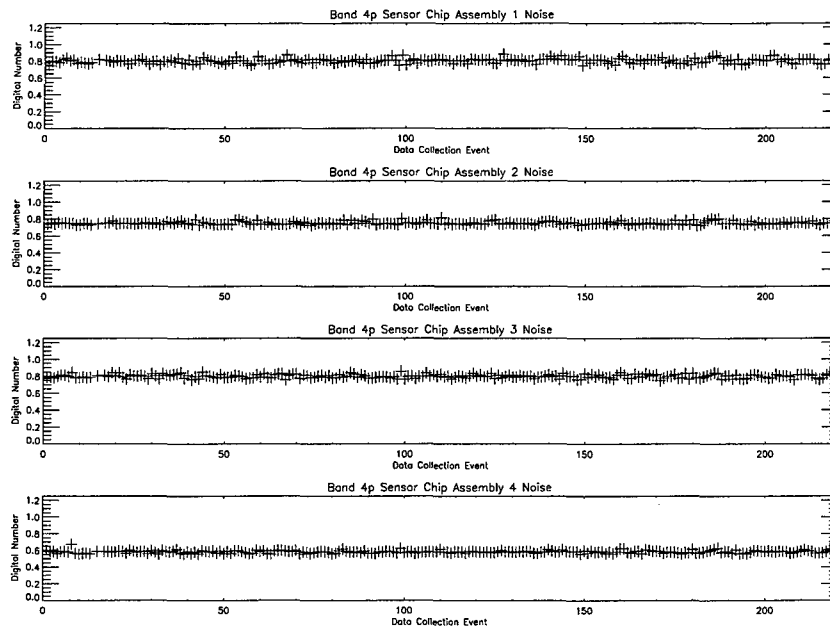


Figure 3-142. Noise trending for Band 4p. Detector outgassing occurred near DCE 55, 140, 160, 190, and 219.

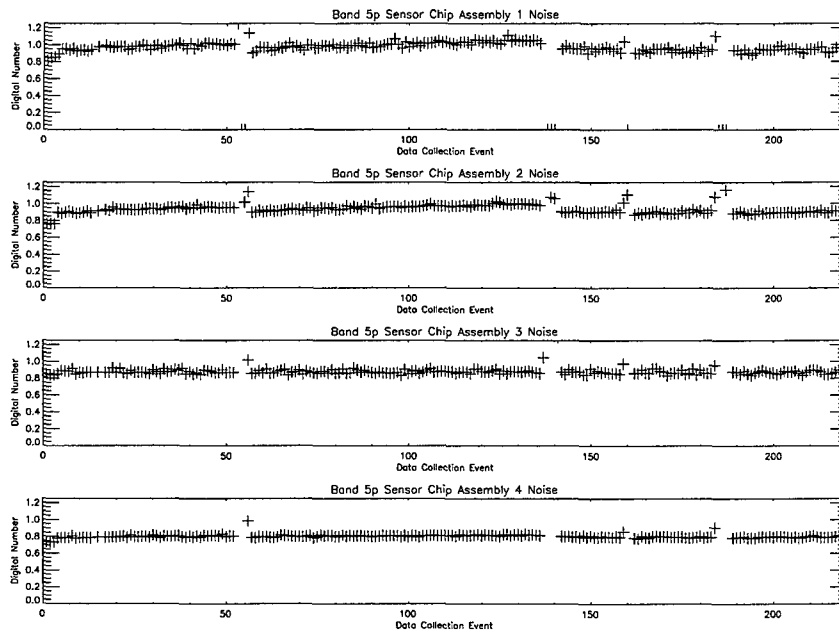


Figure 3-143. Noise trending for Band 5p. Detector outgassing occurred near DCE 55, 140, 160, 190, and 219.

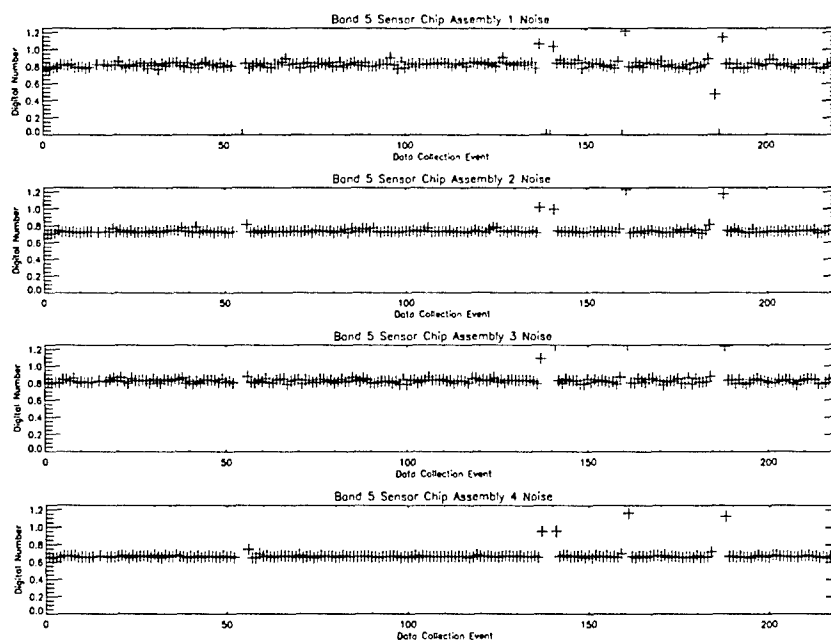


Figure 3-144. Noise trending for Band 5. Detector outgassing occurred near DCE 55, 140, 160, 190, and 219.

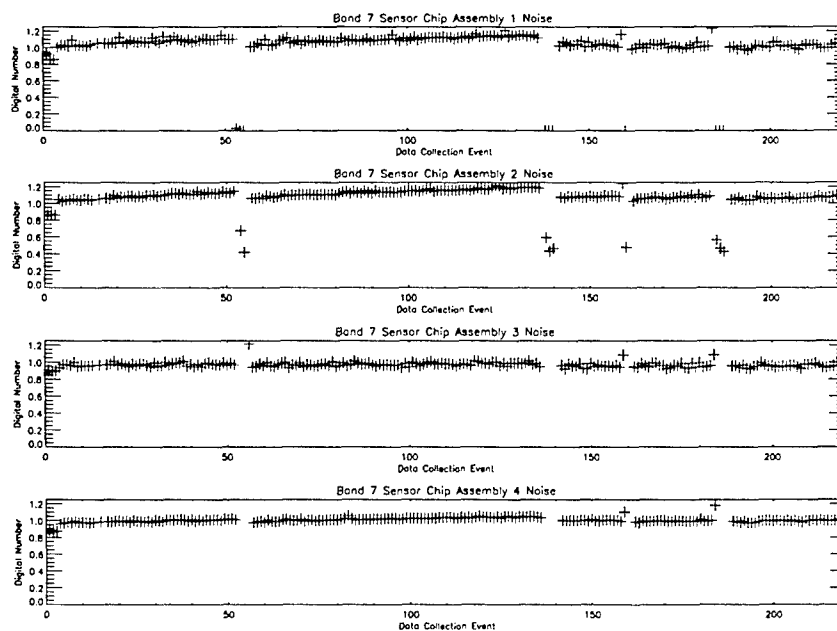


Figure 3-145. Noise trending for Band 7. Detector outgassing occurred near DCE 55, 140, 160, 190, and 219.

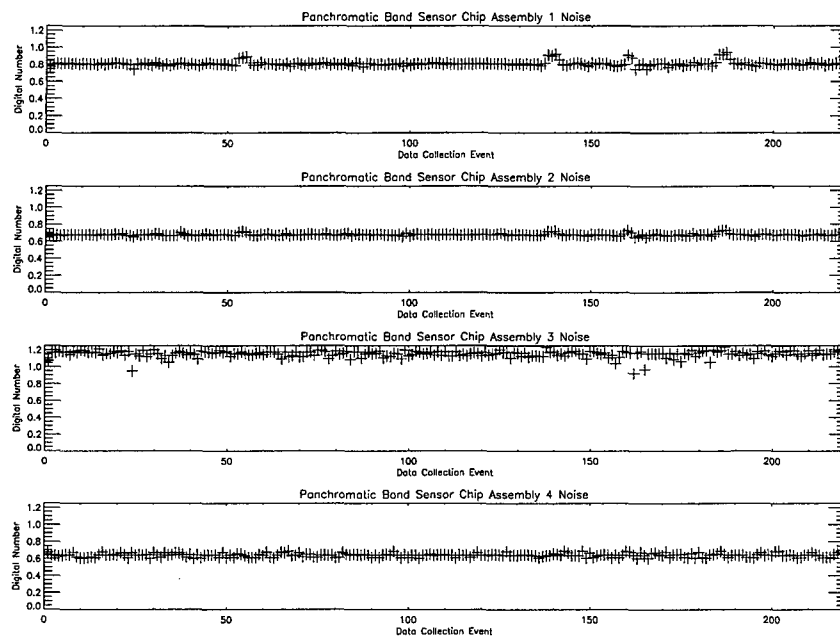


Figure 3-146. Noise trending for the Panchromatic Band. Detector outgassing occurred near DCE 55, 140, 160, 190, and 219.

Table 3-28
Noise trending statistics

Band	SCA	Preflight Mean (Digital Number)	Flight Mean (Digital Number)	Flight Std. Deviation (Digital Number)
1p	1	0.88	0.81	0.030
1p	2	0.86	0.84	0.022
1p	3	0.91	0.83	0.028
1p	4	0.60	0.61	0.014
1	1	0.83	0.78	0.029
1	2	0.73	0.69	0.017
1	3	0.87	0.78	0.021
1	4	0.54	0.55	0.012
2	1	0.82	0.78	0.028
2	2	0.70	0.68	0.017
2	3	0.84	0.77	0.022
2	4	0.53	0.53	0.012
3	1	0.83	0.78	0.030
3	2	0.72	0.69	0.018
3	3	0.85	0.77	0.022
3	4	0.55	0.55	0.010
4	1	0.86	0.80	0.029
4	2	0.77	0.74	0.019
4	3	0.88	0.80	0.022
4	4	0.57	0.57	0.013
4p	1	0.85	0.80	0.027
4p	2	0.78	0.75	0.018
4p	3	0.87	0.80	0.022
4p	4	0.58	0.58	0.016
5p	1	0.92	0.97	0.042
5p	2	0.83	0.94	0.031
5p	3	0.92	0.88	0.021
5p	4	0.75	0.81	0.025
5	1	0.87	0.83	0.035
5	2	0.75	0.74	0.035
5	3	0.89	0.83	0.037
5	4	0.67	0.70	0.024
7	1	0.99	1.06	0.068
7	2	0.90	1.09	0.099
7	3	0.98	0.97	0.031
7	4	0.90	1.01	0.037
Pan	1	0.80	0.81	0.029
Pan	2	0.67	0.68	0.013
Pan	3	1.05	1.15	0.039
Pan	4	0.64	0.64	0.021

3.3.2.1.3 Dark Current Trending

The results of the ALI focal plane dark current trending for Bands 1p, 1, 2, 3, 4, 4p are provided in Figures 3-147-3-158. Each figure depicts the results of an individual band. Within each figure, the results of odd and even detectors for each sensor chip assembly are provided. The results of dark current trending for Bands 5p, 5, and 7 are provided in Figures 3-159 to 3-164. Each figure depicts the results of an individual band. Within each figure, the results of odd and even detectors for each sensor chip assembly are provided. SCA 4 is further divided into four quadrants, owing to the rapid change in dark current near the previously identified 'hot spot' near detector 1200 [3]. Finally, the results of dark current trending for the Panchromatic Band are provided in Figures 3-165 to 3-170. Each figure depicts the results of an individual tri-read. Within each figure, the results of odd and even detectors for each sensor chip assembly are provided.

Table 3-29 lists the mean and standard deviation of dark current values, grouped by bands, in a similar fashion.

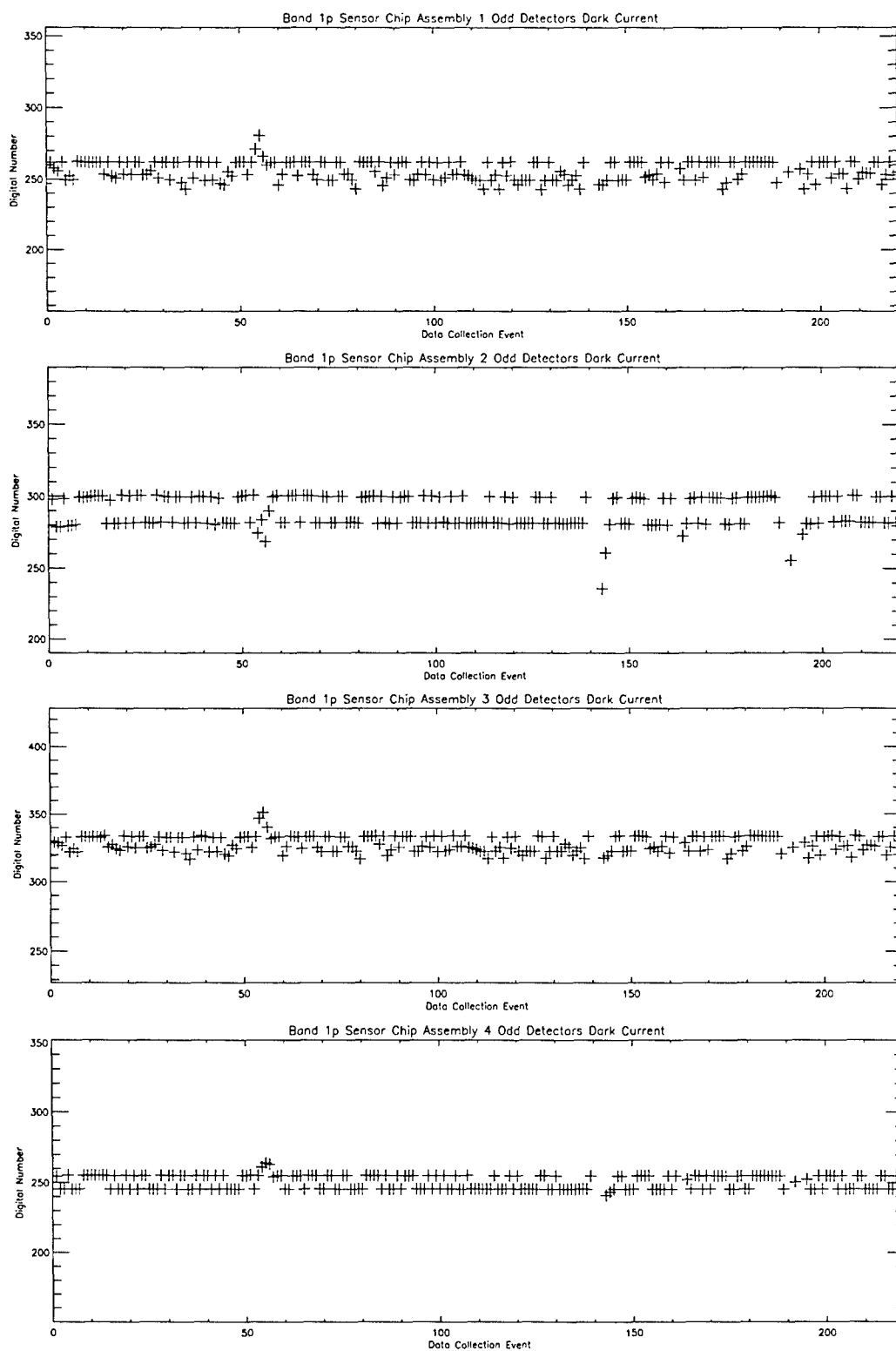


Figure 3-147. Dark current trending for Band 1p odd detectors. Detector outgassing occurred near DCE 55, 140, 160, 190, and 219.

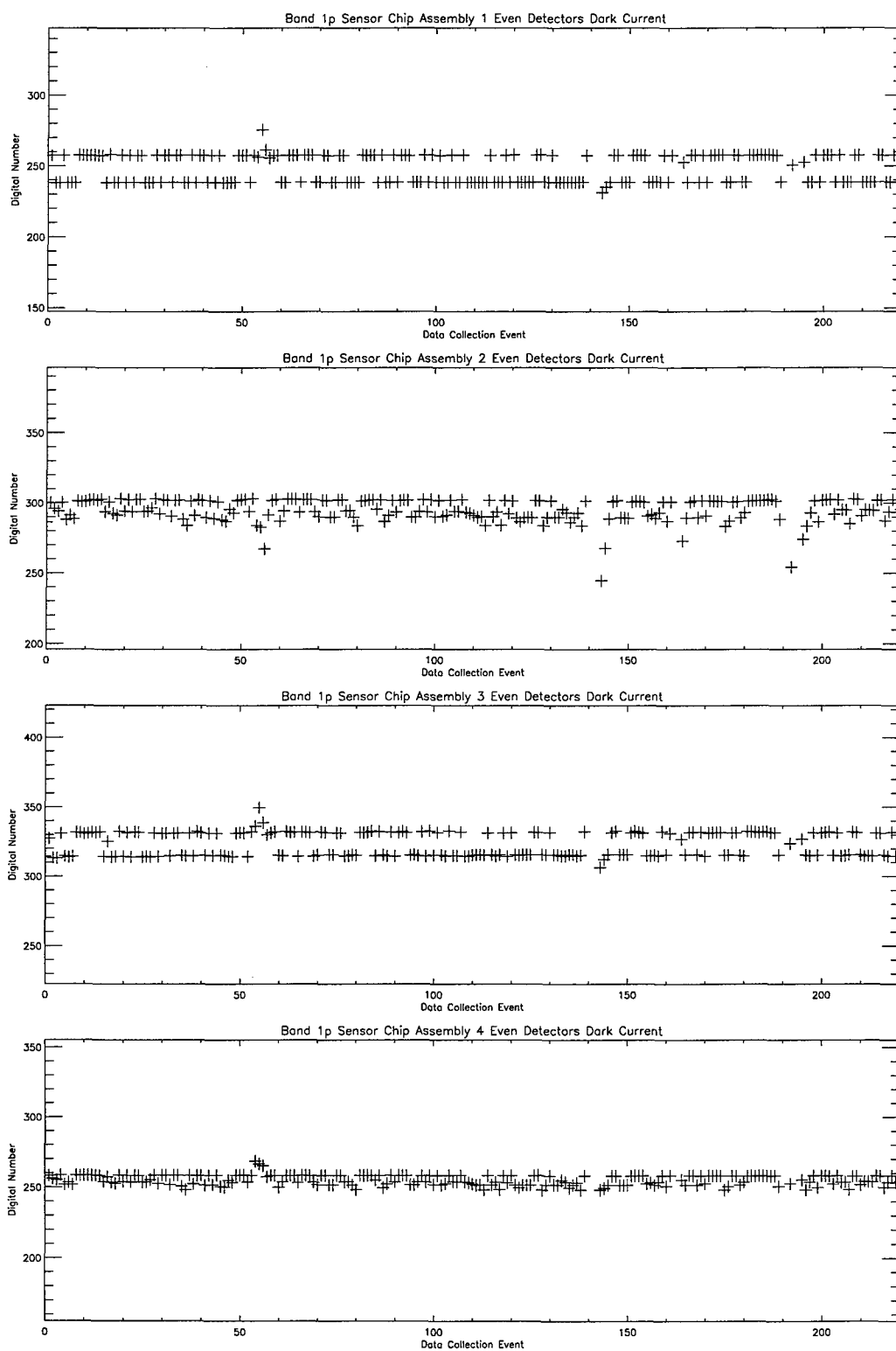


Figure 3-148. Dark current trending for Band 1p even detectors. Detector outgassing occurred near DCE 55, 140, 160, 190, and 219.

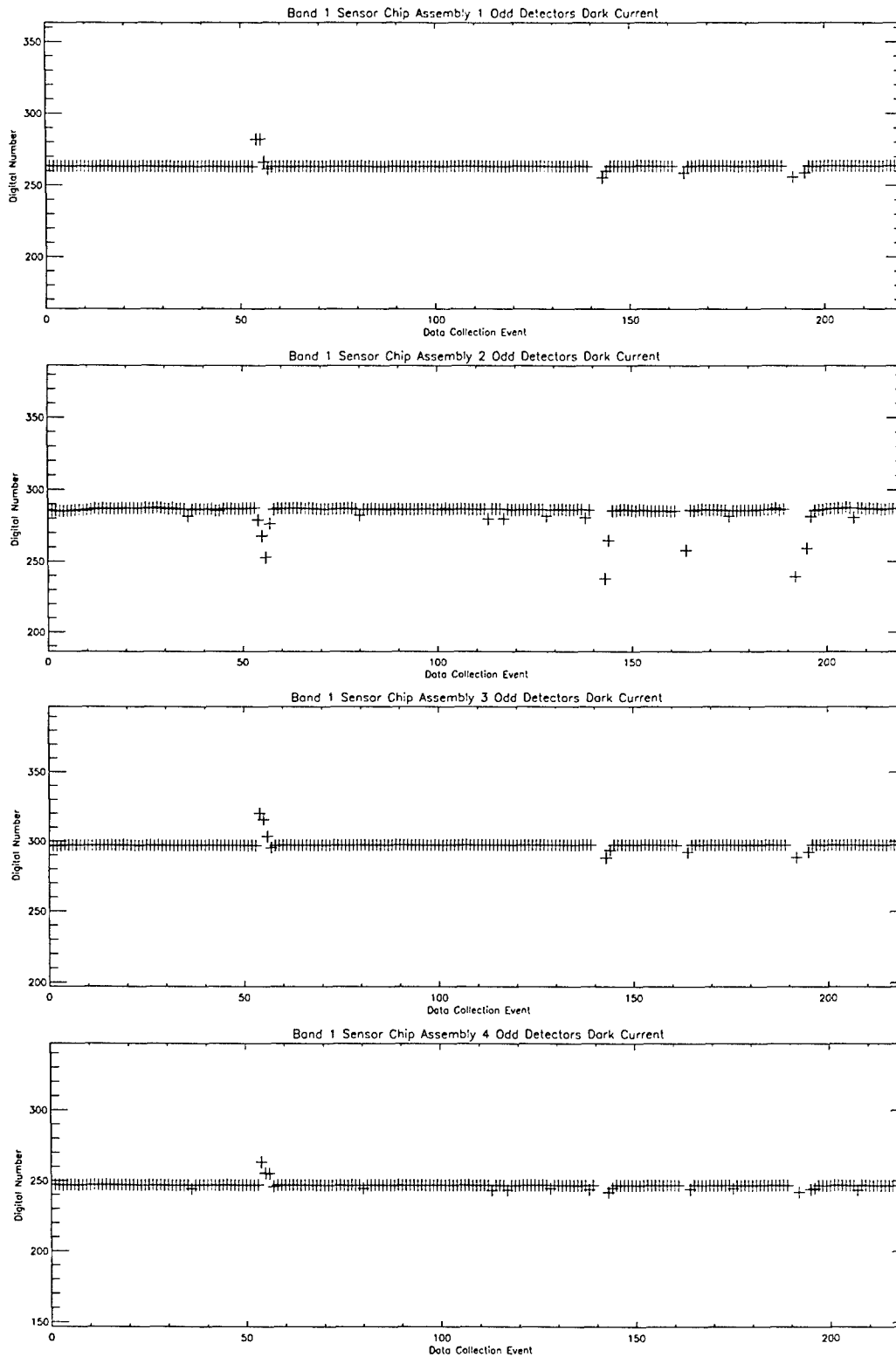


Figure 3-149. Dark current trending for Band 1 odd detectors. Detector outgassing occurred near DCE 55, 140, 160, 190, and 219.

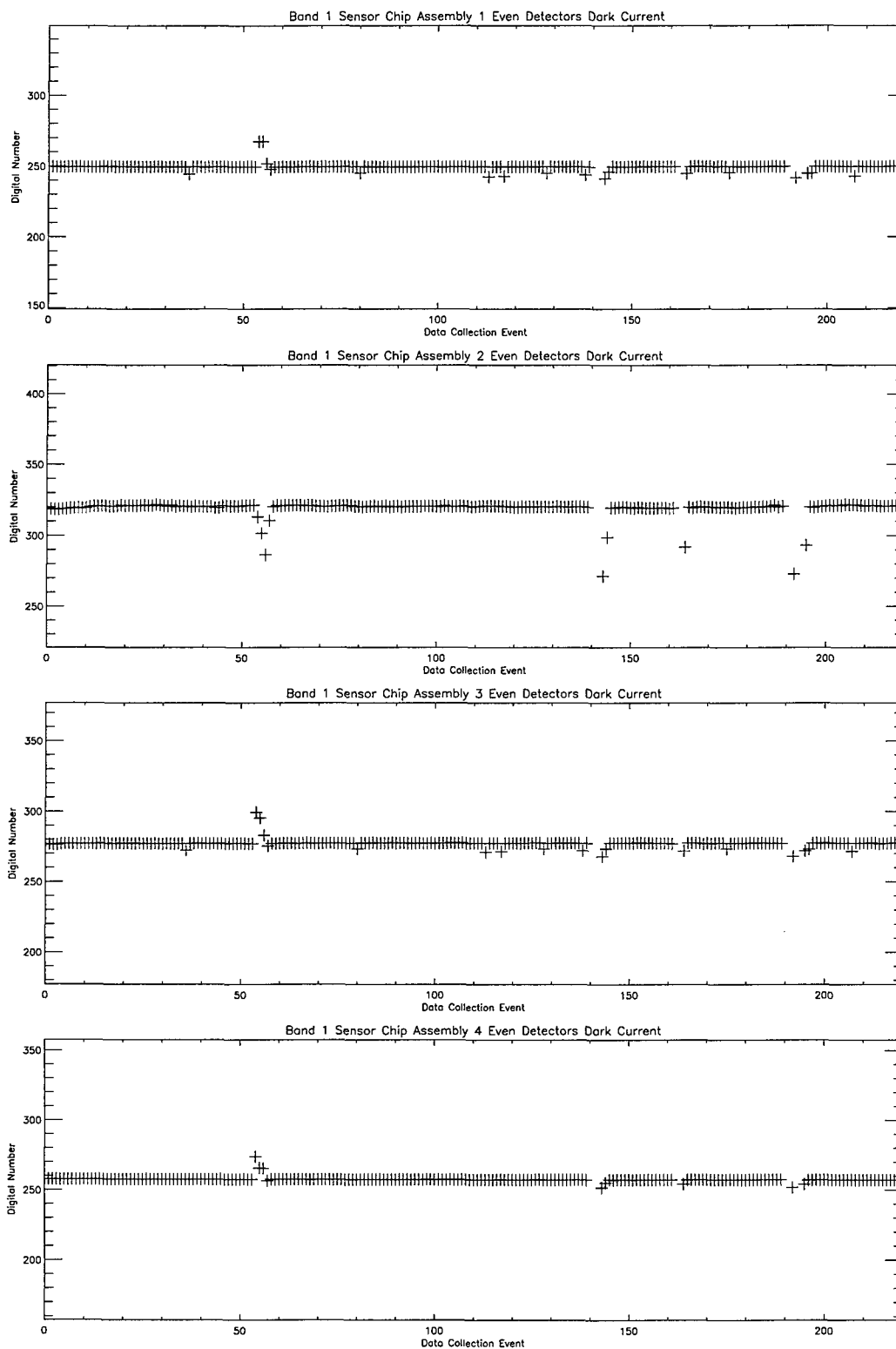


Figure 3-150. Dark current trending for Band 1 even detectors. Detector outgassing occurred near DCE 55, 140, 160, 190, and 219.

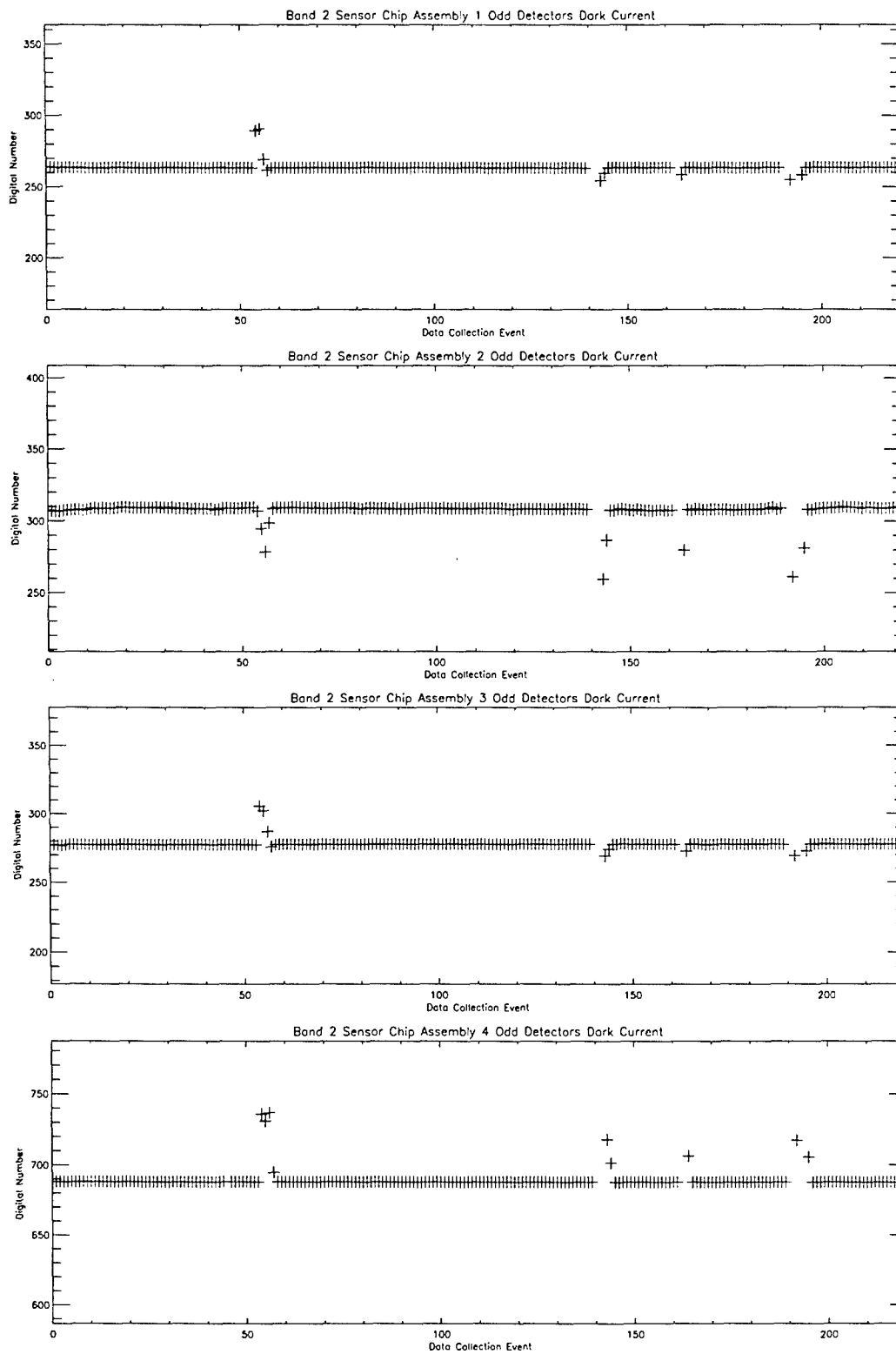


Figure 3-151. Dark current trending for Band 2 odd detectors. Detector outgassing occurred near DCE 55, 140, 160, 190, and 219.

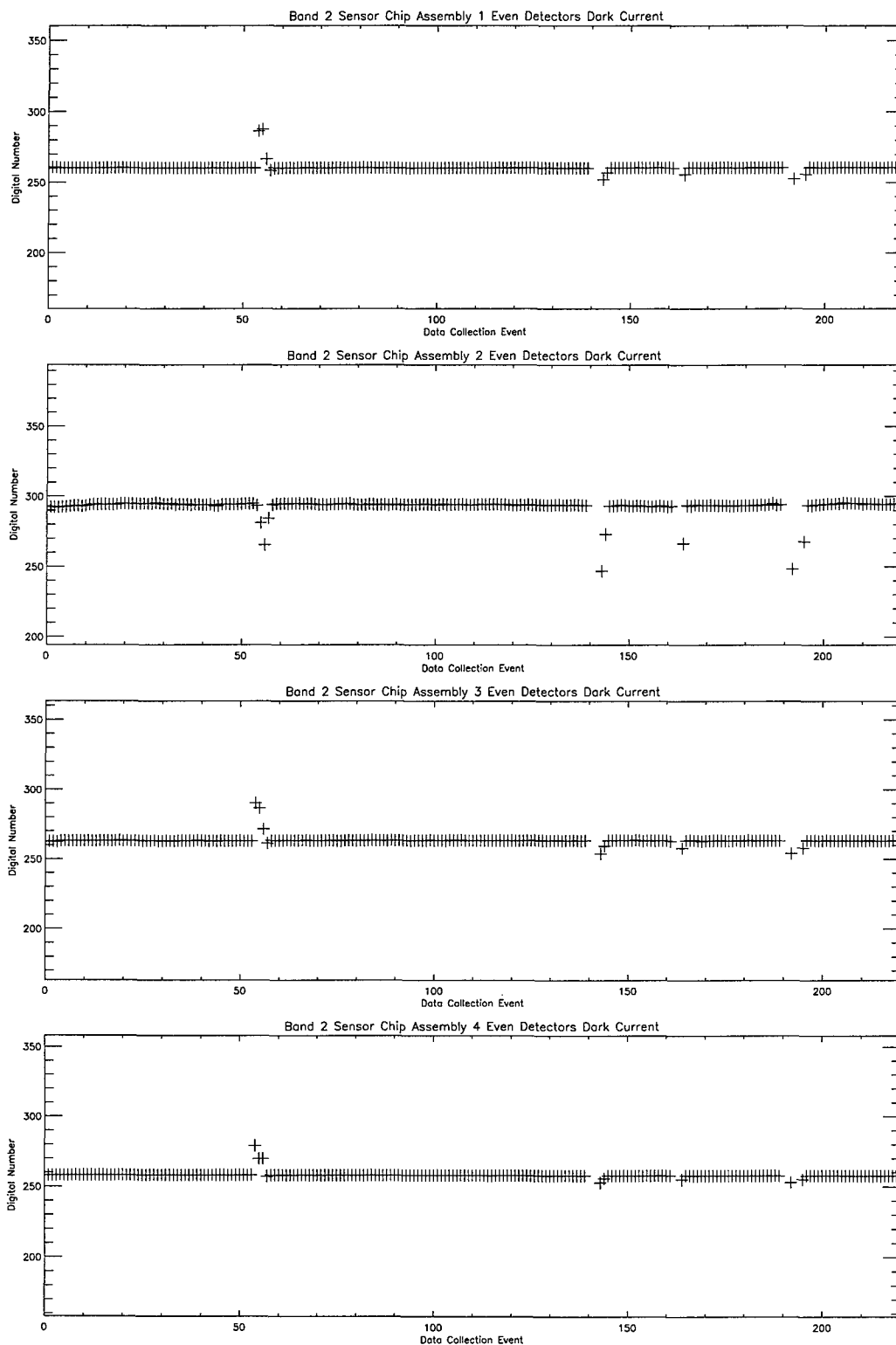


Figure 3-152. Dark current trending for Band 2 even detectors. Detector outgassing occurred near DCE 55, 140, 160, 190, and 219.

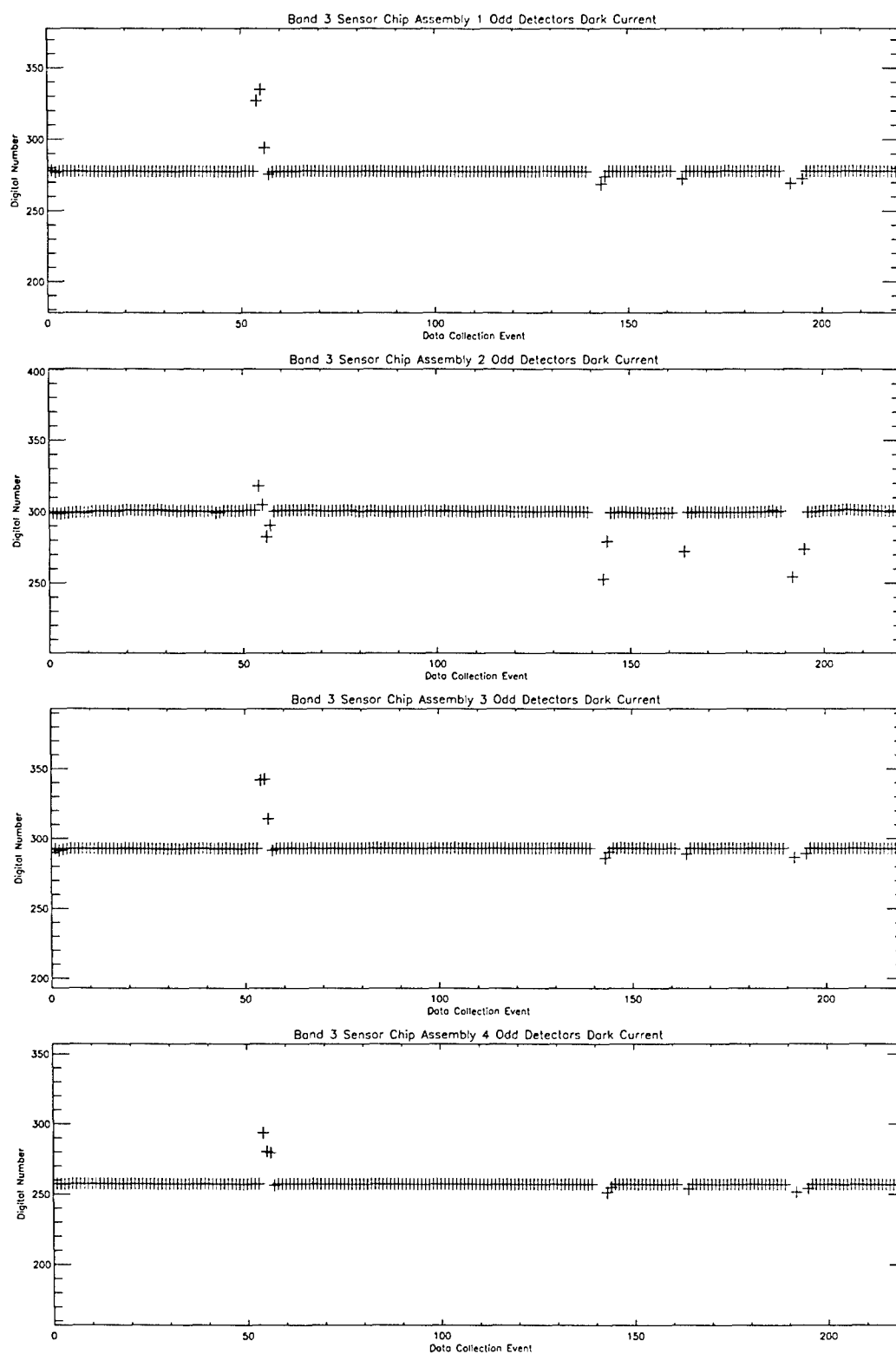


Figure 3-153. Dark current trending for Band 3 odd detectors. Detector outgassing occurred near DCE 55, 140, 160, 190, and 219.

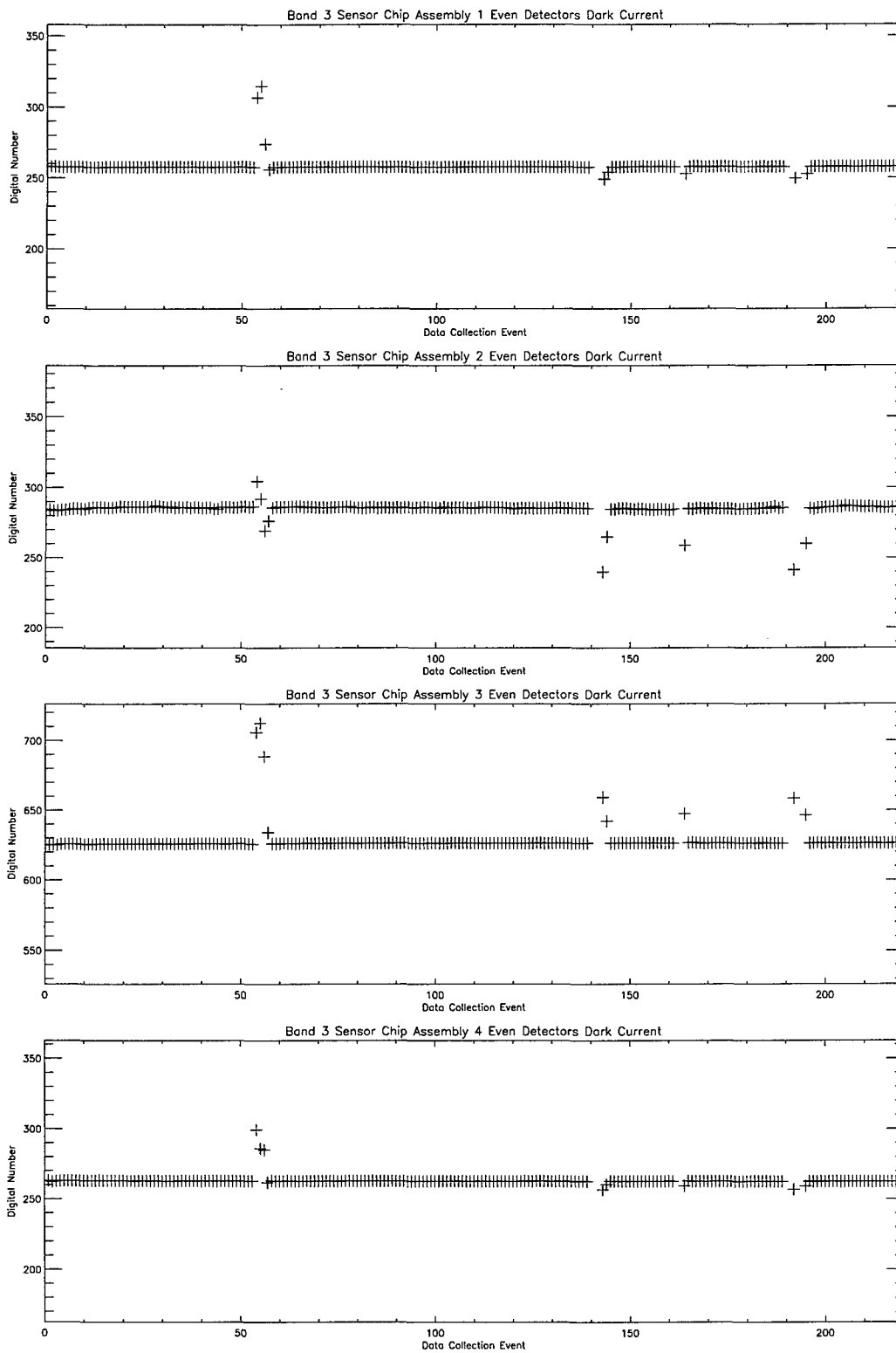


Figure 3-154. Dark current trending for Band 3 even detectors. Detector outgassing occurred near DCE-55, 140, 160, 190, and 219

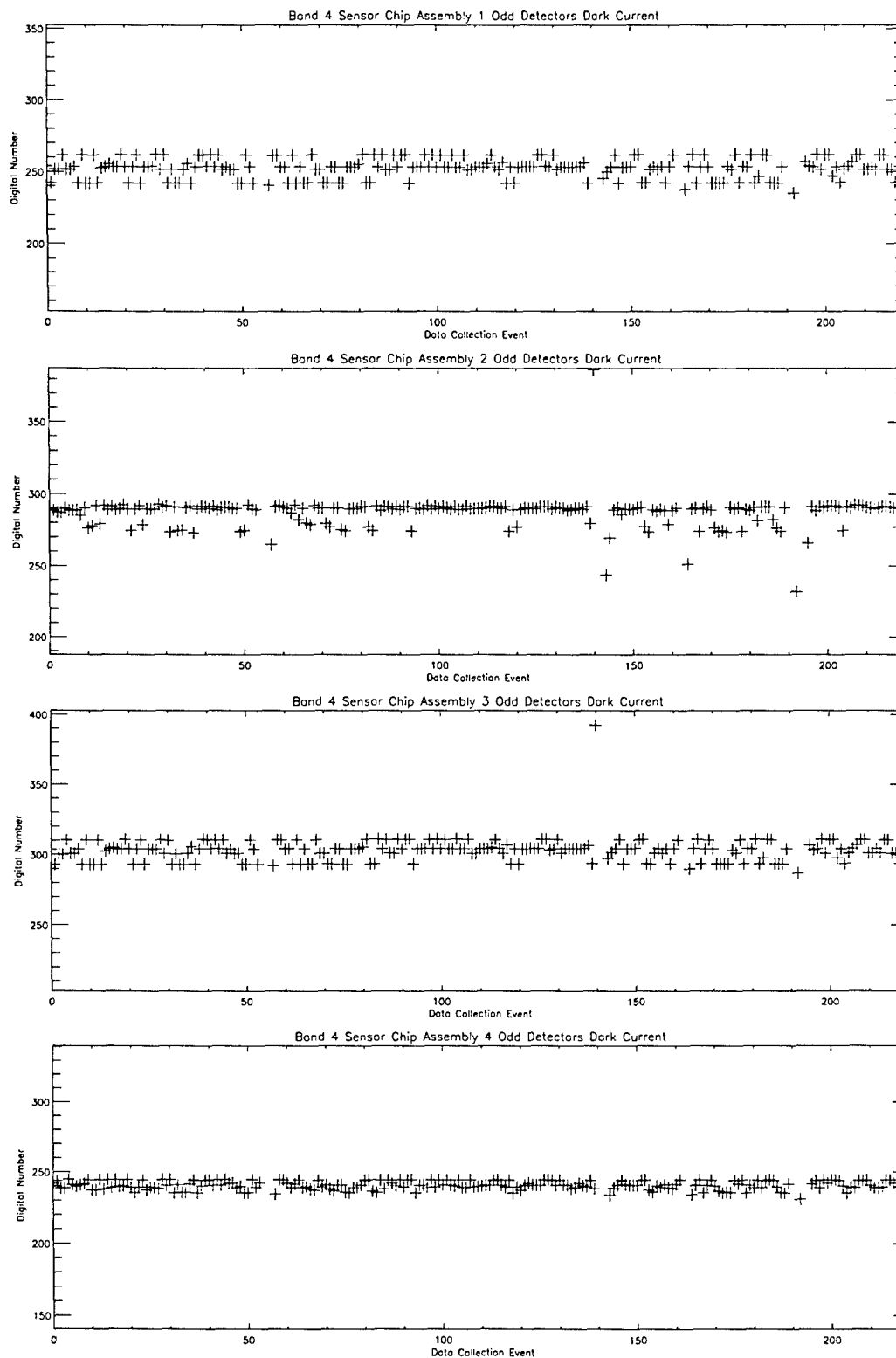


Figure 3-155. Dark current trending for Band 4 odd detectors. Detector outgassing occurred near DCE 55, 140, 160, 190, and 219.

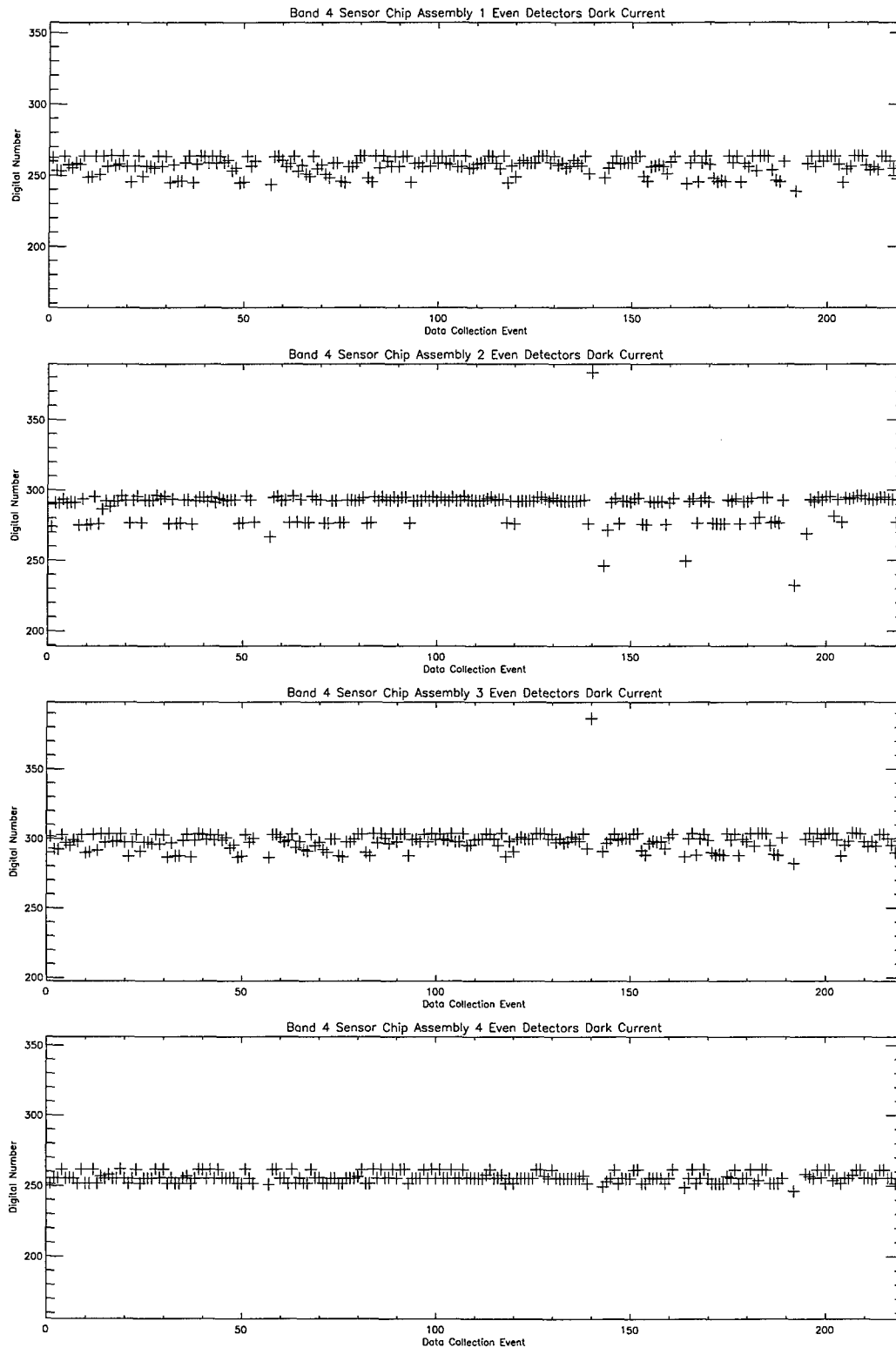


Figure 3-156. Dark current trending for Band 4 even detectors. Detector outgassing occurred near DCE 55, 140, 160, 190, and 219.

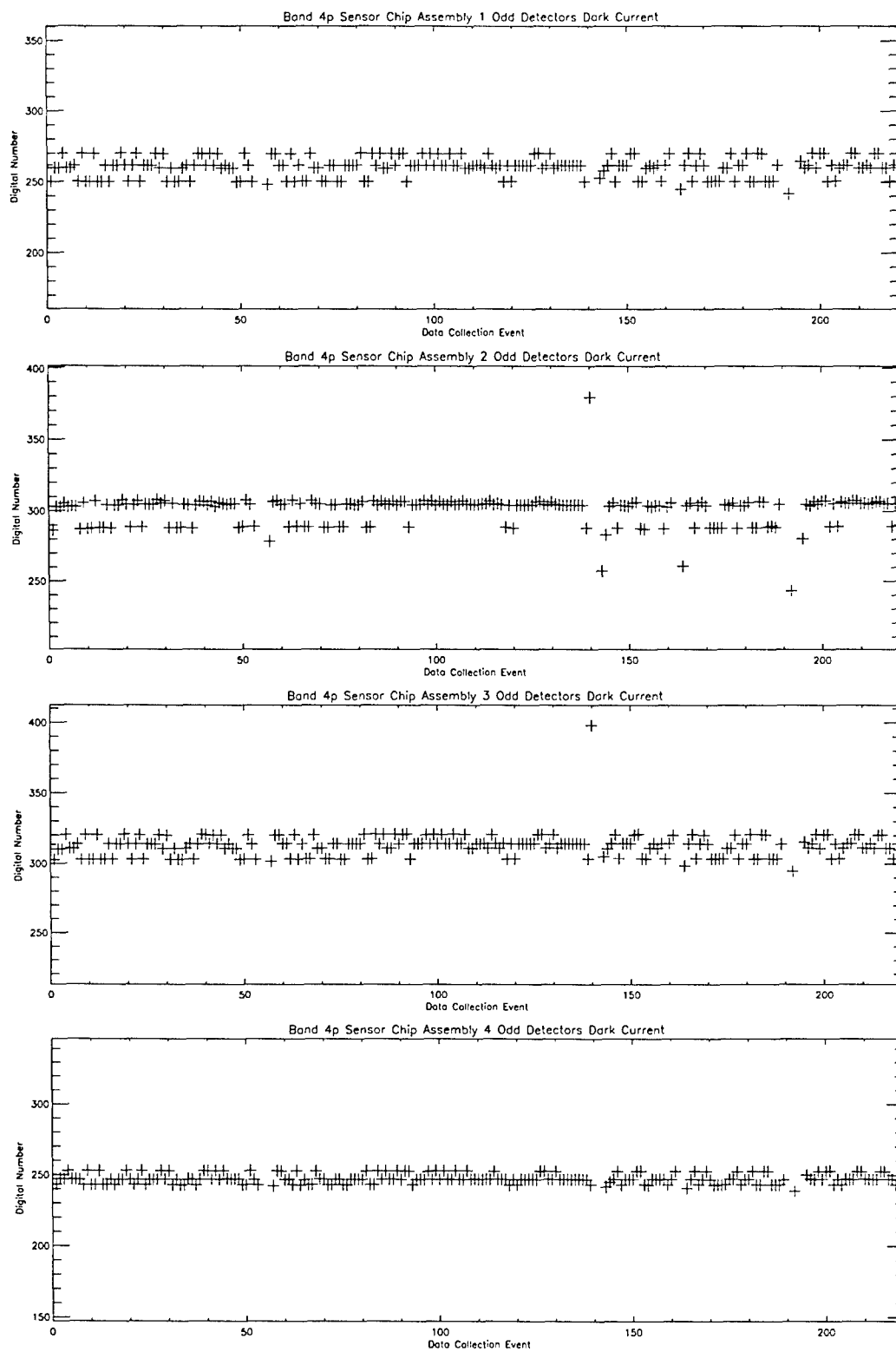


Figure 3-157. Dark current trending for Band 4p odd detectors. Detector outgassing occurred near DCE 55, 140, 160, 190, and 219

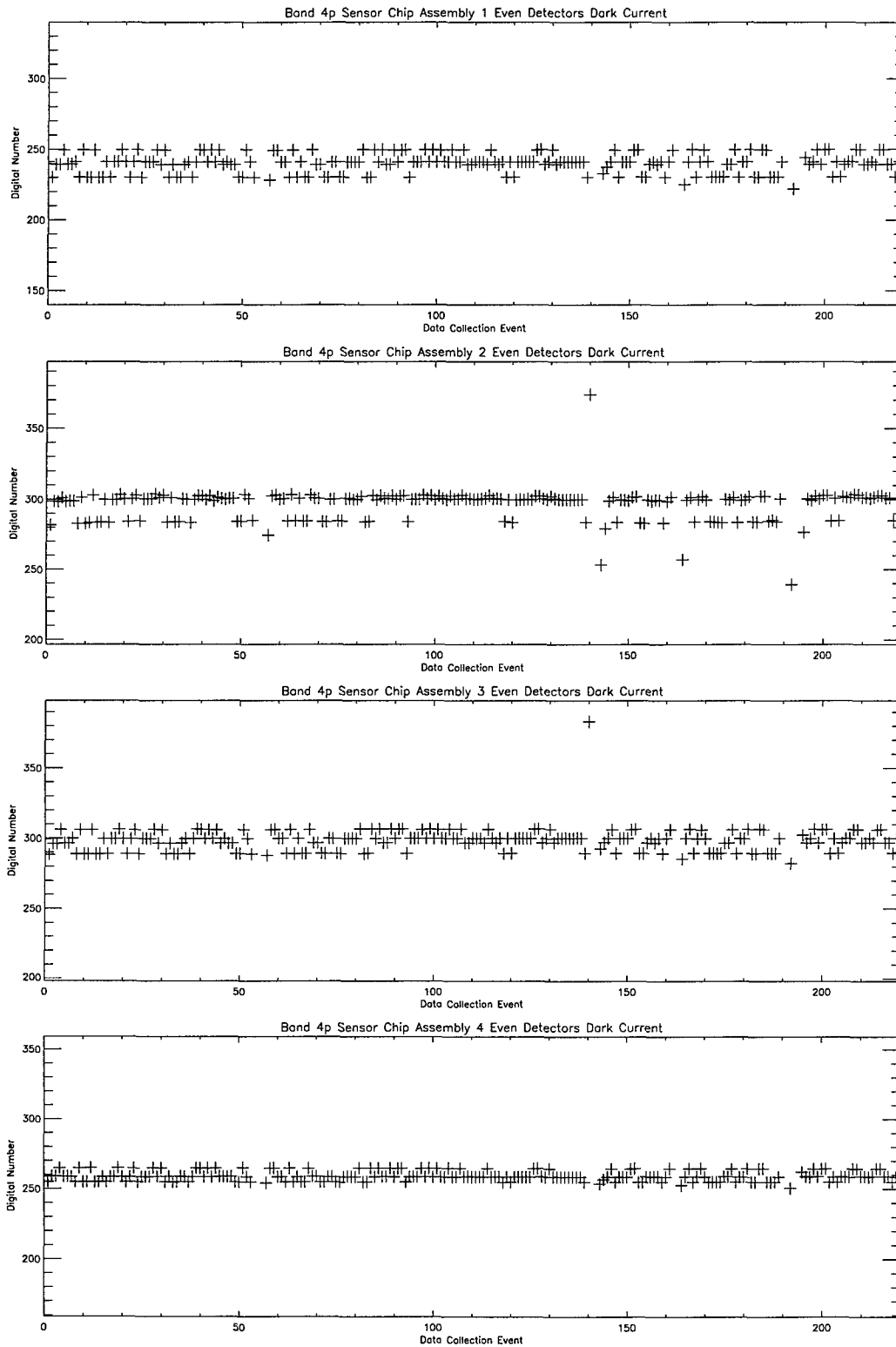


Figure 3-158. Dark current trending for Band 4p even detectors. Detector outgassing occurred near DCE 55, 140, 160, 190, and 219.

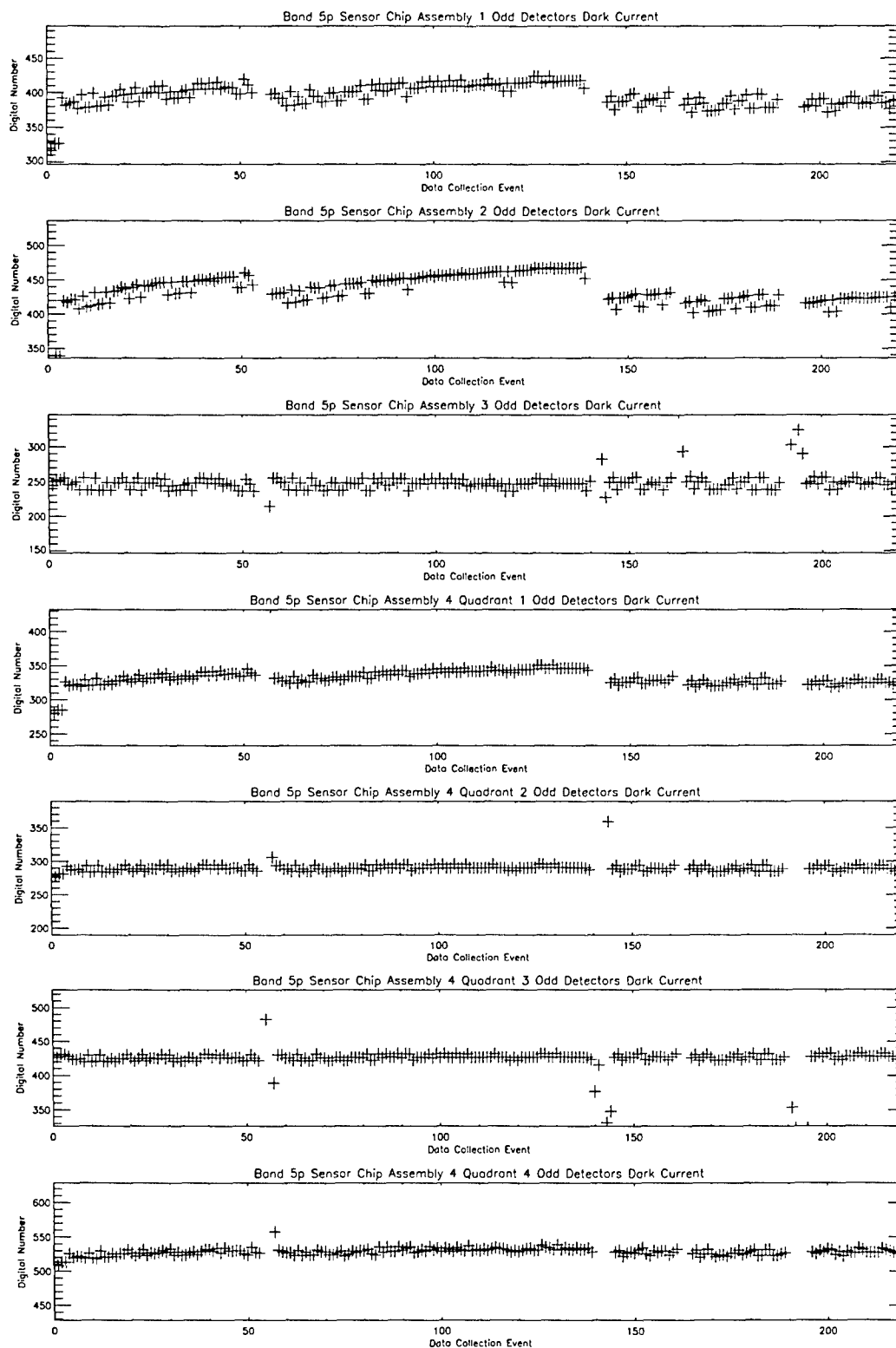


Figure 3-159. Dark current trending for Band 5p odd detectors. Detector outgassing occurred near DCE 55, 140, 160, 190, and 219.

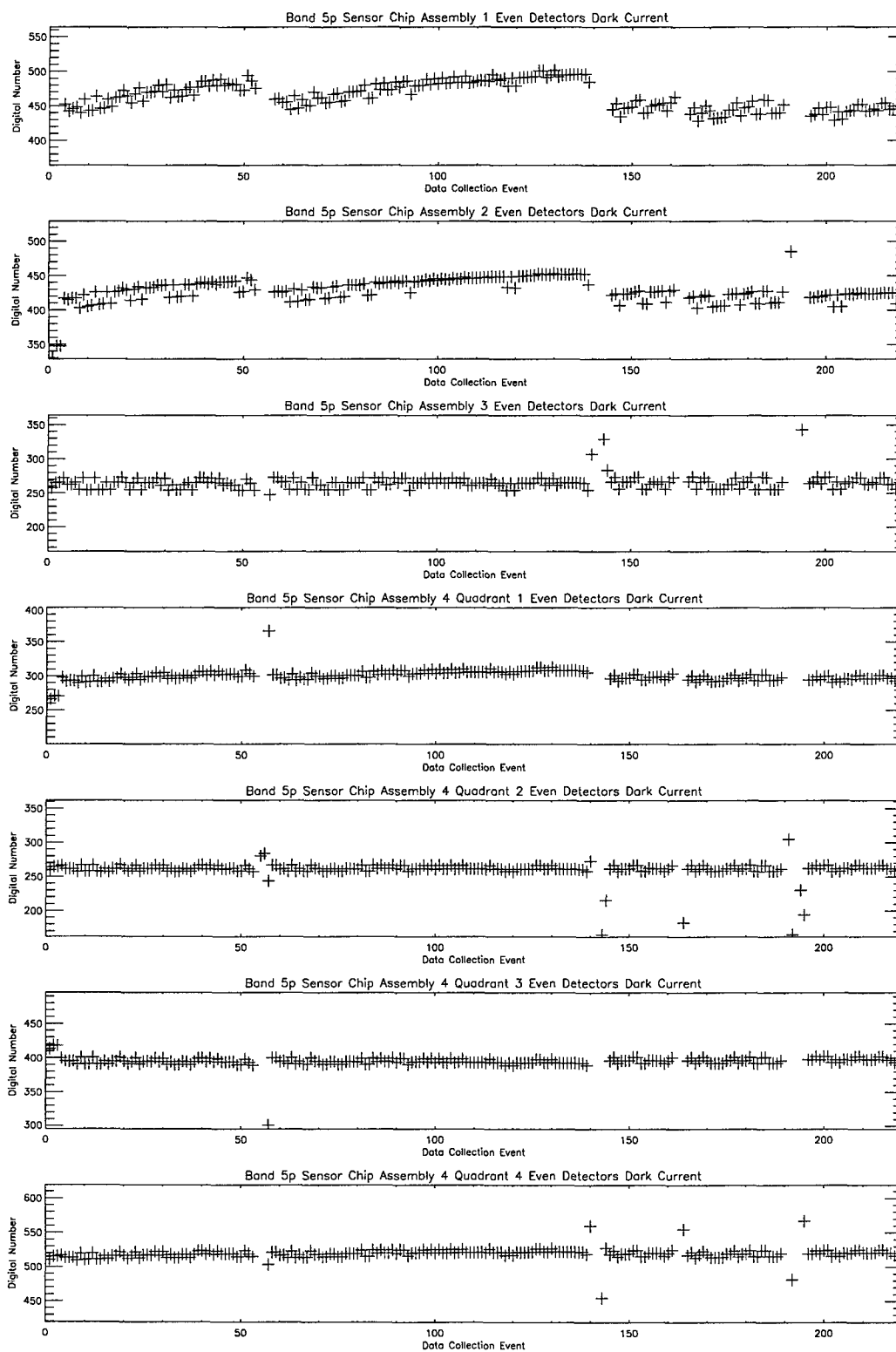


Figure 3-160. Dark current trending for Band 5p even detectors. Detector outgassing occurred near DCE 55, 140, 160, 190, and 219.

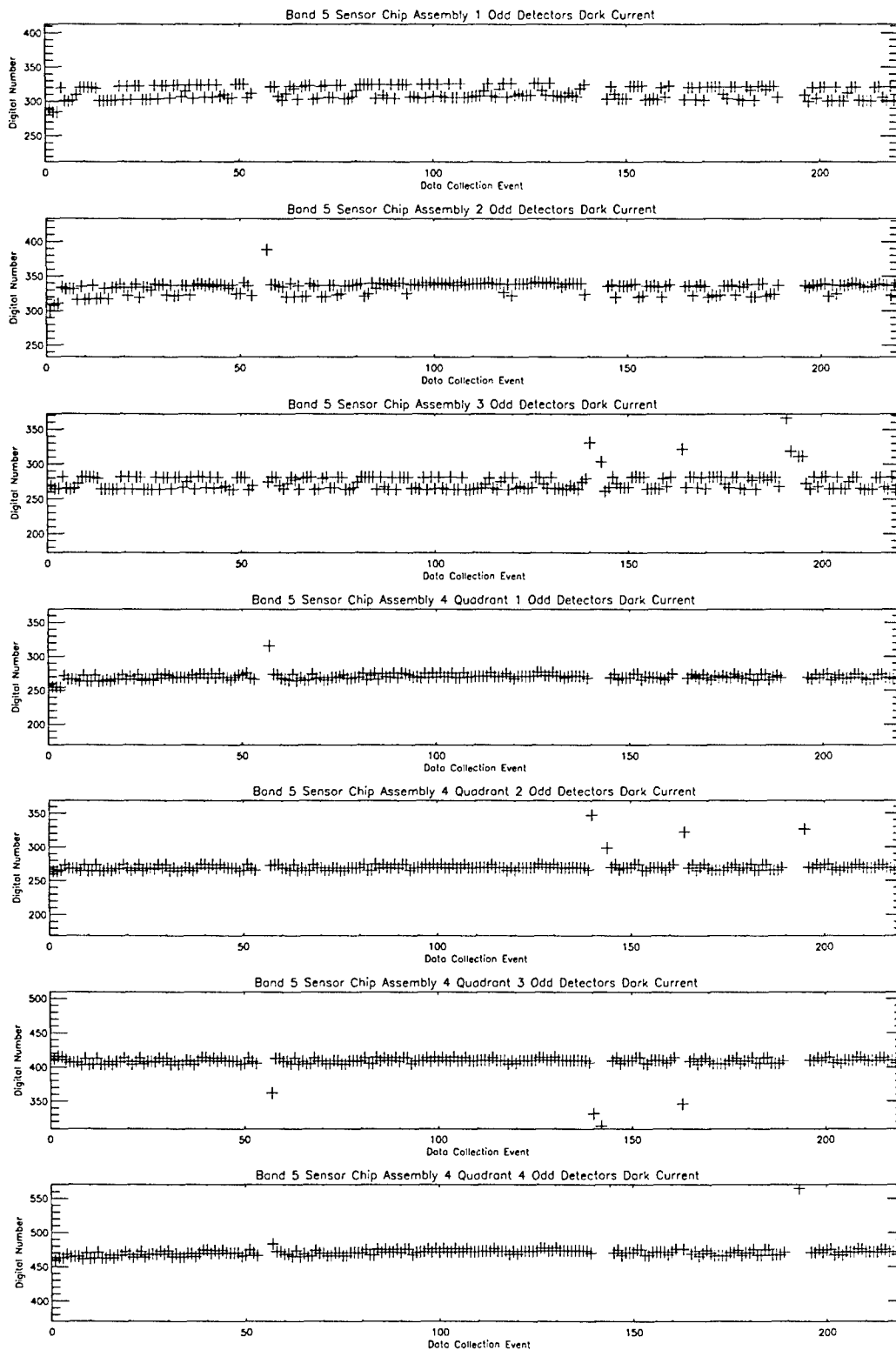


Figure 3-161. Dark current trending for Band 5 odd detectors. Detectors outgassing occurred near DCE 55, 140, 160, 190 and 219.

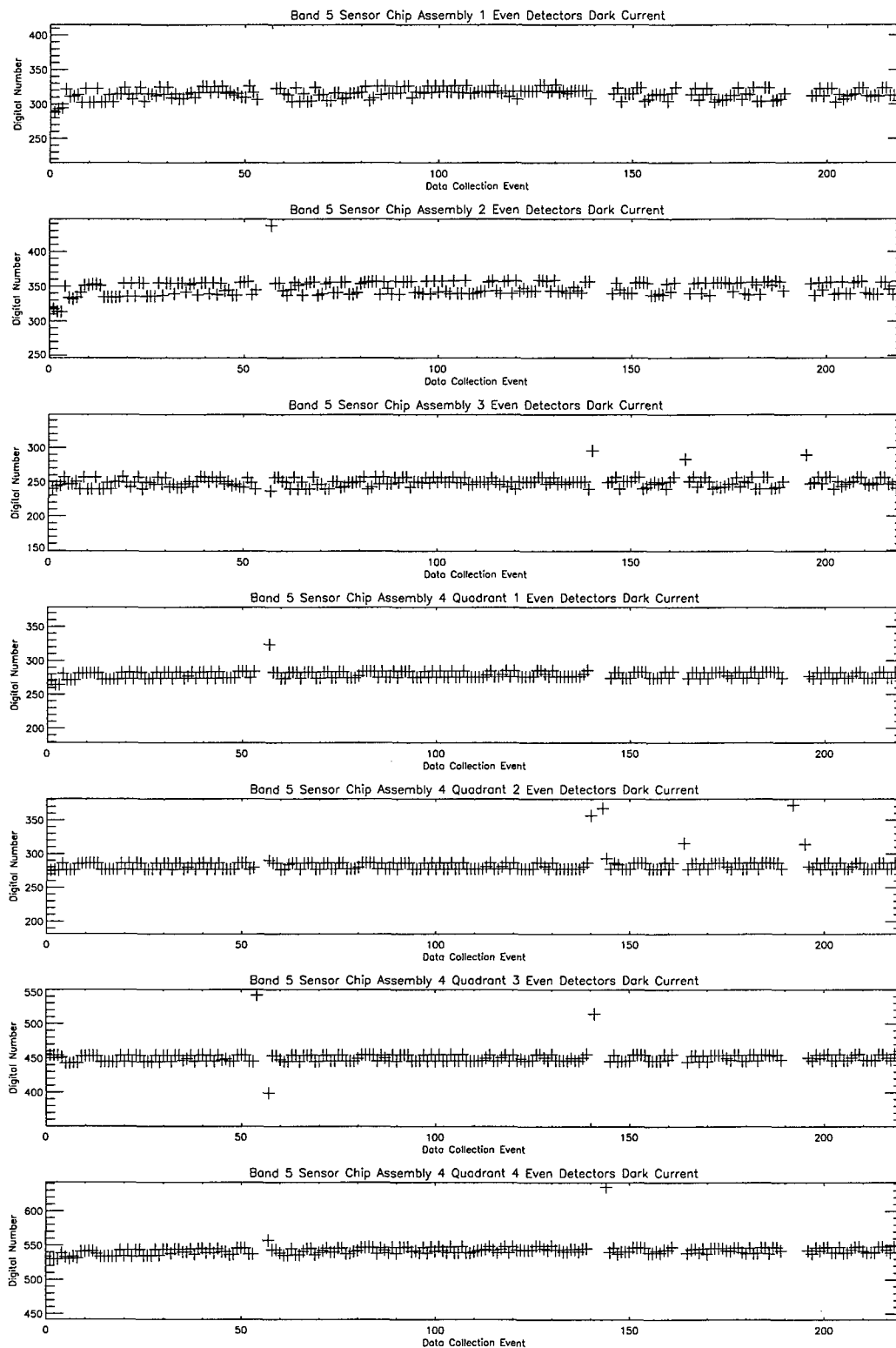


Figure 3-162. Dark current trending for Band 5 even detectors. Detector outgassing occurred near DCE 55, 140, 160, 190, and 219.

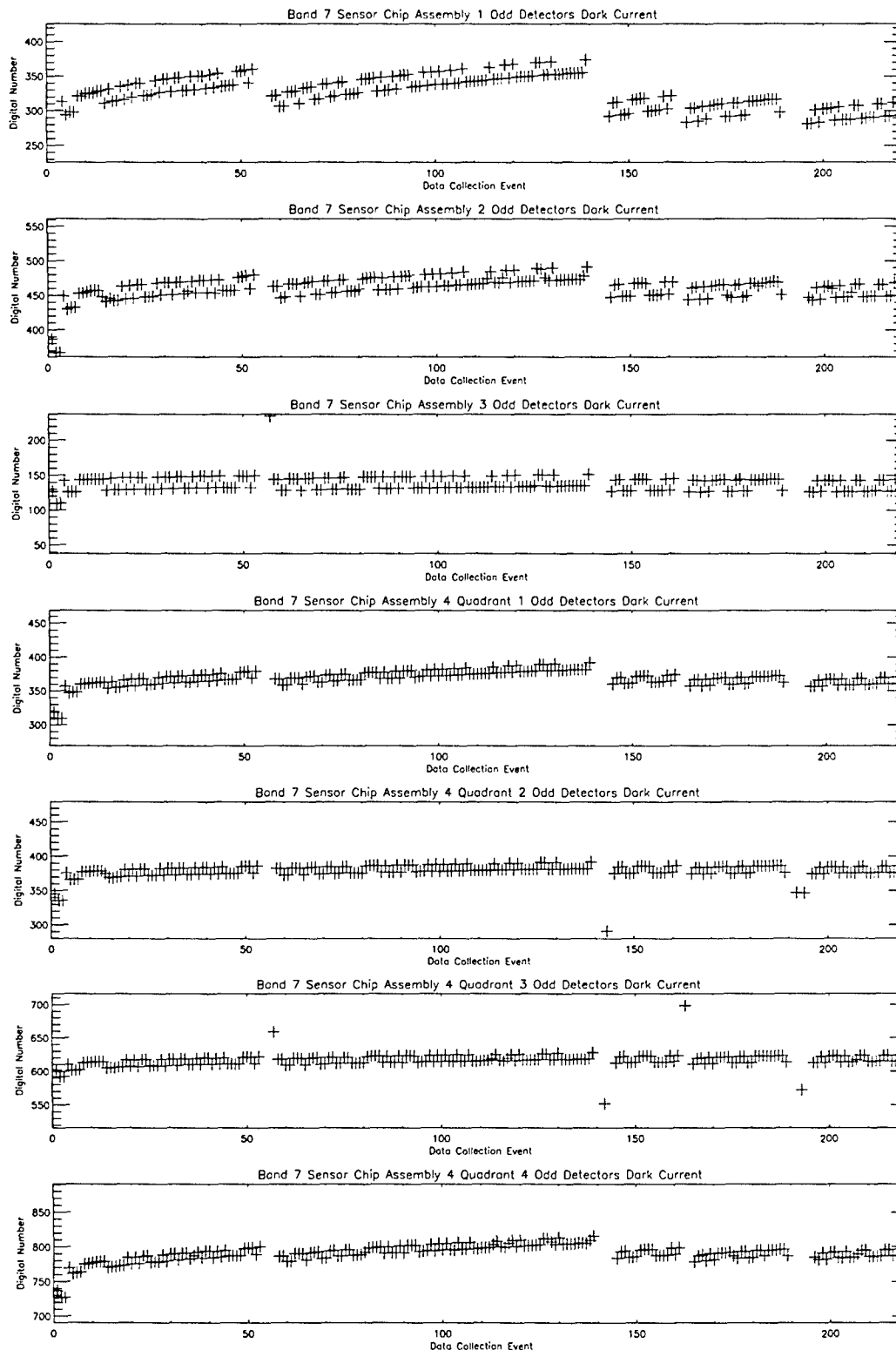


Figure 3-163. Dark current trending for Band 7 odd detectors. Detector outgassing occurred near DCE 55, 140, 160, 190 and 219.

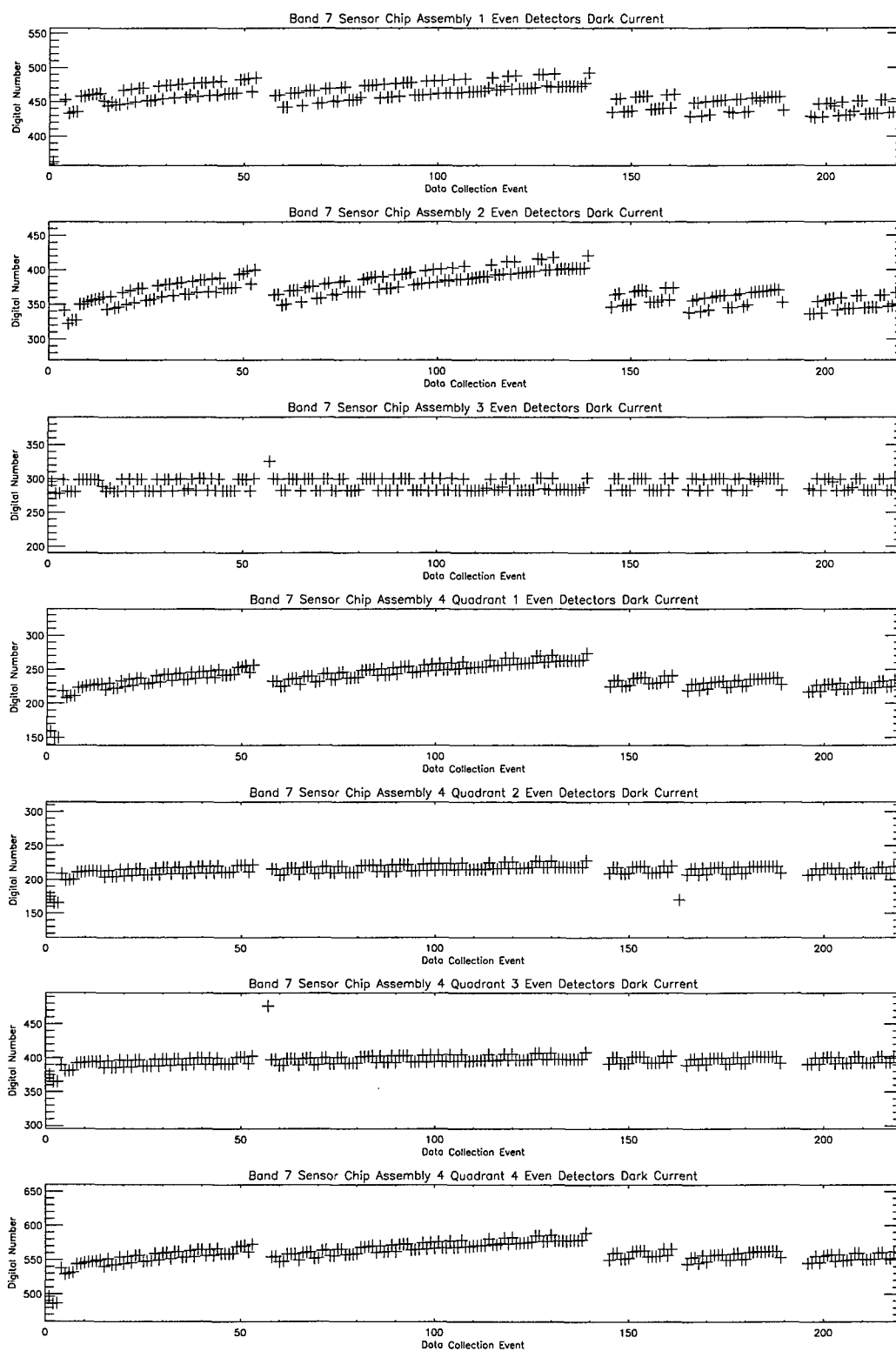


Figure 3-164. Dark current trending for Band 7 even detectors. Detector outgassing occurred near DCE 55, 140, 160, 190, and 219.

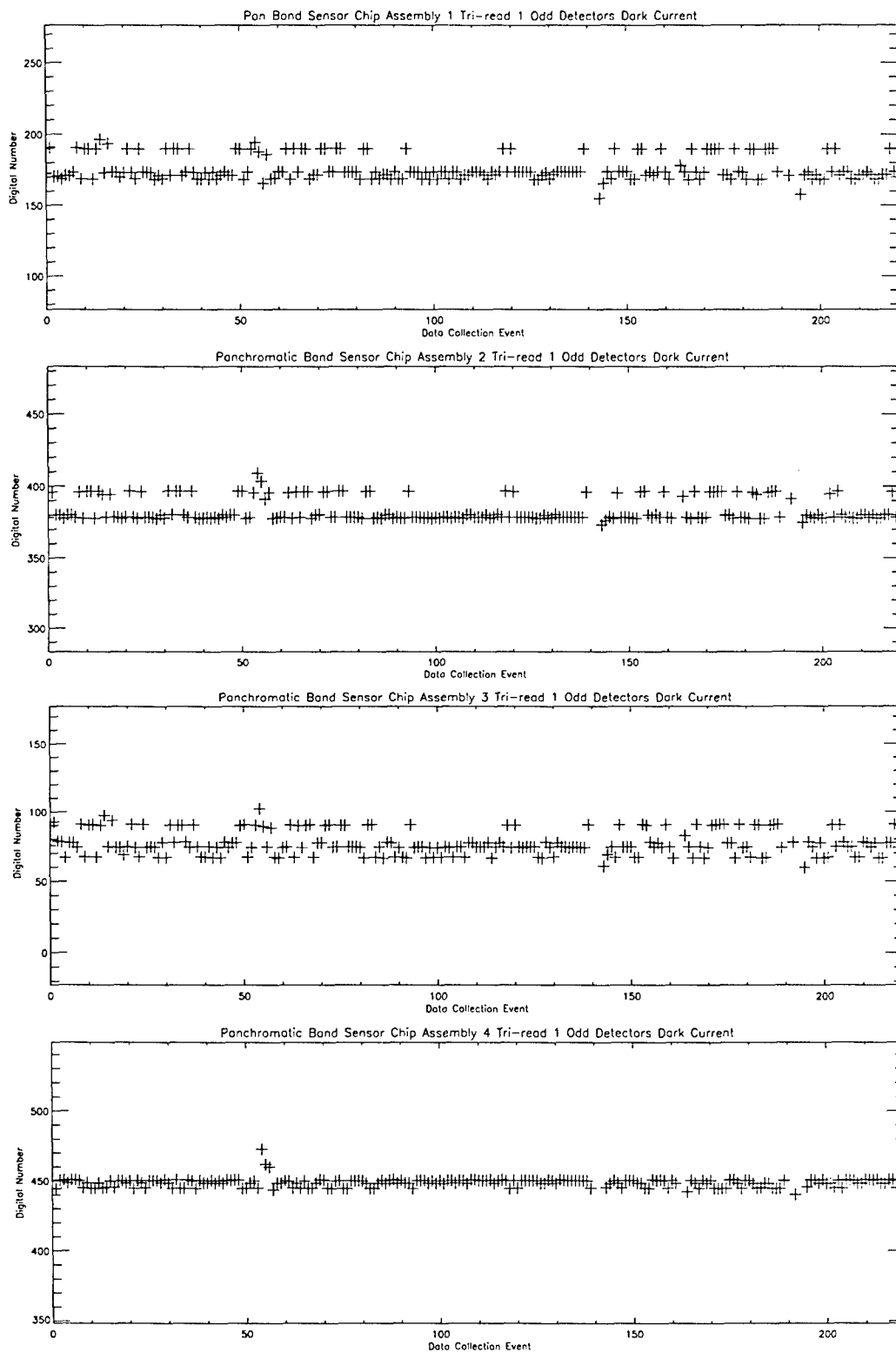


Figure 3-165. Dark current trending for Panchromatic Band tri-read #1 odd detectors. Detector outgassing occurred near DCE 55, 140, 160, 190, and 219.

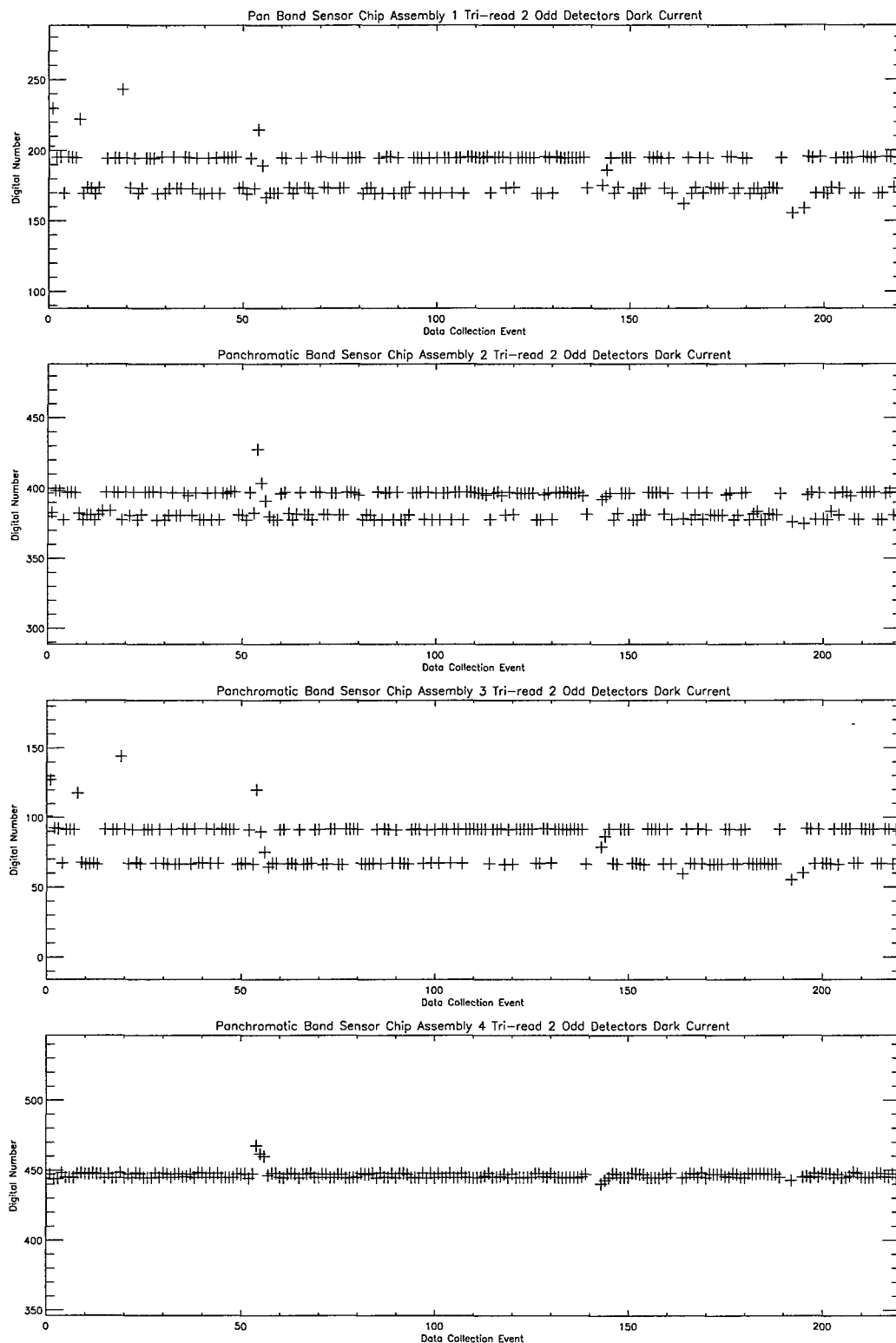


Figure 3-166. Dark current trending for Panchromatic Band tri-read #2 odd detectors. Detector outgassing occurred near DCE 55, 140, 160, 190, and 219

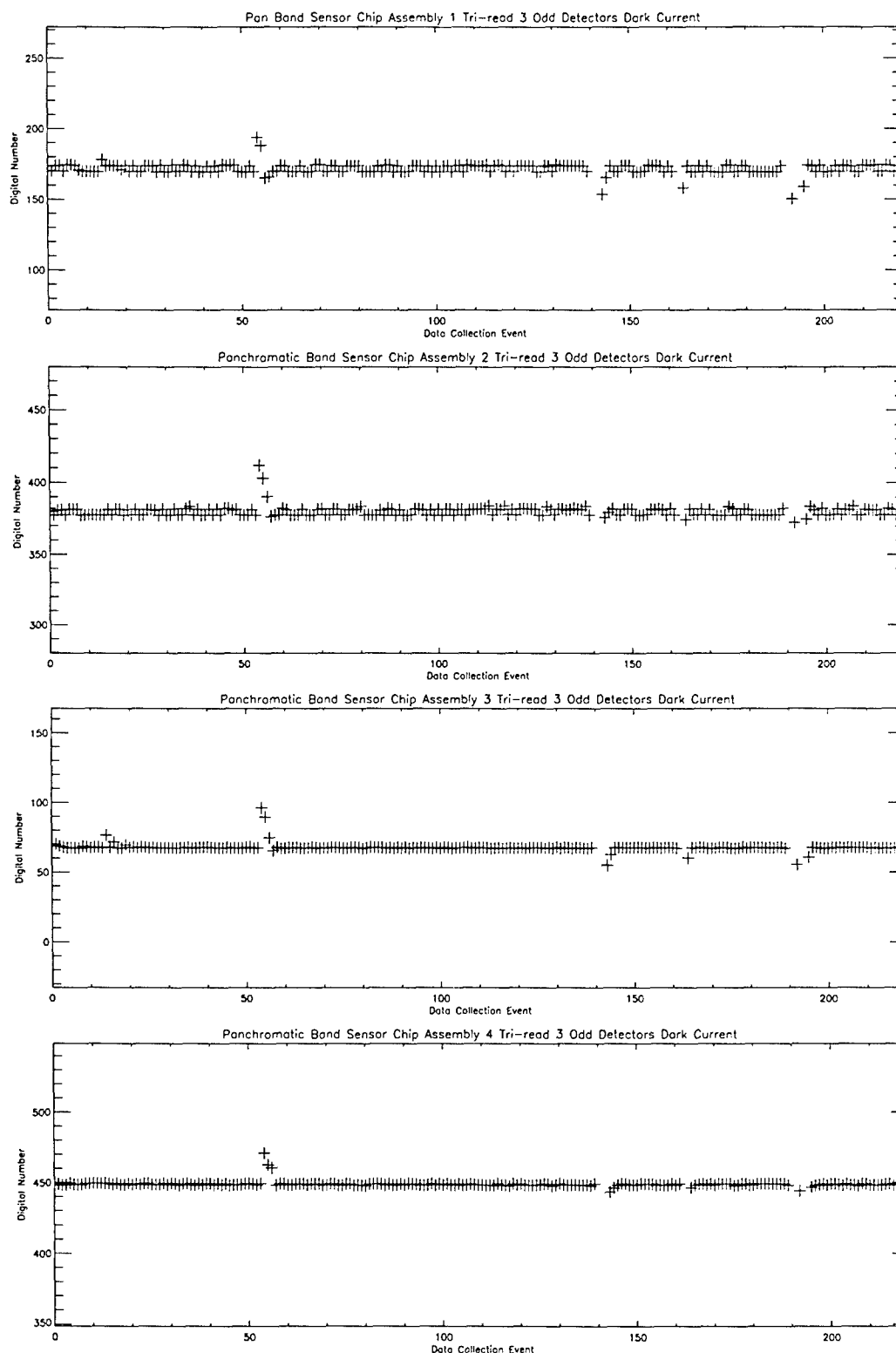


Figure 3-167. Dark current trending for Panchromatic Band tri-read #3 odd detectors. Detector outgassing occurred near DCE 55, 140, 160, 190, and 219.

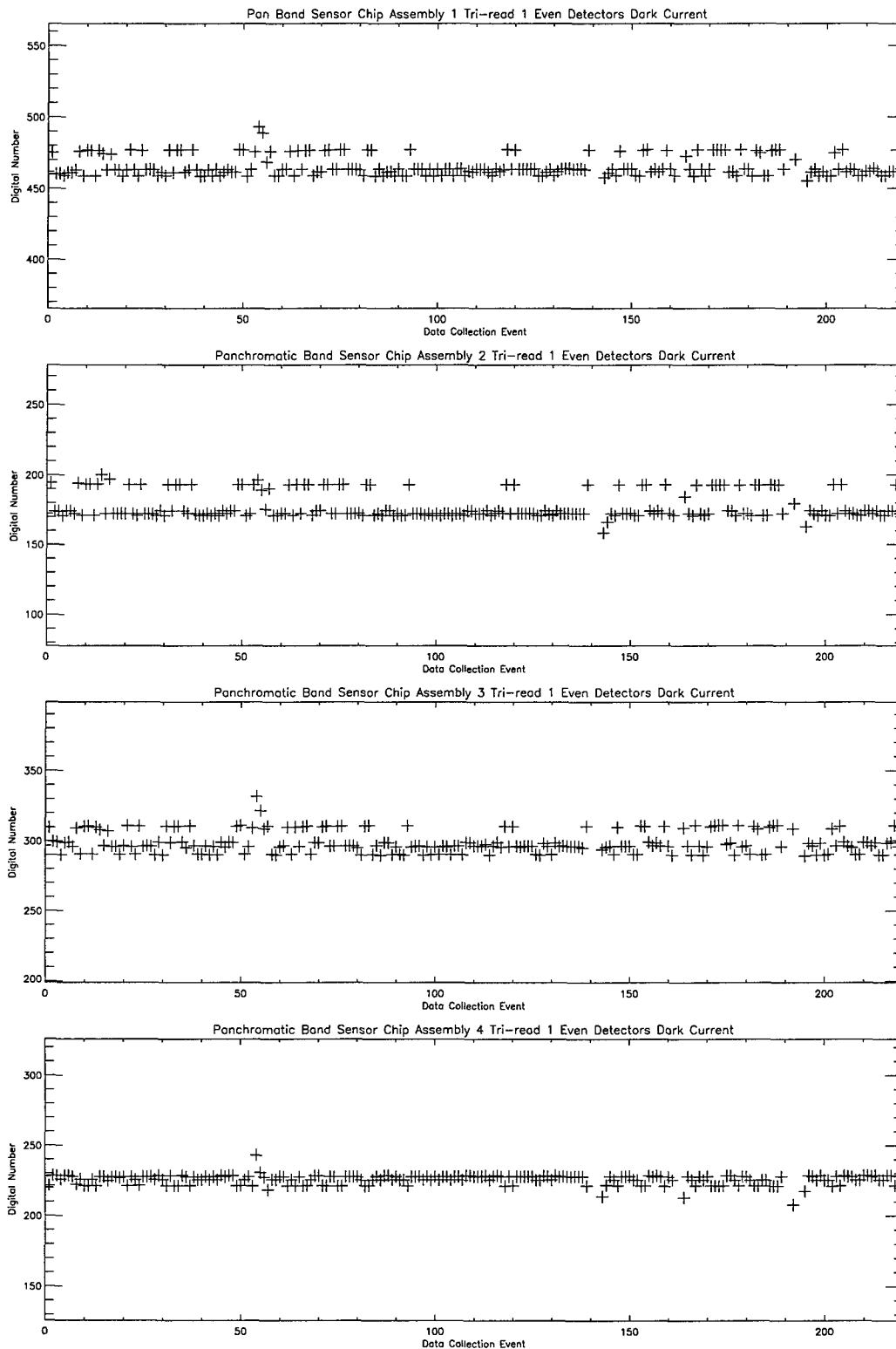


Figure 3-168. Dark current trending for Panchromatic Band tri-read #1 even detectors. Detector outgassing occurred near DCE 55, 140, 160, 190, and 219.

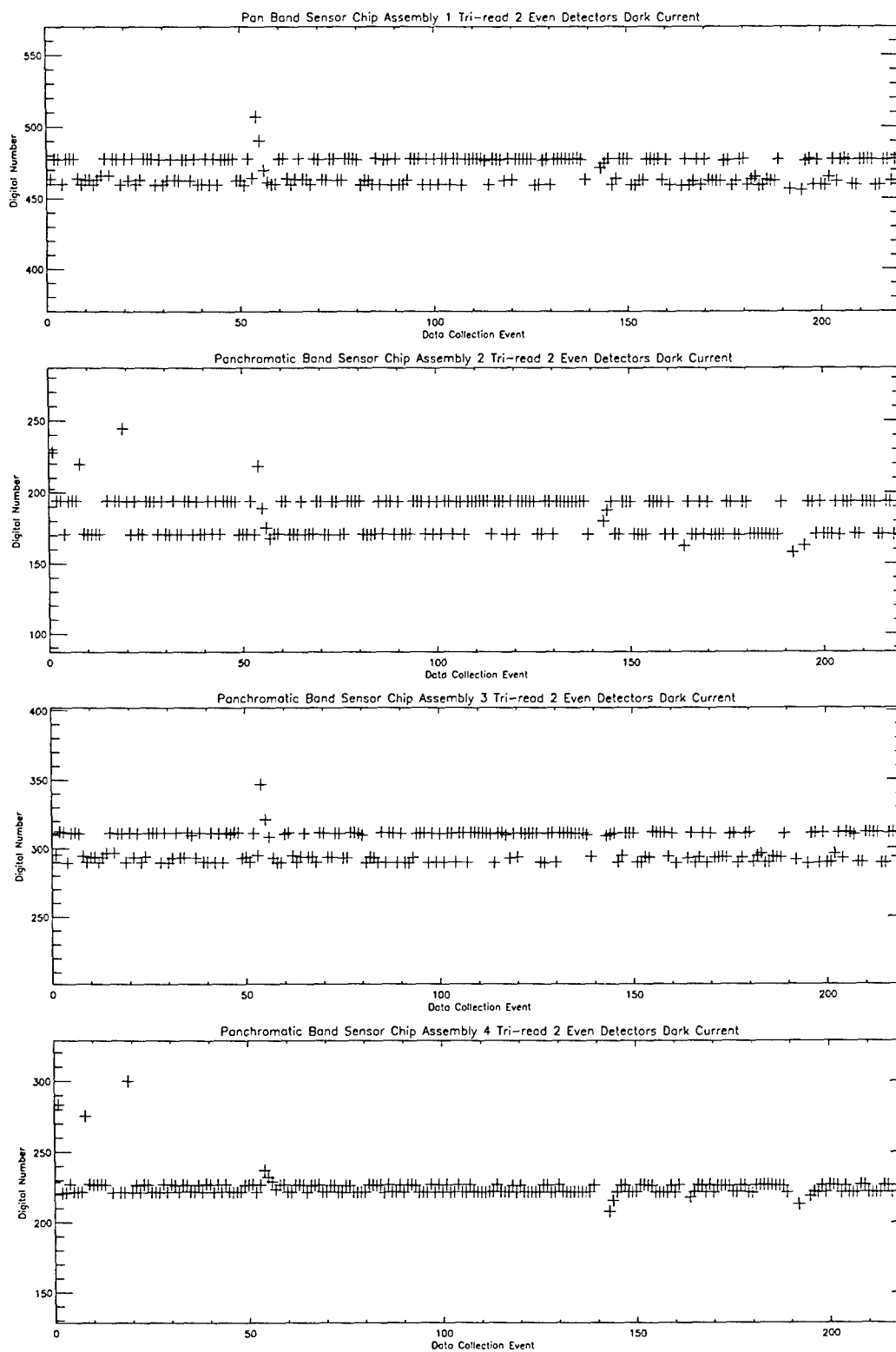


Figure 3-169. Dark current trending for Panchromatic Band tri-read #2 even detectors. Detectors outgassing occurred near DCE 55, 140, 160, 190, and 219.

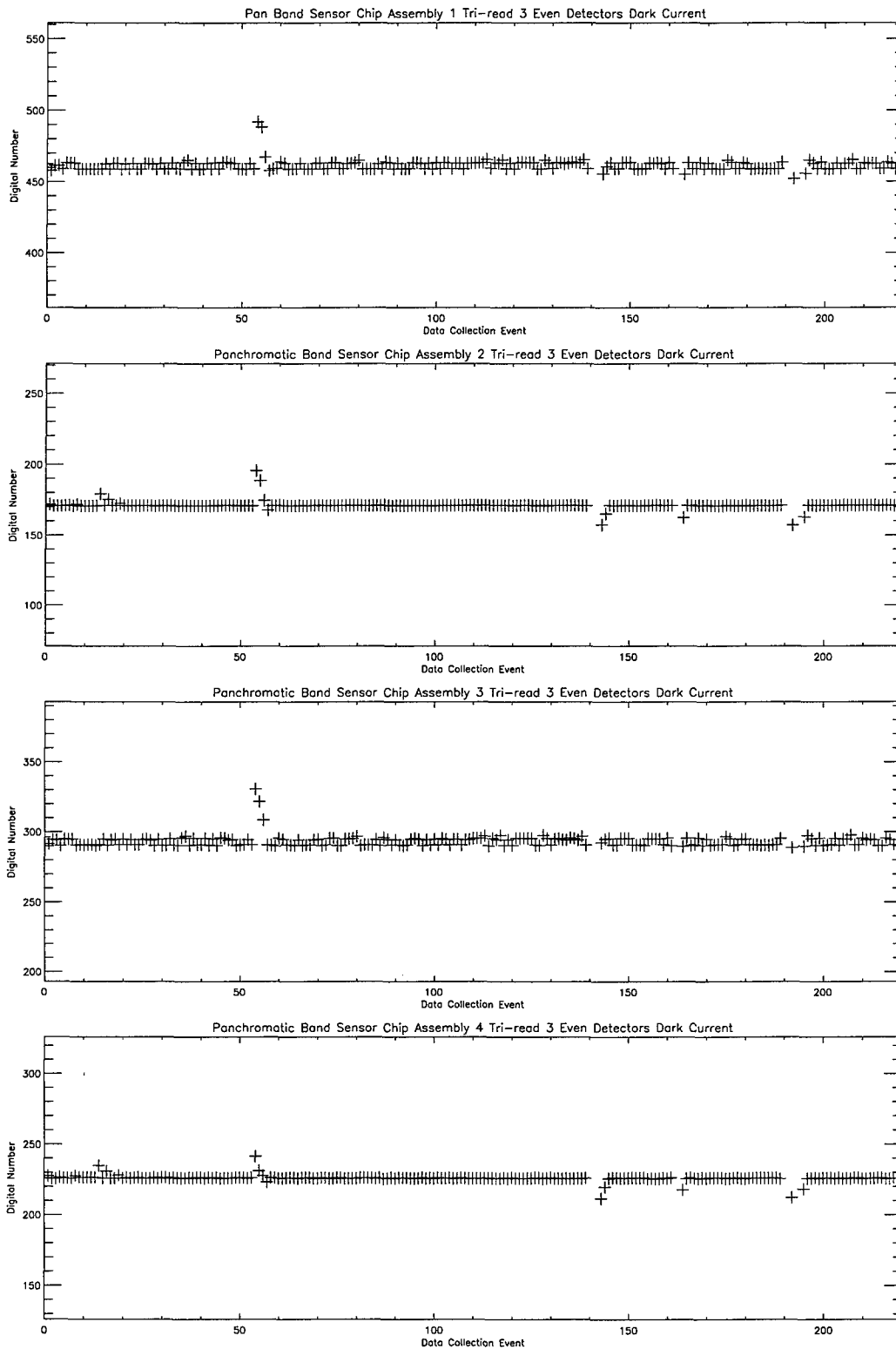


Figure 3-170. Dark current trending for Panchromatic Band tri-read #3 even detectors. Detector outgassing occurred near DCE 55, 140, 160, 190, and 219.

Table 3-29
Dark current trending statistics

Band	SCA	Preflight Mean (Digital Number)	Flight Mean (Digital Number)	Flight Std. Deviation (Digital Number)
1P	1E	238.0	247.4	9.6
1P	1O	248.0	256.0	6.3
1P	2E	290.1	296.1	6.0
1P	2O	282.6	290.1	9.2
1P	3E	315.7	322.8	8.4
1P	3O	321.9	328.0	5.5
1P	4E	251.6	255.2	3.3
1P	4O	246.1	250.0	4.8
1	1E	248.2	249.3	1.2
1	1O	261.8	263.4	0.2
1	2E	318.2	320.5	0.6
1	2O	285.0	286.3	1.3
1	3E	277.7	277.1	1.1
1	3O	297.3	297.3	0.2
1	4E	257.0	257.6	0.2
1	4O	246.1	246.8	0.6
2	1E	259.5	260.5	0.1
2	1O	262.7	263.5	0.1
2	2E	292.0	294.2	0.6
2	2O	306.0	308.8	0.6
2	3E	263.6	263.3	0.2
2	3O	277.8	277.6	0.2
2	4E	257.4	258.0	0.2
2	4O	686.7	686.7	0.2
3	1E	256.9	257.7	0.1
3	1O	277.3	277.9	0.2
3	2E	283.8	285.6	0.6
3	2O	298.0	300.4	0.6
3	3E	625.2	626.2	0.3
3	3O	293.4	300.4	0.6
3	4E	261.6	262.6	0.2
3	4O	256.3	257.2	0.2
4	1E	258.6	257.1	5.8
4	1O	254.3	252.6	6.7
4	2E	292.5	289.2	7.3
4	2O	289.4	287.5	5.9
4	3E	299.9	297.7	5.1
4	3O	305.0	302.8	6.0
4	4E	255.3	255.9	3.4
4	4O	240.4	240.7	2.9
4P	1E	241.5	240.0	6.7
4P	1O	262.6	260.6	6.8
4P	2E	300.6	296.8	7.4
4P	2O	304.8	301.1	7.4
4P	3E	301.0	298.2	6.1
4P	3O	314.5	301.1	7.4
4P	4E	258.9	259.1	3.4
4P	4O	246.8	247.2	3.3
5P	1E	405.9	464.0	26.2
5P	1O	361.7	396.8	17.2
5P	2E	385.9	429.0	18.9
5P	2O	377.6	435.9	23.7
5P	3E	283.8	264.1	6.0
5P	3O	269.8	246.7	6.0
5P	4EQ1	282.7	300.1	7.1
5P	4EQ2	263.4	261.9	3.1
5P	4EQ3	403.8	395.7	4.6
5P	4EQ4	509.7	519.2	4.0
5P	4OQ1	301.1	332.4	11.1

Table 3-29
Dark current trending statistics (continued)

Band	SCA	Preflight Mean (Digital Number)	Flight Mean (Digital Number)	Flight Std. Deviation (Digital Number)
5P	4OQ2	285.4	289.5	3.7
5P	4OQ3	426.5	426.7	3.4
5P	4OQ4	510.5	528.4	4.9
5	1E	307.7	314.8	7.6
5	1O	293.5	312.7	9.9
5	2E	347.9	346.6	9.5
5	2O	340.0	333.1	8.2
5	3E	261.2	248.6	5.6
5	3O	272.1	272.7	7.9
5	4EQ1	276.3	278.6	4.7
5	4EQ2	281.4	281.5	4.5
5	4EQ3	441.0	450.3	4.3
5	4EQ4	535.8	542.0	4.6
5	4OQ1	270.0	269.7	4.0
5	4OQ2	272.4	269.2	3.1
5	4OQ3	406.4	409.5	3.2
5	4OQ4	465.6	470.6	3.9
7	1E	382.3	457.5	22.1
7	1O	235.7	325.7	31.2
7	2E	242.3	369.8	30.1
7	2O	389.1	461.1	17.9
7	3E	300.1	290.6	8.4
7	3O	140.2	137.8	8.8
7	4EQ1	164.5	238.7	18.9
7	4EQ2	181.2	214.1	9.0
7	4EQ3	371.1	395.9	6.9
7	4EQ4	483.0	559.7	15.6
7	4OQ1	318.4	368.8	12.2
7	4OQ2	359.6	379.5	8.4
7	4OQ3	599.1	616.4	6.5
7	4OQ4	726.7	790.8	13.7
PAN	1ET1	465.7	465.5	6.8
PAN	1ET2	479.2	469.8	8.2
PAN	1ET3	465.3	461.2	2.2
PAN	1OT1	176.6	176.4	8.4
PAN	1OT2	197.2	188.1	9.0
PAN	1OT3	175.9	172.0	2.2
PAN	2ET1	172.4	177.7	9.3
PAN	2ET2	193.8	186.9	8.0
PAN	2ET3	171.5	171.1	0.8
PAN	2OT1	381.8	383.3	7.7
PAN	2OT2	396.2	388.8	8.7
PAN	2OT3	378.5	379.7	2.1
PAN	3ET1	295.8	298.9	7.3
PAN	3ET2	311.3	301.8	9.8
PAN	3ET3	295.4	293.0	2.3
PAN	3OT1	74.0	77.6	8.6
PAN	3OT2	91.9	84.2	8.4
PAN	3OT3	67.5	67.6	0.9
PAN	4ET1	226.3	225.9	2.8
PAN	4ET2	229.5	228.4	2.7
PAN	4ET3	224.5	226.2	0.9
PAN	4OT1	448.8	448.6	2.4
PAN	4OT2	451.4	446.3	1.4
PAN	4OT3	447.3	448.7	0.5

3.3.2.1.4 Discussion

The magnitude and repeatability of the EO-1 Advanced Land Imager focal plane noise were excellent during the first sixty days in orbit. The magnitudes presented in Table 3-28 are consistent with those calculated during pre-flight calibration of the instrument [3]. The trending

indicates little change in noise levels throughout this period, except during times when the focal plane was being warmed-up for outgassing.

The magnitude of the ALI focal plane dark current was as expected during the first sixty days in orbit. The magnitudes presented in Table 3-29 are consistent with those calculated during pre-flight calibration of the instrument [3]. Band 2 SCA4 odd detectors and Band 3 SCA 3 even detectors have increased dark current levels compared to the corresponding even and odd detectors respectively. This is due to the influence of previously identified leaky detectors in these bands. Additionally, all SWIR bands exhibit enhanced dark current levels for a region of SCA 4 that is associated with a previously identified 'hot spot' in the focal plane.

Analysis of dark current data indicates excellent stability of all dark current levels within a given observation. However, dark current level variability as high as 30 digital numbers for Bands 1p, 4, 4p, 5p, 5, 7, and the Panchromatic band has been observed from one observation to another and is not well understood at this time. A small (20-50 digital numbers) increase in dark current is also observed in Bands 5p and 7 over the course of the first 150 DCEs. More frequent outgassing (once per week) since then has reduced this drift to less than 10 digital numbers.

Additional changes in noise and dark current levels are observed during times when the focal plane was being heated for outgassing. However, even during these periods, all Visible and Near Infrared bands (1p, 1, 2, 3, 4, 4p) and the Panchromatic Band indicate little change in detector dark current levels. This is undoubtedly the result in differing dark current characteristics between the silicon (VNIR) and HgCdTe (SWIR) detector materials.

The results presented here will serve as baselines for noise and dark current trending during the remainder of the EO-1 mission.

3.3.2.2 Dark Current Stability over One-half Orbit Period

Employing a pushbroom imaging method, the ALI does not have the luxury of observing periodic dark reference periods during each scan that whiskbroom imaging systems enjoy. As a result, dark current measurements of the ALI focal plane can only be performed when the aperture cover is closed, during eclipse, or when viewing deep space. Furthermore, under normal operating conditions, a Landsat type instrument will collect imagery for a great majority of the portion of the orbit illuminated by the Sun. To characterize the dark current stability of the ALI focal plane and hence the required frequency of dark current reference periods for Landsat class missions, a sequence of special dark current collections was performed during the first sixty days on orbit. This section documents the results of this dark current stability test. Additional information may be found in the MIT/LL EO-1-6 Project Report [17].

3.3.2.2.1 Data Collection

The data collected for this study occurred on January 3, 2001. In preparation for this special dark current test, the focal plane was powered and allowed to warm-up for 4 minutes. Once thermally stabilized, the focal plane remained powered for over 40 minutes and two-seconds of data were collected every 5 minutes with the aperture cover closed.

3.3.2.2.2 Analysis

The mean dark current level of each detector of the ALI focal plane is determined for each of the nine dark current collections. A linear fit is then performed on each detector's dark current data. The fitted function is then subtracted from the original dark data and the mean and standard deviations for the *flattened* data are then calculated. Any detector with a standard deviation greater than 1.5 digital numbers is then categorized as a 'non-linear drifter'.

3.3.2.2.3 Results

The results of the thermal drift analysis are provided in Figures 3-171 to 3-182. For each figure, the overall linear drift and the standard deviation of the *flattened* data for each detector are provided. All VNIR bands and the Panchromatic band exhibited less than one digital number drifting during the forty minute period. These bands also exhibited residual drifting of less than 0.5 digital numbers, after linear drifting is subtracted. All SWIR bands exhibited up to 30 digital numbers of linear drifting. However, all but twenty-four SWIR detectors exhibited less than 1.5 digital number of residual drifting (Table 3-30). Twelve of these detectors were previously identified as exhibiting anomalous dark current or noise characteristics during ground calibration [3]. The distribution of SWIR detectors as a function of non-linear drifting threshold (0.5, 1.0, 1.5, 2.0, 2.5, and 5.0 digital numbers) is provided in Figures 3-183 to 3-185. Only the previously identified anomalous detectors exhibit non-linear drifting greater than 2.3 digital numbers.

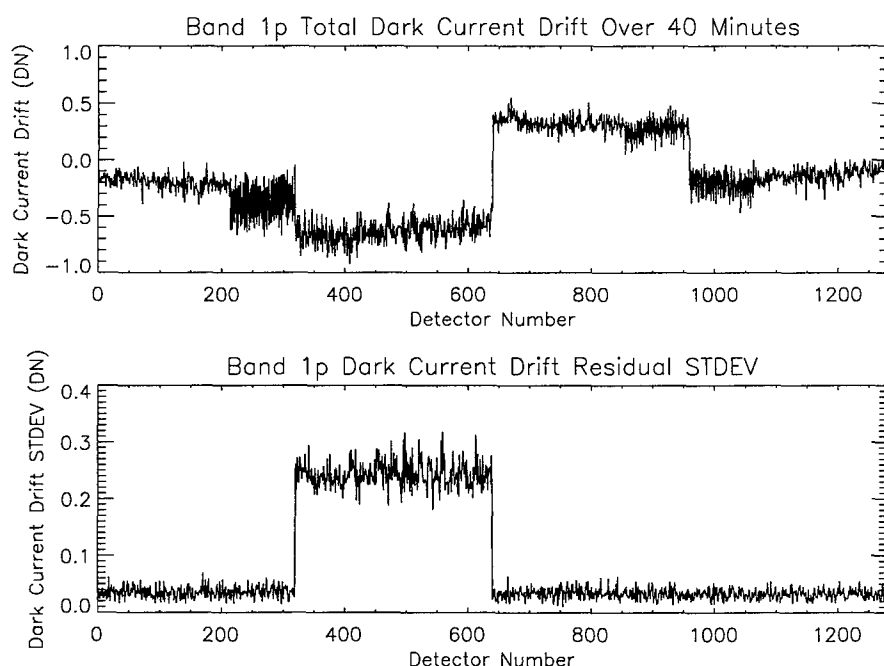


Figure 3-171. Dark current drift for Band 1p.

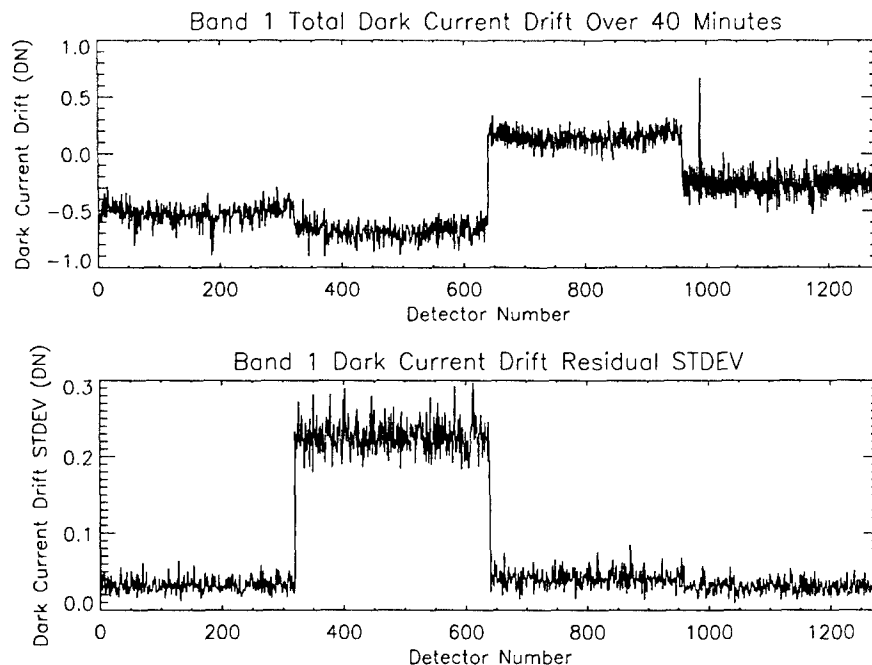


Figure 3-172. Dark current drift for Band 1

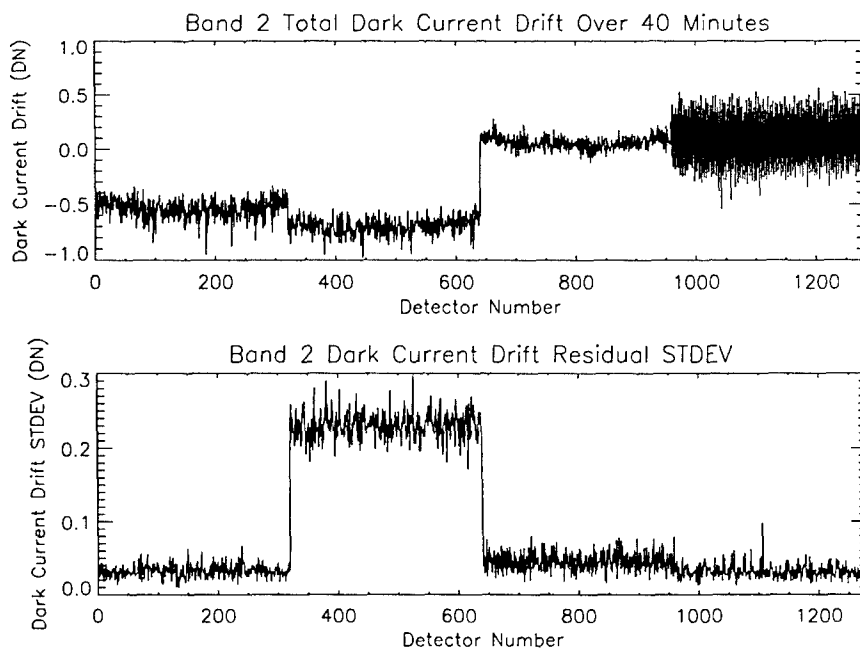


Figure 3-173. Dark current drift for Band 2.

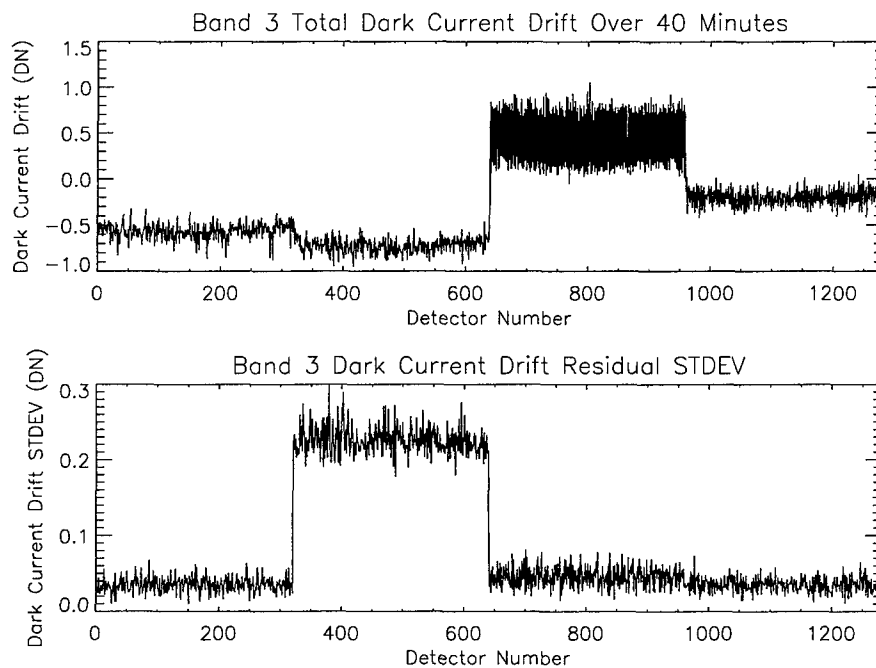


Figure 3-174. Dark current drift for Band 3.

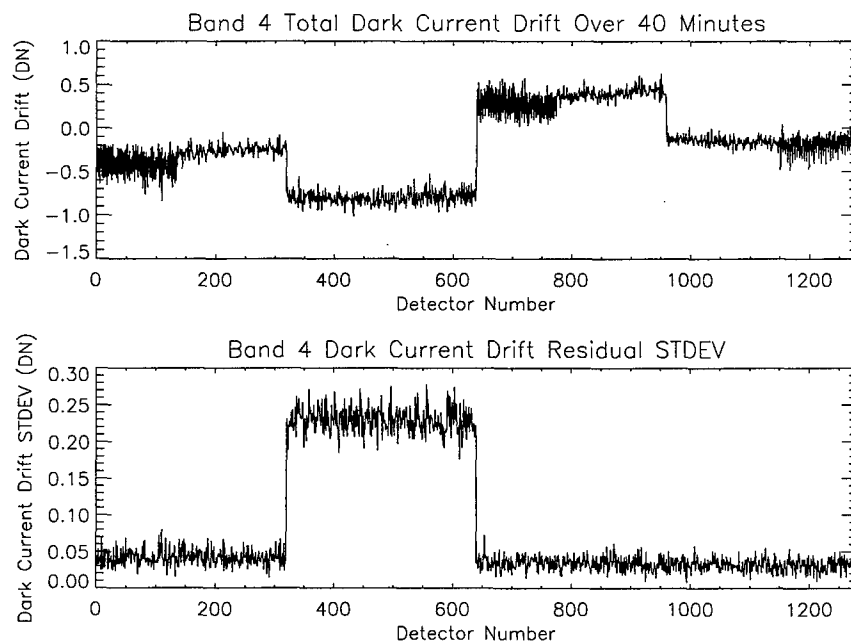


Figure 3-175. Dark current drift for Band 4.

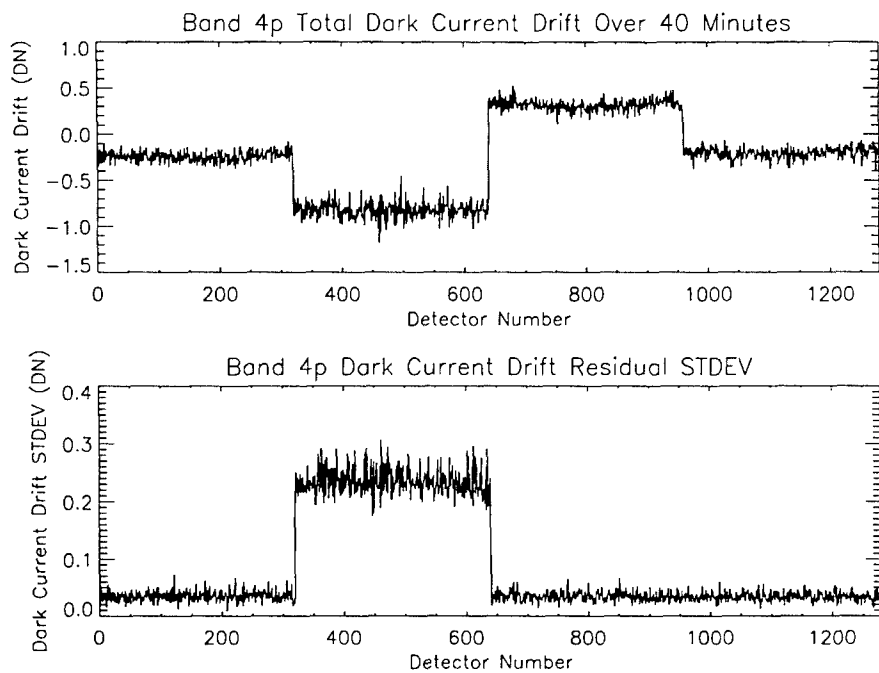


Figure 3-176. Dark current drift for Band 4p.

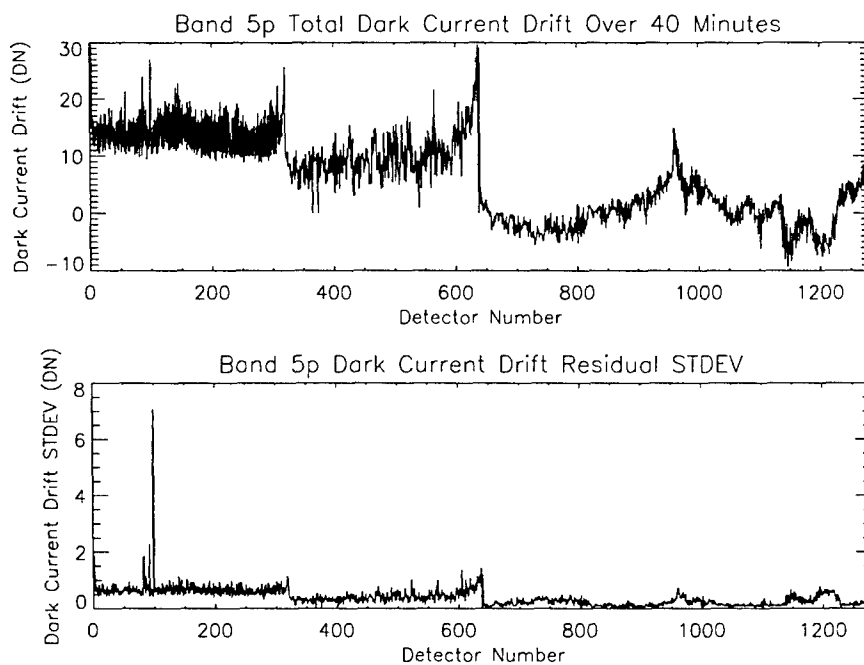


Figure 3-177. Dark current drift for Band 5p.

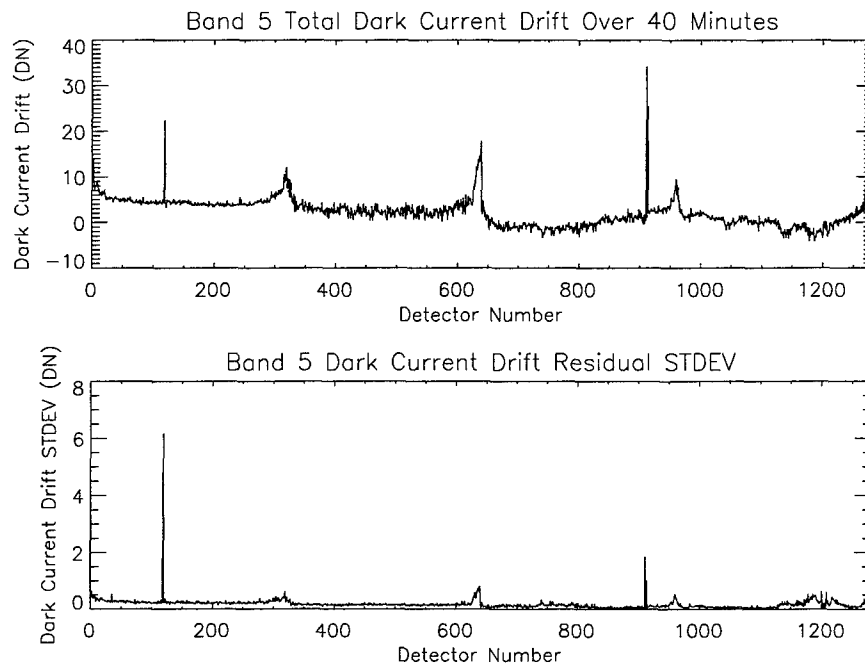


Figure 3-178. Dark current drift for Band 5.

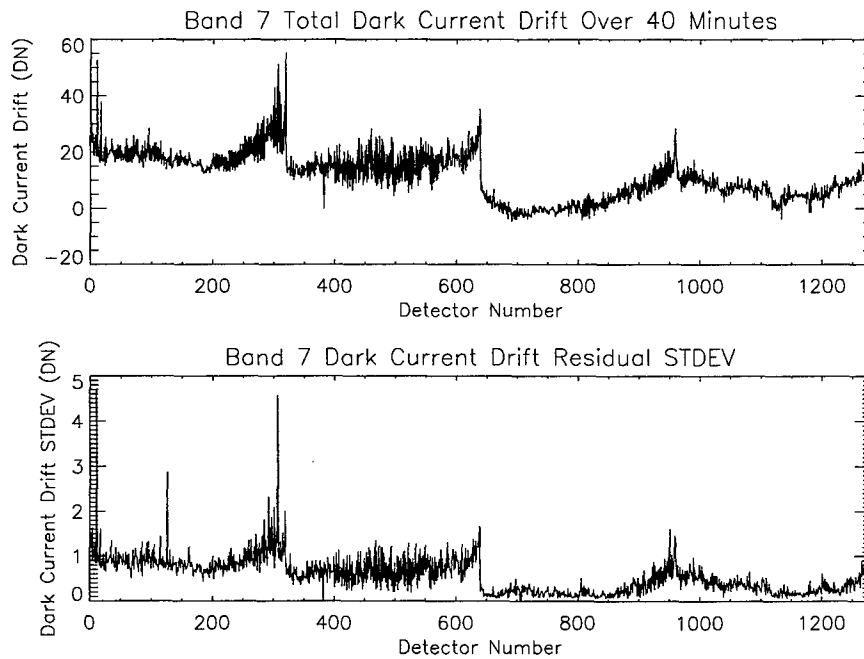


Figure 3-179. Dark current drift for Band 7.

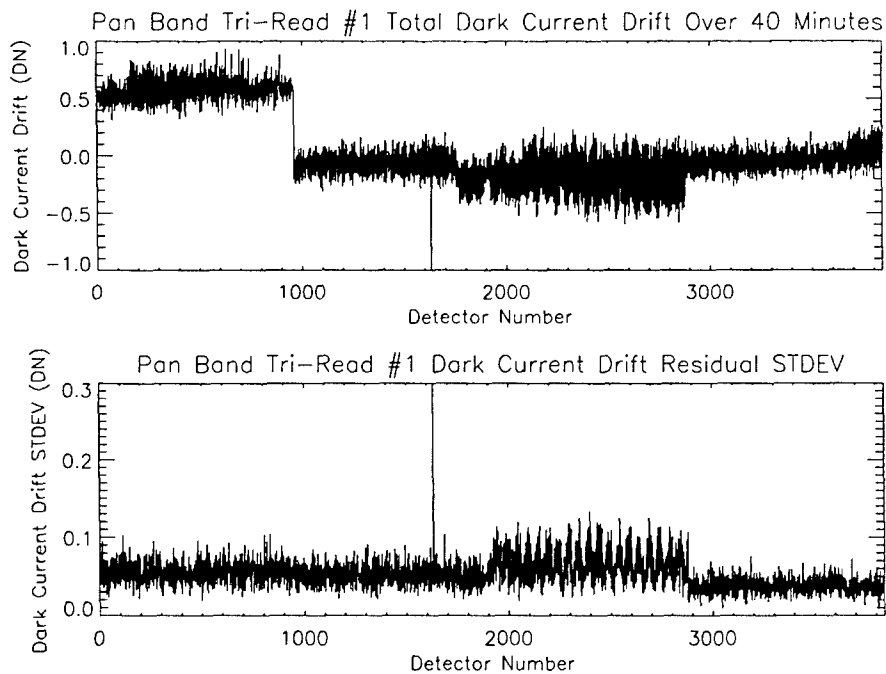


Figure 3-180. Dark current drift for Panchromatic Band tri-read #1.

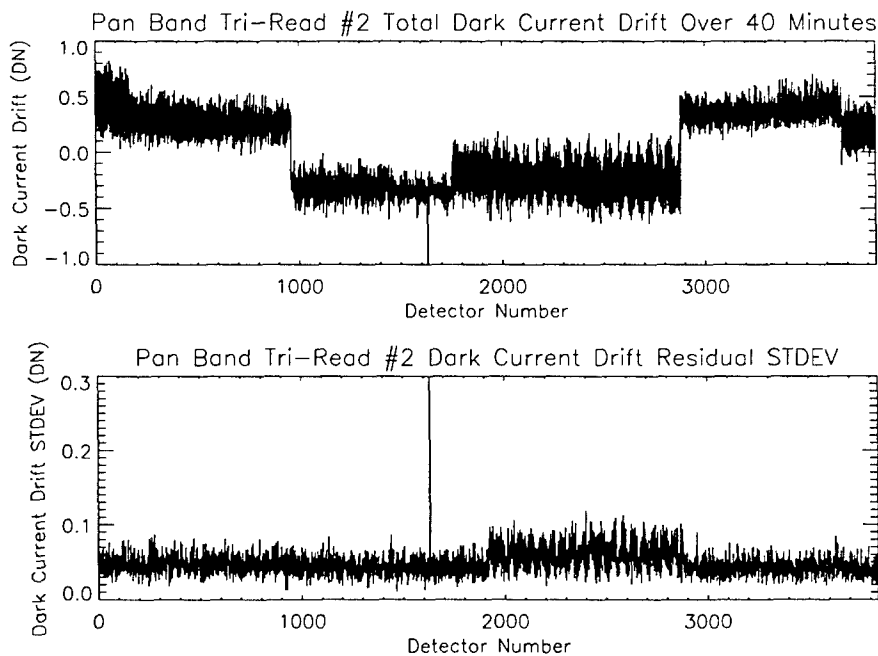


Figure 3-181. Dark current drift for Panchromatic Band tri-read #2.

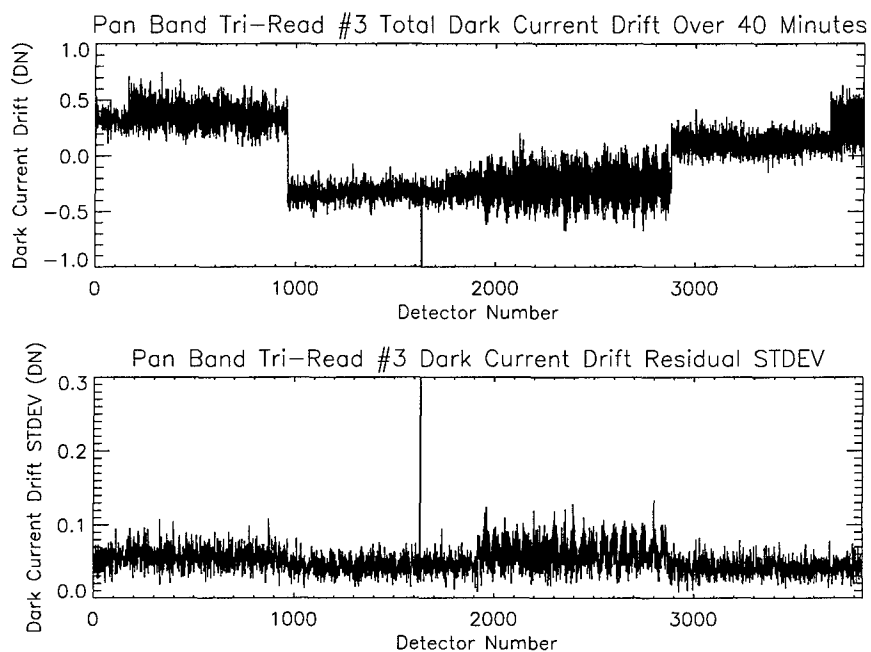


Figure 3-182. Dark current drift for Panchromatic Band tri-read #3.

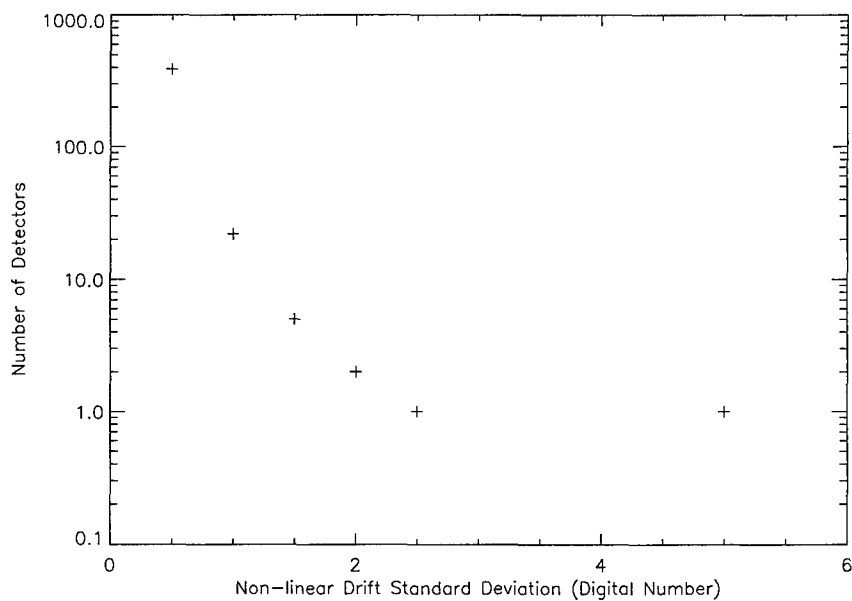


Figure 3-183. Dark current non-linear drift distribution for Band 5p.

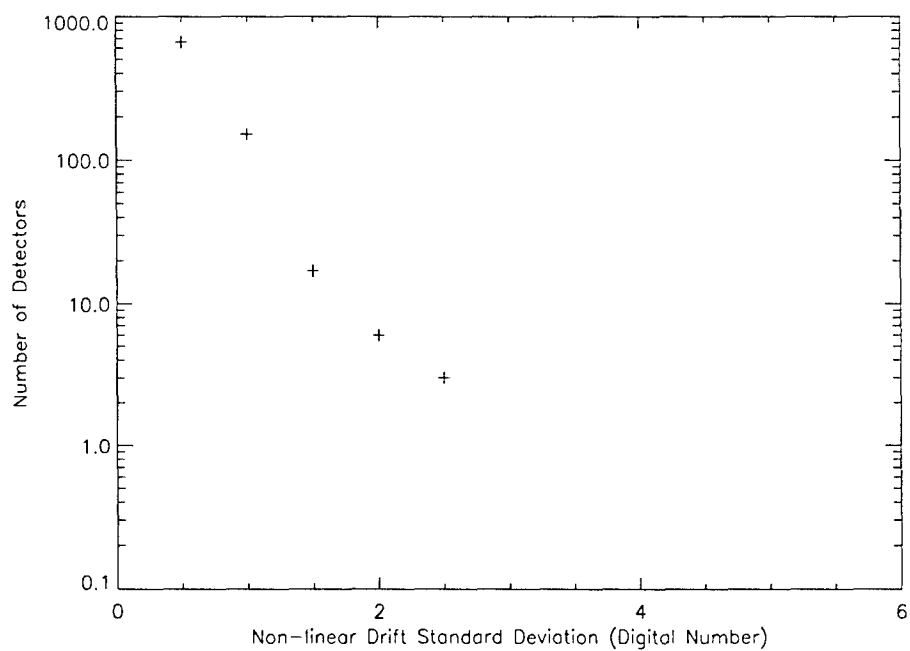


Figure 3-184. Dark current non-linear drift distribution for Band 5.

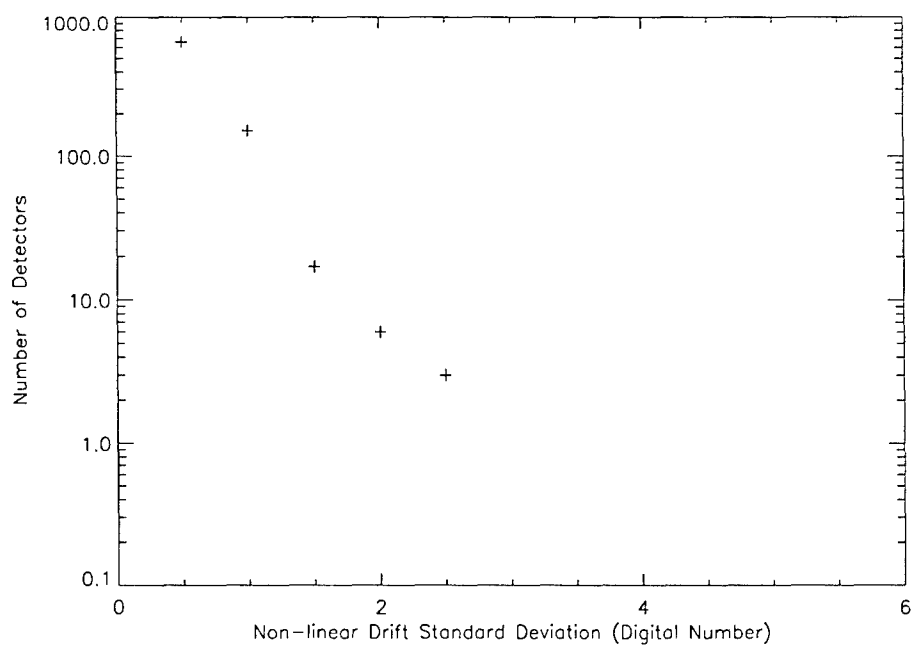


Figure 3-185. Dark current non-linear drift distribution for Band 7.

Table 3-30
Detectors with non-linear drifting greater than
1.5 digital numbers over a 40-minute period

Band	Detector Number	Residual Drift (Digital Number)
5p	2	1.86
5p	82	1.77
5p	83	1.87
5p	92	2.28
5p	99	7.07
5	119	6.16
5	911	1.86
7	0	1.57
7	4	1.63
7	11	4.72
7	17	1.61
7	126	2.86
7	285	1.81
7	292	2.32
7	295	1.64
7	297	1.88
7	301	2.09
7	305	1.55
7	307	4.58
7	315	1.52
7	319	2.01
7	638	1.65
7	639	1.64
7	951	1.60

3.3.2.2.4 Discussion

The above analysis indicates all of the active VNIR and Panchromatic detectors of the EO-1 Advanced Land Imager focal plane are stable to within 1 digital number over a period of forty minutes. However, all of active SWIR detectors exhibit some drifting during this period. Fortunately, 99.4% of these detectors drift linearly and may be easily accommodated through a linear interpolation of dark current measurements obtained as the instrument exits eclipse near the North Pole and enters eclipse near the South Pole. An additional 0.3% exhibit less than 2.3 digital numbers of nonlinear drifting over the 40 minute period. The worst detector drifts by 7.1 digital numbers but has been previously identified as having excessive white and pseudo-random noise [3].

The effect of non-linear drifting will result in the inaccurate subtraction of dark current levels during observations. This will become most evident in regions of poor illumination or low reflectivity (e.g. water). This uncertainty will result in detector-to-detector striping which is dependent on the amount of signal produced by the scene and the amount of non-linear drifting by the detector.

3.3.3 Focal Plane Contamination

Contamination on orbit has been monitored using the internal reference lamps. Figures 3-186 to 3-189 provide a history of focal plane contamination for the first 140 days on orbit for the panchromatic band. Figures 3-186 and 3-187 depict the mean and standard deviation of the ratio of lamp data collected for each day relative to the December 1, 2000 data. As is clearly evident, significant contamination build-up was observed during the first 30 days on orbit. However, once the bakeout frequency was increased to once every six days, the amount of contamination was significantly restricted. Figures 3-188 and 3-189 depict the mean and standard deviations as above, but only for the fourth day after each bakeout. As can be seen, the rate of contamination build-up significantly decreased over the first 15 bakeout periods. Since then, the bakeout frequency has decreased to once every 20 days.

Contamination build-up on the focal plane will continue to be monitored for the duration of the EO-1 mission and the bakeout frequency will be adjusted to maintain radiometric effects below 1%.

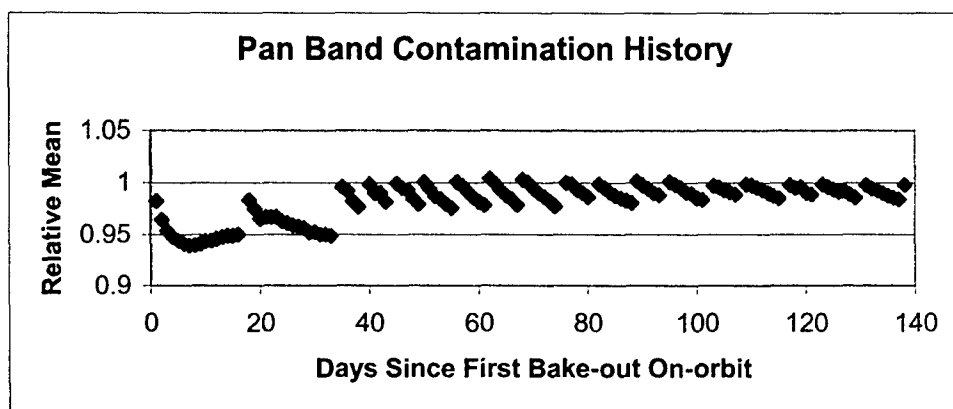


Figure 3-186. Pan Band on-orbit contamination history.

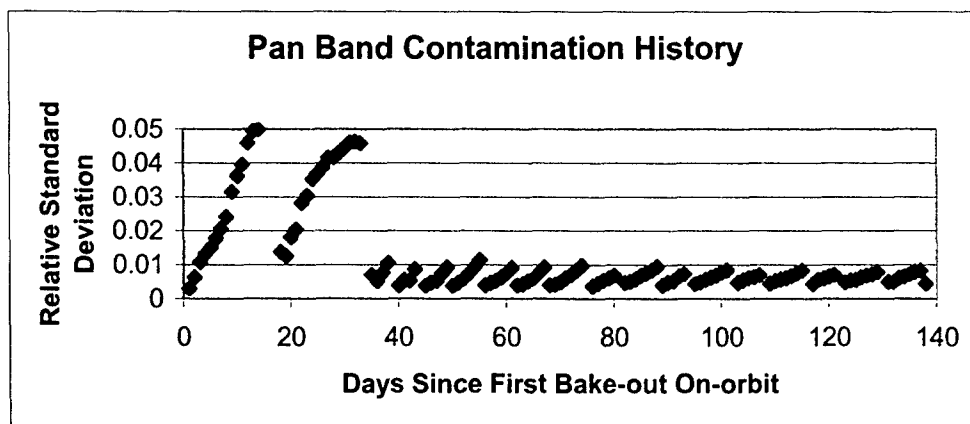


Figure 3-187. Pan Band on-orbit contamination history.

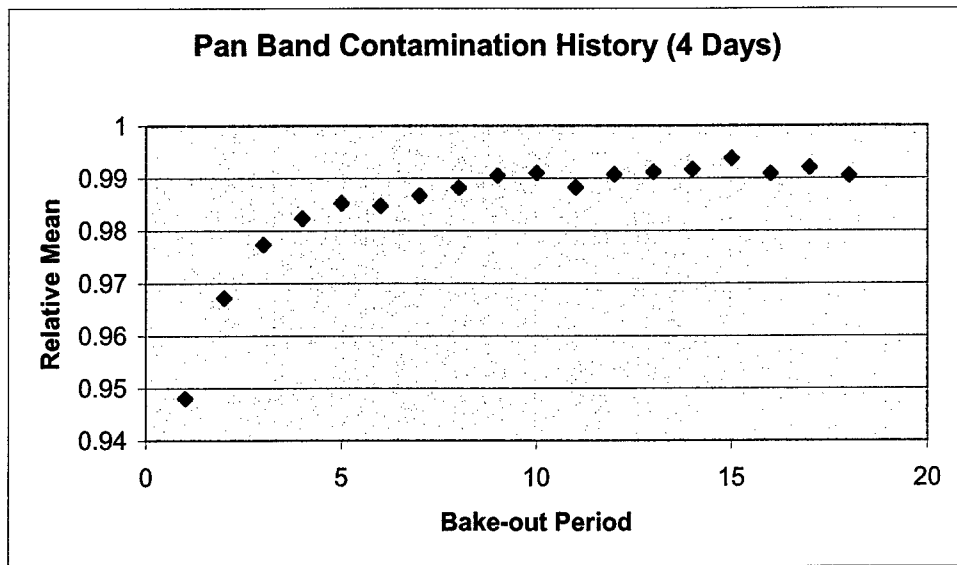


Figure 3-188. Pan Band on-orbit contamination history.

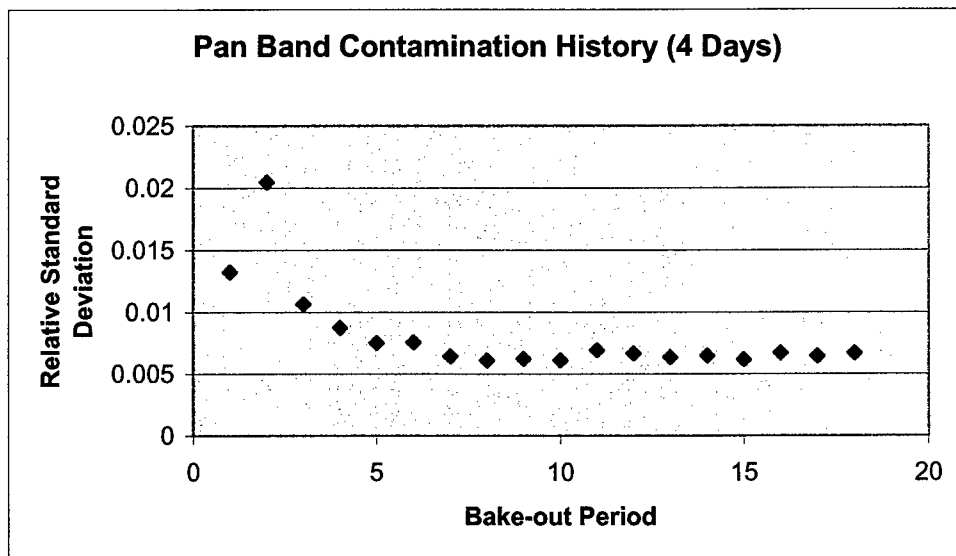


Figure 3-189. Pan Band on-orbit contamination history.

4. ALI LESSONS LEARNED

4.1 INTRODUCTION

A full discussion of "Lessons Learned" is a difficult public exercise. Inevitably, it must contain an enumeration of decisions and actions by the ALI team, as well as colleagues in other organizations, that in retrospect do not look the wisest. It is also an opportunity to take credit for solving difficult problems that may be encountered by other instrument developers. The account that follows attempts to cover everything, the good as well as the bad experiences, with two guiding principles: to be fair and to be the most helpful to future instrument designers.

The ALI lessons learned may be grouped in two categories: those of a programmatic nature and those of technical nature. The programmatic issues will be discussed first.

4.2 PROGRAMMATIC ISSUES

4.2.1 Instrument Additions

The Grating Imaging Spectrometer (GIS) was added to ALI, three months after the program start. The GIS had the strong support of the science community and its addition enhanced the overall support for the mission. However, the GIS specifications and budget were developed in a hurry without the benefit of a full analysis. It turned out that the GIS integration complexity and cost and schedule impact were underestimated. The ensuing cost overrun and schedule slip ultimately led to the elimination of both the GIS and the Wedge Imaging Spectrometer (WIS).

The lesson learned (once again) is that mission changes should be considered very carefully.

4.2.2 Spacecraft Interface Change

The spacecraft structure was changed from composite to aluminum ten (10) months after the program start (26 Feb. 97) requiring substantial redesign of ALI structures. The sequence of events was as follows. The launch vehicle was changed from the Taurus to Delta 2 (28 Jan. 97) increasing mass allocations. The Project Office traded spacecraft mass for cost and decided to switch from composite to aluminum structure. The impact on ALI was not fully appreciated. In the meantime, ALI had been designed with a composite pallet structure and appropriate mounts. After several options were examined, it was concluded that the ALI pallet had to change to aluminum as well, with associated redesigns of the telescope housing and kinematic mounts.

In conclusion, requirements and interfaces need to be frozen early in the design process. Major design changes are costly.

4.2.3 Engineering Development Units

The decision was made to build all electronics assemblies without Engineering Development Units (EDU) or Qualification Units to reduce cost. This approach delayed problem discovery which made correction more difficult and more, not less, expensive.

The lesson is that the EDU serves a useful purpose and should not be skipped.

4.2.4 Contingency Reserve

The mandated 10% reserve proved inadequate for a program for flight-validation of new technologies. It was discovered that the new technologies incorporated in ALI required further development to produce flight hardware. Problems were encountered, e.g., in the fabrication of the Read-Out Integrated Circuit (ROIC) and the SiC telescope truss, that required significant additional time and effort to resolve.

Adequate reserves should be provided, commensurate with the technology readiness, to resolve unanticipated problems and to pursue back-up options. An amount of the order of 30% of the initial cost estimate seems reasonable.

4.3 TECHNICAL ISSUES

4.3.1 Focal Plane Contamination

During the thermal-vacuum tests of the fully assembled ALI at Lincoln Laboratory, a gradual change was noticed in the detector response. The change was manifested while the focal plane was illuminated by the reference lamps included in the instrument. Such measurements were made frequently, interleaved with the various calibration runs. Following an investigation of the problem, it was determined that the change was due to a substance condensing on the cold surface of the spectral filters. This was verified by imaging the filter surface. Under magnification, the condensate appeared as water droplets on a shower door. As the instrument was warmed up, the effect of the contaminant gradually disappeared at temperatures between 250 K and 265 K indicating a boil-off of the substance. At room temperature, the detector response returned to its original value. RGA measurements from the vacuum chamber failed to identify the nature of the contaminant.

In order to vent off the contaminant, the entire instrument was baked out in vacuum, at 40°C for several days with the telescope door open. In a subsequent series of thermal-vacuum tests the effects of contamination were found reduced by an order of magnitude. A second bake-out was performed at the Laboratory just before shipping the instrument and it was believed that the problem had been solved. For good measure, a heater had been added to the focal plane radiator such that should contamination reappear on orbit, the focal plane temperature could be raised to about 273 K to boil off the substance.

Several months later, contamination build-up reappeared during the spacecraft thermal-vacuum tests at NASA/GSFC whereupon another bake-out was conducted. However, the problem persisted. On orbit, the contaminants are boiled off through periodic 8-hour bake-outs (at maximum temperature), which result in a total down time of 20 hours. Performing a bake-out every 10 days, limits the change in the response of the most severely affected band to 2%. Over a period of several months, the severity and rate of contamination build-up have gradually decreased. Since August of 2001 contamination effects are no longer evident in the SWIR bands. It should be noted that while the focal plane is being warmed up, the VNIR data are still good, however, the SWIR data are not.

sources of contamination is the Z-306 black paint used on the telescope baffles and housing. The latter was baked in vacuum at 95°C for 70 hours. Pressure readings from the vacuum chamber suggest that longer bake-out was needed. Cost and schedule sometimes drove the decisions on bake-out duration.

In conclusion, uniform bake-out standards are needed across the board to minimize the contamination potential during vacuum-chamber testing and on orbit. The bake-out duration should be controlled by RGA and/or pressure readings from the vacuum chamber. As an additional precaution, heaters for on orbit bake-out should be provided.

4.3.2 Leaky Detectors

Two ALI detectors, out of a total of 15,360, are coupling their signal to the neighboring detectors creating streaks in the images. The problem was not evident in the original test data collected under flood illumination of the focal plane. Special algorithms have been developed and used in data processing that greatly reduce the effects of leakage, virtually eliminating it.

In the future, Sensor Chip Assemblies should be screened to eliminate any that have leaky detectors.

4.3.3 Vacuum Chamber Window Effects

During instrument calibration under thermal-vacuum, it appeared that the focus of the instrument had shifted, by about 6 mils. It was determined both experimentally and analytically, that the focus shift was due to the chamber window refractive index distortion due to a radial temperature gradient. A technique was developed to eliminate this effect.

In conclusion, it is important to understand all the optical effects of thermal-vacuum chamber windows and address them in the test plan and test procedures.

4.3.4 Instrument Alignment on the Spacecraft

The first images from space showed that ALI and Hyperion were not co-aligned. Review of the pre-launch measurements showed that each instrument's alignment relative to the S/C had been correctly measured and recorded and revealed the misalignment. However, there was not a specification in place or a system engineer to ensure the co-alignment between the two instruments.

Obviously, a System Engineer is needed to oversee and correct critical performance issues at the system level.

4.3.5 Instrument Pointing

Once on orbit, it took several weeks to establish accurate instrument pointing. During this time, the S/C pointing was well established.

Again, the lack of a System Engineer resulted in unnecessary delay in correlating all the available information to establish proper instrument pointing.

4.3.6 Internal Reference Lamps

The brightness of the ALI reference lamps changed on-orbit (increased). Investigation revealed that the filaments of gas-filled lamps run hotter in zero-G because of the absence of gas convection.

So, while gas-filled lamps are very useful for checking day-to-day repeatability, they should not be used as a radiometric transfer standard.

4.3.7 Subsystem Early Consideration

While the use of reference lamps was in the ALI plan from the beginning, design requirements were not given to the mechanical designer early on. When the details of the lamps became known, it proved difficult to accommodate the lamps in the truss design. Eventually the lamps were incorporated in the telescope after substantial design effort.

Since quite often it is difficult to add on subsystems that are not part of the design considerations from the beginning, it is important to include all subsystems in the early planning.

4.3.8 Processing of Flight Data

After launch, the Level 0 data formats changed several times. For example, pixels and bands were shifted and the images were flipped left-to-right. Each time, the Calibration Pipeline that produced the Level 1 data had to be changed requiring additional effort.

To maximize efficiency, the ICD regarding Level 0 processing and the Calibration Pipeline should be completed and frozen before launch.

4.3.9 Schedule

The ALI schedule remained very tight even when it became clear that other parts of the program were slipping. Some opportunities to avoid overtime and do a more thorough instrument calibration were missed.

Harmonizing all delivery schedules can produce some program benefits. However, the potential benefits of any schedule relaxation must be carefully weighed against the additional cost of keeping a larger team on-board for a longer time.

4.4 MORE LESSONS LEARNED

Thorough documentation of all vendor (subcontractor) tests can be very useful for future data analysis and troubleshooting. It does increase the cost though.

Documenting the "as-built" characteristics (e.g., dimensions) of each part can also be valuable in understanding test results. For example, the slit widths of the screen used for the ALI solar calibration were checked for conformity to the specification and passed. However, in interpreting the results of the on-orbit solar calibration, exact knowledge of the "as-built" dimensions became necessary. In the absence of the exact "as-built" measurements of the flight unit, the widths of the

slits were inferred from on-orbit measurements of the slit edge crossing times of the calibration aperture. This resulted in a better match to the analytical estimates than using the nominal values.

Another useful form of documentation is a set of photographs of the instrument prior to delivery, with close-ups of all critical items. After the thermal-vacuum test at GSFC, it was noticed that one of the High Output Paraffin Actuators (HOPA) was partially retracted. The question arose as to when this happened. Examination of pre-delivery photos showed that the condition existed prior to the GSFC testing so the HOPA was in good health. Needless to say, the HOPA was reset prior to the shipping to the launch site.

Comparison of several independent calibration techniques has proved to be extremely valuable both in ground and on-orbit measurements.

Prior to ALI, Landsat imagers had a relatively small number of detectors that required calibration. On the other hand, ALI contains a fairly large number of detectors (15,360), raising the question of whether individual detector calibration could be managed. The instrument calibration at Lincoln Laboratory demonstrated that calibration of a large focal plane is a manageable job but requires thorough preparation of test plans, test instrumentation and associated software to process the large volume of data.

4.5 SUMMARY

Many of the lessons learned have a common thread: a tight development schedule and budget require greatly focused mission objectives. Given that, the most important ingredient for success is a highly motivated, dedicated team that can overcome the inevitable problems associated with a high-risk, technology validation mission.

5. TECHNOLOGY INFUSION OPPORTUNITIES

5.1 INTRODUCTION

This section describes the strategy for the infusion of technology from the Advanced Land Imager. After a brief introduction, the technology from the ALI which is available for infusion into future land imaging instruments is described. The process for technology infusion is then discussed.

The top level performance characteristics of the Advanced Land Imager are illustrated in Figure 5-1. ALI covers ten spectral wavelength bands from 0.4 to 2.4 micrometers in a relatively lightweight, low power system.

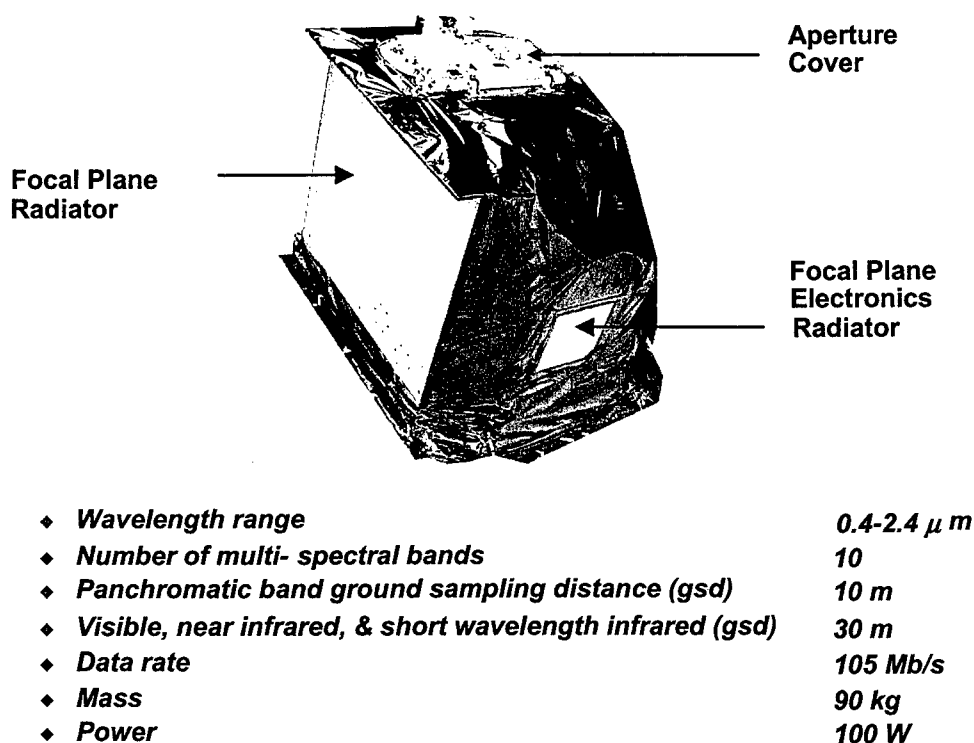


Figure 5-1. Advanced Land Imager Instrument

Candidate missions for ALI technology infusion are the Landsat Data Continuity Mission and other U.S. Government selected missions.

The path for ALI technology infusion is illustrated in Figure 5-2. The Earth Observing-1 mission has validated a number of ALI technologies in orbit. The analysis of on-orbit data to validate the ALI technologies is essentially complete and is being documented to support the transfer to new missions.

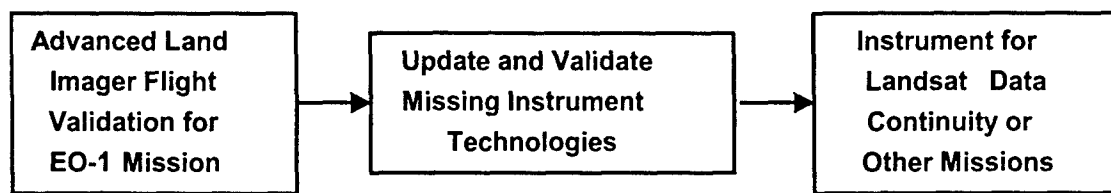
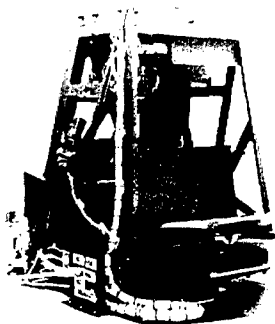


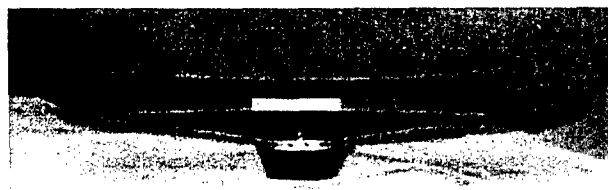
Figure 5-2. Technology Infusion Path

5.2 TECHNOLOGY FOR INFUSION

The first technology, which was developed by SSG, is the wide field of view, silicon carbide optics (Figure 5-3). The design requirements were met for the wavefront quality of the silicon carbide mirrors and telescope over the temperature range of -40°C to $+50^{\circ}\text{C}$. The low scattering requirements of the silicon carbide mirrors were not met on EO-1, but separate efforts with a spare primary mirror did demonstrate acceptable performance according to reports by SSG for NASA. The initial design for ALI included a silicon carbide metering truss, which was changed to Invar because of cost and schedule concerns. Three approaches for future missions are identified. First, the Invar telescope with improved silicon carbide mirror scattering could be validated in ground tests before a new mission. Second, a lighter weight silicon carbide composite telescope structure could be developed and validated in ground tests with improved silicon carbide mirror scattering. Finally, an all aluminum telescope with aluminum mirrors could be designed, analyzed, built, and validated. Several features in the ALI metering truss were associated with the Grating Imaging Spectrometer, which was discontinued during ALI development because of cost and schedule. Those features could be eliminated for simplicity.



Invar Telescope Structure



Silicon Carbide Primary Mirror

Figure 5-3. Wide Field of View, Silicon Carbide Optics

The focal plane system was provided by Raytheon in Santa Barbara. The basic ALI focal plane design was validated, including its mounting frame, rail, thermal link, radiator, heaters, temperature sensors, and cables. The validated design is a ten-band system with seven bands in the visible and near infrared and three bands in the short wave infrared. The fully populated focal plane, illustrated

in Figure 5-4, could be made up of five identical subassemblies like the one that has been validated in orbit with the ALI.

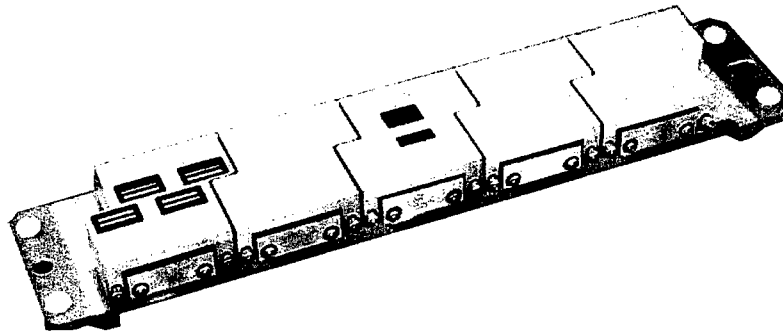


Figure 5-4. Focal Plane Array

An increase in the number of VNIR or SWIR bands would require a new focal plane design. The filter designs were for the specific wavelength bands of the ALI. Other bands would require different filter designs. The ALI focal plane design and passive cooling would not be appropriate for thermal bands.

The Focal Plane Electronics board and chassis are pictured in Figure 5-5. For a fully populated focal plane, the focal plane electronics on the ALI would have to be modified. Some suggestions for the modifications are identified. The science data output format could be simplified, and redundancies could be added for reliability. The multi-spectral and panchromatic circuits could be reproduced five-fold for the full focal plane. A new board layout could be designed to reduce thermal control noise and to remove wedge and grating focal plane circuits and jumper wires. The power converters could be relocated from the ALI Control Electronics onto the Focal Plane Electronics cover-radiator to simplify the interface design. The timing circuits, chassis, connectors, and board packaging should be adequate for the fully populated focal plane.

The mechanisms, pallet, and telescope flexures shown in Figure 5-6 underwent testing at Lincoln Laboratory in preparation for flight. Life tests on the mechanisms covered only the anticipated cycles for a two-year EO-1 mission. There were no failures in the life tests. The tests were halted because the required cycling was achieved. No degradations were identified which would cause the mechanism operations to fail during flight, and they have performed flawlessly during the mission.

The control electronics for the Advanced Land Imager shown in Figure 5-7 were designed for technology validation with significant diagnostics. An operational mission would probably benefit from a number of changes to the design. The Electronic Services Node Multi-Chip Module is no longer available from the supplier. Existing stock could be identified, or replacement parts could be found. Software changes could range from minor to major, if the protocols were preserved from the EO-1 mission or modified substantially. The temperature circuits and sample rates could be reduced for an operational mission. Noise could be reduced by slowing the multiplex circuit rise times and by adding filters. New board layouts could eliminate jumper wires and add redundancy for reliability. The 1773 fiber optic transceivers could be replaced with 1553 links.

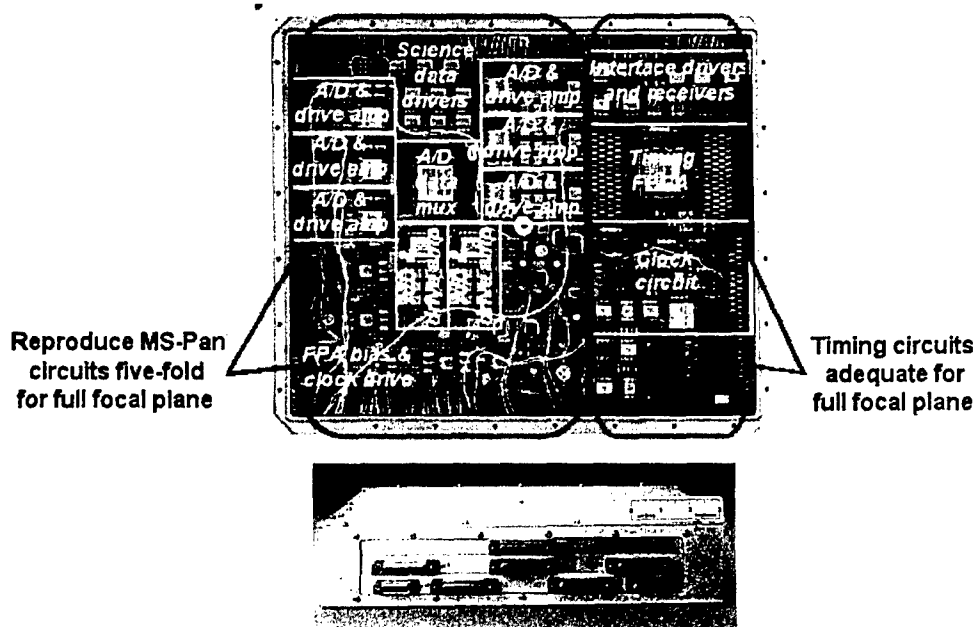
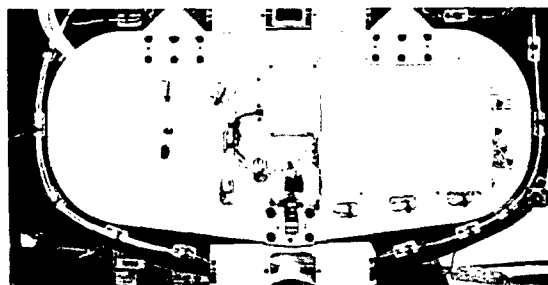


Figure 5-5. Focal plane electronics board and chassis



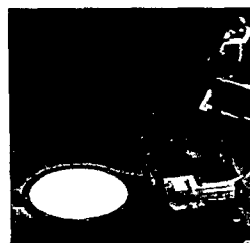
Instrument Pallet



Aperture Cover



Telescope Flexural Mounts



Calibration Diffuser

Figure 5-6. Mechanisms, pallet, and telescope flexures

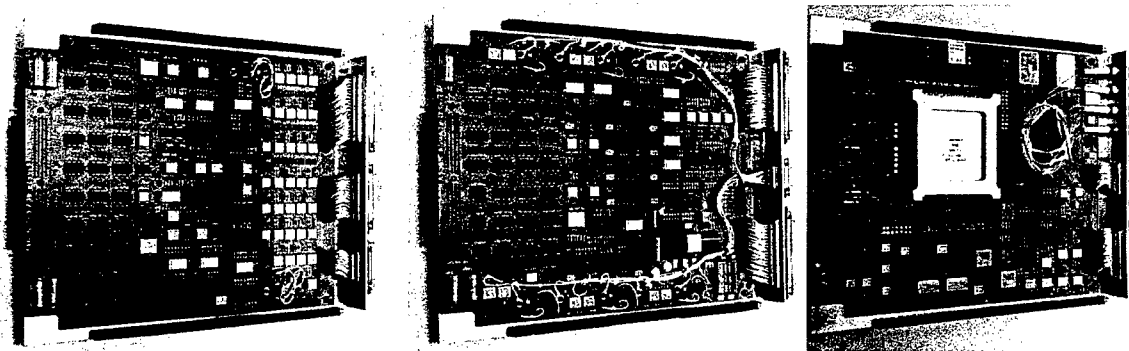


Figure 5-7. Advanced Land Imager control electronics boards

5.3 TECHNOLOGY INFUSION PROCESS

Figure 5-8 illustrates the technology infusion process for the technologies validated on the Advanced Land Imager on EO-1 and the technologies to be updated. All of the updates can be validated adequately in ground testing. For this reason, the technology is in an excellent position for infusion in a Landsat Data Continuity Mission or other missions.

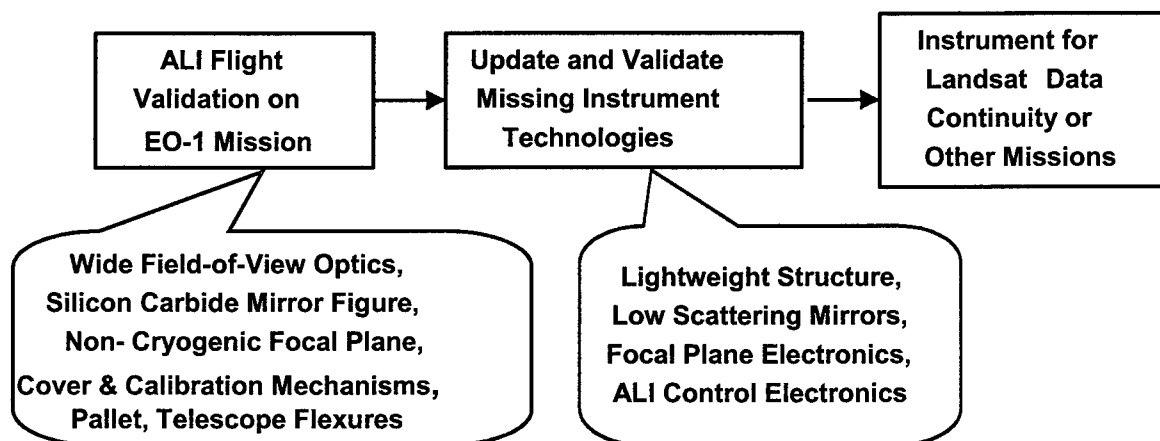


Figure 5-8. Technology infusion path

The Earth Observing-1 Technology Transfer and Infusion Workshop was held on January 9-11, 2001, the EO-1 Mission Technology Forum was held on August 15-16, 2001, and the Advanced Land Imager Technology Forum was held on October 17-18, 2001 at MIT Lincoln Laboratory.

Lincoln Laboratory is prepared to support technology transfer and infusion of the ALI technologies to the LDCM or other missions under NASA sponsorship. MIT Lincoln Laboratory documentation from the Advanced Land Imager project include: System and subsystem Interface Control Documents; Available design drawings and parts lists (some released and some red-lined); Programs for numerically-controlled machining of some parts; Available process procedures; Test plans, procedures, and reports; Review presentations, action items, and responses; System and subsystem requirements; Software and software description for instrument test, status monitoring, operation,

and calibration; System and subsystem schedule experience; and Project reports. More Information on available documentation can be found at The EO-1 Technology Validation, Transfer, and Infusion website: <http://eo1.gsfc.nasa.gov/miscPages/Transfer.html>.

Other possible MIT Lincoln Laboratory capabilities beyond documents which will be assessed for LDCM technology infusion include: available fixtures; facilities, as available; clean thermal-vacuum chamber; thermally-controlled chambers; vibration test systems; clean assembly area; electrostatic-discharge-controlled assembly area; instrumented bake-out chamber; calibration facilities and instrumentation; structural-thermal model (unpolished mirrors and thermal model focal plane) with operating ALI control electronics; analysis, design, fabrication, assembly, and calibration capabilities; some spare parts and an aluminum telescope structure.

5.4 SUMMARY

The New Millennium Program developed the technology of the Advanced Land Imager for validation. The ground and on orbit validations have been completed. A process has been defined for transferring and infusing the ALI technology to future land imaging instruments.

6. CONTACT INFORMATION

Below are the contacts' names, program roles and e-mail addresses.

- Dr. Jeffrey A. Mendenhall, ALI System Engineer, mendenhall@ll.mit.edu
- Dr. Donald E. Lencioni, ALI Instrument Scientist, lencioni@ll.mit.edu
- Dr. David R. Hearn, ALI Instrument Analyst, drhearn@ll.mit.edu
- Dr. Steven E. Forman, ALI Payload Manager, sforman@ll.mit.edu
- Ms. Jenifer Evans, ALI Calibration Pipeline development, jenifer@ll.mit.edu
- Dr. Constantine J. Digenis, ALI Program Manager, digenis@ll.mit.edu

The mailing address for all of the above is:

Massachusetts Institute of Technology
Lincoln Laboratory
244 Wood Street
Lexington, MA 02420-9185.

7. SUMMARY

The Advanced Land Imager (ALI) was developed at Lincoln Laboratory under NASA's New Millennium Program (NMP). The instrument concept incorporates a number of innovations addressing the needs and science goals of NASA's Earth Science Enterprise. The program objective is to develop and flight test advanced technologies that will increase the performance and reduce the cost of future land imaging instruments. Lincoln Laboratory had a major role in the instrument design that was refined further during the Preliminary System Design study performed in collaboration with NASA's Goddard Space Flight Center (GSFC).

Following an instrument definition phase in mid-FY96, Lincoln Laboratory began development of the ALI. The instrument has multispectral imaging capabilities and contains a silicon carbide (SiC) optical system with wide field of view ($1.25^\circ \times 15^\circ$), a partially populated focal plane system, an onboard calibration system, and the ancillary structural, thermal, and electrical components required to form an integrated unit. ALI was flown into space aboard the first Earth Observing satellite (EO-1) which was launched on November 21, 2000. Swales Aerospace developed the spacecraft and provided the essential support functions such as attitude control and onboard power.

The key attributes of ALI are that it is smaller in both size and weight than the Enhanced Thematic Mapper (ETM+) of Landsat 7, by a factor of four, and requires less power to operate, by a factor of five. It has a total of nine Multispectral (MS) bands plus a Panchromatic band, three more than ETM+, but does not have the thermal band. It has increased sensitivity by a factor varying from four to ten depending upon the band. The spatial resolution of the MS bands is the same as that of ETM+ (30 m) but it is better in the Pan band (10 m versus 15 m).

Lincoln Laboratory was assisted in the development of ALI by two subcontractors: Raytheon/Santa Barbara Remote Sensing (SBRS), who developed the focal plane assembly, and SSG, who developed the telescope. The instrument was assembled and aligned at Lincoln Laboratory and underwent electrical and environmental testing at the proto-flight level. It was then calibrated under thermal vacuum and delivered to NASA/GSFC in March 1999. Lincoln Laboratory supported the spacecraft integration and test activities providing on-site support, data acquisition, analysis, and evaluation. A Calibration Pipeline, based on the instrument ground calibration data, was provided to NASA/GSFC at the beginning of the flight test program.

The analysis of the data collected during the instrument ground calibration has been completed. The results have been documented in a series of reports listed in the references. Briefings to the sponsor and industry and conference presentations have been made and will continue throughout the year to implement technology transfer.

ALI has been functionally validated in space collecting up to ten scenes per day, as commanded. Lincoln Laboratory is using the flight data to conduct the instrument performance assessment and comparisons with other imagers (e.g., Landsat7). These comparisons have been very favorable for ALI, demonstrating the instrument's increased sensitivity and spatial resolution.

An updated version of the Calibration Pipeline, reflecting the results of the on-orbit calibrations, has been delivered to NASA and is being used for flight data calibration. The Calibration Pipeline includes routines for correcting various image artifacts. The Pipeline is used to generate calibrated, spatially reconstructed earth scenes for dissemination to other investigators.

Since ground testing of the assembled instrument in thermal vacuum, it was observed that some contaminant gradually accumulates on the cold focal plane. To deal with the problem, heaters have been provided to warm up the focal plane and boil off the contaminant. This operation is carried out every ten days on-orbit and lasts for about twenty hours. While the focal plane is warm, SWIR data cannot be taken due to the increased noise, however the VNIR data are good. The telemetry data is being used for instrument parameter trending and overall health assessment. So far, the instrument has shown excellent stability.

Spacecraft issues that can be addressed through ALI include assessment of jitter and absolute pointing accuracy by earth scene measurements and yaw correction methodology. These investigations are in progress.

Work has been completed at NASA to define the Landsat Data Continuity Mission (LDCM) which is expected to be based on the ALI technologies. Lincoln Laboratory participated in this effort, by assisting NASA in the development of the procurement specifications, and will be available to serve as a technical consultant to the eventual developer.

8. TECHNICAL REFERENCES

1. J. A. Mendenhall et al., "Earth Observing-1 Advanced Land Imager: Instrument and Flight Operations Overview," MIT/LL Project Report EO-1-1, 23 June 2000.
2. "Landsat 7 System Specification," Revision K, NASA Goddard Space Flight Center, 430-L-0002-K, July 1997.
3. J. A. Mendenhall, "Earth Observing-1 Advanced Land Imager: Dark Current and Noise Characterization and Anomalous Detectors," MIT/LL Project Report EO-1-5, 7 May 2001.
4. J. A. Mendenhall, D. E. Lencioni, J. B. Evans, "Earth Observing-1 Advanced Land Imager: Radiometric Response Calibration," MIT/LL Project Report EO-1-3, 29 November 2000.
5. D. R. Hearn, "EO-1 Advanced Land Imager Modulation Transfer Functions," *MIT Lincoln Laboratory Technical Report 1061*, 22 March 2000.
6. D. R. Hearn, "Earth Observing-1 Advanced Land Imager: Detector Line-of-Sight Calibration," MIT/LL Project Report EO-1-4, 29 December 2000.
7. J. A. Mendenhall, D. P. Ryan-Howard, "Earth Observing-1 Advanced Land Imager: Spectral Response Calibration," MIT/LL Project Report EO-1-2, 20 September 2000.
8. J. A. Mendenhall et al., "Initial Flight Test Results from the EO-1 Advanced Land Imager: Radiometric Performance," IGARSS 2001, Sydney, 9 July 2001.
9. D. E. Lencioni, J. A. Mendenhall, D. P. Ryan-Howard, "Solar Calibration of the EO-1 Advanced Land Imager," IGARSS 2001, Sydney, 9 July 2001.
10. eo1.gsfc.nasa.gov/Technology/StrayLightIssues.html
11. "Report and Recommendations from EO-1 ALI SiC Optics Performance Workshop," May 29, 1998, found at eo1.gsfc.nasa.gov/Technology/StrayLightIssues.html
12. "Stray Light Analysis Report No. 3," prepared by Lambda Research Corporation, Littleton, MA 01460-4400, May 4, 1998
13. Thome, K.J., "Absolute radiometric calibration of Landsat 7 ETM+ using the reflectance-based method," *Remote Sensing of Environment*, 78, 2001, 27-38.
14. Bigger, S. F., Private Communication, May 2001.
15. Kieffer, H.H, Anderson, J.A., "Use of the Moon for spacecraft calibration over 350-2500 nm," *Proc. SPIE*, 2438, 325-335, 1998.
16. J. A. Mendenhall and M. D. Gibbs, "Earth Observing-1 Advanced Land Imager Flight Performance Assessment: Noise and Dark Current Trending for the First 60 Days," MIT/LL Project Report EO-1-7, 1 June 2001.
17. J. A. Mendenhall, "Earth Observing-1 Advanced Land Imager Flight Performance Assessment: Investigating Dark Current Stability Over One-half Orbit Period During the First 60 Days," MIT/LL Project Report EO-1-6, 1 July 2001.

9. PUBLICATIONS

1. D. E. Lencioni and D. R. Hearn, "New Millennium EO-1 Advanced Land Imager," *International Symposium on Spectral Sensing Research*, San Diego, Dec. 13-19, 1997.
2. "Report and Recommendations from EO-1 ALI SiC Optics Performance Workshop," May 29, 1998, found at <http://eo1.gsfc.nasa.gov/Technology/StrayLightIssues.html>
3. "Stray Light Analysis Report No. 3," prepared by Lambda Research Corporation, Littleton, MA 01460-4400, May 4, 1998.
4. C. J. Digenis, D. E. Lencioni and W. E. Bicknell, "New Millennium EO-1 Advanced Land Imager," *SPIE Conference on Earth Observing Systems III*, San Diego, California, Proc. SPIE, Vol. 3439, pp. 49-55, July 1998.
5. J. A. Mendenhall, D. E. Lencioni, D. R. Hearn and A. C. Parker, "EO-1 Advanced Land Imager preflight calibration," Proc. SPIE, Vol. 3439, pp. 390-399, July 1998.
6. D. R. Hearn, "Characterization of instrument spectral resolution by the spectral modulation transfer function," Proc. SPIE, Vol. 3439, pp. 400-407, July 1998.
7. J. A. Mendenhall, D. E. Lencioni, D. R. Hearn and A. C. Parker, "EO-1 Advanced Land Imager in-flight calibration," Proc. SPIE, Vol. 3439, pp. 416-422, July 1998.
8. W. E. Bicknell, C. J. Digenis, S. E. Forman and D. E. Lencioni, "EO-1 Advanced Land Imager," *SPIE Conference on Earth Observing Systems IV*, Denver, Colorado, Proc. SPIE, Vol. 3750, pp. 80-88, July 1999.
9. D. E. Lencioni, D. R. Hearn, J. A. Mendenhall and W. E. Bicknell, "EO-1 Advanced Land Imager calibration and performance," *SPIE Conference on Earth Observing Systems IV*, Denver, Colorado, Proc. SPIE, Vol. 3750, pp. 89-96, July 1999.
10. D. R. Hearn, J. A. Mendenhall and B. C. Willard, "Spatial calibration of the EO-1 Advanced Land Imager," *SPIE Conference on Earth Observing Systems IV*, Denver, Colorado, Proc. SPIE, Vol. 3750, pp. 97-108, July 1999.
11. J. A. Mendenhall and A. C. Parker, "Spectral calibration of the EO-1 Advanced Land Imager," *SPIE Conference on Earth Observing Systems IV*, Denver, Colorado, Proc. SPIE, Vol. 3750, pp. 109-116, July 1999.
12. J. A. Mendenhall, D. E. Lencioni and A. C. Parker, "Radiometric calibration of the EO-1 Advanced Land Imager," *SPIE Conference on Earth Observing Systems IV*, Denver, Colorado, Proc. SPIE, Vol. 3750, pp. 117-131, July 1999.
13. H. Viggh, J. Mendenhall, R. Sayer, J. S. Stuart and M. Gibbs, "An Automated Ground Data Acquisition and Processing System for Calibration and Performance Assessment of the EO-1 Advanced Land Imager," *SPIE Conference on Earth Observing Systems IV*, Denver, Colorado, Proc. SPIE, Vol. 3750, pp. 132-140, July 1999.
14. H. Viggh, J. S. Stuart, R. Sayer, J. Evans, J. A. Mendenhall and M. Gibbs, "Performance Assessment Software for the EO-1 Advanced Land Imager," *SPIE Conference on Earth Observing Systems IV*, Denver, Colorado, Proc. SPIE, Vol. 3750, pp. 141-152, July 1999.

15. J. Evans and H. Viggh, "Radiometric Calibration Pipeline for the EO-1 Advanced Land Imager," *SPIE Conference on Earth Observing Systems IV*, Denver, Colorado, Proc. SPIE, Vol. 3750, pp. 153-161, July 1999.
16. B. C. Willard, "Wide field-of-view Schmidt-sphere imaging collimator," *SPIE Conference on Earth Observing Systems IV*, Denver, Colorado, Proc. SPIE, Vol. 3750, pp. 286-296, July 1999.
17. D. R. Hearn, "Vacuum Window Optical Power Induced by Temperature Gradients," *SPIE Conference on Earth Observing Systems IV*, Denver, Colorado, Proc. SPIE, Vol. 3750, pp. 297-308, July 1999.
18. D. E. Lencioni, C. J. Digenis, W. E. Bicknell, D. R. Hearn and J. A. Mendenhall, "Design and Performance of the EO-1 Advanced Land Imager," *SPIE Conference on Sensors, Systems, and Next Generation Satellites III*, Florence, Italy, 20 September 1999.
19. D. R. Hearn, "EO-1 Advanced Land Imager Modulation Transfer Functions," *MIT Lincoln Laboratory Technical Report 1061*, 22 March 2000.
20. J. A. Mendenhall (Editor), "Earth Observing-1 Advanced Land Imager: Instrument and Flight Operations Overview," MIT/LL Project Report EO-1-1, 23 June 2000.
21. J. A. Mendenhall and D. P. Ryan-Howard, "Earth Observing-1 Advanced Land Imager: Spectral Response Calibration," MIT/LL Project Report EO-1-2, 20 September 2000.
22. J. A. Mendenhall, D. E. Lencioni and J. B. Evans, "Earth Observing-1 Advanced Land Imager: Radiometric Response Calibration," MIT/LL Project Report EO-1-3, 29 November 2000.
23. D. R. Hearn, "Earth Observing-1 Advanced Land Imager: Detector Line-of-Sight Calibration," MIT/LL Project Report EO-1-4, 29 December 2000.
24. J. A. Mendenhall, "Earth Observing-1 Advanced Land Imager: Dark Current and Noise Characterization and Anomalous Detectors," MIT/LL Project Report EO-1-5, 7 May 2001.
25. J. A. Mendenhall and M. D. Gibbs, "Earth Observing-1 Advanced Land Imager Flight Performance Assessment: Noise and Dark Current Trending for the First 60 Days," MIT/LL Project Report EO-1-7, 1 June 2001.
26. J. A. Mendenhall, "Earth Observing-1 Advanced Land Imager Flight Performance Assessment: Investigating Dark Current Stability Over One-half Orbit Period During the First 60 Days," MIT/LL Project Report EO-1-6, 1 July 2001.
27. D. R. Hearn, C. J. Digenis, D. E. Lencioni, J. A. Mendenhall, J. B. Evans and R. D. Welsh, "EO-1 Advanced Land Imager Overview and Spatial Performance," IGARSS 2001, Sydney, 9 July 2001.
28. J. A. Mendenhall, D. R. Hearn, J. B. Evans, D. E. Lencioni, C. J. Digenis and R. D. Welsh, "Initial Flight Test Results from the EO-1 Advanced Land Imager: Radiometric Performance," IGARSS 2001, Sydney, 9 July 2001.
29. D. E. Lencioni, J. A. Mendenhall and D. P. Ryan-Howard, "Solar Calibration of the EO-1 Advanced Land Imager," IGARSS 2001, Sydney, 9 July 2001. (Poster Session).

30. J. B. Evans, C. J. Digenis, M. D. Gibbs, D.R. Hearn, D.E. Lencioni, J.A. Mendenhall and R.D. Welsh, "On-Orbit Test Results from the EO-1 Advanced Land Imager," SPIE Conference, San Diego, July 2001.
31. J. A. Mendenhall and D. E. Lencioni, "EO-1 Advanced Land Imager On-Orbit Radiometric Calibration," IGARSS 2002, Toronto, 24-28 June 2002.
32. J. A. Mendenhall and D. E. Lencioni, "EO-1 Advanced Land Imager Stray Light Analysis and Impact on Flight Data," IGARSS 2002, Toronto, 24-28 June 2002.
33. J. A. Mendenhall, D. R. Hearn and D. E. Lencioni, "Comparison of Earth Observing-1 Advanced Land Imager Performance with the Landsat Data Continuity Mission Specification", MIT/LL Project Report EO-1-8, 4 June 2002.
34. J. A. Mendenhall and D. E. Lencioni, "Earth Observing-1 Advanced Land Imager Flight Performance Assessment: Absolute Radiometry and Stability During the First Year," MIT/LL Project Report EO-1-10, 31 May 2002.

REPORT DOCUMENTATION PAGE

Form Approved
OMB No. 0704-0188

Public reporting burden for this collection of information is estimated to average 1 hour per response, including the time for reviewing instructions, searching existing data sources, gathering and maintaining the data needed, and completing and reviewing the collection of information. Send comments regarding this burden estimate or any other aspect of this collection of information, including suggestions for reducing this burden, to Washington Headquarters Services, Directorate for Information Operations and Reports, 1215 Jefferson Davis Highway, Suite 1204, Arlington, VA 22202-4302, and to the Office of Management and Budget, Paperwork Reduction Project (0704-0188), Washington, DC 20503.

1. AGENCY USE ONLY (Leave blank)		2. REPORT DATE 4 June 2002	3. REPORT TYPE AND DATES COVERED Project Report	
4. TITLE AND SUBTITLE EO-1 Advanced Land Imager Technology Validation Report			5. FUNDING NUMBERS C—F19628-00-C-0002	
6. AUTHOR(S) J.A. Mendenhall, C.F. Bruce, C.J. Digenis, D.R. Hearn, D.E. Lencioni				
7. PERFORMING ORGANIZATION NAME(S) AND ADDRESS(ES) Lincoln Laboratory, MIT 244 Wood Street Lexington, MA 02420-9108			8. PERFORMING ORGANIZATION REPORT NUMBER PR-EO-1-9	
9. SPONSORING/MONITORING AGENCY NAME(S) AND ADDRESS(ES) NASA/GSFC Mr. Ralph Welsh Building 16, Room 21 MS740.3 Greenbelt, MD 20771			10. SPONSORING/MONITORING AGENCY REPORT NUMBER ESC-TR-2001-070	
11. SUPPLEMENTARY NOTES None				
12a. DISTRIBUTION/AVAILABILITY STATEMENT Approved for public release; distribution is unlimited.			12b. DISTRIBUTION CODE	
13. ABSTRACT (Maximum 200 words) <p>The primary instrument on the first Earth Observing satellite (EO-1) under the New Millennium Program (NMP) is the Advanced Land Imager (ALI) multispectral instrument. Overall direction of the EO-1 mission and acquisition of the spacecraft is being carried out by the Goddard Space Flight Center (GSFC) of NASA. MIT Lincoln Laboratory developed the Advanced Land Imager with NMP instrument team members Raytheon Systems Santa Barbara Remote Sensing (focal plane) and SSG Inc. (optical system). This instrument includes an optical system, a focal plane system, a calibration system, and the structural, thermal, and electrical components required to form an integrated unit. Lincoln Laboratory was responsible for the design, fabrication, test and development of the instrument, the software and databases for calibration, and is responsible for on-orbit performance assessment.</p> <p>This document provides a detailed overview of the instrument, preflight calibration techniques and results, and pre-flight environmental testing. In-flight calibration techniques and results are also reviewed and lessons learned related to the transfer of ALI technology to the Landsat Data Continuity Mission (LDCM) are provided.</p>				
14. SUBJECT TERMS			15. NUMBER OF PAGES 252	
			16. PRICE CODE	
17. SECURITY CLASSIFICATION OF REPORT Unclassified	18. SECURITY CLASSIFICATION OF THIS PAGE Unclassified	19. SECURITY CLASSIFICATION OF ABSTRACT Unclassified	20. LIMITATION OF ABSTRACT Same as Report	